HETEROGENEOUS CATALYSIS:

Fundamentals and Applications of Metal Oxides

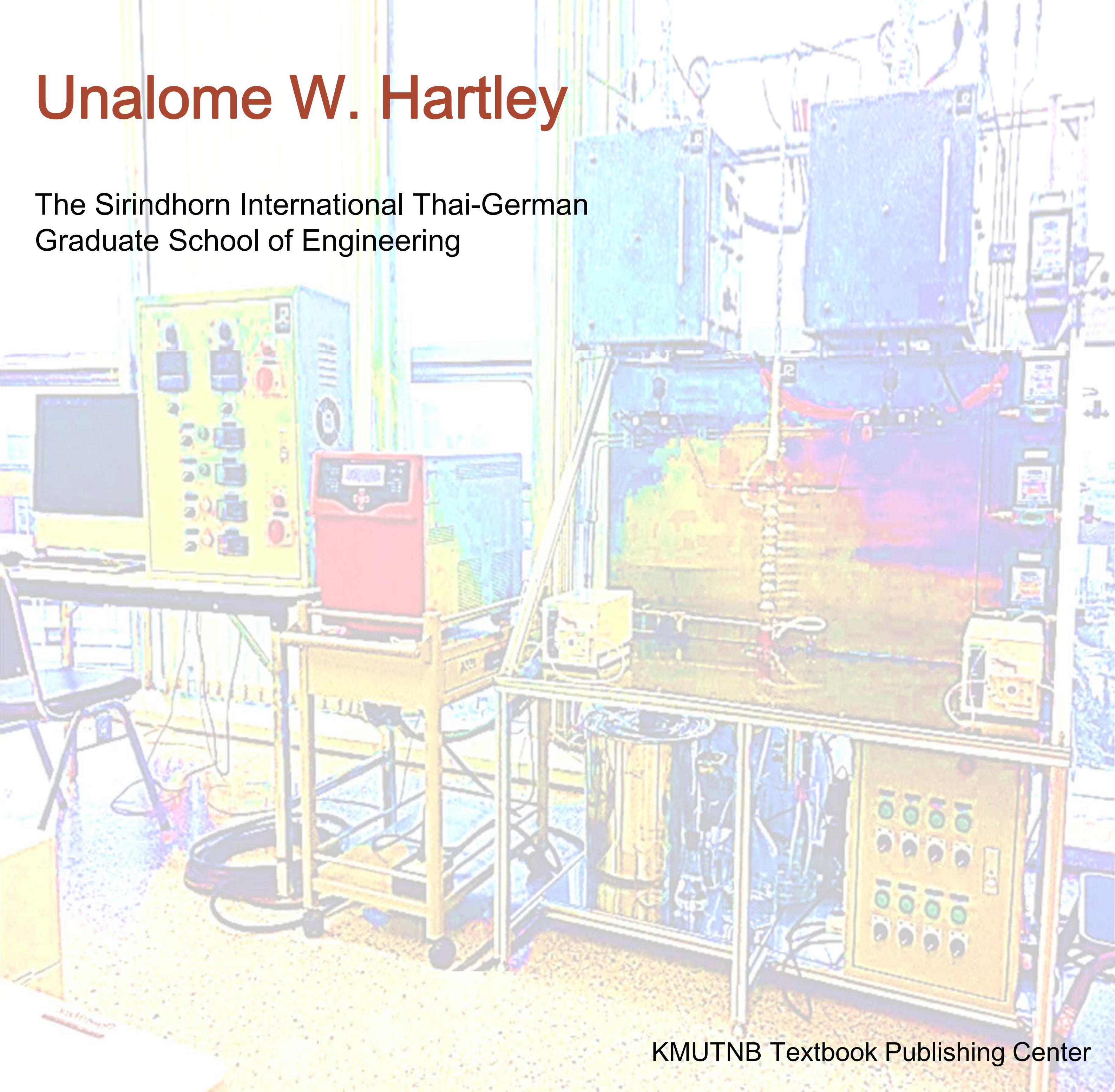

Unalome W. Hartley

The Sirindhorn International Thai-German
Graduate School of Engineering

KMUTNB Textbook Publishing Center

Heterogeneous Catalysis:

Fundamentals and Applications of Metal Oxides

ข้อมูลทางบรรณานุกรมของสำนักหอสมุดแห่งชาติ
National Library of Thailand Cataloging in Publication Data

Unalome Wetwatana Hartley.
Heterogeneous Catalysis:Fundamentals and Applications of Metal Oxides.-- Bangkok : King Mongkut's University of Technology North Bangkok, 2022.
276 p.

1. Catalysts. 2. Metal catalysts. 3. Metallic oxides. I. Title.

660.2995
ISBN 978-616-590-137-6

Edited and Published by Assoc. Dr. Unalome Wetwatana Hartley

ISBN 978-616-590-137-6

First Edition February, 2022 100 copies

Price 300 baht

Printed at Textbook Publishing Center, King Mongkut's University of Technology North Bangkok
1518 Pracharat 1 Road, Wongsawang, Bangsue Bangkok 10800, Thailand
Tel: +66-2555-2000 Ext. 1436, 1437 Fax: +66-2586-9012
www.textpub.kmutnb.ac.th

Heterogeneous Catalysis:

Fundamentals and Applications of Metal Oxides

Unalome Wetwatana Hartley
The Sirindhorn International Thai-German Graduate School of Engineering
King Mongkut's University of Technology North Bangkok

KMUTNB Textbook Publishing Center

PREFACE

Have you ever wondered why the catalyst was invented at all?

Well, every innovation in the world starts from ‘wanting more’. The greedy passion of mankind that is probably related to the hedonic adaptation hypothesis.

When it comes to chemical productions, often the producers would ask themselves – how can I produce more while using less amount of resource under the shorter period of time?

And here we are, where the catalysis science starts to get involved in almost every chemical processes.

A history of chemistry, in many ways, is a history of civilization. Through the rise and fall of all empires, chemistry can be found in almost everything; let it be agriculture, pesticides, writing, death, food preservations or medicines. When the simple agriculture was established since 8,000 years ago, the catalysis was only invented in 1794 by Elizabeth Fulhame, a female and forgotten Scottish chemist, and this is where the whole story begins…

CONTENTS

CHAPTER 1
INTRODUCTION

1.1 CATALYSIS

Catalysis is a process where small amount of a non-reactant substance is used to accelerate the reaction rate (how fast the reaction can go forward). This substance is called catalyst. In general, the catalyst is not overall consumed within the reaction, instead, it is recycled by being regenerated back to its original form by the environmental substances. This is why the catalytic reaction is basically a cyclic process. However, this cycle is not going on forever as the catalyst has a particular life span, depending on its type and nature, and can be deactivated by unfriendly impurities or even the operating temperature. Therefore, most catalysts require a standard handling protocol called ‘regeneration process’ where the deactivated catalyst is activated to be again functional.

Catalyst in fact can alter the chemical pathway, to the easier direction. By saying ‘easier’, this mean having lower activation energy – in another word, the reaction energy’s barrier. A good catalyst can encourage a higher yield of desired products, narrower the range of the product distribution, lower operating temperature and fewer unwanted associated reactions.

Again, why do we use a catalyst? Here is the summary of the major reasons [1];

1. It allows the desired reaction to occur faster.
2. It suppresses the competitive reactions.
3. From 1 and 2, it results in higher selectivity and narrower product distribution.
4. The reaction is able to occur at lower temperature (safer and cheaper) for kinetically limited exothermic near-equilibrium reactions.
5. A catalyst helps us to understand if the reaction is more thermodynamically favored.
6. For endothermic near-equilibrium reaction which needs to be operated at high temperature to overcome its kinetic limitation, the catalyst would allow the reaction to occur at medium high temperature. As a result, the reaction can be rather considered ‘quite thermodynamically favorable’, leading to less energy waste.
7. Lower operating temperature obtained from using the optimized catalyst allows cheaper materials for reactor’s fabrication.

8. Using an appropriate catalyst is like optimizing the chemical reaction i.e. smaller reactor can be used while still keeping the same level of performance, lower number of recycle cycles and shorter residence time.

1.2 HISTORY

One of the oldest catalytic reaction is production of alcoholic beverage (of course!) via fermentation process. However, a more sophisticated reactions; i.e. soap production by fat hydrolysis, diethyl ether production from ethanol dehydration; were started in 16th centuries when the phenomenon of catalysis was officially recognized by Berzelius [2,3]. Around the same time, Mitscherlich [3] also defined the term 'contact catalysis' where the catalyst is solid. This initiates later the term 'heterogeneous catalysis' which is widely used in the last 100 years. In 1895, Ostwald, a Nobel laureate for Chemistry in 1909, proposed a concept defining that a catalyst is not consumed in the process, besides, is only temporarily spent to accelerate the rate of reaction. From 1830 to 1900, more practical industrial-wise processes are developed. Platinum (Pt) wire was used as a catalyst in flameless CO combustion for the first time. Pt was also applied in SO_2 oxidation and NH_3 conversion to NO. Another Nobel laureate in 1912, Sabatier found the use of Ni and Co for catalyzing hydrogenation of ethylene and CO [3]. The first groundbreaking innovation in catalysis is the famous ammonia synthesis, discovered by Haber [3] in 1908. The first high pressure and temperature reactor was made by Bosch [4] using osmium as a catalyst for this ammonia production. The process was later commercialized by BASF in 1913 as Haber-Bosch process [4] which is well utilized for fertilizer production. Iron catalyst was invented by Mittasch [5] for Haber-Bosch process later. From 1928 to 1932, the most distinctive chemical reactions include methanol synthesis from syngas using $ZnO-Cr_2O_3$, petroleum cracking to fuels using acid clay, olefins production and aviator gasoline in the presence of $AlCl_3$ which led to a commercial process of UOP later. In 1938 during the World War II, Bergius [5] found a method to produce liquid fuels from coal via high pressure hydrogenation in the presence of Fe catalyst. During the same period, Fischer-Tropsch process was invented in Germany, the country which has no access to natural petroleum resources [6]. The process is for a production of synthetic fuels (liquid hydrocarbons and oxygenated compounds) from syngas. The process was still beneficial even after the World War II. In 1955, Sasol Co. continued to operate 2 large plants (~3 million ton per annual) in South Africa. Catalytic homogeneous oxo synthesis was found by Ruhr-Chemie in 1942 [7]. This process allows aliphatic aldehydes synthesis from reaction of syngas and olefins over Co carbonyls catalyst. Table 1.1 presents important catalytic processes during and after World War II.

Table 1.1: Commercialized catalytic processes during and after World War II until 1970 [8,9].

Year	Catalyst	Process	Products
1939 - 1945	Pt-Al_2O_3	Dehydrogenation	Toluene from methyl cyclohexane
	Cr_2O_3-Al_2O_3	Dehydrogenation	Butadiene from n-butane
	$AlCl_3$	Alkane isomerization	*i*-C_7-C_8 from n-alkanes
1946 - 1960	V_2O_5	Oxidation of aromatic	Phthalic anhydride from naphthalene and *o*-xylene
	Ni-alumino silicate	Hydrocracking	Fuels from high petroleum fractions
	$TiCl_4$-$Al(C_2H_5)_3$	Polymerization (Ziegler-Natta)	Polyethylene from ethylene
	Fe_2O_3-Cr_2O_3-KOH	Dehydrogenation	Styrene from ethyl benzene
	$PdCl_2$-$CuCl_2$	Oxidation	Acetaldehyde from ethylene
1961 - 1970	Ni-α-Al_2O_3	Steam reforming	Syngas from methane
	Bi-phosphomolybdate	Ammoxidation	Acrylonitrile from propene
	H Zeolite - aluminosilicates	Fluid catalytic cracking	Fuels
	Bimetallic catalysts (Pt, Sn, Re, Ir)	Reforming	Gasoline
	Cu-ZnO-Al_2O_3	Low-pressure methanol synthesis	Methanol from CO, H_2 and CO_2
	Enzymes immobilized on SiO_2	Isomerization	Fructose from glucose (soft drink production)
	ZSM-5, mordenites	Distillate dewaxing	Removal of *n*-alkanes from gasoline
	Hydrorefining	Ni-, Co-MoS_x	Hydro-desulfurization, hydro-denitrification

1.3 WHY SOLID CATALYSTS?

Heterogeneous catalytic process was referred as ‘contact process’ in the past as mentioned previously. Since around 180 years ago when sulfuric production was invented in 1831, the heterogeneous catalysis becomes crucial in industrial chemistry. The production of the catalysts is then unavoidably becoming a big business for chemical industry. How big? Something like 13 billion dollars per year [1,10]. Table 1.2 summarizes some important industrial catalysts.

85% of chemical processes are catalyzed and most of them, by solid catalysts. Why is solid preferred with respect to liquid? Here are some good reasons; (1) Easier separation from fluid reactants, (2) Likely to be more environmentally friendly, (3) Handling procedure is considered safer, (4) Regeneration process could be much simpler and (5) Safer disposal.

Question 1.1
Can you think of any catalysts that might have been already utilized in Thai industries?

Table 1.2: Catalyst families utilized in chemical industries [1].

Catalyst	**Sub-family**	**Reaction/function**	**Process**
Oxide catalysts			
γ-Al_2O_3	Bulk single oxide	Lewis acidic catalyst	Alcohol dehydration to olefins
MgO-Al_2O_3 calcined	Bulk mixed oxide	Basic catalyst	Adol condensation
V/MoNb/Sb oxides		Ammoxidation	Propane to acrylonitrile
V_2O_5-TiO_2	Oxide supported on oxide	Selective oxidation	*o*-xylene to phthalic anhydride
K_2O-Cr_2O_3/Al_2O_3		Dehydrogenation	Iso-butane to iso-butene
K_2SO_4-V_2O_5/SiO_2	Impregnated melt or liquid	Oxidation	SO_2 to SO_3
H_3PO_3/SiO_2		Protonic acid catalyst	Olefin oligomerization

(Continued)

Table 1.2: *(Continued)*

Catalyst	Sub-family	Reaction/function	Process
Zeolite catalysts			
H-BEA	Protonic zeolite	Protonic acid catalyst	Benzene + ethylene to ethyl benzene
Fe-MFI	Metal exchanged zeolite	Redox catalyst	N_2O decomposition/reduction
Metal catalysts			
Fe (CaO, K_2O, Al_2O_3, SiO_2 promoters)	Bulk metal	Hydrogenation	Ammonia synthesis
Pt (Rh stabilizer)	Metal gauze	Selective oxidation	Ammonia oxidation to NO
Pd/Al_2O_3 (Ag promoter)	Supported metal	Preferential hydrogenation	Acetylene hydrogenation in ethylene
$Pt\text{-}Rh/Al_2O_3\text{-}CeO_2\text{-}ZrO_2$		Combustion, NO reduction	Car catalytic mufflers
Pt/carbon		Liquid phase oxidation	Alcohols to aldehydes
Pt/K-L zeolite		Dehydrogenation	Aromatization of paraffins
Sulfide catalysts			
MoS_2	Bulk sulfide	Hydrocracking	Bituminous sands to oil fractions
$NiS\text{-}MoS_2/\gamma\text{-}Al_2O_3$	Supported sulfide	Hydro-desulfurization	Gasoline treatment

For the developing catalysts, knowledge and know-how in the area of research and development can be reached through many international journals and book series. The more developed but not fully commercialized catalysts can be found in patents, as well as some websites of catalyst producers such as Haldor Topsoe, UOP, Axens, Johnson Matthey, Criterion, Clariant, Albemarie, Grace Davision, BASF and ExxonMobil [1].

Question 1.2
What does a catalyst actually do? As an entrepreneur, why would you want to buy it?

1.4 SUMMARY AND PERSPECTIVES

Not only the catalysis has a long history, but also still a long future and plenty of room to develop. This chapter is intended to explain basic ideas, concepts and important milestone in development of the catalysis. History of catalyst use and its process after WWII had been gathered and tabulated. Some of the processes are still going on recently and some are not, but adapted to the better version of its own. The solid catalyst part in this chapter will be explained in more details in later chapters. In detail, basic theories of catalysis has been describe in chapter 2, including rate laws, Arrhenius equation, activation energy, collision theory and parameters between kinetics and thermodynamics. The deeper knowledge has been explained in this chapter too i.e. the basic component of a catalyst system, volcano plot, spillover phenomenon. Besides, some of the calculation-based models of catalysis such as Monte Carlo and DFT were also described. In chapter 3, type of the catalysts were categorized by their natures and functions. The preparation methods and the post-treatment methodologies; i.e. reduction or calcination; of various metal oxides were also summarized. The characterization techniques were gathered and described in chapter 4 whereas modern applications of most metal oxide catalysts were illustrated in chapter 5. For the following chapters, the students/readers are suggested to follow up the interest subjects/topics from the literatures cited.

REFERENCES

[1] G. Busca, Heterogeneous catalytic materials – solid state chemistry and catalytic Behavior, Elsevier, 2014.
[2] J.J. Berzelius, Quelques Idées sur une nouvelle Force agissant dans les Combinaisons des Corps Organiques, Ann. Chim. Phys. 61 (1836) 146-151.
[3] J. Davis, B. H., Ertl, G., Knozinger, H., Weitkamp, Handbook of heterogeneous catalysis (Vol. 1), Wiley-VCH: Weinheim, 1997.

[4] F. Aftalion, A history of the international chemical industry, Philadelphia: University of Pennsylvania Press, 1991.
[5] A. Mittasch, W. Frankenburg, Early studies of multicomponent catalysts, in: 1950: pp. 81-104. https://doi.org/10.1016/S0360-0564(08)60375-2.
[6] F.Fischer, H. Tropsch, Brennstoff-Chem, 4 (1923) 276.
[7] O. Roelen, German Patent 103,362, U. S. Patent 2,327,066 (1943), 1938.
[8] J.K.A. Clarke, J.J. Rooney, Stereochemical approaches to mechanisms of hydrocarbon reactions on metal catalysts, in: 1976: pp. 125-183. https://doi.org/10.1016/S0360-0564(08)60314-4.
[9] A.J. Gellman, The transition state in catalytic surface chemistry, Curr. Opin. Solid State Mater. Sci. 5 (2001) 85-90. https://doi.org/10.1016/S1359-0286(00)00028-0.
[10] Fundamentals of Port & Berth management for oil & gas, (n.d.). https://www.ptit.org/event/detail?id=31.

ABBRIVIATIONS AND ACRONYM

Syngas	*a gaseous mixture of hydrogen (H_2) and carbon monoxide (CO)*

CHAPTER 2
THEORIES

2.1 BASIC CONCEPTS

2.1.1 COLLISION THEORY

A chemical reaction occurs when molecules of reactants collide each other at a correct orientation with enough energy. If the energy of the collision is less than the activation energy of the reaction (energy required to break the pre-existing bonds and form new bonds), the reaction will not occur. On the other hand, if the collision's energy is overcome the activation energy of the reaction, the reaction will occur and products could be formed. These collision is called 'successful collisions'. There are many ways to increase the rate of reaction by adjusting the collision's features; such as number of collisions, energy of collisions and angle of collisions. The methods can include;

1. To increase pressure – the molecules are pressured to be closer to each other and collide more. The more they collide, the more accumulative energy they possess.
2. To increase concentration of the reactants – number of particles is increased that it becomes crowded in the reactor and collide more.
3. To increase temperature – the particles are more excited by heat, resulting in them travelling faster and carrying more energy.
4. To increase the contact surface – the particles can meet each other more at the right orientation.
5. To use a catalyst – this will reduce E_a and mechanistic pathways of reaction.

2.1.2 CHEMICAL REACTIONS, RATES AND ACTIVATION ENERGY

Consider a simple bimolecular homogeneous reaction [1]:

$$A + B \rightleftarrows C + D \tag{2.1}$$

This equation presents a reversible reaction where an equilibrium stage can be achieved. Figure 2.1 illustrates relation between reaction's progress and energy. When A and B are considered reactants (forward reaction), this Figure 2.1 represents an exothermic reaction where the total energy of the products is less than the total energy of the reactants (where the heat of reaction or the change of enthalpy is always negative). On the other hand, this reaction could well be expressed as being an endothermic reaction when we look at the reverse reaction of C and D converting back to A and B (reverse reaction). For the forward reaction, energy of each molecule of A and B needs to be higher than the activation energy (E_{a1}) to form a transition state complex $A - B$ which later becomes C and D. Once the C and D are formed, and if their molecular energies happen to overcome the activation energy of the reverse reaction (E_{a2}), they can be converted back to re-produce A and B. When the rate of the forward and reverse reactions become equal, the overall reaction process then reaches a 'dynamic equilibrium'. If both forward and reverse reactions are elementary reactions, their rates of reaction can be described, respectively, as;

$$r_f = k_f[A][B] \tag{2.2}$$

$$r_r = k_r[C][D] \tag{2.3}$$

Thus, overall equation can be derived as;

$$R_{eq} = \frac{r_f}{r_r} = \frac{k_f[C][D]}{k_r[A][B]} \tag{2.4}$$

Whereas

$$K_{eq} = \frac{k_f}{k_r} \tag{2.5}$$

Where r_f = rate of forward reaction, r_r = rate of reverse reaction, k_f = rate constant of the forward reaction, k_r = rate constant of the reverse reaction, $[i]$ = concentration of substance i, R_{eq} = overall rate reaction at equilibrium condition and, K_{eq} = equilibrium rate constant of the overall reaction.

While kinetics is about how quickly or slowly species react, the thermodynamics is not exactly dynamic, because it's not about anything moving and changing but instead about "how stable they are in one state versus another". What do they tell us then? Thermodynamics which has nothing to do with time can tell us "if the products has lower free energy (more stable than the reactants) or not", whereas, the kinetics is used to explain "how fast things go, but does not tell us anything about the final state of things once it gets there".

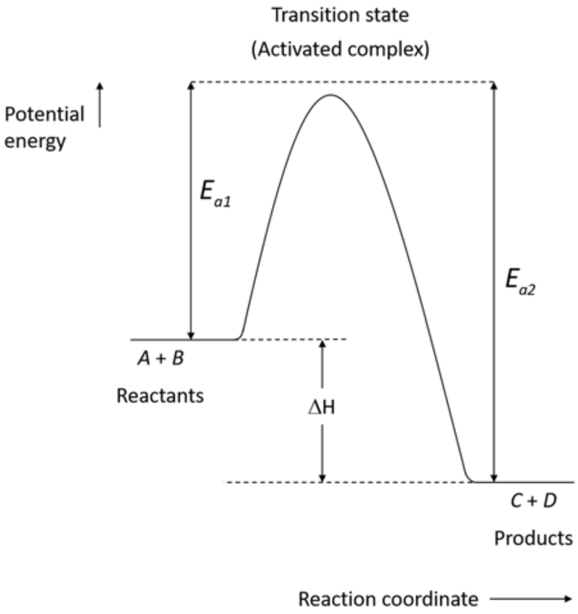

Figure 2.1: Chemical reaction's process and its energies [1].

Question 2.1
Amongst E_1, E_2, ΔH, K_{eq}, k_f, k_r Which variable is referred to kinetics parameter and which to thermodynamics parameter?

Question 2.2
Any ideas if these theories/equations are related to thermodynamics or kinetics aspect or both? 2.2.1 Collision theory 2.2.2 Arrhenius equation 2.2.3 Gibbs free energy equation

Both terms describe rate of reaction. Although **rate law** demonstrates how concentration and rate constant (k) affect the rate of reaction, **Arrhenius equation** explains how the rate of reaction is influenced by temperature (T) and activation energy (E_a). Rate law and Arrhenius equation can be written as equations (2.6) and (2.7), respectively;

$$r = k[A]^a[B]^b \tag{2.6}$$

$$k = k_0 e^{-\left(\frac{E_a}{RT}\right)} \tag{2.7}$$

Thus, together these equations become;

$$r = k_0 e^{-\left(\frac{E_a}{RT}\right)}[A]^a[B]^b \tag{2.8}$$

Where a and b are stoichiometric values of the reaction and orders, k_0 = frequency factor or pre-exponential factor, and R = gas constant.

Considering the Arrhenius equation, k_0 is a factor of frequency and the orientation of the collisions while the term $e^{-\left(\frac{E_a}{RT}\right)}$ demonstrates a fraction between successful collisions and all collisions (f). To increase f, T can be increased while E_a can be decreased. An increase f will increase k (equation (2.7)) resulting in an increase in r (equation (2.7)).

Question 2.3
What does f mean from solving the below questions? 2.3.1 E_a = 40 kJ/mol at T = 100 °C 2.3.2 E_a = 10 kJ/mol at T = 100 °C 2.3.3 E_a = 10 kJ/mol at T = 200 °C

Question 2.4
Having learnt about Arrhenius equation where the rate of reaction depends on temperature and activation energy, we know that T can be changed by adding/withdrawing heat but how can E_a be changed?

Arrhenius equation can be linear plotted by taking natural logarithm of equation (2.7), the equation will then be;

$$\ln k = \ln k_0 - \frac{E_a}{RT} \tag{2.9}$$

The readily usable forms of Arrhenius is the (1) Arrhenius for T change, and another version for (2) Arrhenius for E_a change. The 2 version of equations are derived as shown below;

For T_1 and T_2;

$$\ln k_1 = \ln k_0 - \frac{E_a}{RT_1} \tag{2.10}$$

$$\ln k_2 = \ln k_0 - \frac{E_a}{RT_2} \tag{2.11}$$

The difference between equations (2.10) and (2.11) is;

$$\ln k_1 - \ln k_2 = \frac{E_a}{R}\left(\frac{1}{T_2} - \frac{1}{T_1}\right) \tag{2.12}$$

$$\ln \frac{k_1}{k_2} = \frac{E_a}{R}\left(\frac{1}{T_2} - \frac{1}{T_1}\right) \tag{2.13}$$

$$\boxed{\ln \frac{k_1}{k_2} = \frac{E_a}{R}\left(\frac{T_1 - T_2}{T_1 T_2}\right)} \tag{2.14}$$

For E_{a1} and E_{a2};

$$\ln k_1 = \ln k_0 - \frac{E_{a1}}{RT} \tag{2.15}$$

$$\ln k_2 = \ln k_0 - \frac{E_{a2}}{RT} \tag{2.16}$$

The difference between equations (2.15) and (2.16) is;

$$\ln k_2 - \ln k_1 = \left(\frac{E_{a1} - E_{a2}}{RT}\right) \tag{2.17}$$

$$\boxed{\ln \frac{k_2}{k_1} = \left(\frac{E_{a1} - E_{a2}}{RT}\right)} \tag{2.18}$$

Question 2.5
Explain equations (2.14) and (2.18) using graphical method

2.1.3 MAXWELL-BOLTZMANN DISTRIBUTION

Maxwell-Boltzmann distribution is referred to as a trend of small bar graphs in series defining amount of molecules categorized by their kinetics energy or thermal level [2], in other word, is a bell-curve graph explaining relation between number of molecules and their energies. Only the molecules that have energy higher than the reaction's activation energy are able to become the products. The distribution is not only eligible for fluid, but also solid too. This includes the internal energy of the molecules in solid phase and the potential energy of their position. This graphical distribution illustrates that the higher yield of products can be achieved by either (1) increase the process's temperature so that the particles are excited and have higher energy to overcome E_a (2) reduce the E_a, by using a catalyst. Figure 2.2 shows the Maxwell-Boltzmann distribution comparing what the reaction rate/yield is altered when the temperature is increased (a) and when the E_a is decreased (b).

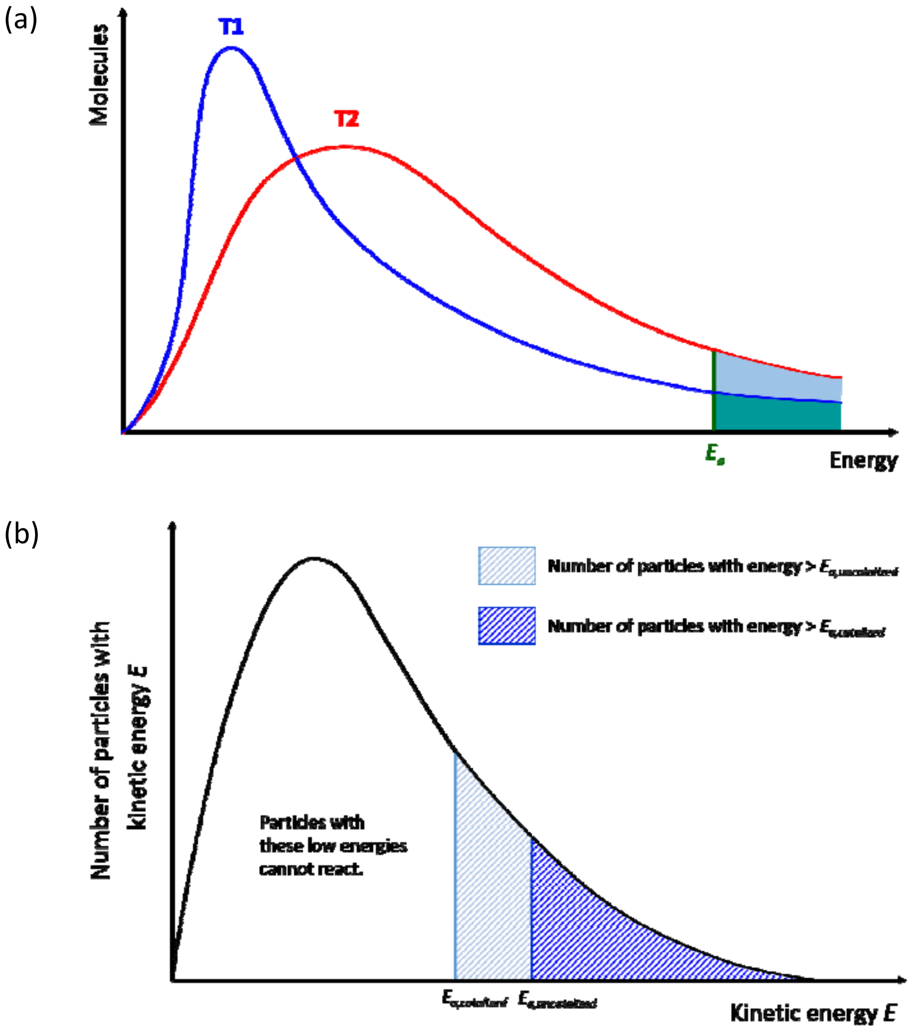

Figure 2.2: Maxwell-Boltzmann distribution when an increase in temperature (a) and a decrease in E_a (b).

Question 2.6
Show that $E_1 - E_2 \; = \; \Delta H$. Remember that $k_1 = Ae^{-\frac{E_1}{RT}}$

Question 2.7
A reaction has E_a= 50,000 j/mol, please describe how the rate is altered if; 2.7.1 Increase the reaction’s temperature from 25 to 35 °C 2.7.2 With the help from a catalyst, the E_a is reduced to 25,000 J/mol while T is constant at 25 °C

2.2 HETEROGENEOUS CATALYSIS

Heterogeneous catalysis is a process where the catalyst and the reactants are in different phase. Normally the heterogeneous catalyst is solid, while the reactants can be either gas and/or liquid. It is well-known that the heterogeneous reaction pathway occurs via 7 steps as shown in Figure 2.3.

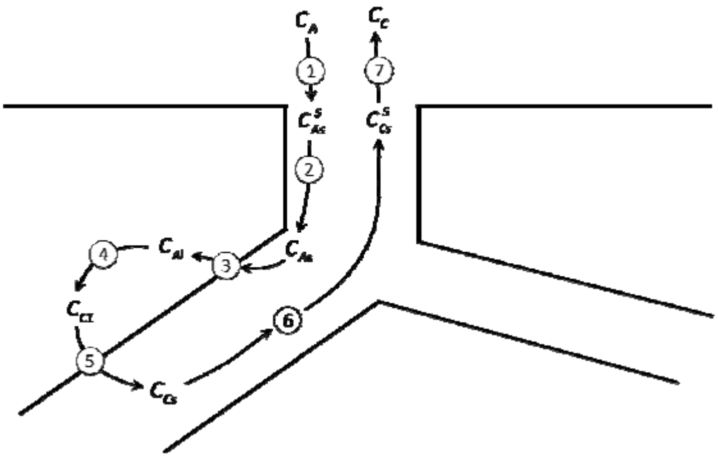

Figure 2.3: 7 steps of heterogeneous reactions.

These steps illustrate how the reactant's molecules are moving from its fluidic bulk stream to reach the catalyst's surface inside its pore. The 7 steps are;

1. Transport of reactant, A, from the main stream to the surface of the catalyst particle.
2. Transport of A in the catalyst's pore.
3. Adsorption of A on the catalyst's active site (the reactive spot of the catalyst).
4. Surface chemical reaction occurs amongst adsorbed species.
5. Desorption of product, C.
6. Transport of C inside the catalyst's pore back to the surface of the catalyst's particle.
7. Transport C from the surface of the catalyst's particle back to the main fluid stream.

Only step 3, 4 and 5 are considered crucial as they occur at the catalyst's surface. The rest of the steps are referred to as diffusion steps. Rate of step 1 and 7 depend on the reactant's flow rate. A too slow flow rate will create a static film-like between the catalyst's surface and the bulk stream whereas a fast flow rate will make this smaller and become easier for reactant's molecules to travel through. Thus, step 1 and 7 can be eliminated totally, by flowing the reactant at a sufficient flow rate that is fast enough to overcome this. On the other hand, step 2 and 6 depend on shape and size of both (1) reactant's molecule and (2) catalyst's pore. The catalyst's pore depends on the catalyst's particle size. Larger particle size will create smaller pore size, thus, small particle size is commonly required. However, the smaller particle size generates greater pressure drop across the catalyst's bed due to its low void fraction. One solution to reduce the pressure drop is to pelletize the catalyst. This will keep the pore size of the catalyst small, while installing an inter-particle diffusion within the pelletized catalyst. The rate of step 3, 4 and 5 together is considered an intrinsic kinetics reaction rate which can be measured by experiment [3]. The process is generally optimized and set to eliminate mass transfer limitation which are step 1, 2, 6 and 7. Often the flow rate was varied to predict whether or not the measuring rate or conversion is overcome the mass transfer limitation or so-called diffusion-control regime [3].

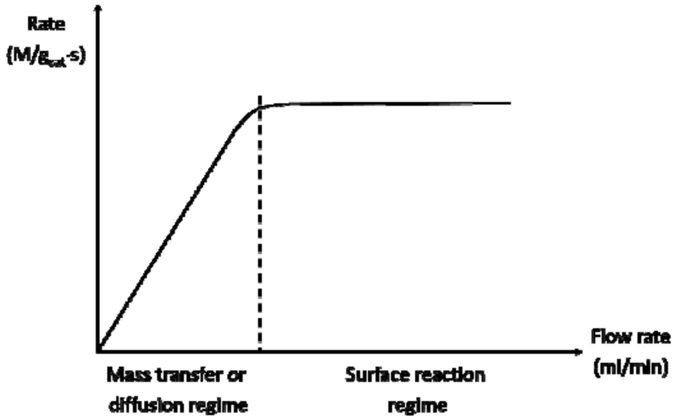

Figure 2.4: Relation between rate of reaction and reactant flow rate.

2.2.1 VOLCANO PLOT

This concept is for heterogeneous catalysis, proposed by Paul Sabatier [4]. The theory states that the interaction between the 'adsorbed species' and the 'catalyst's active site' needs to be just right. If the interaction is too weak, the surface adsorption (step 3 from Figure 2.3) will be hindered. On the other hand, if the interaction is too strong, the surface desorption (step 5 from Figure 2.3) will be suppressed, leading to a failure in the surface dissociation to form a product. The volcano plot expresses relation between (1) a rate of reaction and (2) a measure of intermediate's stability. The stability of the intermediate (adsorbed species) can be practically measured as 'heat adsorption of one of the reactant' or 'heat formation of a bulk compound relative to the surface compound' or even 'heat of formation of any bulk compound that can be correlated with the heat of adsorption' [4]. Figure. 2.5 represents volcano plot for the decomposition of formic acid on various transition metals.

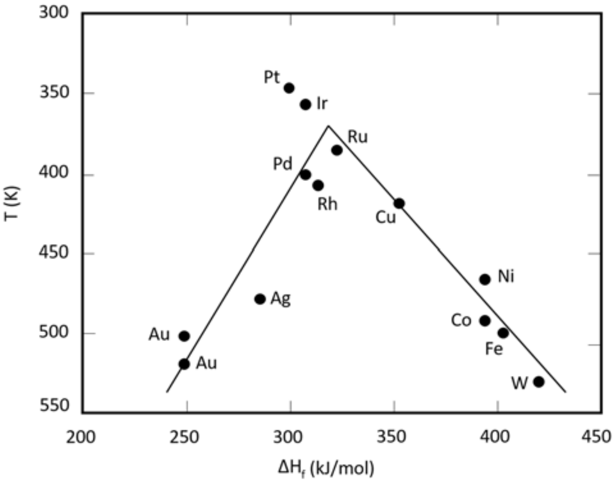

Figure 2.5: Volcano plot for formic acid decomposition using different type of transition metals.

This decomposition of formic acid process was studied by Balandin [5]. The study found that the reaction intermediate is the surface formate, thus, the heat of formation (ΔH_f) of the metal formate salt (x-axis) was plotted against the reaction temperature (T), where a specific reaction rate was reached, (y-axis). From Figure 2.5, when ΔH_f is lower than 300 kJ/mol, bonding's strength between the reactant and the surface is week, thus, a certain rate of reaction is achieved at high temperature (the adsorption rate is too slow, requiring high heat to push the kinetics forward). When ΔH_f is higher than 320 kJ/mol, the bonding's strength becomes too strong for the molecules to decompose/desorb/release product. The higher reaction temperature is also required in this case, to encourage the rate of desorption. Therefore, the best metal catalyst for this reaction is observed at moderate ΔH_f where the rate of adsorption and the rate of desorption are appropriate (too not poor and not too high).

2.2.2 ACTIVE SITES

According to the Sabatier's principle, the transition state (surface intermediate) are formed from the gaseous reactants and catalyst's surface. This is commonly the formation between the reactant's functional group and the catalyst's 'active site'. Langmuir proposed a model of chemisorption on metal surfaces [6]. The model suggested all the surface sites have equal activity with similar energy. These sites are ideally assumed to not reacting to each other, but will adsorb a molecule of the gaseous reactant and become an adsorbed active species. These sites are called 'active sites'. This concept is leading to the well-known 'Langmuir adsorption isotherm' afterwards. Taylor [7] later realistically states that it is possible that all the different atoms on the surface are active, yet as well possible that all the atoms are rarely active. In other words, the surface properties can be very diverse and the shape of surface could be very various i.e. flat, corner or edge. For example, nanocatalyst has a large number of edges and corners (per total surface area) due to its nanostructure. These edges and corners show different coordination numbers, leading to different reactivities and activities. Often, the surface's composition is different from the bulk's composition and, in fact, is gradiently different by each planar crystal of the multi-component materials. This can be looked at as 'surface-segregation' where some elements in the solid catalyst can travel within the crystallographic plan due to the solid concentration gradient. This is called 'solid diffusion'. According to the Taylor's work, the terms 'structure-sensitive' and 'structure-insensitive' reactions were defined by Boudart [8]. The structure sensitive catalyst is a catalyst that its structure plays the main key in its catalytic performance whereas the structure insensitive catalyst is the opposite, where different plans or different crystal offer the same catalytic activity. Most of the solid catalysts are surprisingly considered structure insensitive. Taylor also expressed that, in some particular reactions, the catalyst's surface can adapt itself to suit the reaction's condition such as the surrounding reactants, temperature or pressure. This is called 'surface-reconstruction' [9]. The urge of this phenomenon is explained by the theory of 'minimization of the surface free energy'. Thus, the most precise method for the surface property's characterization is an in situ method where the active sites are observed under the operating condition. The active sites can be anything from metals, metal cations, metal anions, Lewis acids, Brønsted acids, chemisorption of acid-basic pairs, organometallic compounds or immobilized enzymes. Active sites can also be a group of atoms or species and can be embedded in the surface of a metrix in which the neighboring atoms act as ligands. This is defined as 'coordinatively unsaturated sites' by Burwell [10] or 'coordinatively unsaturated metal sites' (CUMSs). The surface coordination chemistry or surface organometallic chemistry may be the key to study solid catalyst's surface phenomenon. In addition, 'band theory' was proposed by Hauffe [11], to correlate catalytic performance with bulk electronic properties. The theory, for mainly oxide catalyst, was later made more completed by Stone [12].

2.2.3 PROMOTERS AND MODIFIERS

Modifiers are the catalyst's additives which are used to adjust performance of the catalyst in real industries. If the modifier encourage the catalytic performance of the catalyst, the modifier in this case is called 'a promoter'. The modifier that suppress the catalytic performance, on the other hand, is called 'a catalyst poison', which could be useful to hinder the unwanted associated reactions in order to reduce yield of the unwanted products, leading to an increase in selectivity [4]. For example, in an exothermic reaction (such as selective catalytic oxidation) where a hot spot sometimes occurs from poor heat transfer management (heat released from the reaction is accumulated at a particular spot of the catalyst due to bad heat transfer). This hotspot sometimes generates undesirable products (such as CO and CO_2) and can lead to thermal deactivation of the catalyst. If the hotspot is occurred from too high exothermic-reaction rate, a modifier is required to decrease the rate. Thus, in this case, the modifier is considered a poison because it slows down the rate, but also a promoter as it still enhances selectivity and stability. Modifiers work by altering the binding energy of active sites or their structures e.g. alloying active and inactive metals together. For example, iron (Fe) based catalysts, for ammonia synthesis is promoted, by adding alumina (Al_2O_3) and potassium oxide (K_2O) into the catalyst system. Alumina acts as a 'textural promoter' because it increases the overall melting point of the catalyst's system, thus preventing the iron coagulation on the surface. Also iron on the surface could well be stabilized by alumina. In this case, it works as a 'structural promoter'. Meanwhile, potassium oxide has influences on (1) adsorption kinetics of dinitrogen (N_2) (2) dissociation of dinitrogen and (3) binding energy of nitrogen on the iron sites. Thus, the potassium oxide is considered as 'electronic promoter'. Another example is a bi-functional catalyst, Pt-supported alumina. The alumina is made super acidic by adding chloride. This catalyst appears to lose chloride during the catalytic process due to the high operating temperature, therefore, CCl_4 is fed into the system to maintain the chloride level.

2.2.4 SUPPORTS AND THEIR INTERACTION TO THE ACTIVE SPECIES

Because the heterogeneous catalytic reaction can only occur at contacting area (i.e. between the solid catalyst and the fluid reactants). Thus, the more surface area of the catalyst, the more rate of reaction is achieved. The catalyst's support is generally a high surface area solid material that is added into the catalyst's system, aiming to increase the surface area of the overall system. In supported catalyst system, the active phase (metal, oxide, sulfide) is unavoidably interacting with the support. This is largely measured by the 'surface free energy of the support phase and active phase' and by the 'interfacial free energy between the support phase and active phase' [4]. Normally the solid state mobility occurs when the temperature is half of the bulk solid's melting point, called 'Tammann temperature'. The solid state mobility leads to the active site wetting the support surface, resulting in a monolayer-type catalysts. The active species normally have high surface free energy which made them very active. Thus, the active species tend to agglomerate to reduce their energy. The support is then added to the catalyst system to stabilize the active species by interacting with the active species. This phenomenon is defined as 'metal-support interaction (MSI)'. In additions, smaller size of particles are more influenced by the active-support interactions in terms of its physical properties and morphology. The nature of support material therefore affects the catalytic properties of the active species. The active species can be encapsulated by the support material if it's treated under some particular conditions; i.e. reducing atmosphere, high temperature; causing the 'strong metal-support interactions' (SMSI). While the electronic properties of the active species are influenced by SMSI, the decrease in adsorption capacity (between active site and reactant) is largely affected by its geometry. For better understanding, Figure 2.6 illustrates active site-support interactions in various conditions. When the active metal is impregnated on the support, the metal particles are equally spread uniformly over the support (Figure 2.6 (a)). After low temperature calcination (in air), the metal oxide compound is generally formed on top of the support (Figure 2.6 (b)). If it is afterwards treated under reducing atmosphere, e.g. 10%H_2/N_2, the oxygen in the metal oxide compound will be released causing a well-dispersed metal particles over the support (Figure 2.6 (c)). This metal particles can be reversed back to metal oxide compound too by treating it again under oxidizing atmosphere, e.g. air or O_2 (Figure 2.6 (b)).

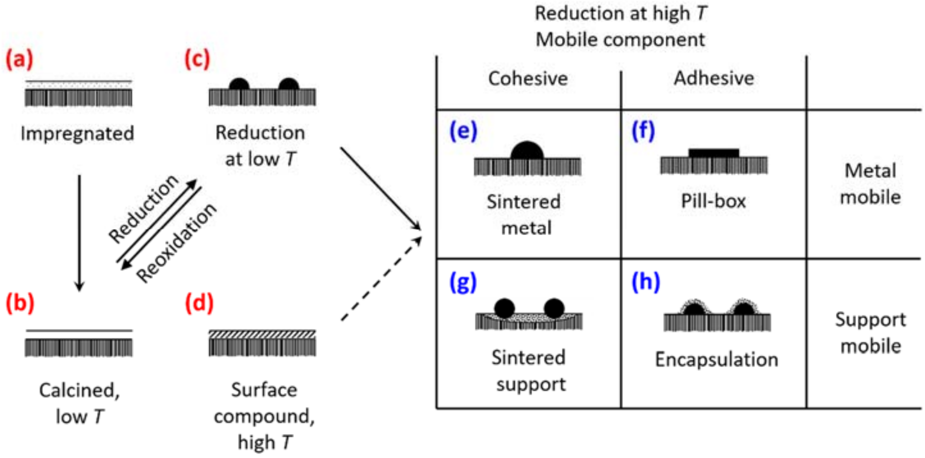

Figure 2.6: Active site-support interactions under various conditions [4].

The calcination temperature that is too high, will enable solid diffusion of elements contained in the support to the surface, causing the formation of other surface compounds (d). Also high temperature under reducing condition could result in metal agglomeration. When the cohesive force is dominant, the agglomeration is classified as 'sintered metal' morphology (Figure 2.6 (e)). On the other hand, if the adhesive force plays larger role, the agglomeration is seen as 'pill-box' morphology (Figure 2.6 (f)). These cases happen when the metal gets mobile. Contradictorily, when the support phase is travelling, the 'sintering' of support could occur while the small metal particles can be still stabilized (by cohesive force) on the smaller surface area of the support

(Figure 2.6 (g)). However, if the adhesion force is dominant, the 'encapsulation' of the support over the active metal particles is obtained via the SMSI effect (Figure 2.6 (h)).

2.2.5 PHENOMENON BETWEEN ACTIVE SITES, SUPPORTS AND MODIFIERS

2.2.5.1 SPILLOVER PHENOMENON

Spillover is a phenomenon where the adsorbed active species can transfer from its origin site to others such as another functional active species or even a support. Figure 2.7 represents H_2 spillover from platinum site (active) to iron site (relatively in-active). The spillover is normally used to explain 'synergistic effects' of the combination of each composition in the catalyst system.

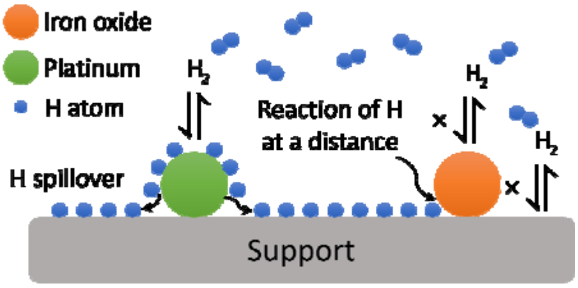

Figure 2.7: H_2 spillover from active metal (Pt) to an in-active metal oxide (FeO) and surface of the support [13].

2.2.5.2 SITE-ISOLATION AND PHASE-COOPERATION CONCEPTS

These 2 theories were proposed for the first time by Grasselli [14,15] for partial oxidation, ammoxidation and selective oxidation. The theories are useful for discovering new catalysts. The 'site-isolation' theory suggested that the active sites, in this case is active oxygen lattice, must be spread and away from each other for all over the surface of the catalyst, in order to eliminate the chance of over-oxidation to occur. This means that, the number of active sites should be tailor-made to match the number of hydrocarbon activating elements, stoichiometrically. For example, around 2 to 5 adjacent surface oxygen atoms are required for the selective oxidation of propene to the desired product 'acrolein'. Thus, if there is more than 5 surface oxygen atoms in one lattice, it will lead to total oxidation, giving unwanted products such as CO and CO_2. In contrast, if there is only 1 surface oxygen in the lattice, the catalyst will become either inactive for the desired reaction or active for the undesired reaction (i.e. producing allyl radicals instead). Figure 2.8 shows principle of site isolation. There are several methods for site-isolation which could be found further in other literature [5], i.e. partial surface reduction and doping.

Whereas 'phase cooperation' concept suggested that 2 functionally diverse but complimentary phases are working together to create the effect of 'synergistic'. Thus, the higher yields of desired selective oxidation products can be obtained more than two of the phases when work separately. This cooperation of phases is important especially when all of the key catalytic functionalities cannot be incorporated into one single phase. In order to establish the phase cooperation, the 2 phases must be brought intimately in close contact, in fact, on a nanoscale [15]. One of the good example is multicomponent molybdate (MCM) systems where the catalyst's structure is demonstrated as shown in Figure 2.9.

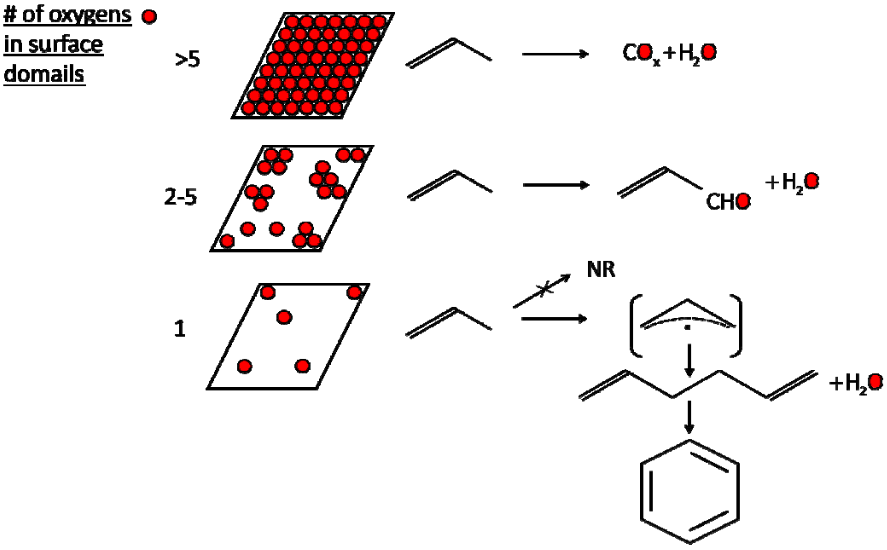

Figure 2.8: Illustration of lattice oxygen arrangements on catalyst's surface for selective oxidation of propylene [15].

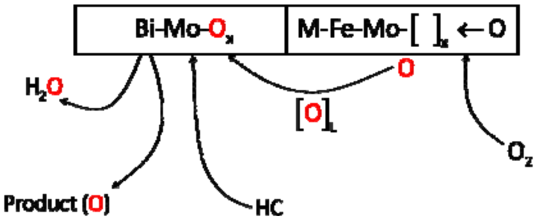

Figure 2.9: Schematic showing cooperation of 2 phases that are different and supporting each other in MCM.

Site isolation and phase cooperation are 2 of 7 principles governing selective oxidation. These principles describe general concepts of lattice oxygen or solid oxygen in the reducible metal oxides.

The 7 principles of selective oxidation catalysis, AKA 7 pillars of oxidation catalyst, include;

1. Lattice oxygen: the lattice oxygen or surface oxygen, contained in reducible metal oxides, is a nucleophile and can work as a 'more flexible agent' and as a more 'selective oxidizing agent' than gaseous oxygen.
2. M-O bonds: the M-O bond must possess intermediate strength (Sabatier's principle) in order to deliver a successful oxidation process. Over-oxidation is expected if the bonding is too weak, whereas, no reaction is occurred if the bonding is too strong.
3. Host structure: host the desirable M-O bonds and anion vacancies (being reduced) without the catalyst's structural collapse (from losing oxygen), yet can provide rapid electron transfer, oxygen vacancy and O^{2-} diffusion.
4. Cyclic redox agent: the lattice oxygen can be removed and refilled by the gaseous reactants, making it a good redox material.
5. Multi-functionality: the effective catalytic metal oxides are generally multi-metallic (at least bi-metallic) and multi-functional (at least bi-functional).
6. Site isolation: the active lattice oxygen must be distributed appropriately on the surface of the catalyst. The arrangement needs to provide a limitation of the number of active lattice oxygen in spatially isolated groupings (domains).
7. Phase cooperation: at least 2 functional phases are closely combined to create synergistic effect in its overall function.

2.2.6 KINETICS OF HETEROGENEOUS CATALYSIS AND MODELS

The kinetics of the heterogeneous catalysis starts from considering a mechanism of the reaction, where a series of elementary steps; including adsorption, surface diffusion, surface reaction which is chemical transformation of the adsorbed species and desorption; is described. For all the steps mentioned above, the 'transition state' or 'active intermediate' is assumed valid. All the kinetic estimation will be accurate only if the mass transfer is not the limitation of the overall reaction, in other word, the rate of step 1, 2, 6 and 7 from Figure 2.3 should be higher than the rate of step 3, 4 and 5. The rate of catalytic reaction is observed by dynamics of individual steps and can be categorized as a hierarchy of continuum model [16], shown as Figure 2.10, which was first proposed by Ertl [16]. The rate of the reaction in the 'macroscopic regime' is achieved by a set of experiments, meaning that the rate of the catalytic reaction is modelled by fitting empirical equations i.e. power laws to experimental data. This regime is therefore related to measurable experimental values, giving a kinetic insight regarding a relation between the rate of reaction VS concentration/partial pressure dependency degree (by rate law) and temperature (by Arrhenius). This gives useful correlation between the surface parameters (unmeasurable but predictable from bulk phenomenon) and the bulk parameters (actual and measurable parameter). The correlated surface parameters in atomic level, called ‘microkinetics’, are characterized and identified by available modern techniques (such as XRD, XPS or Raman spectroscopy). The process of the correlation can be called ‘continuum model’ in which the well-known Langmuir theory (assuming that all the adsorbed species are identical and not reacting to each other) is applied in the approximation.

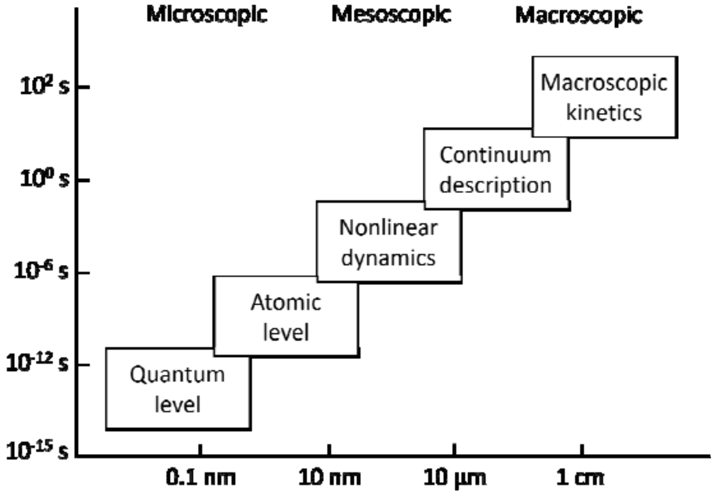

Figure 2.10: Conceptual hierarchy continuum correlation of surface reaction dynamics [16].

The ‘non-linear dynamics’ is derived as a function of time (applicable and useful for continuous process), to gain the more realistic behavior of the process where the mass and heat transfer in the process are likely to be unavoidably involved. This can be seen as ‘a mesoscopic’ region where the mass diffusion and heat transfer are implement to the rate of reaction as a function of time. This results in the formation of spatiotemporal concentration profiles which is often a rapid transient, and incredibly fluctuate. The atomic scale is created to compromise the unrealistic Langmuir theory, because, in reality, the adsorbed species have different energy and nature, plus they are reacting to each other. In this level, the surface science investigation is applied to justify the complexity of the catalyst’s behavior. The transition-state theory is valid for the quantum level where the temperature is only the essential measurable parameter. The theory is based on the only assumption stating that – the thermal equilibrium is established throughout the reaction – meaning that the heat bath, the energy exchange between all degrees of freedom of the particles reacting with the solid, is faster than the elementary step which induces nuclear motion [16].

2.2.6.1 MODELS

All catalytic reactions start from chemisorption of reactant on the catalyst's surface. This is why the rate of reaction is often approximated in a unit of 'per surface area' or even 'per number of active site'. As mentioned before, the Langmuir model has some flaws as the adsorbed species are not identical, yet possibly reacting with each other. Thus, the other models are developed for the bimolecular reactions (e.g. A and B as reactants, converting to C and D) to maximize the accuracy. Some of the main models are tabulated in Table 2.1.

Table 2.1: Heterogeneous kinetic models for bimolecular reactions [17].

Mechanistic Model	**General kinetic equation**
Power law model	$r = k_0 P_A^m P_B^n e^{-\left(\frac{E_a}{RT}\right)}$
Langmuir-Hinshelwood model (LH)	$r = \frac{kKP_AP_B}{1+KP_A}$
Eley-Rideal model (ER)	$r = \frac{kK_AP_AK_BP_B}{(1+K_AP_A+K_BP_B+K_CP_C)^2}$
Mars van Krevelen model (MvK)	$r = \frac{k_{ox}k_{red}PO_2^nP_P}{k_{ox}PO_2^n+k_{red}P_P}$

Before looking at the details of the equations and how they can be derived for a specific reaction, the attention should be brought to each model's assumptions.

1. Power law model
   Power law model is actually the previously derived equation (2.8), in which it combines the rate law together with the Arrhenius equation. The power law model is often used as the first approximation for kinetic study of the catalytic reactions.
2. Langmuir-Hinshelwood model (LH)
   Langmuir-Hinshelwood model in bimolecular reaction assumes that; (1) both A and B, gaseous reactants, need to be adsorbed on the surface before being able to react to each other (2) based on the Langmuir original theory, all the adsorbed species at the surface is uniform and not reacting to each other (3) all the stages are at their thermodynamic equilibrium. The LH model could be quite difficult to derive as rate determining step is not required to be initially assumed. The example of reaction

$$A_2 + 2B \leftrightarrow 2AB \tag{2.19}$$

is demonstrated in Table 2.2.

Table 2.2: Langmuir-Hinshelwood mechanistic model for bimolecular reaction.

Step of reaction	**Mechanism**	**Equation number**
Adsorption (of A) on the active site ($*$)	$A_2 + * \leftrightarrow A_2^*$	(2.20)
Dissociation	$A_2^* + * \leftrightarrow 2A^*$	(2.21)
Adsorption (of B) on the active site ($*$)	$B + * \leftrightarrow B^*$	(2.22)
Surface reaction	$A^* + B^* \leftrightarrow AB^* + *$	(2.23)
Desorption	$AB^* \leftrightarrow AB + *$	(2.24)

3. <u>Eley-Rideal model (ER)</u>
   The difference between the LH and ER is that while LH requires all the gaseous reactants to be adsorbed on the surface of the catalyst, ER only requires one species to be adsorbed before being able to react further with other gaseous (or weakly adsorbed) reactants. Based on the bimolecular reaction prescribed earlier as equation (2.19), its ER model can be derived as follows;

Table 2.3: ER mechanistic model for bimolecular reaction.

Step of reaction	**Mechanism**	**Equation number**
Adsorption (of A) on the active site ($*$)	$A_2 + * \leftrightarrow A_2^*$	(2.25)
Dissociation	$A_2^* + * \leftrightarrow 2A^*$	(2.26)
Surface reaction between the adsorbed A and the gaseous B	$A^* + B \leftrightarrow AB + *$	(2.27)

For the ER, the rate of reaction will increase with increasing coverage until the surface is fully covered by A^*, whereas for LH, the rate will probably reach a maximum and then steeply dropping to near-zero because the surface is fully covered by A^*. This occurs because the gaseous B also requires an active site to be adsorbed on. Relations between rate (r) and the surface coverage (θ_A) of LH model and ER model are compared as shown in Figure 2.11.

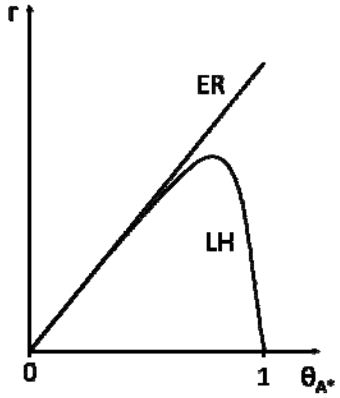

Figure 2.11: Relationship of rate of reaction (r) and surface coverage (θ_A), comparing between LH and ER mechanistic model.

The surface coverage (θ_A) is a fraction between a number of adsorbed species (C^*) and a number of active sites (C_t) which can be described as in equation (2.28)

$$\theta_t = \frac{C^*}{C_t} \tag{2.28}$$

4. <u>Mars van Krevelen model (MvK)</u>
   This redox model was first developed for naphthalene oxidation. This model suggested that during a solid-state redox reaction, the oxygen comes from the lattice of the catalyst, called 'lattice oxygen' or 'surface oxygen'. After losing the oxygen, the catalyst is then re-oxidized by the gaseous 'oxygen containing reactant'. The 'stationary state' is expected when the rate of oxidation rate is equal to the reduction rate. This can be determined by a ratio of rate constants of both reactions.
   In addition, a sub-category of this MvK is called 'steady-state adsorption model' or SSAM. This model is used to explain kinetics of the gas phase oxidation of *o*-xylene in the presence of vanadium oxide. In this model, a steady-state is assumed between the rate of oxygen uptake (the rate of oxygen adsorption on the catalyst surface) and the rate of oxygen release (the rate of oxygen removal by the surrounding gaseous reactant).

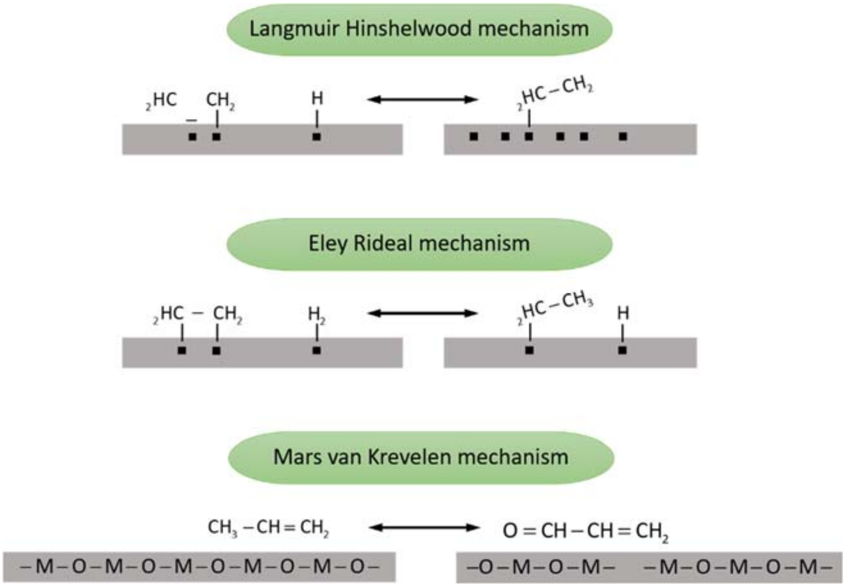

Figure 2.12: Schematic illustration of 3 important mechanistic models in heterogeneous catalysis [17].

The three mechanistic models were illustrated as shown in Figure 2.12. The MvK is often encountered for metal oxides involved in oxidation reactions and oxygen storage capacity (OSC). For instance, a use of CeO_{2-x} in a catalytic converter. If the reduction is too difficult, the catalyst will not be active. On the other hand, if the reduction is too easy, the catalyst will be very active (giving very high conversion), but poor in selectivity (wide product distribution). Therefore, the rate of oxygen release should be compatible with the rate of the oxygen uptake, as well as with the rate of electron and ions transfer within the catalyst. The relative rate value of the reduction and oxidation step is important for the selectivity of the product.

2.2.6.2 HETEROGENEOUS KINETICS

2.2.6.2.1 HETEROGENEOUS KINETICS OF BIMOLECULAR PROCESS

Considering again equation (2.1) where reactants A and B are converting to products C and D with E_{a1} (Figure 2.1). Because this reaction is reversible, C and D can be also converted back to A and B at the cost of E_{a2}. If the solid catalyst is applied for this process, thus, it becomes a heterogeneous reaction where its surface reactions play an important role. Using LH model, the equation (2.1) becomes;

$$A + B \overset{1}{\rightarrow} A^* + B^* \overset{2}{\rightarrow} (AB)^* \overset{3}{\rightarrow} C^* + D^* \overset{4}{\rightarrow} C + D \qquad (2.29)$$

The equation (2.29) can be schematically explained by Figure 2.13.

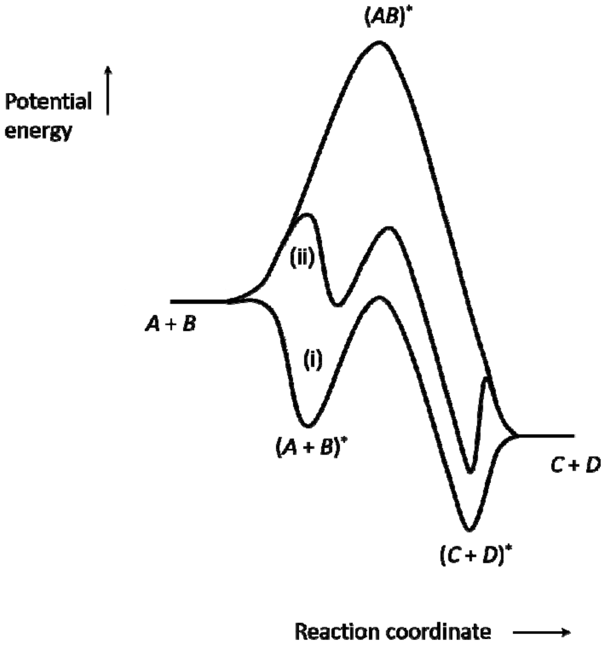

Figure 2.13: Schematic illustration of the bimolecular adsorption via LH model where $A + B \leftrightarrow C + D$.

Note: this schematic is not realistically presented because the heat of adsorption for A, B, C and D will be different. Yet, the activation energies of adsorption steps of the 2 reactants will be different. So as desorption steps of the 2 products are not the same. This diagram should be used to express how the catalyzed reaction occurs only.

From Figure 2.13, a simplified single value energy $(A + B)^*$is shown as A^* and B^*, as well as a simplified $(C + D)^*$is shown for C^* and D^*. Pattern (i) represents a situation in which A and B both are adsorbed with no cost of E_a although pattern (ii) demonstrates an opposite situation where there is E_a for adsorption of A and B. Once A and B are adsorbed, they can convert the adsorbed products C and D, via $(AB)^*$ which is the 'transition state' of the reaction. The adsorbed C and D will then be desorbed to release gaseous C and D at the latest process. This schematic diagram should give a very conceptual perspective of how a catalyst surface can provide many alternative routes and how one particular route could be much more energetically preferred.

From equation (2.29), the first pathway 'step 1' explains competitive adsorption of the bimolecular A and B, with no dissociation. The surface coverage (θ_A) can be derived by the following method;

$$A + * \leftrightarrow\ A^* \tag{2.30}$$

$$B + * \leftrightarrow\ B^* \tag{2.31}$$

Find A^* and B^*, in terms of C_t, C_A and C_B (because these are measurable values – from macroscopic parameters (see Figure 2.10), unlike the adsorbed species, A^* and B^*, that are unmeasurable;

$$C_t =\ C^* + C_A^* + C_B^* \tag{2.32}$$

If all steps are assumed to reach its equilibrium, meaning that, 'the rate of $\underline{A\ \text{adsorption}}$ is equal to rate of $\underline{A\ \text{desorption}}$', similarly, 'the rate of $\underline{B\ \text{adsorption}}$ is also equal to rate of $\underline{B\ \text{desorption}}$', thus;

$$R_A =\ r_{a,A} - r_{d,A} \tag{2.33}$$

At its equilibrium, $r_{a,A} = r_{d,A}$, thus $R_A =\ 0$;

From equation (2.30),

The rate of A adsorption is obtained as;

$$r_{a,A} = k_{a,A} C_A C^* \tag{2.34}$$

Whereas the rate of A desorption is;

$$r_{d,A} = k_{d,A} C_A^* \tag{2.35}$$

Replace equations (2.34) and (2.35) into equation (2.33);

$$R_A =\ k_{a,A} C_A C^* - k_{d,A} C_A^* \tag{2.36}$$

The same goes for B adsorption and desorption, thus;

$$R_B =\ k_{a,B} C_B C^* - k_{d,B} C_B^* \tag{2.37}$$

Considering A adsorption overall process, R_A in equation (2.36) is then equal to zero, therefore,

$$k_{a,A} C_A C^* =\ k_{d,A} C_A^* \tag{2.38}$$

$$\frac{k_{a,A}}{k_{d,A}} = \frac{C_A^*}{C_A C^*} \tag{2.39}$$

Because, $$K_A = \frac{k_{a,A}}{k_{d,A}} \tag{2.40}$$

So that equation (2.39) becomes;

$$K_A = \frac{C_A^*}{C_A C^*} \tag{2.41}$$

Giving; $$C_A^* = K_A C_A C^* \tag{2.42}$$

Similar derivation goes for B species, equation (2.42) is then imitated;

$$C_B^* = K_B C_B C^* \tag{2.43}$$

Substitute equations (2.42) and (2.43) into the cite balance equation, equation (2.32), the below equation is obtained;

$$C_t = C^* + K_A C_A C^* + K_B C_B C^* \tag{2.44}$$

$$C_t = C^*(1 + K_A C_A + K_B C_B) \tag{2.45}$$

$$C^* = \frac{C_t}{(1 + K_A C_A + K_B C_B)} \tag{2.46}$$

Put equation (2.46) to both equations (2.42) and (2.43) where A and B is re-referred as i component;

$$C_i^* = \frac{C_t K_i C_i}{(1 + K_A C_A + K_B C_B)} \tag{2.47}$$

From equation (2.28), where $\theta_t = \frac{C^*}{C_t}$;

$$\theta_i = \frac{K_i C_i}{(1 + K_A C_A + K_B C_B)} \tag{2.48}$$

Question 2.8
Find the surface coverage (θ_A) of a unimolecular reaction with dissociation; $A_2 + 2* \leftrightarrow 2A^*$

Question 2.9
Find the surface coverage (θ_A) of a unimolecular reaction with no dissociation; $A + * \leftrightarrow A^*$

2.2.6.2.2 HETEROGENEOUS KINETICS OF UNIMOLECULAR PROCESS

Energy level of a unimolecular process;

$$A \leftrightarrow R \tag{2.49}$$

is plotted against the reaction coordinate as shown in Figure 2.14. The reaction is a decomposition of molecule A to give R. The forward reaction is exothermic while the reverse reaction is endothermic. The top curve represents the homogeneous reaction (uncatalyzed reaction) which has its activation energy at E_1 for the forward reaction $(A \rightarrow R)$ and at E_2 for the reverse reaction $(R \rightarrow A)$. Therefore, the enthalpy of the homogeneous reaction (ΔH) equal to $E_1 - E_2$. Unsurprisingly, the enthalpy is negative value as E_2 is larger than E_1, making the reaction exothermic. The bottom curve represents the heterogeneous reaction (catalyzed reaction) through surface phenomenon which are;

1. Adsorption; where the gaseous reactant A is adsorbed on the catalyst's surface, forming an adsorbed species, A^*. The heat of adsorption $\left(\Delta H_{A(ads)}\right)$ depends on the nature of the reaction/process. It may or may not be considered an activation energy (E_{ads}) in this step.
2. Surface reaction; the surface reaction is taken place when the reactant adsorbed species, A^* is converted to the adsorbed product species, R^*. The activation energy of this step is equal to E_{SR}.
3. Desorption; where the adsorbed product, R^*, is released to gaseous product, R, and leaving an active site $(*)$ available again for the gaseous reactant. The product, R, is desorbed with an activation energy of E_{des} while the product species, when looking at the desorption of P (reverse reaction) is being adsorbed with an adsorption energy of $\Delta H_{R_{ads}}$.

It can be seen that energy of the initial state and final state between the 'catalyzed process' and 'uncatalyzed process' remains the same. This illustration shows that the catalyst changes the mechanistic pathway by reducing the activation energy, but not to change the overall reaction's thermodynamic equilibrium.

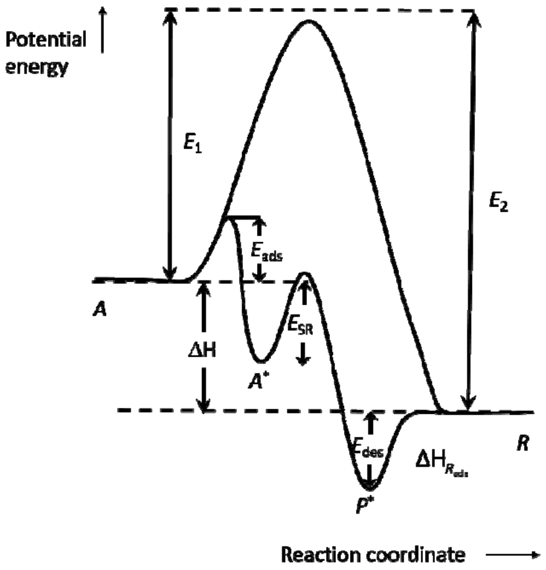

Figure 2.14: Energy profile of a unimolecular reaction with and without a catalyst.

Question 2.10

Nitrous oxide (N_2O) decomposition was studied over $La_{0.3}Sr_{0.7}Co_{0.7}Fe_{0.3}O_{3-\delta}$ perovskite catalyst [18] as shown in an exothermic reaction;

$2N_2O \leftrightarrow 2N_2 + O_2.$

Where ΔH = -82 kJ/mol, and the E_a is 43 kJ/mol (from the abstract). Please remake Figure 2.14 for this reaction from your understanding.

For the reversible single reaction of a unimolecular with no dissociation;

For the reversible reaction of a unimolecular with no dissociation (equation (2.49)), its **adsorption step** can be written as;

$$\boxed{A + * \leftrightarrow A^*} \tag{2.50}$$

Where k_a = rate constant of A adsorption, $k_{a\prime}$ = rate constant of A desorption, and $K_a = \frac{k_a}{k_{a\prime}}$ which is the equilibrium constant of the overall adsorption process

$$R_a = r_a - r_{a'} = k_a C_A C^* - k_{a\prime} C_A^* \tag{2.51}$$

$$R_a = k_a C_A C^* - \frac{k_a}{K_A} C_A^* \tag{2.52}$$

$$R_a = k_a \left(C_A C^* - \frac{1}{K_A} C_A^* \right) \tag{2.53}$$

The **surface reaction step** is afterwards taken over;

$$\boxed{A^* \leftrightarrow R^*} \tag{2.54}$$

Where k_{sr} = rate constant of surface reaction of A^* to R^*, $k_{sr\prime}$ = rate constant of surface reaction of R^* to A^*, and $K_{sr} = \frac{k_{sr}}{k_{sr\prime}}$ which is the equilibrium constant of the overall surface reaction process

$$R_{sr} = r_{sr} - r_{sr'} = k_{sr} C_A^* - k_{sr\prime} C_R^* \tag{2.55}$$

$$R_{sr} = k_{sr} \left(C_A^* - \frac{1}{K_{sr}} C_R^* \right) \tag{2.56}$$

The desorption takes place at last;

$$\boxed{R^* \leftrightarrow R + *} \tag{2.57}$$

The rate constant of the forward reaction of this step is represented by k_d and $k_{r\prime}$ whereas the rate constant of the reverse reaction is $k_{d\prime}$ and k_r (subscript d stands for desorption of R, R stands for adsorption of R)

$$R_d = r_d - r_{d'} = r_{r'} - r_r = k_{r'} C_R^* - k_r C_R C^* \tag{2.58}$$

Where;

$$K_D = \frac{1}{K_R} = \frac{k_d}{k_{d\prime}} = \frac{k_{r\prime}}{k_r} \tag{2.59}$$

Thus;

$$R_d = k_{r\prime}\left(C_R^* - \frac{k_r}{k_{r\prime}} C_R C^*\right) \tag{2.60}$$

$$R_d = k_{r\prime}\left(C_R^* - \frac{1}{K_D} C_R C^*\right) \tag{2.61}$$

$$R_d = k_{r\prime}\frac{k_r}{k_{r\prime}}\left(\frac{1}{K_R} C_R^* - C_R C^*\right) \tag{2.62}$$

$$R_d = k_r\left(\frac{1}{K_R} C_R^* - C_R C^*\right) \tag{2.63}$$

Since the overall reaction is the sum of each steps, the ordinary thermodynamic equilibrium constant for the overall reaction is;

$$K = K_a K_{sr} K_d \tag{2.64}$$

$$K = \frac{K_a K_{sr}}{K_r} \tag{2.65}$$

This relation can be used to eliminate one of the equilibrium constants, often, the unknown K_{sr} is selected.

From the total cite balance;

$$C_t = C^* + C_A^* + C_R^* \tag{2.66}$$

<u>Using the steady state approximation</u>;

$$r_a = r_{sr} = r_d = R_a \tag{2.67}$$

Eliminating the unobservable variables such as C^*, C_A^*, C_R^* in terms of the fluid phase composition C_A, C_R;

$$\boxed{R_a = \frac{C_t\left[C_A - \left(\frac{C_R}{K}\right)\right]}{\left[\left(\frac{1}{K_a k_{sr}} + \frac{1}{k_A} + \frac{1}{K k_R}\right) + \left(\frac{1}{K_a k_{sr}} + \frac{1+K_{sr}}{K k_r}\right) K_a C_A + \left(\frac{1}{K_a k_{sr}} + \frac{1+K_{sr}}{K_{sr} k_A}\right) K_r C_r\right]}} \tag{2.68}$$

Equation (2.68) gives the reaction rate in terms of fluid phase compositions and the parameters of the various steps. However, because the Langmuir-Hinshelwood model assumption is based on the overall reaction is at its thermodynamic equilibrium, meaning that all the rates of each steps are more or less equal to each other. This makes the derivation very complicated (you can look at equation (2.68) again if you want!) or even impossible to solve by hand. Thus, quite often, one of the steps is usually assumed to be much slower than another. This is called ‘rate limiting step’ or ‘determining step’ or even ‘rate controlling step’. This useful assumption allows us to eliminate some of the unknown variables and big terms. Less headache!

For example, if the surface reaction is assumed to be the slowest step;

$$k_a, k_r \gg k_{sr} \tag{2.69}$$

The equation (2.68) is then eased to;

$$\boxed{R_A = \frac{K_a k_{sr} C_t\left[C_A - \left(\frac{C_R}{K}\right)\right]}{1 + K_a C_A + K_R C_R}} \tag{2.70}$$

If the adsorption of A is assumed to be the limiting step, thus;

$$k_{sr}, k_r \gg k_a \tag{2.71}$$

$$r_A = \frac{k_a C_t\left[C_A - \left(\frac{C_R}{K}\right)\right]}{1 + \left(1 + \frac{1}{K_{sr}}\right) K_R C_R} \tag{2.72}$$

$$\boxed{r_A = \frac{k_a C_t\left[C_A - \left(\frac{C_R}{K}\right)\right]}{1 + \frac{K_a}{K} C_R + K_R C_R}} \tag{2.73}$$

From the complexity of equation (2.68), this is why the limiting step should be assumed prior. If the surface reaction is the determining step, equation (2.70) is the derived, and if the adsorption of A is the determining step, equation (2.73) is achieved.

Question 2.11

From question 2.10, the authors found the reaction could follow the Eley-Rideal mechanism.

2.11.1 From the paper, what are the evidence that the N_2O decomposition occurred via Eley-Rideal mechanism?

2.11.2 From page 25, the author proposed 2 possible models of the mechanistic pathways. What the mechanism would be if the reaction occurred via Langmuir-Hinshelwood model?

Question 2.12

From equation (2.68), derive equations (2.70) and (2.73).

2.2.6.3 MOLECULAR MODELING IN HETEROGENEOUS CATALYSIS

Modeling of catalytic reactions is applied at many levels of complication including several orders of length and time scales. It starts from a reaction of 'adsorbate - adsorbate interactions to the 'simple mean-field approximations' and 'macrokinetic models' discussed previously. Table 2.4 shows several levels of models that used for heterogeneous catalysis reactions.

Table 2.4: Hierarchy of methods of modeling catalytic reactions [4,17].

Method of modeling	Simplification	Application
Ab initio calculation	Most fundamental approach	Not yet significant in heterogeneous catalysis
Density Functional Theory (DFT)	Replacement of the N-electron wave function by the electron density	Dynamics of reactions, activation barriers, adsorbed structures, frequencies
Kinetic Monte Carlo (kMC) (quantum chemistry)	Details of dynamics neglected	Adsorbate-adsorbate interactions on catalytic surfaces and nanoparticles
Langmuir-Hinshelwood (mean-field approximation, MF)	Detailed configuration of the adsorbate structure neglected	Microkinetics modeling of catalytic reactions in technical systems
Power law kinetics	All mechanistic aspects neglected	Scale-up and reactor design for 'black-box' system

2.2.6.3.1 DENSITY FUNCTIONAL THEORY (DFT)

Recently, the most beneficial method for heterogeneous catalysis is the density functional theory (DFT). It can explain (1) adsorption, (2) surface properties and (3) reactions at surfaces of metals, semi-conductors and insulators [17]. DFT theory is applied to predict reaction enthalpies, reaction entropies, structure of the transition state, identify the mechanism of the reaction, and properties of the surface. For oxide catalysts, to be able to determine their thermodynamics and kinetics aspects, the required parameters for DFT estimation include theoretical details of electronic structure, description of energy of the its defects, localized states, position of valence and conduction bands. Implementations of DFT are generally based on Kohn-Sham (KS) equations using local density or generalized gradient approximation for the exchange correlation functional. In catalysis, the main challenge is to determine the band gap of an oxide as the position of the top of the valence band (VB) and bottom of the conduction band (CB). The KS band gap is the difference between eigenvalues of CB minimum and VB maximum. There are 2 major methods for DFT simulations in catalysis;

1. 'The cluster algorithm'; this method assumes that all the metal molecules are in clusters including ones that adsorbed on surfaces.
    a. The advantages of this method include (1) the special shape of catalytic cluster can be taken into account, (2) methods developed for gas-phase chemistry can be applied, (3) computational cost is relatively low.
    b. Whereas, the disadvantages are (1) the number of atom in the cluster is limited, (2) metal clusters have different properties to 3-dimensional metals.
    c. Some software tools for this method are GAUSSIAN and TURBOMOLE [4].
2. 'Planar waves' or 'Periodic boundaries'; this method is more widely applied compared to the cluster algorithm. While the cluster algorithm is interested in a super-cell approach i.e. structures to be calculated must be periodic in 3-dimension.
    a. This method is beneficial when considering surface structures because the real solid surface is built on expansion from a small metal cluster or metal slab into 3-dimension. Thus, the metallic properties are generally better described.
    b. The 3rd dimension is a disadvantage, as the solid cell must be periodic in this direction.
    c. The software tools for this method are CASTEP, DACAPO and VASP [4].

Stabilities and frequencies of all reactants, products and intermediates can be calculated using DFT, as well as the activation energies of all the elementary reactions. Recently, solely applied DFT can estimate a complete series of reaction mechanism and the properties of intermediates.

For example, decomposition of N_2O on Fe-ZSM-5 was studied using DFT [19]. The results show that the DFT allow better understanding from fine details of catalytic reaction; i.e. the effect of surface steps on stability of intermediates, impact of coverage on activation energies; to the broader picture of reactions; such as a relationship between activation energy and chemisorption energy.

2.2.6.3.2 KINETIC MONTE CARLO SIMULATION (kMC)

This method, can be also called 'dynamic Monte Carlo method' or 'Gillespie algorithm', is used to simulate the reaction evolution by time [20]. It considers time scales and diffusion. The kMC algorithm requires 'known transition rates amongst states' as data input. These can be obtained by other methods such as diffusion experiments, molecular dynamics or DFT simulation. The basic features of kMC is beneficial for calculation of the surface diffusion, dislocation mobility, surface growth, vacancy diffusion in alloys, coarsening of domain evolution, defect mobility and clustering in ion or neutron irradiated solids such as damage accumulation and amorphization/recrystallization models. For example, there is system containing individual atoms which are deposited on a surface one at a time, however, many of these atoms are migrating on the surface with some 'known jump rate' (defined here as r_{jump}) (which is the required input data for this kMC). The atoms in this case are considered 'objects' of the kMC algorithm. If the 2 atoms are getting closer to each other, so close that they become immobile. Therefore, the flux of incoming atoms (defined as $r_{deposit}$) can be predicted with this kMC method, considering that all the deposited mobile atoms have not yet met a pair to become immobilized. The following phenomenon are then considered as the possible 'events' at each kMC step; (1) a new atom is coming in at the rate of $r_{deposit}$ (2) the deposited atoms is jumping one single step at the rate of r_{jump}. Once a particular event is selected and performed following the kMC algorithm, the facts of whether any of the new atoms just jumps in and become sudden adjacent to one another or not. If so, the newly jumped-in atoms need to be removed from the list of mobile atoms, thus, their jump events should be correspondingly removed from the list of possible events. However, realistic chemical processes are not fully compatible with kMC's assumptions as the real chemical rates are not generally well-defined.

2.2.6.3.3 MEAN-FIELD APPROXIMATION

This method works for a 'continuous explanation' of local states of catalytic surface in the scale of macroscopic or mesoscopic rather than the 'detailed configuration' mentioned previously in the modelling section. In this method, the local states of the surface on large scale can be represented by mean values when the adsorption of the adsorbates on the surface is assumed to be randomly and uniformly distributed. The state of surface is described by temperature and the surface coverage. The surface temperature and surface coverage depend on time and spatial position in the macro scale (this can be viewed as a scale of reactor), although averaged over the local fluctuations in microscopic level, According to these assumptions, a chemical reaction can be demonstrated as [21];

$$\sum_{i=1}^{N_g+N_s+N_b} v'_{ik}\, A_i \rightarrow \sum_{i=1}^{N_g+N_s+N_b} v''_{ik}\, A_i \tag{2.74}$$

Where A_i represents species in either gas-phase, surface, or bulk; N_g stands for gaseous species, $N_s$refers to surface species that are adsorbed on the top of monoatomic layer; N_b is bulk species that found in the inner or bulk catalyst. Steric effect or configurations of the adsorbed species can be taken into account by following these concepts; (1)

surface structure is related to surface site density (Γ) in which it describes the maximum number of species that can be adsorbed on unit surface area (2) each surface species is associated with a coordination number (σ_i) describing the number of surface sites which are covered by this species. According to the assumptions set-up, a multi-steps mechanistic reaction pathways can be predicted. The net production rate in molar is then defined as;

$$\overline{S_i} = \sum_{k=1}^{K_S} v_{ik} k_{fk} \prod_{j=1}^{N_g+N_S+N_b} c_j^{v'_{jk}} \tag{2.75}$$

Where K_S = number of surface reactions, c_i = concentrations of the species (the unit of N_S is mol. m^{-2}, of N_g and N_b both are in mol. m^{-3}). To define $\Theta_i = c_i \sigma_i \Gamma^{-1}$, the variations of surface coverage then become;

$$\frac{\partial \Theta_i}{\partial t} = \frac{\overline{S_i}\sigma_i}{\rho\Gamma} \tag{2.76}$$

Since the local position in the reaction has a strong influence on temperature and concentration of gaseous species, the position also affects the set of surface coverage. The binding states of adsorptionof all the species depend on the surface coverage. The rate coefficient can be modified by adding this coverage dependence. The upgraded rate constant can be referred as [21];

$$k_{fk} = A_k T^{\beta_k} e^{-\left(\frac{E_a}{RT}\right)} \prod_{i=1}^{N_S} \Theta_i^{\mu_{ik}} e^{\left(\frac{\varepsilon_{ik}\Theta_i}{RT}\right)} \tag{2.77}$$

2.2.6.3.4 DEVELOPMENT OF MECHANISTIC SURFACE REACTION

The development is a complicated process. The ‘predicted’ mechanism can be proposed based on (1) experimental surface studies, (2) analogy to gas-phase kinetics and organometallic compounds, and (3) theoretical studies such as DFT, kMC or semi-empirical calculations. These mechanism should be presented as ‘elementary-like’ and applicable for wide range of conditions.

2.3 SUMMARY AND PERSPECTIVES

This chapter is detailed in principle and theory of the heterogeneous catalysis. Basic understanding starts from simple collision theory, heterogeneous kinetics i.e. chemical reactions, elementary reactions, rates and activation energy. Relationship between number of particles and their different kinetic energy were explained using Maxwell-Boltzmann distribution. Heterogeneous reaction steps were illustrated as 7 minor steps including both transport phenomena and surface reaction steps. The component of the catalyst system was also explained. This includes reaction phenomenon and their effects on the overall efficiency of the catalyst system. Important mechanistic models of the heterogeneous catalysis such as Langmuir-Hinshelwood model and Eley-Rideal model were demonstrated with some decent examples. DFT could be highly beneficial for future research.

REFERENCES

[1] J.R.H. Ross, Heterogeneous catalysis - fundamentals and applications, (2012).
[2] D. Camuffo, Consequences of the Maxwell-Boltzmann distribution, in: Microclim. Cult. Herit., Elsevier, 2014: pp. 347-366. https://doi.org/10.1016/B978-0-444-63296-8.00010-X.
[3] V. Tongnan, T. Sornchamni, N. Laosiripojana, U.W. Hartley, Study of crystal growth and kinetic parameters of Zn/ZnO oxidation in the presence of H_2O and CO_2, React. Kinet. Mech. Catal. 125 (2018). https://doi.org/10.1007/s11144-018-1411-3.
[4] O. Deutschmann, Heterogeneous catalysis and solid catalysts, Wiley-VCH, 2009.
[5] A.A. Balandin, Modern state of the multiplet theory of heterogeneous catalysis1*The paper was prepared for publication by E.I. Klabunovskii, in: Adv. Catal., 1969.
[6] I. Langmuir, Chemical reactions at low pressures, J. Am. Chem. Soc. 37 (1915). https://doi.org/10.1021/ja02170a017.
[7] H.S. Taylor, A theory of the catalytic surface, Proc. R. Soc. London. Ser. A, Contain. Pap. a Math. Phys. Character. 108 (1925) 105-111. https://doi.org/10.1098/rspa.1925.0061.
[8] M. Boudart, A. Aldag, J.E. Benson, N.A. Dougharty, C. Girvin Harkins, On the specific activity of platinum catalysts, J. Catal. 6 (1966) 92-99. https://doi.org/10.1016/0021-9517(66)90113-8.
[9] G.A. Somorjai, Surface reconstruction and catalysis, Annu. Rev. Phys. Chem. 45 (1994) 721-751. https://doi.org/10.1146/annurev.pc.45.100194.003445.
[10] R.L. Burwell, G.L. Haller, K.C. Taylor, J.F. Read, Chemisorptive and catalytic behavior of chromia, in: Adv. Catal., 1969: pp. 1-96. https://doi.org/10.1016/S0360-0564(08)60268-0.
[11] K. Hauffe, R. Glang, H.J. Engell, Der Einfluß der Elektronenfehlordnung oxydischer Katalysatoren auf die Zerfallsgeschwindigkeit des Stickoxyduls, Zeitschrift Für Phys. Chemie. 201 (1952) 223-245. https://doi.org/10.1515/zpch-1952-20118.
[12] F.S. Stone, The significance for oxide catalysis of electronic properties and structure, J. Solid State Chem. 12 (1975) 271-281. https://doi.org/10.1016/0022-4596(75)90319-9.
[13] W. Karim, C. Spreafico, A. Kleibert, J. Gobrecht, J. Vandevondele, Y. Ekinci, J.A. Van Bokhoven, Catalyst support effects on hydrogen spillover, Nature. 541 (2017) 68-71. https://doi.org/10.1038/nature20782.

[14] R.K. Grasselli, Fundamental principles of selective heterogeneous oxidation catalysis, Top. Catal. 21 (2002) 79-88. https://doi.org/10.1023/A:1020556131984.

[15] R.K. Grasselli, Site isolation and phase cooperation: two important concepts in selective oxidation catalysis: A retrospective, Catal. Today. 238 (2014) 10-27. https://doi.org/10.1016/j.cattod.2014.05.036.

[16] G. Ertl, Dynamics of reactions at surfaces, in: Adv. Catal., 2000: pp. 1-69. https://doi.org/10.1016/S0360-0564(02)45012-2.

[17] J.C. Védrine, Metal oxides in heterogeneous catalysis, Elsevier, 2018. https://doi.org./10.1016/C2016-0-01790-4.

[18] U.W. Hartley, V. Tongnan, N. Laosiripojana, P. Kim-Lohsoontorn, K. Li, Nitrous oxide decomposition over $La_{0.3}Sr_{0.7}Co_{0.7}Fe_{0.3}O_{3-\delta}$ catalyst, React. Kinet. Mech. Catal. 125 (2018) 85-97. https://doi.org/10.1007/s11144-018-1398-9.

[19] A. Heyden, A. Bell, F. Keil, Kinetic modeling of nitrous oxide decomposition on Fe-ZSM-5 based on parameters obtained from first-principles calculations, J. Catal. 233 (2005) 26-35. https://doi.org/10.1016/j.jcat.2005.04.003.

[20] S.A. Serebrinsky, Physical time scale in kinetic Monte Carlo simulations of continuous-time Markov chains, Phys. Rev. E. 83 (2011) 037701. https://doi.org/10.1103/PhysRevE.83.037701.

[21] P. Stolze, Handbook of heterogeneous catalysis, 2nd ed., Weinheim: Wiley-VCH, 2008.

ABBRIVIATIONS AND ACRONYM

r_f	*rate of forward reaction*
r_r	*rate of reverse reaction*
k_f	*rate constant of the forward reaction*
k_r	*rate constantof the reverse reaction*
$[i]$	*concentration of substance i*
R_{eq}	*overall rate reaction at equilibrium condition*
K_{eq}	*equilibriumrate constant of the overall reaction*
k	*rate constant*
T	*absolute temperature*
E_a	*activation energy*
a, b	*stoichiometric values and orders*

R	*gas constant*
f	*fraction between successful collisions and all collisions*
ΔH_f	*heat of formation*
CUMSs	*coordinatively unsaturated metal sites*
MSI	*metal-support interaction*
SMSI	*strong metal-support interactions*
MCM	*multicomponent molybdate*
M-O	*metal-oxygen*
XRD	*X-Ray Powder Diffraction*
XPS	*X-Ray Photoelectron Spectroscopy*
LH	*Langmuir-Hinshelwood model*
ER	*Eley-Rideal model*
MvK	*Mars van Krevelen model*
θ_A	*surface coverage*
SSAM	*steady-state adsorption model*
OSC	*oxygen storage capacity*
DFT	*density functional theory*
kMC	*kinetic Monte Carlo*
MF	*mean-field approximation*
KS	*Kohn-Sham equations*
VB	*valence band*
CB	*conduction band*
Γ	*surface site density*

CHAPTER 3
TYPE OF SOLID CATALYSTS

3.1 DEVELOPMENT OF SOLID CATALYSTS AND HIGH-THROUGHPUT EXPERIMENTATION

Solid catalysts have a long story since the concept was created. Appropriate catalysts have been always researched and studied in a sequence of steps at different levels and aspects. Lab-scale reactor is well-known to be an initial equipment used to screen the most promising catalysts. Figure 3.1 presents schematic evolution of catalyst development and design [1].

Because the overall process of catalyst development can be tedious and expensive, several commercial catalyst companies; e.g. Symyx Technologies, Johnson Matthey, Santa Clara; are offering a method called 'high-throughput experimentation' or HTE. The HTE technique enables parallel testing of small amount of catalyst in an automated system [2]. The first step of HTE process usually is scanning through a large catalyst's library (a few hundred catalysts) in order to select the best catalyst, by using a quick and simple analysis method such as infrared thermography or IRT. The chosen catalysts from the first step (possible around 50 catalysts) will be tested further in the second step where they are applied at the more realistic conditions. More detailed characterization techniques are usually applied in this step too. Afterwards, parallel reactor systems are developed for prompt and precise quantitative analysis. The popular analyzer for the method is a gas chromatography (GC) which when it is coupled with the HTE, the overall process is then called 'high-throughput multiplexing gas chromatography' [3]. This technique allows injections of samples into the separation by means of a special multiplexing injector. A convolution of overlapping time-shifted chromatogram is the obtained instead of a series of an individual single chromatograms, although the convolution needs to be de-convoluted before the results can be interpreted.

3.2 CATEGORIZATION OF SOLID CATALYSTS

The solid catalysts can be classified in many aspects, although in this book the catalysts are classified based on their compositions and functions. These catalyst families are (1) unsupported catalysts or bulk catalysts, (2) supported catalysts, (3) confined catalysts or ship-in-a-bottle catalyst, (4) hybrid catalysts, and (5) polymerization catalysts.

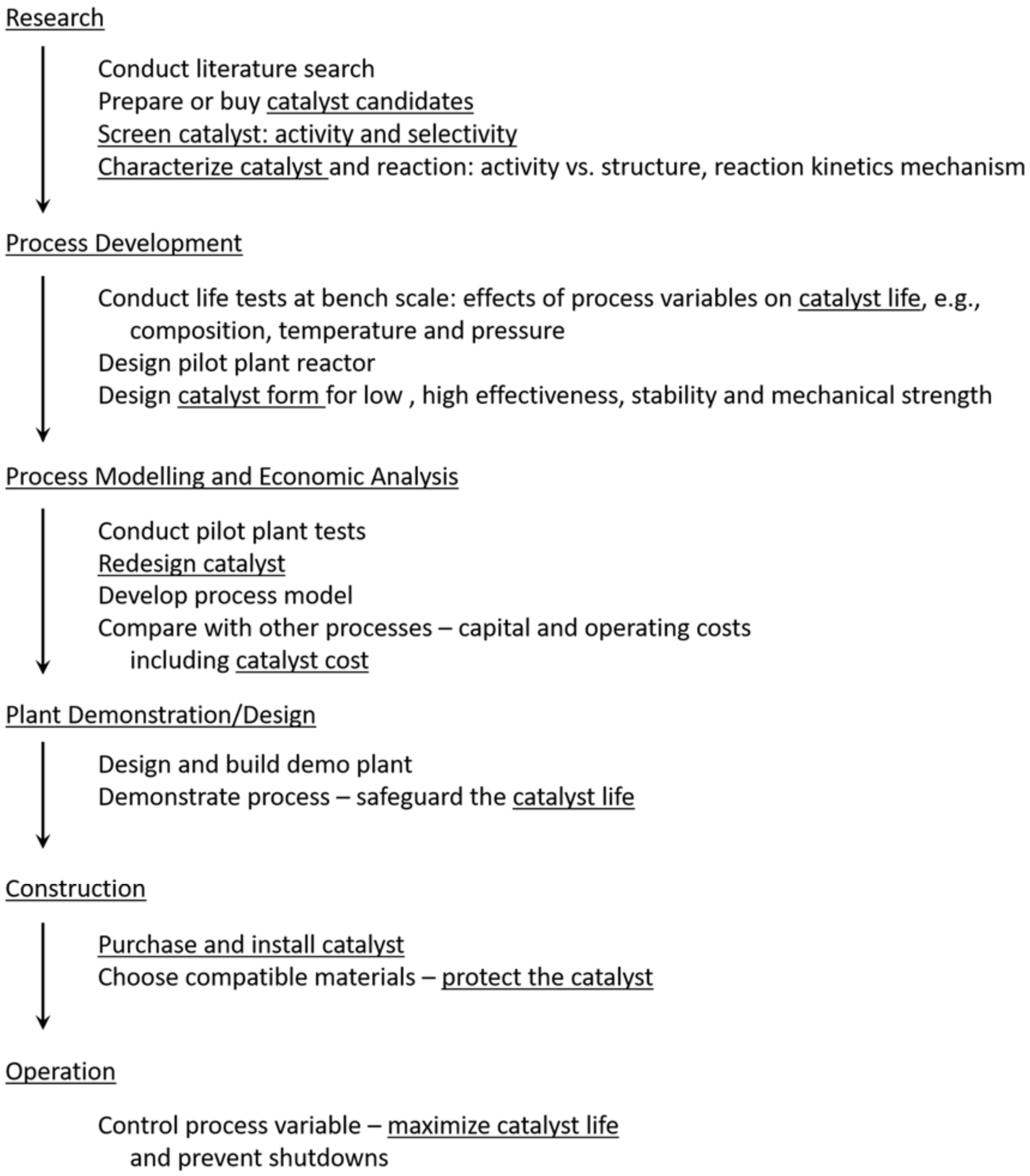

Figure 3.1: Illustration of catalyst development and design [1].

Question 3.1
Apart from catagoring the catalysts by their compositions and functions, how else they can be classified or grouped?

3.2.1 UNSUPPORTED CATALYSTS

3.2.1.1 METAL OXIDES

The compound of metals and oxides are commonly solid. The oxygen (O) atom in the oxides is strongly electronegative component. The bonding character between metal (M) and oxygen (O) has an effect on the bulk properties of the compound. The electronic properties of the metal oxides compounds can be anything i.e. insulators (such as Al_2O_3, SiO_2), semi-conductors (TiO_2, NiO, ZnO), metallic conductors (reduced transition metal oxides, for instance, TiO, NbO, tungsten bronzes), super-conductors ($BaPb_{1-x}$, Bi_xO_3), and high temperature super-conductor ($YBa_2Cu_3O_{7-x}$) [4]. Metal oxides are well-known for their ability to develop acid-base characteristic and redox property. Metal oxides can be simply composed of 1 or 2 type of metals, although many distinguished metal oxides are complex multi-component materials, like perovskites.

3.2.1.1.1 SIMPLE BINARY OXIDES

Simple binary oxides could be acidic, basic or even amphoteric [4]. These properties are related to their dissolution behavior in contact with aqueous solutions. Amphoteric oxides; e.g. Al_2O_3 or ZnO; will form cations in acid environment while form anions in basic environment. Acidic oxides; e.g. SiO_2; will dissolve with formation of acids or anions. Basic oxides; e.g. MgO or lanthanide oxides; will form hydroxides or dissolves by forming bases or cations. Transition metal oxides in their highest oxidation state; e.g. V_2O_5, CrO_3, behave similarly within the same family. The dissolution properties directly influence surface properties of the oxides, in which it is in contact with the reactants, and the degree of hydration/hydroxylation of the surface become crucial. This dissolution properties should be taken into account when it comes to a design whether the metal oxides will be used as active phase or support phase.

1. Alumina;
   As mentioned before, are amphoteric oxides. Alumina can be formed in various phases; i.e. bayerite, nordstrandite, boehmite and gibbsite; depending on (1) the nature of their precursors (hydroxide or oxide hydroxide) and (2) their thermal decomposition. The thermal stability, which depends on degree of crystallinity, of alumina is defined as low stability (η-,Θ-, γ-, χ- and κ- Al_2O_3) and as high stability (α-Al_2O_3). The α-Al_2O_3 or so-called corundum is considered the final crystalline and thermodynamically stable, or in the other word, the most thermally stable. The alumina phase evolution is generated and shown in Figure 3.2.

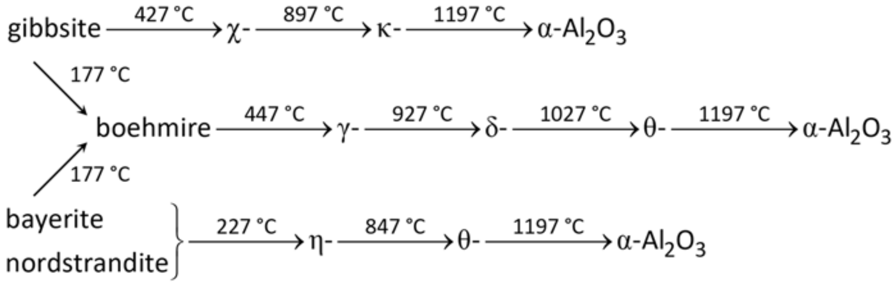

Figure 3.2: Phases of alumina by calcination temperature.

The alumina's structure consists of close-packed layers of oxo anions (in this case, metal oxides or alumina) with Al^{3+} cations. The cations are distributed between tetrahedral and octahedral vacancy positions. Different crystallographic form of alumina is resulted from different stacking of the oxo anions. In catalysis, η-and α-Al_2O_3 are the most utilized as they possess a defect spinel structure in which it incorporates Al^{3+} cations in both tetrahedral and octahedral. The Al sub-lattice is very disordered, thus, the irregular occupation of the tetrahedral interstices results in a tetrahedral distortion of the spinel structure. Relatively, γ-Al_2O_3 shows higher occupancy of tetrahedral cation positions, whereas η-Al_2O_3 in contrast has the higher density of stacking faults in its oxygen sub-lattice. The crystallites are covered by anion layers as the lattice terminates. These layers are occupied by hydroxyl groups to adjust energy of the surface. Alumina surface has specific catalytic properties. Its acidic and basic sites can be tested by many techniques; e.g. transient iso-proponol probe reaction or temperature-program desorption (TPD) of NH_3. Thermal treatment of hydroxylated oxides lead to partial dehydrozylation with formation of coordinatively unsaturated O^{2-} ions (basic sites) and an adjacent anion vacancy which exposes 3- or 5-coordinate Al^{3+} cations (Lewis acid sites). The remaining hydroxyl groups can be terminal or doubly or triply bridging with the participation of Al^{3+} in tetrahedral and/or octahedral positions. The properties of the resulting OH^- species range from weak Brønsted acid to strong basic and nucleophilic [4]. Alumina can be used solely as a catalyst in many processes; e.g. elimination reactions, alkene isomerization; as well as a support for other catalyst system. Alumina is widely used as a support due to (1) its controllable surface area and particle size, which can be adjusted by the preparation conditions, (2) its redox properties, (3) its thermal stability ensuring a long life time of use.

2. Silica;

   Silica is considered a weak Brønsted acidic oxides and can be formed in many structures, for example, quartz, tridymite and cristobalite [5]. However, the most popular phase of silica that has been heavily used in catalysis is amorphous silica. A block of SiO_2 tetrahedra is linked to each O atom, bonding 2 Si atoms together with covelent bond throughout the bulk solid. The bulk structure will be covered by hydroxyl group (silanol) or SiOH, if the surface is fully hydrated. Silica in general is not used as an active catalyst on its own because the surface hydroxyl groups are weak Brønsted acid and hardly react with anything. In addition, the siloxane bridges are also unreactive especially after being treated at high temperature. However, SiO_2 is feasible as a good support as its surface area, particle size, morphology, porosity and mechanical stability can be tailor-made by controlling the preparation conditions. Amorphous SiO_2 can be used as parent siliceous extreme of Zeolite ZSM-5 due to its MFI structure, by using hydrothermal method for the synthesis. This method creates the crystalline microporous silica silicalite I [6]. Porosils, large pore mesoporous SiO_2, can be synthesized having their linear and parallel pores sized varied from 2 to 10 nm. The porosils is well-known for accommodating large molecules or functional groups. Activity of SiO_2 towards acid catalysis can be created by substituting some foreign elements such as Al^{3+} for Si^{4+}, to induce its Brønsted acidity [6].
3. Magnesium oxide;

   Magnesium oxide (MgO) is a basic catalyst where Mg ion is bonded with O with octahedral coordination. Its electronic structure was found to be strongly ionic [7]. The lattice is generally envisaged to terminate in (1 0 0) planes incorporating 5 coordinate (5c) Mg^{2+} and O^{2-} ions [8]. Although the (1 0 0) planes are electronically neutral, hydroxyl group are presented on the surface of polycrystalline MgO. These groups and O^{2-} anions are the cause for MgO's basic properties, while the unsaturated Mg^{2+} ions represent weak Lewis acid. In terms of reaction, Brønsted acids have been shown to be chemically adsorbed on the MgO surface, to form surface-bound carbanions and surface hydroxyl groups [9]. MgO is widely used as a host metrix for transition metal ions as a whole concept of solid solutions. The MgO is good for isolating the transition metals, installing the metal's good dispersion.
4. Transition metal oxide;

   Transition metal oxides consist of dense packs of anions bonding with cations interstices, by mixed ionic-covalent bonds [10]. Some of the transition metal oxides sometimes can develop metallic-like character i.e. bronzes. Surface of the transition metal oxides are often classified acidic as they are likely to be partially covered by hydroxyl groups. However, their distinguish catalytic redox properties are due to their (1) non-stoichiometric characteristic (2) ability to form a mixed valence compound (3) various oxidation states. The transition metal oxides are widely utilized in many redox reactions, particularly selective oxidation and dehydrogenation reactions. **Titania (TiO_2)** is a transition metal oxide that has 2 major crystallographic forms; anatase and rutile. Anatase is generally more used in catalysis applications as it has higher surface area. One of its disadvantages is its stability because it can transform to rutile phase at temperature higher than 627 °C, approximately. Addition of Vanadium (V) into titania was found to reduce thermodynamic stability of the catalyst system, from ~627 °C to 547 °C. In contrast, adding surface sulfate or phosphate can stabilize anatase phase. VO_x/TiO_2 is recognized as a catalyst for selective oxidation and NO_x reduction [10]. Titania is also well-known in photo-catalysis field, due to its wide band gap as a semi-conductor. Another example of transition metal oxides is **Zirconia (ZrO_2)** which is commonly used as a support because it is thermally and mechanically stable. The most beneficial crystallographic phases of ZrO_2 are tetragonal and monoclinic [11]. As the monoclinic is the more thermodynamically stable, therefore, the tetragonal phase is usually easier to be modified for higher surface area, where the metastable tetragonal ZrO_2 is stabilized at relatively low temperature by sulfate or tungstate impurities. ZrO_2 based catalyst system is recognized as high oxygen storage capacity material, acting as a lattice oxygen source. ZrO_2 is utilized in many catalytic applications such as solid state electrolyte sensor for measuring oxygen partial pressure, fuel cells, and selective oxidations [12]. **Ceria (CeO_2)** or cerium oxides has a fluorite structure as its most stable crystallographic phase, for all range of treatment's temperatures [13,14]. Ceria, used on its own, is a high electronic conductor where the ionic transference number of a sintered CeO_{2-x} is less than 0.002 under operating temperature ranging from 600 to 1,300 °C. The electronic conductivity of ceria is generally higher than its ionic conductivity. Thus, ceria is not feasible for solid oxide fuel cells (SOFCs) application due to its high electronic conductivity. However, the ionic conductivity of ceria can be developed by adding some foreign trivalent cations of rare earth metals such as Gd^{3+}, Sm^{3+}, and Nd^{3+} or divalent cations of alkaline earth elements i.e. Ca^{2+}, Sr^{2+}, and Ba^{2+} into the ceria based catalyst system. This improvement is due to an increase in the number of oxygen vacancies by charge compensation. Ceria is mostly used on selective oxidation, redox reaction or combustion reaction [15-17]. **Other transition metal oxides** are also mainly used as supports or as constituents of complex multicomponent catalysts. A few of these act as unsupported binary oxide catalysts i.e. Fe_2O_3 and Cr_2O_3 are used to catalyze oxidative hydrogenation of butene to butadiene. Fe_2O_3 based catalysts can be used for clean combustion, high temperature water gas shift reaction (WGS) and dehydrogenation of ethylbenzene [18]. Modybdenum trioxide (MoO_3) can be used for formaldehyde production via oxidative hydrogenation of methanol [19]. Zinc oxide (ZnO) is the first generation solid material that is used for chemical looping process [20] although it is a cause of the process's complication due to its phase change. ZnO is also utilized in oxidation of cyclohexanol to cyclohexanone.

3.2.1.1.2 COMPLEX MULTICOMPONENT OXIDES

Complex multicomponent oxides are oxides of mixed metals that establish unique catalytic characteristics. These oxides play major role in catalysis and here are some examples;

1. Aluminum silicates;
   Aluminum silicates consists of 4 valent Si-atoms, that are isomorphously substituted by trivalent Al atoms, and are one of the most crucial ternary oxides. The substitution installs a negative charge framework of the interconnected tetrahydra. Cations exchange are mandatory for the charge compensation when protons are incorporated as charge-compensating cations, hydroxyl groups bridging between Si- and Al- atoms are created, which serve as Brønsted acidic sites in the catalyst system [21].
2. Zeolites;
   Zeolite is a large family of crystalline aluminosilicates, and can be prepared by hydrothermal synthesis. Zeolite is considered a microporous material with pore size ranging from 3 to 7 Å [21]. ZSM-5 has a well-defined structure called molecular sieve, according to its ability to let particular molecules pass through its pore. In addition, ZSM-5 is also well-known for its ion exchange ability and its high surface area. Zeolites are formed between corner-linked $\mathrm{SiO_4^{4-}}$ and $\mathrm{AlO_4^{5-}}$ tetrahedral and 2-coordinate oxygen atoms bridging 2 tetrahedral centers (T atoms). Zeolite frameworks contain of (1) straight/sinusoidal channels or (2) spherical/other-shaped cages. H forms of the zeolites are strongly acidic and thus play an important role in large-scale industrial processes such as catalytic cracking, methanol to gasoline or ethanol to olefins. Apart from Al and Si atoms, P atoms can be incorporated in zeolites structure, as well as, Ti, V, Cr atoms can be substituted for Si, leading to an outstanding oxidation catalyst of which titanium-silicate-1 (TS1) is used for oxidation, hydroxylation and ammoxidation with aqueous H_2O_2 [22]. Zeolites can be adapted to possess basic properties by ion-exchanging with large alkali metal ions such as Cs^+. Zeolites are commonly

used in hydrocarbon cracking processes and other shape-selective molecular reactions.

3. Aluminum phosphates;

   Aluminum phosphates or AIPO share some similar features with ZSM-5. They can be considered as a subspecies of Zeolites where the T atoms are Al and P. AlPOs normally have atomic ratio of Al to P equal to 1, thus, the framework composition is neutral as $AlPO_4$ [6]. This material itself has limited applications in catalysis, however, substitution of Al^{3+} by divalent atoms can yield 'metal alumino phosphates (MAPOs)' or yield 'silico alumino phosphates (SAPO)', which encourage the material's acidity. This catalyst family contains members with various topologies which span a wider range of pore diameter than alumino silicate zeolites. In additions, Si atom can be replaced by Al atoms in the MCM-type oxides to achieve a mesoporous acidic catalyst.
4. Clays;

   Aluminosilicate minerals are, in other word, considered clays. These include montmorillonite, phyllosilicates (smectites), bentonites etc. Most of clays used in catalysis are montmorillonite based where they consist of alumino hydroxyl silicate compounds. Besides, Montmorillonite is considered a 2 to 1 clay, this means one octahedral AlO_6 layer is sandwiched between 2 tetrahedral SiO_4 layers. Normally the montmorillonite is used as a catalyst's support. It is reversibly swellable, due to containing of swelling agent, and possesses ion-exchange ability. When the swelling agent is evaporated by high temperature, the clay's structure can be prevented from collapsing by using inorganic pillars to link structural layers together [6]. Pillaring is a process where a layered compound is transformed into a more thermally stable micro- and/or mesoporous material with retention of the layer structure. The pillaring agent can be any compounds that maintain spacing between the adjacent layers upon removal of the solvent and which induces an experimentally observable pore structure between the layers called 'interlayer region' accessible to molecules at least as large as N_2. Thus, pillaring agent can be anything from inorganic pillars to organic surfactants [23].
5. Mixed metal oxides

   Mixed metal oxides are multimetal oxide compounds, generally containing of several transition metals. The mixed metal oxides have large variety in properties, therefore, they are very difficult to characterize in details. Bulk mixed metal oxide catalysts are commonly applied in selective oxidation, oxydehydrogenation, ammoxidation, chemical looping reactions, thermochemical cycles, and other redox reactions. Perovskites are considered a type of mixed metal oxides too.

Table 3.1 gives examples of mixed metal oxide catalysts for various applications. The examples of mixed metal oxides and their applications were tabulated in Table 3.1.

Table 3.1: Examples of mixed metal oxide catalysts and their applications [15-17,20,24-29].

Catalyst	Active phase	Process
Copper chromite	$CuCr_2O_4$, CuO	Low temperature Co conversion, oxidations, hydrogenation [24]
Zinc chromite	$ZnCr_2O_4$, ZnO	Methanol synthesis (high pressure), chemical looping [20]
Copper/zinc chromite	$Cu_xZn_{1-x}Cr_2O_4$, CuO	Methanol synthesis (low pressure) [24]
Iron molybdate	$Fe(MoO_4)_3$, MoO_3	Methanol to formaldehyde [24]
Zinc ferrite	$ZnFe_2O_4$	Oxidative dehydrogenation [24]
Chromia-alumina	$Cr_xAl_{2-x}O_3$	Dehydrogenation of high alkanes [24]
Ceria-zirconia	CeO_{2-x}/ZrO_{2-x}	DMC production, 2 steps thermochemical cycles, steam reforming, chemical looping [15, 16]
Ceria-chromite	$Ce_xCr_{1-x}O_2$	Methanation, 2 steps thermochemical cycles [17]
Ceria-zirconia-alumina	$Ce_xZr_{1-x}O_2/Al_2O_3$	2 steps thermochemical cycles in microchannel reactors [15, 16]
Perovskites	$BaFeO_{3-\delta}$, $La_{0.3}Sr_{0.7}Co_{0.7}Fe_{0.3}O_{3-\delta}$, $La_{0.6}Sr_{0.4}Co_{0.2}Fe_{0.8}O_{3-\delta}$	H_2 production and syngas production via thermochemical cycles, applications in reactive ceramic membrane reactor, nitrous oxide decomposition [25-29]

6. Vanadium phosphates;

Vanadium phosphates i.e. $VOHPO_4 \cdot 0.5H_2O$ are precursor for the VPO catalysts which are commonly utilized in ammoxidation, selective oxidation of n-butane to maleic anhydride. Besides, vanadyl pyrophosphate $(VO)_2P_2O_7$ is believed to play an important role in VPO catalyst system. Appropriate catalysts for oxidation or ammoxidation are required to be multifunctional and have 2 or more vicinal oxide species of optimal bond strength of metal-oxygen. Both species must have high redoxibility. The individual active sites of the catalysts should follow the site-isolation concept by being spatially separating from one another. The active site should be able to dissociate oxygen and incorporate the oxygen. The material is considered non-stoichiometric thus it should tolerate a certain density of anion vacancies without structural collapse. Grasselli [30] has set up a criteria of catalyst functionalities for oxidation/ammoxidation catalysts; (1) the catalysts should possess an α-H-abstracting component. This could be Bi^{3+}, Sb^{3+}, Te^{4+} or Se^{4+}, (2) the catalysts should allow alkene/ammonia chemisorbed species to occur. They also should have a component that inserts oxygen/nitrogen (Mo^{6+}, Sb^{5+}), and (3) the catalysts should have a redox couple such as Fe^{2+}/Fe^{3+}, Ce^{3+}/Ce^{4+} or U^{5+}/U^{6+} to accommodate the lattice oxygen transfer between bulk-surface.

7. Bismuth molybdates;

   Bismuth molybdates or BMO are visible light driven photo-catalysis materials. This group of catalyst is classified as a ternary oxide catalysts and has attracted a lot of attention in recent years due to its non-toxicity, efficiency, visible light response. The general formula of this catalyst is $Bi_2O_3{\cdot}nMoO_3$ where n = 3, 2, 1, correspondingly to 3 crucial phases of this catalyst system which are α-$Bi_2Mo_3O_{12}$, β-$Bi_2Mo_2O_9$, and γ-Bi_2MoO_6, respectively. BMO structure can be adjusted by changing solvent, pH, surfactant or even temperature [31]. BMO is widely utilized in photo-catalysis applications such as water treatment, organic pollution removal and semi-conductor industry.

8. Antimonites;

   Antimonites are salt of antimony (Sb) such as $NaSb(OH)_4$ and $NaSbO_2$ and can be prepared by reaction of alkali and antimony trioxide (Sb_2O_3). The antimonites are useful for ammoxidation/oxidation reactions. Some foreign elements such as U, Fe, Sn, Mn or Ce can be added into the catalyst system to establish its multiple oxidation states. Some complicated compositions e.g. $Na_{0.3}(Cu,Mg,Zn,Ni)_{0\text{-}4}(V,W)_{0.05\text{-}1}Mo_{0.1\text{-}2.5}Te_{0.2\text{-}5}Fe_{10}Sb_{13\text{-}20}O_x$ has been commercialized [32].

9. Scheelites;

   Scheelites are made of calcium (Ca) and tungsten (W) in which its simplest chemical formula could be $CaWO_4$. Scheelites can be synthesized using a method called 'Czochralski process' [33]. The crystallographic of the scheelites are tetragonal. Its application in catalysis include selective oxidation and ammoxidation of alkenes, propylene oxidation to acrolein, propylene ammoxidation to acrylonitrile and butene oxidative dehydrogenation to butadiene. Scheelies in its general form ABO_4 tolerate cation replacements irrespective of valency provided that cation A is larger than B, so that there is a balance in charge. One of the distinguish properties of scheelites is that they are often mechanically stable even when they lose 30% of their anion cation sub-lattice (30% vacancy) [34].

10. Perovskites;

    Perovskites are a type of mixed metal oxides, represented by ABO_3. The common features are quite similar to scheelites where the B cations are small and highly charged and A cations are relatively larger and lower charge while having 12 fold coordination with oxygen atoms. Perovskites find their applications in many modern and green chemical productions and energies [24-29,35]. Calcium titanate ($CaTiO_3$) was the first mineral discovered as a type of perovskites, defined following the name of the discoverer, Lev Perovskite, a Russian mineralogist. Perovskites offer diverse physical and chemical properties in bulk and surface, of the solid materials, including (1) ferroelectricity in $PbTiO_3$, (2) colossal magneto resistance in $La_xCa_{1-x}MnO_3$, (3) ion conductivity for protons $(Ba,Sr)CeO_3$, (4) lithium mobility in $(Li,La)TiO_3$, (5) anion-intercalation pseudo-capacitors $LaMnO_{3-\delta}$, and (6) oxygen diffusion in $LaGaO_3$ for solid-state devices such as solid oxide fuel cells (SOFCs) [35]. Perovskites have various applications in heterogeneous catalysis i.e. oxidation of small molecules such as CO, electrochemical/thermochemical decomposition of hydrocarbons or nitrous oxides or H_2O or carbon oxides [24-29], reduction of CO_2 and/or N_2 and/or O_2. The flexibility of the electronic and crystal structure and chemical versatility of the perovskites can be used to establish design principles for highly active, selective and stable catalysts. Via a sophisticated design, the perovskites can be tailored-made to thermodynamically overcome reaction's electrochemical and chemical barriers [35].

11. Hydrotalcites;

    Hydrotalcites are a type of clay minerals and is another family of solid materials that have flexible compositions [36]. Chemical formula of the first compound of hydrotalcite was proposed by Manasse in Sweden around 1842 and was called magnesium aluminium hydroxycarbonate or $Mg_6Al_2(OH)_{16}CO_3{\cdot}4H_2O$ [37] while its layered structure is elucidated independently. The name of hydrotalcites are derived from its resemblance with talc and its high water content. The materials in this family are called 'hydrotalcite-like compounds" or HTlc or layered double hydroxides (LDH) and are generally represented by an empirical formula $[M(II)_{1-x}\,M(III)_x(OH)_2]^{x+}[A^{n-}{}_{x/n}]^{x-}.mH_2O$ where M(II) and M(III) are bi- and trivalent metal cations with suitable ionic radius, A is the interlayer exchangeable anion with charge -n, x is the molar ratio M(III)/[M(III)+M(II)] which ranges between 0.2 and 0.4, and m is the mol of co-intercalated water [37]. In catalysis, the hydrotalcites find their uses in fine-chemical synthesis, polymerization of alkene oxides, aldol condensation, or precursors for metal oxide catalyst's preparation.

12. Heteropolyanions;

    Heteropolyanions are polymeric oxo anions (polyoxometalates) formed by condensation of more than two kinds of oxo anions. The amphoteric metals of group 5 (such as V, Nb and Ta) and group 6 (such as Cr, Mo and W) in the +5 and +6 oxidation states, respectively, form weak acids which readily condense to form anions containing several molecules of the acid anhydride, which has only one containing in isopolyacids and their salts. Other acids can also form heteropolyacids and salts via condensation. The central heteroatoms in heteropolyanions can be approximately 70 elements [38]. The structures of heteropolyanions are classified into various families, according to their composition and structure, such as Keggin type $XM_{12}O_{40}^{n-}$, Dawson type $X_2M_{18}O_{62}^{n-}$, and Anderson type $XM_6O_{24}^{n-}$, where x stands for the heteroatom. The Keggin anion type, where the M atoms could be Mo or W, is most commonly utilized in catalysis. Keggin anion type can be used as a heterogeneous catalyst in hydration, dehydration, condensation, reduction, oxydehydrogenation of ethane, carbonylation and oxidation of methacrolein.

3.2.1.2 METALS AND METAL ALLOYS

Metals and metal alloys are used mainly in the form of gauzes or grids, acting as a bulk catalysts in highly exothermic reactions which require small height of the catalyst’s bed. For instance, platinum-rhodium grids are utilized in ammonia oxidation in the nitric acid process. Another example is dehydrogenation of methane to formaldehyde over silver grids. The first commonly used form of this type of catalysts is **skeletal (Raney-type) catalysts**. The remarkable one is made of nickel (Ni) which has its use in liquid-phase hydrogenation reactions, fine chemical productions and pharmaceuticals. Skeletal catalysts can be synthesized by selective removal of aluminum from Ni-Al alloy particles, performed by leaching with aqueous sodium hydroxide [39]. Skeletal Co, Cu, Pt, Ru, Pd catalysts have been prepared with surface area ranging from 30 to 100 m^2/g. One of the skeletal catalysts is that they can be active straight away without any pre-insitu reduction process because the active metals are somehow stored within. Another type is called **fused catalysts** which are normally used as alloy catalysts. This kind of catalysts can be prepared by homogeneous melt using rapid cooling, which yields metastable compositional materials [40]. Amorphous alloy such as metallic glasses have been also prepared successfully. The fused catalysts can be made of oxide materials. These oxides exhibit a complex and reactive internal interface structure which could be useful for either oxidation reactions or in the process of predetermining of their micromorphology. The prototype of this kind of catalyst is the multiply promoted iron oxide precursor of catalysts used for ammonia synthesis.

3.2.1.3 CARBIDES AND NITRIDES

According to the Sabatier's principle, the interactions between reacting species and a catalyst surface must be somehow 'at the right' value. Therefore, in this type of materials, C was firstly added to W to produce W_2C which is useful for isomerization of 2,2-dimethylpropane to 2-methylbutane. A number of elements such as C, N, P and B was incorporated into some transition metal lattices. Monometallic carbides and nitrides of transition metals normally have simple crystal structures where the metal atoms can be arranged in cubic close-packed (ccp), hexagonal close-packed (hcp) or simple hexagonal (hex) arrays, as tabulated and shown in Table 3.2. Their interstitial positions between metal atoms (aka interstitial alloys) can be occupied by C and N atoms. These kind of compounds have very high melting point (more than 3,027 °C), high hardness (more than 2,000 $kg \cdot mm^{-2}$) and high mechanical strength (more than $3x10^5$ MPa). Despite the fact that their physical properties resemble those of general ceramic materials, however, their electronic and magnetic properties are similar to typical metals [41].

Table 3.2: Common crystallographic of various carbides and nitrides of transition metals.

Crystal structure	Compound
ccp	TiC, ZrC, HfC, VC, NbC, TaC, TiN, VN, NbN, γ-Mo_2N, β-W_2N, Re_2N
hcp	β-Mo_2N, W_2C, Re_2C
hex	WC, MoC, δ-WN

These materials provide rich chemistry, thus offer great opportunity to new catalyst's development with a large ability for their applications, especially with the synthesis of these materials as well dispersed nanoparticles. The unique catalytic behaviors of this group of materials could be attributed to the changes in the electronic properties of the metal surface induced by the ligands and/or the geometry by which the metal and the ligands are arranged at the catalyst's surface. Hence, the metal surface reactivity is passivated by these ligands. This circumstances can be identified using some molecular simulations [42]. Bulk carbides and nitrides of either tungsten or molybdenum can be synthesized using advanced preparation methods. Their common surface area are found to range between 100 and 400 m^2/g. The materials can catalyze hydrogenation processes, hydrazine decomposition, methane reforming, liquid hydrocarbons synthesis via Fischer-Tropsch reaction, hydro-desulfurization, ammonia synthesis and hydrodenitrogenation. The catalytic properties of the materials can be tailored-made by oxygen treatment, leading to the formation of oxy carbides. In conclusion, carbides and nitrides of tungsten and molybdenum can be considered as substitutes for expensive Pt and other metals from group 8 to 10 [43].

3.2.1.4 CARBONS

Carbons in the history of catalysis have diverse roles as a support, a poison and an active phase. Many function of the carbons can be explained by wide variability of structures from combinations of strong homoatomic bonds between sp, sp^2, and sp^3 hybridized atoms [44]. In general, the catalytic properties of the carbons are due to the trigonal sp^2 and the tetrahedral sp^3, whereas the linear sp hybrid can be considered uninvolved. Because of these trigonal planar and the tetrahedral bonding, many carbon materials are structured as ‘inorganic carbon’. Inorganic carbon chemistry is different from organic carbon chemistry by its low hydrogen contents, with an arbitrary of fewer than 0.5 H atoms per C atom. Carbons exist in a variety of thermodynamic meta-stable phases, called ‘allotropes of carbon’ [45]. For example, graphite and diamond are 2 different inorganic carbon allotropes; where graphite is exclusively made of trigonal planar connectivity of the carbon, and diamond are having carbons atoms exclusively connected to one another by tetrahedral bond. The carbon materials have been extended to ‘SSAM’ or SCA (but beware, it’s not made of a single type of atoms so it can’t really be called allotropes) in the past decade. In these more modern compounds of carbon, atoms of carbon are hetero-bonding with other elements. Less useful carbons are also known such as soot or carbon black which are the carbons with large proportion of sp^3 centers in sp^2 matrices. These inert and very hard carbons can be prepared on metallic or oxidic substrates in the form of thin films with thicknesses ranging from nanometers to micrometers. The ‘glassy carbon’ is the only one type, derived from this kind of carbons, which find its use in electrolysis applications. Because the carbons are so various according to its nanostructures, Table 3.3 is used to classify some forms of carbons.

Carbon surfaces can contain a variety of functional groups, particularly those containing oxygen, depending on the provenience and pretreatment of the carbon. 2 functions of the carbon surface act simultaneously during the reaction; first, the reactants are chemisorbed selectively on the carbon surface by ion exchange via oxygen functional groups or directly by dispersion forces involving the graphite valence-electron system, the second function, the production of atomic oxygen occurs on the graphene basal faces of all sp^2 carbon materials. Catalytic applications of carbons include oxidation of sulfurous to sulfuric acid, selective oxidation of hydrogen sulfide to sulfur with oxygen in the gas phase at 127 °C, reaction of phosgene and formaldehyde, selective oxidation of creatinine by air in physiological environments and removal of NO.

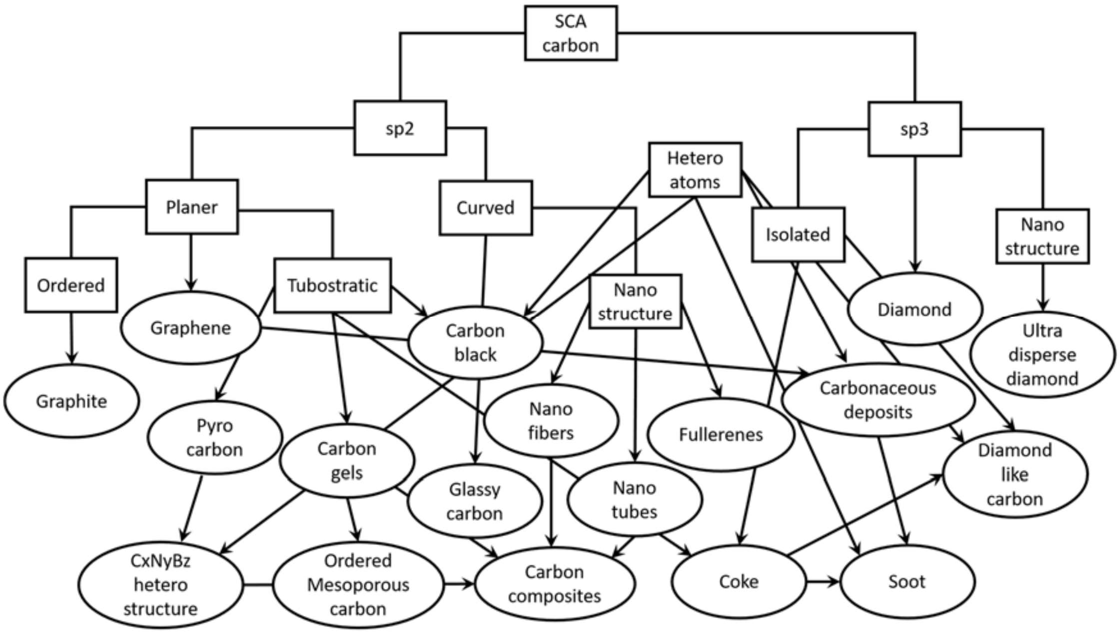

Figure 3.3: Linking of selected properties of carbon structures (rectangular) with families of carbon structures (ovals).

However, one of its limitation is when reacted in a gas phase under oxidizing condition, the reaction is close to irreversible oxidation. For more recent applications of carbons in catalysis, carbon nanotubes (CNT) and carbon nanofibers (CNF) are utilized as a catalyst and a catalyst's support. Both types of the materials, especially the CNT, has attractive properties in terms of electronic, mechanical and thermal characteristics. CNT-base catalysts are also privileged in liquid phase reactions due to their high mechanical strength and high resistance to abrasion while still offering high accessibility of the active sites. In additions, the CNT-based catalysts can be applied in as a carrier materials for proton exchange membrane fuel cells (PEMFCs) and direct methanol fuel cells (DMFCs) because of their high electrical conductivity and high oxidation stability.

3.2.1.5 ION-EXCHANGE RESINS AND IONOMERS

Ion-exchange resins or ion-exchanger are insoluble acidic organic polymers which have a backbone of cross-linked polystyrene and side chains of ion-active groups and can be synthesized by suspension copolymerization of styrene with divinylbenzene and subsequent sulfonation of the cross-linked polymer matrix [46,47]. By the mentioned preparation method, spherical beads obtained will have their diameters ranging from 0.3 to 1.25 mm. The size distribution, estimated by GAUSSIAN, is adjustable by the polymerization parameters. By the copolymerization, networks of micropores are produced proportioning to the amount of cross-linking agent. An open sponge-like structure of the beads and accessible inner surface within are obtained by using an inert solvents such as isoalkanes during the polymerization in which they dissolve the reactive monomers and precipitate the resulting monomers. Such metrix is a conglomerate of microsphere, interconnecting with cavities or macropores. The degree of cross-linking influences the size of micropores and macropores with the former's ranging from 0.5 to 2 nm, and the latter's from 20 to 60 nm. One of their disadvantageous is they become unstable at temperature higher than 127 °C, due to the split of sulfonic acid leading to a decrease in catalytic activity. Acidic resins are industrially used in the production of methyl tert-butyl ether. The ionomer Nafion is a perfluorinated polymer consisting of pendant groups of sulfonic acid which is believed to develop its super acidic properties. Nafion is well-known for its usefulness in alkylation, isomerization and acylation.

3.2.1.6 MOLECULARLY IMPRINTED CATALYSTS

Molecular imprinted catalysts are the catalysts that was firstly developed to imitate bio-catalysts or enzymes. They allow heterogeneous supramolecular catalysis occurring on surfaces of organic and inorganic materials with substrates. This kind of catalysis requires a materials that have shape and/or size selection capability on the surface or in the bulk. The transition states are stabilized by imprinting their features into cavities or adsorption sites, using stable transition-state analogues as templates is of particular interest. This type of materials can be prepared by doping Al^{3+} on silica gel and cross-linking polymers [48]. In addition, chiral molecular footprint can be also designed and imprinted on the surface of Al^{3+}-doped silica gel by using chiral template molecules. Specific adsorption sites are created when the transition-state are used as templates for molecular imprinting. Such molecular footprints on silica gel consist of a Lewis site and structures complementary to the template molecules which are able to stabilize a reacting species in the transition state and lower the activation energy of the reaction, so that, the active sites of bio-catalysts such as natural enzyme and catalytic antibody can be imitated.

3.2.1.7 METAL-ORGANIC FRAMEWORKS

Metal-organic frameworks (MOFs) are highly porous and consisted of metal ions/clusters (3 dimensional) which coordinate to multidentate organic ligands to form 1 or 2 or 3-dimensional structured materials. MOFs are one kind of coordination polymers, but porous. These organic ligands are sometimes referred to as 'struts' or 'linkers'. Similarly to Zeolites, the spatial organization of the structural unites gives rise to a system of channels and cavities on the nanoscale. One of the first MOFs which was early synthesized in 1999 was MOF-5 in which it consists of tetrahedral Zn_4O^{6+} clusters linked to terephthalate groups and has a specific surface area of 2,900 m^2/g. Another

MOFs that has an outstanding value of surface area is MOF-177 which has approximately 4,500 m^2/g. Pore size of MOFs can be tailored by using different length of linker. MOFs are considered attractive for various applications due to their ultra-high surface areas and their adjustable pore structures, relating to their size, shape and function. MOFS are widely used in the adsorption of the gases, natural gas's impurity removal and pressure-swing separation of noble gases e.g. krypton or xenon. Despite having more metal content, compared to the zeolites, however, the use of MOFs in catalysis is limited due to their relatively low stability at high temperature and in the presence of water vapor. The existence of the organic linker molecules can block the metal ions in MOFs, resulting poor accessibility in catalytic reactions [49].

3.2.1.8 METAL SALTS

Metal salts are considered Lewis acidic catalysts, containing of metals and salts; such as $FeCl_3$, $ZrCl_4$, $AlCl_3$, $CuCl_2$, $NiCl_2$, $ZnCl_2$, $MnCl_2$, $Fe(NO_3)_3{\cdot}9H_2O$, $Bi(NO_3)_3{\cdot}5H_2O$, $Zr(NO_3)_4{\cdot}5H_2O$, $Cu(NO_3)_2{\cdot}6H_2O$, $Ni(NO_3)_2{\cdot}6H_2O$, $Zn(NO_3)_2{\cdot}6H_2O$, $Fe_2(SO_4)_3$, and $CuSO_4$. The metal salts with highly electronegative cations have been used to catalyze liquid-phase nitration of benzene by NO_2 to nitrobenzene under solvent free conditions [50]. Some of other metal salts, i.e. $CrCl_2$ and $Al_2(SO_4)_3$, can be applied as a catalyst in transformation of glucose to 5-hydroxymethylfurfural (HMF). These metals are earth-abundant and commercially available, offering inexpensive and environmentally-friendly catalyst resources for conversions of carbohydrates [51]. Alkaline metal salts are often used as a base for organic synthesis and product purifications. These alkaline metal salts are commonly stable where their most stable oxidation state is +1. One of the catalysts in this group is K_2CO_3 which can be derived from wood ash and utilized as fertilizer or sustainable chemical. K_2CO_3 can be applied in a catalytic direct synthesis of carbamate from CO_2. Such material can be used solely without any ligands because it can activate both aliphatic and aromatic amines by itself. Carbonate and carboxylate however play an important role in proton abstraction from amine group [52].

3.2.2 SUPPORTED CATALYSTS

As explained previously, supports are important for the catalyst system in many aspects including to increase the surface area, to stabilize the active site's dispersion, to enhance mechanical and thermal stability etc. When the supports are involved, the knowledge in surface chemistry is mandatorily required. Even though supports are generally inert, but they are not always. They can either encourage the catalytic process, or in the other hand, interfere. For instance, the active site and support can work together as a bifunctional catalyst i.e. highly dispersed noble metals supported on the surface of an acidic carrier. Supports are normally very porous and thermally/mechanically stable [53].

3.2.2.1 SUPPORTS

Some of the bulk materials that are classified as the unsupported catalysts in the previous section can be seen as supports too. The binary oxides are well-known to be used as supports in many catalysis applications. This includes transitional alumina compounds such as α-Al_2O_3, SiO_2, MCM-41, TiO_2 (anatase), ZrO_2 (tetragonal), amorphous SiO_2-Al_2O_3, zeolites, MgO and many more. Other kind of supports are aluminophosphates, mullite, kieselguhr, bauxite, carbons and calcium aluminates. Some typical supported are gathered and tabulated as shown in Table 3.3.

Table 3.3: Properties and applications of various typical catalyst supports [4].

Support	Crystalline phase	Properties/Applications
Al_2O_3	mostly α- and γ-	SA* up to 400, thermally stable, 3-ways cat**, steam reforming
SiO_2	amorphous	SA up to 1,000, thermally stable, hydrogenations
Carbons	amorphous	SA up to 1,000, unstable in oxide environment, hydrogenations
TiO_2	anatase, rutile	SA up to 150, limited thermal stability, SCR cats
MgO	ccp	SA up to 200, rehydration is complicated, steam reforming
Zeolites	various	highly defined pore system, shape selective, bifunctional cats
Silica/Alumina	amorphous	SA up to 800, medium acid sites, dehydrogenation cats, bifunctional cats

*SA – surface area in m^2/g
**cat/cats – catalyst/catalysts

Some more examples in details are described here; Silicon carbide (SiC) has high thermal and mechanical stability, thus, is utilized in many catalysis applications i.e. dehydrogenation, H_2S oxidation, automotive exhaust, selective isomerization and alkanes oxidation [53]. SiC can be synthesized using various methods defining by phases of the reactants such as solid-state method, gas phase method and gas-solid method. One of the preparation method that gives the highest porosity and surface area is biotemplating [54]. This methodology offers ceramic composite materials with biomorphic microstructures. The source of carbon can be biologically extracted from wood by high temperature pyrolysis (827-1827 °C). This carbon can be used further as a template for infiltration with gaseous or liquid Si to form SiC or SiSiC ceramics. These materials are considered low density, low weight, while exhibit high-temperature stability. Monolithic supports are supported that have been fabricated into a desired shape of monolith. The monolithic supports are generally made unidirectional macrochannels and applied heavily in automotive emission control catalysis. One big advantage of monolith is that it can decrease the system's pressure drop by letting the fluidic stream of reactants and/or products passing through the whole catalyst's bed. The wall of the channels are normally non-porous, although may contains some macropores [55]. The monoliths are generally made of ceramic compounds (or cordierite) to give high mechanical strength and low thermal expansion. This together offer thermal shock resistance. Cordierite is a natural aluminosilicate ($2MgO{\cdot}2Al_2O_3{\cdot}5SiO_2$) which offers high accessible surface area, corresponded with geometric surface area of the channels. High surface area can be created by depositing a layer of a mixture of up to 20 different inorganic oxides, including transitional aluminas as a common constituent. This method of the catalyst deposit is called 'wash-coat' technique, allowing a relatively higher surface area of 50 to 300 m^2/g. Silica and polymers are the other type of materials that can be used as a catalyst's support. Silica or MCM-41 can be functionalized for the preparation of immobilized or hybrid catalysts. The functional groups may serve as anchoring sites (surface bound ligands) for complexes and organometallic compounds. Chiral groups can be introduced for the preparation of enantioselective catalysts [4].

3.2.2.2 SUPPORTED MIXED METAL OXIDE CATALYSTS

These materials consist of at least one active metal oxide component dispersing on the surface of an oxide support. The active sites of this catalyst system are often transition metal oxides whereas the supports are transitional aluminas (commonly γ-Al_2O_3), SiO_2, TiO_2 (anatase), ZrO_2 (tetragonal), and carbons [56]. In addition, these transition and noble metals are frequently used as a catalyst itself too, where their high catalytic activities are due to the outer electron configuration [57]. Single metal oxides can have different local coordination and morphologies i.e. isotropic, anisotropic or amorphous. The crystallization process of majority of metal oxides can occur at room temperature, although many crystallographic phases may remain amorphous at moderate calcination temperature. Besides, the isotropic (without preferential orientation) is the most common morphology of the one component metal oxides where its surface is ended with M-OH, M-O-M, M=O, or M-( ) (represents oxygen vacancy).Oxides containing 2 or more different metals are considered mixed metal oxides (MMOs) catalysts. Oxides can be binary, ternary or even quaternary, depending on the number of different metal cations. They can be classified whether they are crystalline or amorphous. The coordination and nature of the adjacent cations strongly influence the arrangement of cations, which governs the type of bonding between cations. The metal oxides and mixed metal oxides can be prepared by various methods i.e. sol-gel, wet-impregnation, mechanochemical synthesis, hydrothermal method, co-precipitation and microwave irradiation [15-17,20,25-29,58,59]. Due to their redox and acid-base properties, metal oxides are utilized in many catalysis applications; e.g. barium based-perovskites such as $BaCeO_3$, $Ba_{0.6}Sr_{0.4}CeO_{3-\alpha}$, $Ba_{0.6}Sr_{0.4}Ce_{0.9}Y_{0.1}O_{3-\alpha}$, and $BaCe_{0.6}Zr_{0.4}O_{3-\alpha}$ were applied in ceramic electrolysis cell for syngas production from CO_2 and H_2O [59], ceria-based catalysts were used as mixed metal oxide catalysts for 2 steps thermochemical cycles of co-splitting between CO_2 and H_2O [15], a double perovskite, $La_{0.3}Sr_{0.7}Co_{0.7}Fe_{0.3}O_3$, was found to be promising in syngas production via CO_2/H_2O co-splitting process [16,25], $Ce_xCr_{1-x}O_2$ was applied as a catalyst's support for Ni in methanation process for 2 types or reactors which are a packed-bed and a microchannel reactor [17], Zn/ZnO oxidation process was utilized in chemical-looping syngas production [20], $BaFeO_{3-\delta}$ was implemented in a high temperature water splitting process for high purity H_2 production [26], $La_{0.3}Sr_{0.7}Co_{0.7}Fe_{0.3}O_3$ was doped by 10%Ni and used as a support in syngas production process via integration of nitrous oxide decomposition and methane partial oxidation [27], $La_{0.6}Sr_{0.4}Co_{0.2}Fe_{0.8}O_{3-\delta}$ was bio-inspired fabricated as an active ceramic membrane for oxygen permeation material applications [28], $La_{0.6}Sr_{0.4}Co_{0.2}Fe_{0.8}O_{3-\delta}$ was applied in nitrous oxide decomposition process [29], CaCoAl-HTlcs are used for NO_x capture, decomposition and reduction [60], a mixed oxide from Mo, Nb, Sb, and V for the selective oxidation of propane [61], Ni/Mg-Al mixed metal oxide catalyst for steam reforming of ethanol [62], Mg-V-Al mixed metal oxides for oxidative dehydrogenation of propane [63], mixed metal oxides $La_{2-x}Sr_xCuO_{4-\delta}$ for hydroxylation of phenol [64], Al_2O_3 supported mixed metal oxides for destructive oxidation of $(CH_3)_2S_2$ [65], a trimetallic sulfide Re-Ni-Mo/Al_2O_3 was used in deoxygenation process of palm feedstock [66], Yttria-stabilized zirconia (YSZ) was applied in a solid oxide fuel cells (SOFCs) for simultaneously clean energy generation coupled with greenhouse gas treatment [67], Ni and Rh doped on Al_2O_3 was utilized in a process of H_2 production from oxidative reforming of n-butanol [68], Cu-ZnO/Al_2O_3 was implemented in a methanol synthesis in a slurry phase reactor [69], Ceria-based catalysts were applied in bio-oil production via hydrothermal pyrolysis of food wastes [70], and CeO_2/ZrO_2 and Al_2O_3 were used as supports for Ni metal in catalytic steam reforming and autothermal reforming of used lubricating oil (ULO) [71]. Due to their broad scope in catalysis field, they are also necessarily useful for many applications in organic synthesis and pharmaceutical industry. Mixed metal oxides have often higher catalytic activity than component oxides because they tend to have (1) higher surface area, (2) higher functional properties i.e. acidic sites or basic sites. These characteristics can increase yields of products, conversions and reduce reaction time.

3.2.2.3 SURFACE-MODIFIED OXIDES

The acidity or basic of MMOs can be improved using modifiers, e.g. incorporation of Cl^- on Al_2O_3 can enhance the catalyst system's acid strength. This can be achieved by chloride impregnation, $AlCl_3$ deposition, CCl_4 surface reaction [4]. On the other hand, Basic properties of the MMOs can be developed by adding some alkali metal compounds or their hydroxides such as KNO_3, $KHCO_3$ and K_2CO_3 on the MMOs, for instance, Al_2O_3 [72]. In addition, ultra strong acidic MMOs can be obtained by sulfation of several oxides such as ZrO_2, which is well-known for its super-acidic property. Another example is tungstated ZrO_2 in which it can catalyze the isomerization of n-alkanes to iso-alkanes at low temperature [73].

3.2.2.4 SUPPORTED METAL CATALYSTS

Metals in general have relatively high surface free energies which resulted in agglomeration of the metal particles on the surface and reduce its overall surface area. Thus, metals catalysts are rarely used on their own, but 'doped on' or 'supported by' high surface area porous materials [74]. The nanoparticles of the active metals can be spread and stabilized on the surface of the supported materials by the interaction of the active metals and the supports. This influences the electronic properties of the particles relative to the bulk materials. This concept is crucial for the raft-like particles of monatomic thickness where all atoms are surface atoms. Model supported metal catalysts having a uniform particle size and structure can be synthesized using anchoring molecular carbonyl clusters on support surfaces, followed by decarbonylation [75]. Supported metal catalysts can be bimetallic, containing 2 different kinds of metals which may be either miscible (e.g. Ni and Cu) or immiscible (e.g. Os and Cu) as macroscopic bulk alloys. The combination of an active and an inactive metal will dilute the active metal on the particle surface. Thus, the catalytic performance of reactions requiring ensembles of several active metal atoms rather than single isolated atoms is influenced [76]. Therefore, the selectivities of the catalytic processes can be optimized. Normally the surface composition of the binary alloys is different from its bulk composition. Lower surface free energy components are enriched at the surface. In addition, quite often that the surface composition of the binary alloys is altered by the reaction condition and atmosphere. In industrial scale applications, sometimes the supported metal catalysts are fabricated into macroscopic shapes i.e. spherical or cylindrical. Metal concentration within the pellets can be controlled by a special impregnation procedures. Besides, the profile of an appropriate metal concentration is important for the selectivity of a process due to the interplay between transport and reaction in the porous mass of the pellet. Noble metals (i.e. Pt, Pd or Rh) and non-noble metals (i.e. Ru, Ni, Fe or Co) on supports such as Al_2O_3, SiO_2 or active carbon have their applications in hydrogenation and dehydrogenation reactions. Another example is Ag doped on Al_2O_3, which is applied in ethane epoxidation. As well as Au, which is doped on a support, can work for low-temperature CO oxidation. Multi-metal catalysts is the catalysts that have more than 2 different metals in the system. Pt-Rh-Pd doped on CeO_2/Al_2O_3 can be used as an oxygen carrier in a large scale 3-ways car exhaust catalysts. Pt doped on chlorinated Al_2O_3 is the bifunctional catalyst used for catalytic steam reforming and isomerization of petroleum fraction. Pt is also can be modified by cinchona additives to be utilized in the enantioselective hydrogenation of α-ketoesters.

3.2.2.5 SUPPORTED SULFIDE CATALYSTS

Oxide precursors of metals such as MoO_3 or WO_3 can be treated under sulfidation process in a stream of H_2/H_2S, to achieve sulfide catalysts which can be doped on supports e.g. γ-Al_2O_3 or active carbons. Co and Ni can also promote the catalyst's system for hydro-treating process of crude oil or even hydro-desulfurization (HDS) [77]. Mostly, CoMoS and NiMoS are acceptably considered as active phase, which consists of a single MoS_2 layer or stacks of MoS_2 layers in which the promoter atoms are coordinated to edges. Co is believed to function as Co_9S_8 and as a solid solution in the Al_2O_3 support matrix. The catalytic activity of MoS_2 layers is related to the creation of sulfur vacancies at the edges of MoS_2 platelets. These vacancies have been seen virtually on MoS_2 crystallites by scanning tunneling microscopy (STM).

3.2.2.6 HYBRID CATALYSTS

Hybrid catalysts, which are catalysts that combine homogeneous catalyst and heterogeneous catalyst, can be obtained by immobilization or heterogenization of active metal complexes, organometallic compounds or enzymes on a solid support [78]. This kind of materials possesses advantages of both type of catalysts. For the homogeneous catalyst, its advantages include high activity, selectivity, and variability of steric and electronic property by choosing an appropriate choice of ligands or chiral ligands. Whereas the advantages of the heterogeneous catalysts are simple separation and recovery of the catalyst. The followings are several methods of immobilized homogeneous catalyst synthesis;

1. The active phases are anchored on the surface of suitable inorganic or organic supports; e.g. SiO_2, mesoporous MCM-41, zeolites, polystyrenes and styrene-divinylbenzene copolymers; via covalent bonds. This can be carried out through polymerization or copolymerization of feasible functionalized monomeric metal complexes.
2. Chemical fixation by ionic bonding using ion exchange.
3. Deposition of active species on surfaces of porous materials by chemi-or physisorption, or chemical vapor deposition (CVD). This preparation method is applied for the 'ship-in-a-bottle' catalysts which will be briefly described in another section.
4. The immobilized active organometallic species can be also prepared by a method of molecularly defined surface organometallic chemistry.

Alkoxy- or chlorosilanes can be used as a reagent for covalent bonding on silica-based materials such as SiO_2 or MCM-41. These reagents are often anchored to the surface by condensation reactions with surface hydroxyl groups. Functional groups thus created on the surface can include phosphines or amines. These functional groups serve as anchored ligands for active species that undergo ligand-exchange reactions. The spatial separation of active complexes (site isolation) can be achieved by a precise control of the density of functional groups. This helps avoiding undesired side reactions [79].

1. Immobilized enzymes;

   Immobilized enzyme is made of an enzyme connected to an inert insoluble materials such as calcium alginate. This type of catalyst is often used in bio-catalysis and in organic synthesis. The immobilized enzymes can increase resistance to changes in conditions i.e. pH and temperature [80]. In this catalyst system, the enzymes are hold in place throughout the reaction which results in an easy separation between the product stream and the catalyst. Advantages of the immobilized enzymes include convenience, affordable economy and high stability. Several preparation methods; affinity-tag binding, adsorption on glass, entrapment, cross-linkage and covalent bond; are used to prepare the immobilized enzymes [81,82].
2. Dendrimers;

   The functionalized at the ends of the dendritic arms can be used for immobilization of metal complexes. A catalytic effect is thus generated at the periphery of the dendrimer. Dendrimers sometimes can be called arborols or cascade molecules. Dendrimers consist of repetitive branched molecules and typically symmetric around the core, adopting a spherical three-dimensional morphology. The resemblance of the produced structures to prosthetic groups in enzymes let to the introduction of the word dendrizymes [83]. One of its outstanding applications is in membrane reactors. The selective oxidation reactions such as hydrogenation or C-C coupling reactions can be catalyzed by the immobilized homogeneous catalysts which had been proven to be very efficient in asymmetric synthesis [84].

The immobilized catalysts can be used in other specific processes such as supported (solid) liquid-phase catalysis (SLPC) [85] and supported (solid) aqueous-phase catalysis (SAPC) [86]. In SLPC, a solution of the homogeneous catalyst in a high boiling solvent is introduced into the pore volume of a porous support by capillary forces, and the reactants pass the catalyst in the gas phase. On the other hand, hydrophobic organic reactants are converted in the liquid phase. The catalyst consists of a thin film of water on the surface of the support such as SiO_2 and contains an active hydrophilic organometallic complex. SLPC can be adapted with ionic liquids for immobilization of homogeneous catalysts in supported ionic liquid phases (SILP) systems. Its advantages is that (1) they have low vapor pressure and (2) allowing long-term immobilization of homogeneous catalysts. The solid catalysts with ionic liquid layer (SCILL) has been conceptually utilized as a method to improve the selectivity of heterogeneous catalysts [87].

3.2.2.7 SHIP-IN-A-BOTTLE CATALYSTS

Ship-in-the-bottle catalyst (or tea-bag catalysts) is a catalyst that the active phase; i.e. metal complex; is inserted inside a host material which has small pores and is highly selective in shape e.g. zeolite. The active phase of the catalyst system tend to act in a very different behavior, compared to itself in a bulk form, where this phenomenon is considerably called 'the confinement effect' [88]. The ship-in-a-bottle catalyst can increase the rate of the desired reactions, resulting in higher selectivity. Its high activity is due to their well-separated particles inside the pores of the host material. The electron mobility of the active phase is hindered by the limited space inside the pores, thus, their light emission color could change making this type of catalyst applicable for micro lasers. This concept allows possibility of microfunctional materials in which the guest and the host are doing different tasks as the guest or active phase is confined, thus, the host and the guest together produced novel properties. The method can be improved by studying thermodynamics of the material using an established Pourbaix-enabled guest synthesis (PEGS). The operating conditions and the precursors should be chosen carefully as they play important role in deactivation of the host. A good example is a metal complex that is physically entrapped in the confined spaces of zeolite cages (confine catalysts). The metal complex is then believed to retain many solution properties. Their catalytic performance is therefore modified in a synergistic manner by shape selectivity, the electrostatic environment and the acid-base properties of the zeolite host. The metals can be centered by ligands in the zeolite cages include ethylenediamine, di-methylglyoxime, Schiff bases, phthalocyanines and porphyrines [89,90]. The entrapped complexes can be established by 3 main methods;

1. Flexible ligand method, where the zeolite cages are filled with the reaction of the preformed flexible ligand with transition metal.
2. Ship-in-a-bottle-technique, ligand from smaller species are assembled inside the pores of the zeolite.
3. Zeolite synthesis technique, synthesis of the zeolite structure around the preformed transition metal complex.

This kind of catalysts is also demonstrated as a model compound for mimicking enzymes, so-called ‘zeozymes’ in which the zeolite replaces the protein mantle of the enzyme and the entrapped metal complex resemble the active phase of the enzyme such as iron porphyrin.

3.2.2.8 POLYMERIZATION CATALYSTS

There are 3 main types of catalysts that is used in polymerization processes;

1. Ziegler-Natta catalyst;
   The Ziegler-Natta catalyst are mixtures of solid and liquid compounds containing a transition metal such as Ti or V [91]. For example, olefin polymerization can be catalyzed by $TiCl_4$ combined with $Al(C_2H_5)_3$ or other alkyl aluminum compounds. $TiCl_4$ can also be supported on $MgCl_2$, SiO_2 or Al_2O_3 to create more active catalysts where they increase the amount of active titanium. Conventionally, Ziegler-Natta catalysts can be prepared by ball-milling $MgCl_2$ with 5% (approximately) of $TiCl_4$ and the co-catalyst is $Al(C_2H_5)_3$.
2. Phillips catalysts;
   The hexavalent surface chromate is doped on high surface area silicate which acts as a support. Cr^{6+} is reduced by ethylene or other hydrocarbons to Cr^{2+} or Cr^{3+} which are probably served as the active species.
3. Metallocenes single site catalysts;
   Metallocenes single site catalysts are also developed for polyolefin production. The activity of these materials is enhanced by activation with methylaluminoxane (MAO), obtained by incomplete hydrolysis of $Al(CH_3)_3$. The activity of this type of catalysts are considered more flexible than the conventional Ziegler-Natta or Phillips catalysts. The selection of metal complexes and ligands can tailor the activity of the catalysts and the nature of the polymeric products [4,91].

3.2.3 COATED CATALYSTS

Apart from the (1) bulk catalysts, and the (2) supported catalysts, the (3) coated catalysts can be classified as the third category. The coated catalysts are catalytically active layers applied on inert structured surfaces which are different from the classical catalysts; i.e. powders, tablets, spheres and rings [4]. The active layers are made of bulk or supported catalysts. The examples of the popular catalyst systems are; egg-shell catalysts deposited on an inert carrier, monolithic honeycombs for environmental applications or for multiphase reactions, structured packing, foams and sponges, fibers and cloths, catalytic-wall reactors, catalytic filters for flue gas treatment and diesel exhaust after treatment, membrane or electrode assemblies for fuel cells, microstructured reactors with coated channels. The coated catalysts have advantages in optimal usage of the active mass, high selectivity at low diffusion lengths, highly efficient mass transfer and low pressure drop.

3.3 PREPARATION AND PRODUCTION OF HETEROGENEOUS CATALYSTS

The process companies; i.e. IG Farben, BASF, standard oil company and UOP; based in Germany and USA are solely in charge for producing solid catalysts until the end of World War II. Later on, many more independent catalyst companies were found across the world. These companies; i.e. Johnson Matthey, Synetix (ICI), Davison chemicals and Grace, SUD-Chemie catalyst group, Monsanto, Shell and criterion catalysts, Akzo chemicals, Haldor Topsoe, Evonik Degussa, Nippon Shokubai and Nikki chemical; are producing multitonne scale per year [92]. The solid catalyst's world market steeply increasing in 1990's and eventually reached 13 x 10^9 US dollars in 2008 [93]. Around 24 to 28% of the market went to the chemical industry whereas 38 to 42% went to petro chemical companies including refineries. In this amount, 28 to 32% were applied for environmental protection purpose, while 3 to 5% was utilized in the production of pharmaceuticals. For the solid catalysts, the selected preparation method; as well as operating conditions and the precursor's nature and quality; highly influences the catalyst's properties. In this case, physical and mechanical properties of all the intermediates and every details of the production steps are normally controlled, to receive a trustable reproducibility of the catalyst production – meaning that all batches are uniformly reproducible and replaceable by continuous operations. All this steps include precipitation, filtration, drying, calcination and forming. Recently, some automation system and control has been applied in catalyst production. For instance, static process control (SPC) and quality assurance (QA) have been integrated into the catalyst's production process. ISO standard has been also implemented, especially in

Europe and USA, to guarantee the quality of the produced catalysts. The production of unsupported catalysts and supported catalysts are generally using different techniques. In this section, the preparation methods for these 2 categories, which may differ significantly, are gathered and explained. As mentioned previously, the catalyst's component consists of active phase, support and promoter. The main methods are divided into 2 subcategories, which are (1) wet preparation methods and (2) dry preparation methods.

Question 3.2
3.2.1 What are the differences between the function of promoter and support? 3.2.2 What could be the synergistic effects of using a support? Can it somehow work as a promoter in that case?

3.3.1 CHOICE OF THE STARTING COMPOUNDS

Even if the elements containing in the catalyst's system are fixed, still the precursors and the preparation techniques are a choice. Where the choice in industry-scale production is based on the price of the precursors and the cost of the techniques that in academic world is rather based on nature, purity and simplicity of both precursors and the preparation methods. For example, sodium silicate is normally used in silica-based materials in industry, whereas silicon alkoxides are popularly used in academic research [94]. Another main concern about the selection of precursors is to avoid the unwanted interaction between the precursors, especially for inorganic catalysts as the synthesis process generally involves many kinds of salts, one of whose ions contains the desired element, usually a metal. This influences the contamination of the resulting catalysts, resulting in its poor purity.

3.3.2 WET PREPARATION METHODS

3.3.2.1 PRECIPITATION AND CO-PRECIPITATION (FROM AQUEOUS SOLUTIONS)

This is considered the most common method to prepare oxide materials in which exhibit high specific surface area where the precipitation from an aqueous solution is controlled by adjusting pH. Metal ions are generally soluble in acidic water solution while they can precipitate in hydroxide forms when the pH is adjusted to neutral or basic conditions. Therefore, the procedure of base metal oxides includes precipitation of the corresponding hydroxides or hydroxy-salts at an appropriated pH (normally slightly basic), then followed by the usual calcination to decompose the residual hydroxides/acid salts, which is normally occurring at around 200 to 550 °C. The precipitation can be quite easy if the different base metal cations share the mutual solubility of cations in the hydroxide phases; e.g. brucite-type hydroxides of bivalent cations, for instance, Mg^{2+}, Ni^{2+}, CO^{2+}, Zn^{2+} or oxy-hydroxides of trivalent metals such as Al^{3+}, Ga^{3+}, Fe^{3+} etc. For the more complicated cases, the co-precipitation of the trivalent and bivalent cations can be achieved by precipitating hydrotalcite-like layered mixed hydroxides in the form of hydroxy-carbonates, hydroxy-carbonates, hydroxy-nitrates or hydroxy-chlorides [94]. Because the precursors residual needs to be removed by calcination afterwards, thus, the use of the easily desorb compounds such as ammonia, amines, urea, ammonium carbonate or bi-carbonate are usually chosen as they are more appropriate for the high purity oxides.

Alumina is an interesting example because it is one of the main oxides used in catalysis. Moreover, it also illustrates a clear evidence of the experimental parameters which affect the characteristics of the final prepared catalysts such as pH, time, and temperature [95]. Aluminum salts can be dissolved in either acidic or basic solutions in which it is presented as $[Al(H_2O)_6]^{3+}$ and $[Al(OH)_4]^-$, respectively. In addition, the $[Al(OH)_4]^-$ is also known as 'aluminate' ions, denoted in a form of AlO_2^-. Looking at the detail, the aluminum hydroxides first occurs in a medium range of pH by basification of the $[Al(H_2O)_6]^{3+}$ or acidification of the $[Al(OH)_4]^-$. Aluminum hydroxide is one of the metal oxides that can appear in different crystallinity or structure which the set polymorph depends on the precipitation's condition. For example, neutralization of acidic solutions usually creates amorphous gels. Gibbsite (γ-$Al(OH)_3$) and Bayerite (α-$Al(OH)_3$) are the aluminum hydroxides that can be formed at low to moderate temperature ranges. Gibbsite is generally crystallized at either low or very high pH. As it is the most stable form of the aluminum hydroxides, thus, it is favored at long time of ageing in solutions. Bayerite is rather synthesized in a basic solution where the pH is independent from the precipitation's parameters. Besides, it's also a kinetic product that is precipitated immediately and thus is favored by short ageing times. The main difference between the gibbsite and bayerite is their structures which are the stacks of $Al(OH)_3$ hydroxides layers. In addition, the morphology of the particles are also different. The gibbsite structure is rather formed as flat platelets while the bayerite sheets are aggregated in a form of small elongated or conical structure. Another type of aluminum hydroxides, called boehmite (γ-AlOOH), is form if prepared at relatively higher temperature (up to 100 °C or slightly above), so called '**hydrothermal process**'. Boehmite as well exhibits a layered structure, although significantly different from those $Al(OH)_3$ mentioned previously. The crystallinity of the boehmite is increasing by ageing time, changing from a poor-crystallized pseudoboehmite (water-rich) to a well crystallized material.

The characteristics of the hydroxides such as the degree of crystallinity and morphology, as well as the interconnections of the different aluminum hydroxides are strongly relevant to the precipitation's conditions. The details are gathered and tabulated as shown in Figure 3.4, illustrating that the different forms of alumina are obtained depending on its nature and microstructure. These aluminas are considered 'transition aluminas' because they are transitioning from between aluminum hydroxides and the densest form of alumina, corundum α-Al_2O_3.

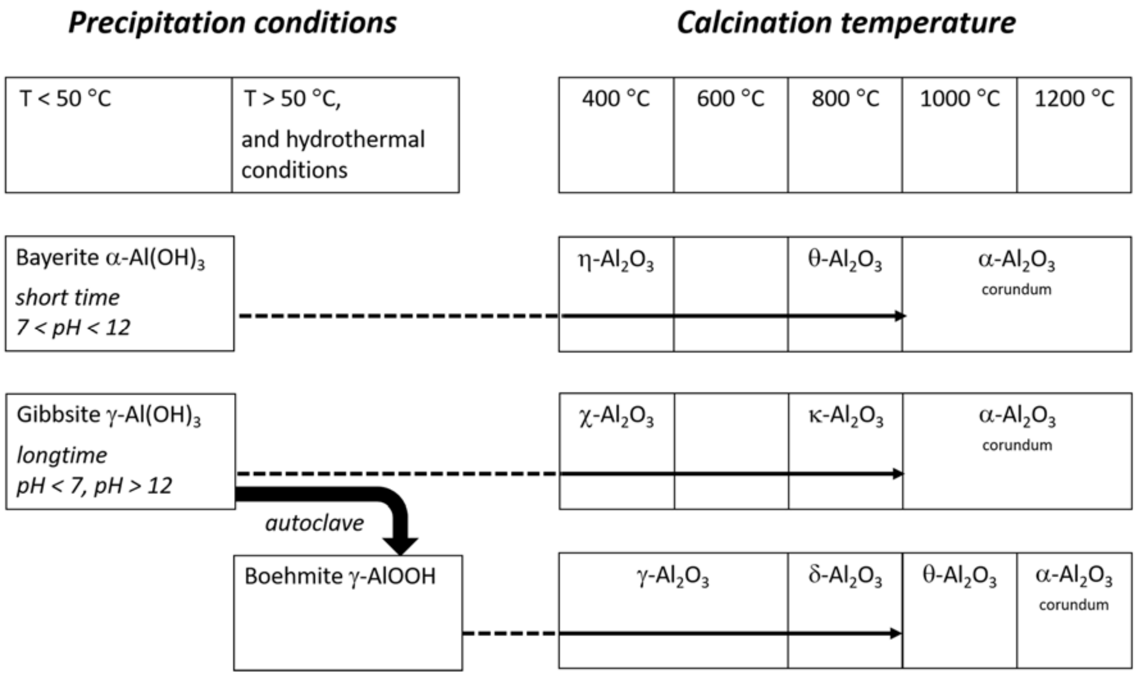

Figure 3.4: Thermal transformations of aluminum hydroxides [95].

Besides, the industrial production of precipitated catalysts usually involves (1) preparation of metal salt solution and of precipitating agent (dissolution and filtration), (2) precipitation, (3) ageing of the precipitate, (4) washing of the precipitate by decantation, (5) filtration, (6) washing of the filter cake (spray drying), (7) drying, (8) calcination, (9) shaping/fabricating/pelletizing, and (10) activation [4]. Some of the catalyst systems which can be prepared by precipitation or co-precipitation method are illustrated as shown in Table 3.4.

Table 3.4: Catalytic materials prepared by precipitation or co-precipitation method [4].

Catalysts	Precursors	Applications
Alumina	Na aluminate, HNO_3	Support, dehydration, Claus process
Silica	Na silicate (water glass), H_2SO_4	Support
Fe_2O_3	$Fe(NO_3)_3$, NH_4OH	Styrene production
TiO_2	Fe titanate, titanyl sulfate, NaOH	Support, Claus process, NO_x reduction
CuO-ZnO-(Al_2O_3)	Cu, Zn, (Al)nitrates, Na_2CO_3	LTS, methanol synthesis
Fe molybdate	$Fe(NO_3)_3$, $(NH_4)_2MoO_4$, NH_4OH	Methanol oxidation to formaldehyde
Vanadyl phosphate	Vanadyl sulfate, $NaHPO_4$	Butane oxidation, to maleic acid anhydride
NiO-Al_2O_3	Ni, Al nitrates, Na_2CO_3	Hydrogenation of aromatics
NiO-SiO_2	Ni nitrate, Na silicate, Na_2CO_3	Hydrogenation of aromatics

The co-precipitation of a mixed metal oxide catalyst can be illustrated as shown in Figure 3.5.

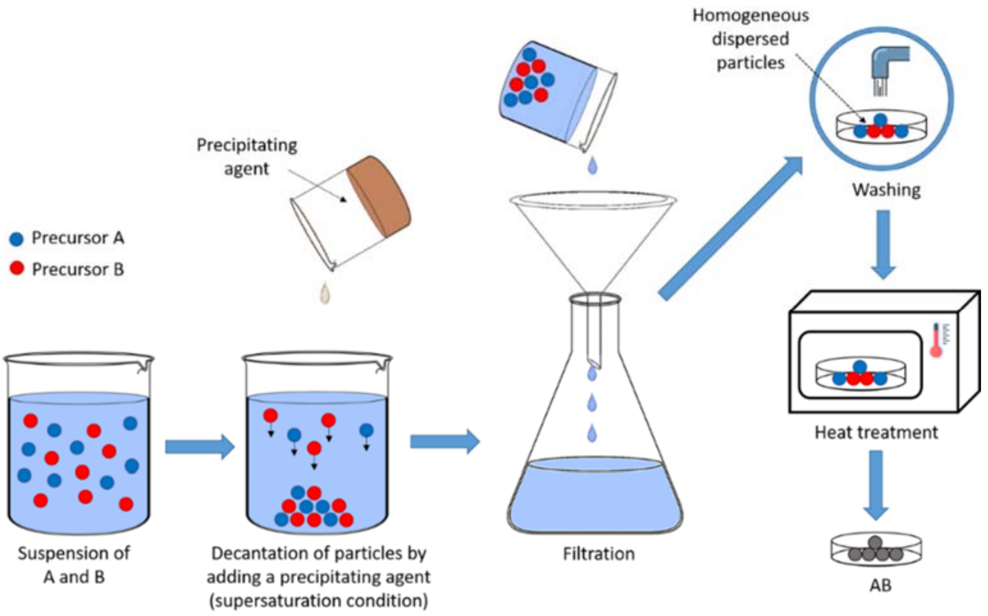

Figure 3.5: The schematic diagram of co-precipitation method where A and B is a metal precursor, forming a mixed metal oxide of A and B [96].

3.3.2.2 SOL-GEL

The main difference between precipitation and the sol-gel is the solvent. While the solvent used in precipitation technique is water, it is an organic solvent, usually alcohol, in the sol-gel process. The small or zero amount of water in the process enables better control over the catalyst's synthesis as it eliminates the precursor's condensation. This process when handled at high temperature is called 'solvothermal synthesis' which is comparable with the hydrothermal process in the precipitation technique, see Table 3.5.

Table 3.5: Classification of catalyst's preparation in terms of solvent and experimental conditions [97].

	Low Temperature	High Temperature
Solvent: Water Reactant: Water	Precipitation	Hydrothermal process (T>100 °C, autogenous P)
Solvent: Organic Reactant: Water	Sol-gel	Solvothermal synthesis (reflux, or T>boiling point, autogenous P)
Solvent: organic Reactant: Organic		Non-hydrolytic sol-gel process (T = 5-200 °C)

The solvothermal is to heat the solution in a closed system vessel under autogenous pressure above the boiling point of the solvent, which is generally polyol. The hydrated metal nitrates or alkoxides ($M(OR)_x$) and gels or preformed nanoparticles can be chosen as precursors. The hydroxide or the oxide particles form following a dissolution-nucleation-growth process, using the 'low amount of water available for controlled hydrolysis' and organic stabilizers such as long chain amines or acids which can be introduced in the reacting mixture to control the size and shape of the particles. The nanoparticles of oxides of the first line of transition metals; i.e. Mn, Fe, Co, Ni, Cu, Zn; and rare oxides; i.e. Nb_2O_5; are normally synthesized using the solvothermal synthesis.

The general sol-gel process is hydrolytic in which it involves alkoxide precursors $M(OR)_x$ dissolved in the parent alcohol ROH. This is carried out at low temperature. The oxide synthesis is initially created by addition of a controlled amount of water in order to hydrolyze the M-OR bonds or the alkoxide into M-OH group, which initiates the condensation via oxolation reactions.

$$\mathrm{M(OR)_x + H_2O \rightarrow M(OR)_{x-1}(OH) + ROH}$$

$$\mathrm{M(OR)_{x-1}(OH) + M(OR)_{x-1}(OH) \rightarrow M(OR)_{x-1} - O - M(OR)_{x-1} + H_2O}$$

$$\mathrm{M(OR)_{x-1}(OH) + M(OR)_x \rightarrow M(OR)_{x-1} - O - M(OR)_{x-1} + ROH}$$

Unavoidably, the tridimensional polymerization will occur, leading to either the formation of a precipitation of highly divided and uniform sized particles, or of a gel in which the solvent is retained within the continuous cross-linked network of the oxide. The addition of complex organic molecules e.g. acetates or acetylacetonates is able to tailor the polymerization rate, the crystallinity and the morphology of the oxide. Materials prepared by sol-gel offer higher specific surface area compared to those prepared by precipitation method, by giving around 900 m^2/g or more. For this reason, the sol-gel materials should be handled with care in terms of thermal treatment because too severe thermal conditions could be damaging to the overall surface area, caused by sintering, phase transformation or even the collapsing of the structure. Sol-gel materials are good for coating or further fabrication too, as it can be dried to xerogels or aerogels, occurring when the elimination of the solvent takes place in supercritical conditions.

On the other hand, the non-hydrolytic sol-gel process is when the synthesis occurs in an organic solvent solution with no water at all. In this process, the solvent is also the reactant that works as a donor of the oxygen atom, forming the oxide by bridging metallic ions together. Chlorides or acetates are normally used as precursors [98].

$$\mathrm{MCl_x + ROH \rightarrow MCl_{x-1}(OH) + RCl}$$

$$\mathrm{M(OAc)_X + ROH \rightarrow M(OAc)_{X-1}(OH) + AcOR}$$

$$\mathrm{M(OAc)_X + M(OR)_y \rightarrow M(OAc)_X - O - M(OR)_y + AcOR}$$

The non-hydrolytic sol-gel process is thermally activated in a closed vessel with temperature ranging from 50 to 200 °C. The advantages of sol-gel include high yield, low operating temperature and low cost.

3.3.2.3 AEROGEL (SOL-GEL CHEMISTRY FOLLOWED BY SUPERCRITICAL DRYING)

The history of the aerogels began in the beginning of 20th century when some researchers realized that the gas can replace the liquid in the pores to form an aerogel. Despite finding this out, the pores of the gels were usually destroyed by the strong surface tension of liquid-vapor interfaces during the poor drying process of evaporation [99]. Aerogels can be obtained by eliminating the solvent from a sol under supercritical conditions. This method is invented to improve the normal drying process of the gel via normal evaporation under ambient pressure which increases the capillary pressure, leading to shrinkage of the network. The typical solvents for aerogels preparations are methanol, ethanol and CO_2. The supercritical drying process to form aerogels consists of 3 major steps: (1) pressuring and heating the system to achieve the supercritical (SC) conditions; (2) eliminate the solvent by flushing with fresh SC fluids continuously; and

(3) depressurizing to remove the fluid phase. However, the pressurizing and heating must be performed in a slow process in order to avoid the shear stress and nanostructural cracking. Examples of the catalysts that can be prepared by aerogels are TiO_2, WO_3-ZrO_2 and V_2O_5-TiO_2 for photo-catalytic reactions, acid catalyzed reactions and oxidation catalytic reactions for VOC removal, respectively [100-102]. Figure 3.6 represents aerogel preparation.

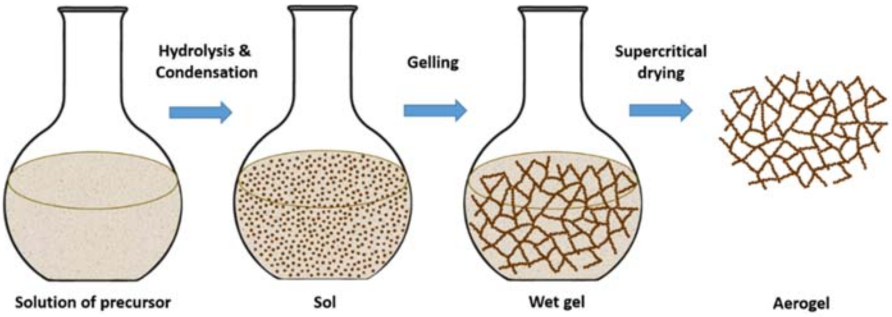

Figure 3.6: Schematic illustration of the aerogel preparation method [99].

3.3.2.4 DIRECT SOL-GEL IN SUPERCRITICAL LIQUIDS

Sol-gel method can be performed using supercritical fluids (SCFs), e.g. water or CO_2, which are somehow environmentally friendly to use, therefore, adding ecological credits to the sustainability of the sol-gel process. In addition, CO_2 has been utilized widely in industrial scaled polymerizations, food productions and nutrition productions [4]. The use of SCFs also gives advantages as the resulting materials are instantly dried in the process after the SCF venting. Another advantage is that the kinetics of the reaction can be precisely adjusted by operating temperature and pressure. This methodology enables the synthesis of materials which are difficult to synthesize, including the metal oxide nanoparticles in a continuous reactor. Other advantages of this direct sol-gel in supercritical liquids are: (1) the dielectric constant of water, which is tunable by this method, could help controlling the solubility of the solutes, apart from only the SCF density; (2) obtaining the high crystallinity of the metal oxides; (3) lower operating temperature range for the formation of some crystal in SCW.

3.3.2.5 MICROEMUSION AND REVERSE MICELLE

This method is a colloidal synthesis method where the surfactant molecules are used to limit particle growth using microemulsions [103]. The microemulsions are a combination of (1) an oil phase, (2) a surfactant and, (3) an aqueous phase. Thus, they can be either 'oil-in-water' or 'water-in-oil', depending on the concentration of the components. This transparent solutions consist of small droplets of an immiscible phase dispersing in a continuous phase. The interfacial tension between the immiscible dispersed and continuous phase can be reduced by surfactants, in order to stabilize the droplets. The sized of the droplets can be adjusted by altering the concentration of the dispersed phase and the surfactant. This gives the possibility of the droplets size varying from 1 to 100 nm, approximately.

For the reverse micelle method, the micelles will be produced from a nonpolar solvent with a polar core immersed in the reverse micelle. In the polar micelle, the small amount of water is presented in which the precipitation of the nanocrystal of oxides or other materials can occur. The reverse micelle method is useful for preparation of the unsupported metal nanoparticles where the reducing agent is added to the system in order to reduce the aqueous salt to the pure metal. The reverse micelles prevent the forming nanoparticles from agglomerations which results in larger particles. After the reaction, the surfactant remains adsorbed to the surface of the nanoparticles stabilizing them against aggregation and oxidation. This method can be assisted with the sol-gel method to prepare some of the supports e.g. silica for silica-supported metal catalysts. Metal or alloy nanoparticles can also be prepared using this method.

3.3.2.6 TEMPLATE-DRIVEN HYDROTHERMAL FOR POROUS MATERIALS

Organic molecules such as alkylammonium cations or structure directing agents (SDAs); can be used as a template in this synthesis method, to create porous materials such as zeolite [104]. In this case, the zeolite structure will be formed around the templates or even encapsulating around them closely between the organic groups and the pore walls. The number of organic units, that are allowed to be accommodated, will be controlled by such steric requirement. Therefore, for the templates like quaternary salts that serves as charge-balancing cations, the organic guest species impose a restriction on the zeolite framework charge density, leading to products of increased Si/Al ratio. Recently, most zeolites are prepared using templates, which need to be eliminated from the structure from calcination. The open-pore materials can be produced for their use in sorption and catalysis. However, the organic SDA's cost is the limitation as they cannot be recycled or recovered, thus, the new efficient template-free methodology is recently being developed.

3.3.2.7 SOLUTION COMBUSTION

In this method of synthesis, a saturated aqueous solution of the relevant metal nitrates are used as oxidizing agents while appropriate organic fuels; i.e. urea, hydrazine, carbohydrazide and maleic hydrazide; are employed as reducing agents. The mixture of redox agents will ignite upon heating at a determined temperature to initiate a self-propagating exothermic reaction that sustains high temperatures for a sufficient period of time to decompose all the organic material and metal salts. A well-crystallized material with nanometric size clusters are achieved as a resulting material. The material usually has high specific surface area as well as a positive consequence because a large amount of gases are produced during the synthesis process.

3.3.2.8 CITRATE AUTOCOMBUSTION

This kind of synthesis method was developed for mixed oxide catalyst's preparation. Citric acid is used in this method to allow the complexation of most metal cations. The citrate solution enable a good dispersion and mixing of cations in a single phase. The resulting solution will be dried by evaporation, giving solid powder which will be heated in air. The citrate ions will be decomposed by calcination, resulting in a high surface area mixed oxides. In addition, cellulose, examethylenetetramine, tartaric acid, glycine and urea can be utilized as complexing agents or fuels [105].

3.3.2.9 IMPREGNATION

Impregnation is a method where the pores of the supports are filled with active phase in a carrier form. In other words, this method is designed to fill pores of the supports with a solution of the catalyst's precursor such as a metal salt of sufficient concentration to achieve the desired loading. The impregnation can be performed more than once in case that the higher loading with active phase is required, which is normally done after drying or calcination. The impregnation method can be divided into 2 main types which are (1) 'dry impregnation' or 'incipient wetness' or 'pore volume' where the solution volume does not exceed the pore volume of the support and, (2) 'wet impregnation' where an excess of such solution is used [4,94,106]. Dry impregnation depends on retaining the species in the pores during the drying process, rather than on a specific interaction, in which it however plays more important role for the wet impregnation. One of the main advantages of the dry impregnation is the control over the weight of added component which is incorporated in the catalyst. However, its downside is that the catalyst prepared by dry impregnation may not be as uniform as that prepared by wet impregnation. For example, some catalysts might have larger pores so they can accommodate higher concentrations of the active species than in others. Therefore, the larger pores will take more volume of solution, leading to a high chance of receiving larger crystallines of the precursors, trapped in these pores, as shown in Figure 3.7.

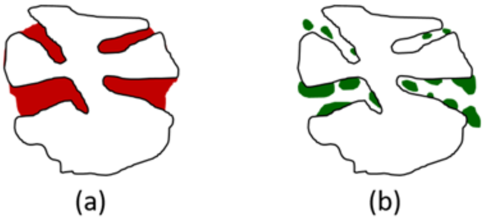

Figure 3.7: Illustrations of the (a) pore filling phenomenon via wet impregnation and (b) the active phase in the pores after the drying process [106].

Besides, the active phase can be badly formed at the mouths of the pores or even moved to the outer surface of the support, if the dry impregnation is not handled properly. For this reason, the distribution of the pores and the active materials therefore rely on the parameters of the pelletizing process. In addition, the wet impregnation is more difficult to control, compared to the dry impregnation. If the concentration of solute ions is low, all the solutes ions may be taken up at the mouth of the pores while none of them will be formed in the bulk of the support. The formation of an 'egg-shell catalyst' with a high concentration of active component at the outer surface of the pellet may of course be desirable if (1) this active phase is expensive or, (2) the reaction occurs mostly near the outer surface of the catalyst pellets due to limitation of pore diffusion. However, if the reaction is kinetically controlled in which all the bulk of the catalyst is utilized, thus it is desirable that all the active phase is uniformly spread throughout the pellet. In this case, the multiple impregnation may be required, as mentioned before, to ensure that the active phase is impregnated in all parts of the support and presented in a sufficient concentration. For both dry and wet impregnation, the drying process after the impregnation is crucial. If the drying rate is too high, the liquid contained in the pores will be removed from the pores due to the vapor being created from the inner part of the pores. This will result in unwanted deposition of the active phase on the exterior surface of the support. This will be strongly adhered on the support's surface, thus, the dusting (accumulation of a dust of active phase down-stream of the catalyst bed) will be likely to occur. This sometimes can cause a blockage of the reactor's exit. The calcination process is just as important. The flowing carrier gas is generally required to flush away the oxides of salts, which are formed from decomposition of the salts (precursors) such as nitrates. This will prevent the undesired products to be formed on the catalyst's surface. The elimination of water is to be handled with care too as water vapor can lead to sintering in some oxides. If the catalysts need to be reduced before used, the reduction rate should be kept low.

3.3.2.10 ION EXCHANGE AND ADSORPTION

Ion exchange methodology occur when a precursor from an aqueous solution is in contact with the support. The precursors; such as metal cations, oxoanions or other ionic species; are dissolved in the aqueous solution. These ionic species will be electrostatically attracted to the surface of the support by charged sites. After a certain contacting time, the solid will be separated from the solution by filtration. This ion exchange and adsorption process is often used for cationic zeolite production from protonic zeolites. The process presumably occurs via the exchange between cation and proton at equivalent number in terms of total charge. Ions therefore can be adsorbed on the surface, such as that of an oxide carrier. The cations adsorption is supposed to happen when pH is more than the point of zero charge (PZC) of the carrier, as shown in Table 3.6, while the adsorption of anions occur at pH lower than PZC.

Table 3.6: Point of zero charge of metal oxides.

Metal oxides	**PZC**	**Metal oxides**	**PZC**
MgO	10.8	ZrO_2	6.3-7.1
ZnO	8.6-10.3	CeO_2	6.5
Al_2O_3	8.5-9.0	TiO_2	5.1-6.4
NiO	7.5-10.5	SnO_2	3.9-4.9
Fe_2O_3	7.5-9.3	Nb_2O_5	3.5-4.0
La_2O_3	6.7-9.6	SiO_2	2.0-3.8

3.3.2.11 GRAFTING

Grafting is a process to dope the active phase on the support by putting the active species in contact with the surface of the support. This could be carried out in either gaseous or aqueous solution. For example, volatile metal chlorides from any organic solutions react specifically with the surface hydroxyl groups of silica. This process allows the hydrophobilization of the silica's surface due to the partial disappearance of the silanols after the reactions with alkoxysilanes [94].

Question 3.3

3.3.1 What kind of implementation could microemulsion and reverse micelle be useful for?

3.3.2 Can you think of the benefits of performing ion-exchange on zeolitic catalysts? i.e. enhancing acidic or basic properties? Give some examples

3.3.3 DRY PREPARATION METHODS

Dry preparation methods are when the precursors react without having to be dissolved in any solutions.

3.3.3.1 THERMAL DECOMPOSITION OF PRECURSORS

The thermal decomposition of precursors; e.g. hydroxides, nitrates, carbonates, hydroxy-carbonates or other salts; are used for preparation of some inorganic solids such as metal oxides. This methodology is often occurred at relatively moderate temperature range, where the original structures are broken and allowing high surface area materials to be prepared [94].

3.3.3.2 SOLID-STATE REACTION

Simple component oxides can be prepared using this thermal treatment of solid phase substances. $NiAl_2O_4$ can be synthesized by heating NiO and Al_2O_3 together at 1,200 °C. The method usually gives well-crystallized complex solids with low surface area [94].

3.3.3.3 FLAME HYDROLYSIS OF METAL CHLORIDES

Metal oxides can be synthesized by reactions between the corresponding volatile metal chlorides; i.e. $SiCl_4$, $TiCl_4$, $ZrCl_4$, $CeCl_4$ and $AlCl_3$; in a hydrogen-oxygen flame at 1,000 °C. By this method, the resulting materials will have small nonporous oxide primary particles that tend to agglomerate in linear and branched chain-like structures. This method is widely used for commercial productions of alumina, silica, and titania [94].

3.3.3.4 SOLID-STATE WETTING

Solid-state wetting is a method where low melting point compounds disperse over the surface of the catalyst’s support. Metal anhydrides such as V_2O_5 and MoO_3 can spread over typical oxides such as alumina, titania and zirconia while the supports are heated at high temperature. The materials prepared by this method offer catalytic efficiency/performance as high as those prepared by the more classical method i.e. wet impregnation method [94].

3.3.3.5 SOLID-STATE ION EXCHANGE

Zeolites or other ion exchanger solid can be also exchanged in solid-state reaction too. Theoretically, the concept is quite similar to those carried out in liquid state. For example, when the mixture exchanger salt or protonic zeolite are heated at high temperature, the cation exchange occurs and HCl is evolved. This can be utilized with the preparation of copper/zeolites using $CuCl_2$ as the salt's precursor and protonic zeolites [96].

3.3.3.6 COMBUSION SYNTHESIS

This method is also well-known as 'self-propagating high-temperature synthesis'. It is a general method that is used to prepare inorganic materials from exothermic combustion reactions. The combustion synthesis can be completed in relative short time and demands much less energy, compared to the classical solid-state synthesis which needs longer operating time and higher operating temperature. The combustion synthesis requires much lower external energy as the system has its heat energy released within the reactor upon the progress of the reaction. Thus, many industrial scale catalytic inorganic material productions opt for this combustion synthesis method as it provides an efficient and feasible procedure. One of the recent development of this method is the carbon combustion synthesis of oxides. It is novel and economical for producing micro- and nano-particles of complex oxides which are further utilized for advanced device applications. The carbon sources; i.e. pure carbons (graphite or soot) and carbon compounds (starch); will be added to the reactant mixture to generate the required heat (created by ignition). Afterwards, the mixture will be introduced into a reactor where it is exposed to oxygen. The reaction between the carbon and oxygen is highly exothermic, generating a high heat which made the reactor 'self-sustaining' in terms of energy. The materials prepared by this method are normally having high porousity (70%) and having particle size ranging from 50 to 800 nm [94].

3.3.3.7 PREPARATION OF FUSED CATALYSTS

This method is a common methodology for the 'iron-ammonia synthesis' which is a fusion of the magnetite Fe_3O_4 precursor with promoters; i.e. silica, alumina, potash calcium oxide; at high temperature, higher than 1,400 °C. The finishing process includes melting, cooling and grinding. The preparation of fused catalysts can be applied for iron catalyst's preparation for Fischer-Tropsch reaction as well.

3.3.4 ASSOCIATED EQUIPMENT USED FOR MOST TECHNIQUES

Most of the mentioned techniques can be applied with a use of additional equipment such as microwave, ultrasound etc. to improve the quality of the materials and to make the preparation procedure more efficient i.e. shorter preparation time. This use of equipment generally helps reduce the preparation time from days to minutes and yet allows screening of a wide range of experimental conditions for optimization and scaling-up, with even lower energy consumption.

3.3.5 INTERMEDIATE AND FINAL TREATMENTS IN PREPARATION CHEMISTRY

This can be considered as a kind of unit operation in the catalyst field. In the industrial scale, continuous operations are favored because of the larger capacity, lower operational cost and better quality control. Recently, environmental concerns and hazards to human health are taken into account where these issues can be managed more easily.

3.3.5.1 FILTRATION AND WASHING

The filtration is carried out in order to separate the precipitates from the residuals while the washing is to remove any possible by-products and impurities which might be contaminated the final products. In batch operation, often the ‘plate-and-frame filter’ presses are applied [107]. The filter cake is usually washed in the countercurrent, to the filtration direction. Another popular filter is the ‘continuous vacuum rotary filter’. The quantity of filtered slurry and the thickness of the filter is adjustable by changing the speed of the filter drum. When the drum is rotating, the water will be sprayed against the moving cake. The washed filter cake is then scraped out for further treatment. Another well-known method for separation is the ‘centrifuge’ which can be operated under either discontinuous or continuous operation. The centrifugal separation is an available choice when the filtered material is grainy or crystalline, for example, zeolite. Washing can be performed within the centrifuge machine by introducing washing agent into the centrifuge.

3.3.5.2 DRYING

Drying is one of the crucial catalyst’s finishing processes because it can alter the physical properties of the catalysts. Therefore, it is important to measure and keep the drying parameters; i.e. drying rate, drying temperature, drying duration and drying gas flow rate; constant. For example, the drying parameters of impregnated support can change the distribution of the active phase. In this case, the uniform dispersion can be achieved only via spontaneous liquid evaporation in which the heat of evaporation can go up to 127 °C [107]. Various tools are used for the drying process in continuous operation. These tools include box furnaces with trays (this can be used to dry small batches of catalyst precursors), drum dryers, rotary kilns and spray dryers. The main downsides of the drums and rotary dryers are the feeding of the wet filter cake and removal of adhering material from the walls because the material lumps are usually formed during the drying process, thus, the resulting material must pass a granulator equipped with a sieve. Whereas the spray dryers offer microspherical materials with a small particle size distribution. The spray dryer can be assisted with a nozzle or a rotating disk to disperse the watery slurry of the filter cake in a stream of hot air.

3.3.5.3 CALCINATION

Calcination is a thermal treatment of the materials. This can be performed in an oxidizing or reducing surrounding atmosphere (gaseous agents flowing through the furnace and in direct contact with the materials) and is carried out to stabilize both physical and chemical properties of the catalysts. At the beginning, the thermally unstable compounds/precursors (carbonates, hydroxides and other organic compounds) will be converted to the more stable form. For example, in the thermal decomposition of Cu or Ni nitrate deposited on alumina, not only CuO and NiO are formed, but also Cu and Ni aluminate [108]. Calcination can make the amorphous materials become crystalline. It can also change the physical (such as pore structure) and mechanical properties of the catalysts too. Researchers often choose the calcination temperature to be slightly higher the selected reaction temperature. Rotary kilns are mostly chosen for the calcination of powder and granulate catalysts, whereas box furnaces or muffle furnaces with trays are more favorable for smaller batches or powder catalysts. Belt and tunnel furnaces are usually utilized for calcination of pellets and extrudates. Because the tunnel furnaces can operate at higher temperature, compared to the belt furnaces, they are normally used for calcination of ceramic materials.

3.3.5.4 REDUCTION, ACTIVATION AND PROTECTION

These methods can be considered as the latest step of the catalyst finishing treatments. This can be done by either the catalyst producers or in the plant by the users (in situ). The well-known example will be the reduction of NiO-kieselguhr where the activated Ni can be obtained by reduction process, carried out by the catalyst's producer. The reduction of powders is performed on an industrial-scaled fluidize bed reactors. The reduced material is pyrophoric and its oxidation with air must be prevented by coating it with inert fat such as tallow. The finished catalysts are generally sold in the form of flakes or pastilles [107]. The reduction of metal oxide catalysts i.e. NiO, CuO, CoO or Fe_2O_3 is carried out by treating it with flowing gaseous H_2 at elevated temperature. Its brief mechanism consists of 2 main steps; (1) metal nuclei are formed and; (2) nuclei accumulate to form metal crystallites. A narrow distribution of metal crystallite size can be achieved by reduction process which handled at relatively low temperature (< 300 °C). Whereas the broader distribution could be obtained when reduced at higher temperature (> 400 °C). Some of oxides such as those formed from Cu and Fe will need to be performed with diluted H_2 in inert gases such as N_2, Ar or He due to its highly exothermic reduction reaction. In this reduction process, often that the water, as a by-product, is very much unwanted as it gives negative effect on the rate of reduction and the degree of reduction. For this reason, when the H_2 is recycled (mostly in an industrial-scale catalyst manufacturing), water will be abated by either freezing out or molecular sieve adsorption. Partial reduction is applied when the activity of the catalyst needs to be tailor-made. For example Ni catalysts for fat and oil hydrogenation contain about 50 to 60% by weight of metallic Ni, 35 to 45% by weight of NiO and around 5% by weight of Ni silicate. For the protection or passivation, when the reduced catalysts are made, the readily active materials are protected or passivated with high boiling point liquids (higher aliphatic alcohols or C_{14}-C_{18} paraffins). During this method, chemisorbed hydrogen is removed in a gas stream composed of N_2 and about 0.1 to 1.0% by volume of O_2 at ambient temperature. After the treatment, the catalysts can be handled in air. The catalysts will be reactivated by H_2 treatment again by a user.

3.3.5.5 CATALYST FORMING

Catalysts may need to be fabricated into shapes or other forms for many reason. To reduce the pressure drop within the reactor is one of them. Reactions in the liquid phase normally require small particle or fine powders with the particle size ranging from 50 to 200 µm. The materials are then prepared by grinding of a dried or calcined precursors, then bring sieved to the desired uniform particle size. Larger size of the catalysts (0.05 to 0.25 mm) are required for fluidized bed reactors. These catalysts are generally made by spray drying technique or by cooling the molten materials droplets e.g. V_2O_5 in an air stream. Al_2O_3, SiO_2 or aluminosilicate in a spherical shape, sizing from 3 to 9 in diameter, are fabricated by mainly the so-called ‘oil-drop’ method, to be used in moving-bed or ebullating-bed reactors. Spherical shaped catalysts prepared by this method are sufficiently resistant to abrasion during the reaction procedure. Another method for producing spherical shaped catalysts is based on agglomeration of powder by moistening on a rotating disk (spherudizer). The spheres are removed automatically when the desired diameter is reached and then transported to the dryer and calcination reactor. This kind of method is suitable to prepared spherical catalysts for fixed bed reactors. In addition, the hollowed-out hemispherical catalysts can be prepared using a briquetting technique where the plastic mixture of catalyst powder with a binder is fed between 2 rotating rolls.

Extrusion of catalyst pastes (consist of catalyst, binder (calcium aluminate cement), lubricant (poly vinyl alcohol, powdered stearin and Al) and other additives) is widely used for industrially shaping method. In addition, if the catalyst contains alumina, peptizing agents such as nitric acid are added in order to improve the mechanical strength. Either a press or a screw extruder is generally applied, depending on the physical properties of the pastes. Press extruders are more suitable with viscous pastes while the screw extruders are more for thixotropic masses. For both extruders, the pastes will be forced through holes and cut to a certain length. Afterwards, they will be dropped onto a moving belt transporting it to a dryer or calciner. The extruders can produce materials in many shapes such as cylinders, hollows or ribbed cylinders. Their typical sizes are ranging from 1.5 to 15 mm in diameter. Pelletizing is a basic method for catalyst forming or shaping. The methodology includes a compression of a certain volume of powder in a mold between 2 moving punchers. Afterwards, the pelletized catalysts are normally crushed and sieved to a certain size range. Sometimes; lubricants such as graphite, Al stearate, poly (vinyl alcohol), kaolin and bentonite; are added into the catalyst's recipe before entering the pelletizer. The lubricants and other additives can be eliminated afterwards by calcination. The fluidity of the material is required to be homogeneous. Comparing between the extruding and the pelletizing, the extruding tends to be less expensive, but less resistance to abrasion compared to the pellets. In addition, industrial pelletizers (with pressures in a range of 10 to 100 MPa) are able to produce around 10 liter of pellets per hour or more. Pellets can be made in a form of rings, cogwheels, spoked wheels or multi-hole pellets [107].

3.3.5.6 COATING OF INERT SUPPORTS

Coating of inert supports with a thin layer of active phase is a well-known method to produce a sophisticated catalyst system. One way to classify these many method is to look at (1) material-dependent methods and (2) material-independent methods for coatings. Material-dependent methods are anodic oxidation of aluminum or its alloys which gives rise to a layer with a one-dimensional and uni-directional pore system with adjustable properties and formation of porous layers on FeCrAl alloys by thermal treatment. Whereas the material-independent methods can be grouped according to the state of aggregation of the catalyst precursor. The chemical-vapor deposition (CVD) or physical vapor deposition (PVD) can be applied to transform the gaseous catalyst precursors into coating layers. Generally, sol-gel method, deposition of catalyst suspension or the combination of those are chosen for the coating method, depending on the adjusted viscosity of the sols or suspension. Besides, the liquid precursors can be applied on surfaces by dip-coating, spraying, printing or even rolling, whereas the solid catalysts can be applied by flame spray deposition or powder plasma spraying. One of the most intensively studied catalyst forming in the past decades is monoliths. The oxides such as Al_2O_3, CeO_2 or ZrO_2 can be wash-coated on the monoliths with a honeycomb-like structure. This kind of materials is used widely as vehicle pollution control units.

Question 3.4
3.4.1 What is calcination for?
3.4.2 What is the criteria for selection the calcination temperature for a certain catalyst under a certain reaction?

3.4 SUMMARY AND PERSPECTIVES

The aim of this chapter is to classify and specify the type of catalysts as well as to address their suitability to a specific process. This chapter also includes guidance on catalyst preparation methods which began with the choice of the starting compounds and each individual means of preparation categorized by phase of the precursor i.e. wet preparation method, dry preparation method and others. The post treatment processes such as filtration/washing, drying, calcination, reduction/activation and the catalyst fabrication e.g. monolith, coating. Membrane were also explained. Future development in the catalyst preparation should focus on green synthesis while rely more on DFT or other computational based pre-research. This should emphasize on environmental impact, energy, water usage and toxic release from cradle to grave. Up-scaling process could be different from what presented here in this chapter which is a lab-scale based and more as an academic level and research.

REFERENCES

[1] C.H. Bartholomew, R.J. Farrauto, Fundamentals of industrial catalytic processes, 2nd ed., Focus Catal. 2006 (2006) 8. https://doi.org/10.1016/s1351-4180(06)71799-8.
[2] O. Brümmer, K.A. Hall, M. Leclerc, S.E. Lee, V. Murphy, Combinatorial methods in catalysis and materials science, in: Ullmann's Encycl. Ind. Chem., 2003. https://doi.org/10.1002/14356007.f07_f02.
[3] O. Trapp, Gas chromatographic high-throughput screening techniques in catalysis, J. Chromatogr. A. 1184 (2008) 160-190. https://doi.org/10.1016/j.chroma.2007.10.086.
[4] O. Deutschmann, Heterogeneous Catalysis and Solid Catalysts, Wiley-VCH, 2009.
[5] P. Van Der Voort, K.C. Vrancken, E.F. Vansant, Gas-phase chlorosilylation of silica gel: Effectiveness, surface coverage and stoichiometry, J. Chem. Soc. Faraday Trans. 91 (1995) 353-357. https://doi.org/10.1039/FT9959100353.
[6] J.M. Thomas, R.G. Bell, C.R.A. Catlow, G. Ertl, H. Knozinger, J. Weitkamp, Handbook of heterogeneous catalysis (Vol. 1), Weinheim: Wiley-VCH, 1997.
[7] E.A. Colbourn, W.C. Mackrodt, A theoretical study of co chemisorption at {001} surfaces of non-defective and doped MgO, Surf. Sci. 143 (1984) 391-410. https://doi.org/10.1016/0039-6028(84)90549-1.
[8] S. Coluccia, A.J. Tench, Proc. 7th Intern, Congr. Catal. (1980) 1160.

[9] R.N. Spitz, J.E. Barton, M.A. Barteau, R.H. Staley, A.W. Sleight, Characterization of the surface acid-base properties of metal oxides by titration/displacement reactions, J. Phys. Chem. 90 (1986) 4067-4075. https://doi.org/10.1021/j100408a047.

[10] C.N.R. Rao, B. Raveau, Transition Metal Oxides, Weinheim: Wiley-VCH, 1995.

[11] P. Pichat, G. Ertl, H. Knozinger, J. Weitkamp, Handbook of heterogeneous catalysis (Vol. 4), Weinheim: Wiley-VCH, 1997.

[12] W. Gopel, K.D. Schierbaum, G. Ertl, H. Knozinger, J. Weitkamp, Handbook of heterogeneous catalysis (Vol. 3), Weinheim: Wiley-VCH, 1997.

[13] D.A. Solís-Casados, A. Gómez-Cortés, G. Díaz, Textural and redox properties of CeO_2 nanoparticles prepared by using a non-ionic surfactant, in: Stud. Surf. Sci. Catal., 2006: pp. 363-368. https://doi.org/10.1016/S0167-2991(06)80928-6.

[14] M. Anwar, A. Muchtar, M.R. Somalu, Effects of various co-dopants and carbonates on the properties of doped ceria-based electrolytes: A brief review, Int. J. Appl. Eng. Res. 11 (2016) 9921-9928.

[15] N. Ngoenthong, M. Hartley, T. Sornchamni, N. Siri-nguan, N. Laosiripojana, U.W. Hartley, Comparison of packed-bed and micro-channel reactors for hydrogen production via thermochemical cycles of water splitting in the presence of ceria-based catalysts, Processes. 7 (2019) 1-12. https://doi.org/10.3390/pr7100767.

[16] N. Ngoenthong, V. Tongnan, T. Sornchamni, N. Siri-nguan, N. Laosiripojana, U.W. Hartley, Application of a micro-channel reactor for process intensification in high purity syngas production via H_2O/CO_2 co-splitting, Int. J. Hydrogen Energy. 46 (2021) 24581-24590. https://doi.org/10.1016/j.ijhydene.2019.11.240.

[17] C. Wongsartsai, V. Tongnan, T. Sornchamni, N. Siri-nguan, N. Laosiripojana, M. Hartley, U.W. Hartley, CO_2 utilization via methanation using 40%Ni/$Ce_xCr_{1-x}O_2$ as a novel catalyst: a comparative study of packed-bed and micro-channel reactors, React. Kinet. Mech. Catal. (2020). https://doi.org/10.1007/s11144-020-01853-1.

[18] K. Kochloefl, G. Ertl, H. Knozinger, J. Weitkamp, Handbook of heterogeneous catalysis (Vol. 5), Weinheim: Wiley-VCH, 1997.

[19] M. Muhler, G. Ertl, H. Knozinger, J. Weitkamp, Handbook of heterogeneous catalysis (Vol. 5), Weinheim: Wiley-VCH, 1997.

[20] V. Tongnan, T. Sornchamni, N. Laosiripojana, U.W. Hartley, Study of crystal growth and kinetic parameters of Zn/ZnO oxidation in the presence of H_2O and CO_2, React. Kinet. Mech. Catal. 125 (2018) 99-110. https://doi.org/10.1007/s11144-018-1411-3.

[21] J. Weitkamp, Zeolites and catalysis, Solid State Ionics. 131 (2000) 175-188. https://doi.org/10.1016/S0167-2738(00)00632-9.

[22] G. Bellussi, V. Fattore, P.A. Jacobs, N. Jaeger, L. Kubelkova, B. Wichterlova, Zeolite chemistry and catalysis, Appl. Catal. 73 (1991) N7. https://doi.org/10.1016/0166-9834(91)85130-n.

[23] W.P. Gates, J.T. Kloprogge, J. Madejová, F. Bergaya, Infrared and raman spectroscopies of clay minerals, Dev. Clay Sci. (2017).

[24] P.G. Menon, B. Delmon, G. Ertl, H. Knozinger, J. Weitkamp, Handbook of heterogeneous catalysis (Vol. 1), Weinheim: Wiley-VCH, 1997.

[25] T. Khamhangdatepon, V. Tongnan, M. Hartley, T. Sornchamni, N. Siri-Nguan, N. Laosiripojana, K. Li, U.W. Hartley, Mechanisms of synthesis gas production via thermochemical cycles over $La_{0.3}Sr_{0.7}Co_{0.7}Fe_{0.3}O_3$, Int. J. Hydrogen Energy. (2020). https://doi.org/10.1016/j.ijhydene.2019.12.148.

[26] A. Ngoensawat, V. Tongnan, N. Laosiripojana, P. Kim-Lohsoontorn, U.W. Hartley, Effect of La and Gd substitution in $BaFe_{O3-\delta}$ perovskite structure on its catalytic performance for thermochemical water splitting, Catal. Commun. 135 (2020) 105901. https://doi.org/10.1016/j.catcom.2019.105901.

[27] C. Khajonvittayakul, V. Tongnan, T. Kangsadan, N. Laosiripojana, S. Jindasuwan, U.W. Hartley, Thermodynamic and mechanism study of syngas production via integration of nitrous oxide decomposition and methane partial oxidation in the presence of 10%NiO-$La_{0.3}Sr_{0.7}Co_{0.7}Fe_{0.3}O_{3-\delta}$, React. Kinet. Mech. Catal. 127 (2019) 839-855. https://doi.org/10.1007/s11144-019-01600-1.

[28] T. Li, T. Kamhangdatepon, B. Wang, U.W. Hartley, K. Li, New bio-inspired design for high-performance and highly robust $La_{0.6}Sr_{0.4}Co_{0.2}Fe_{0.8}O_{3-\delta}$ membranes for oxygen permeation, J. Memb. Sci. 578 (2019) 203-208. https://doi.org/10.1016/j.memsci.2019.02.042.

[29] U.W. Hartley, V. Tongnan, N. Laosiripojana, P. Kim-Lohsoontorn, K. Li, Nitrous oxide decomposition over $La_{0.3}Sr_{0.7}Co_{0.7}Fe_{0.3}O_{3-\delta}$ catalyst, React. Kinet. Mech. Catal. 125 (2018) 85-97. https://doi.org/10.1007/s11144-018-1398-9.

[30] R.K. Grasselli, Selective oxidation and ammoxidation of olefins by heterogeneous catalysis, J. Chem. Educ. 63 (1986) 216-221. https://doi.org/10.1021/ed063p216.

[31] R. Kumar, A. Sudhaik, P. Raizada, A. Hosseini-Bandegharaei, V.K. Thakur, A. Saini, V. Saini, P. Singh, An overview on bismuth molybdate based photocatalytic systems: Controlled morphology and enhancement strategies for photocatalytic water purification, J. Environ. Chem. Eng. 8 (2020). https://doi.org/10.1016/j.jece.2020.104291.

[32] Y. Sasaki, T. Nakamura, Y. Nakamura, K. Moriya, H. Utsumi, S. Saito, Process for production of acrylonitrile, US 4370279, 1983.

[33] J.F. Brazdil, Scheelite: A versatile structural template for selective alkene oxidation catalysts, Catal. Sci. Technol. 5 (2015) 3452-3458.https://doi.org/10.1039/c5cy00387c.

[34] A.W. Sleight, J.J. Burton, R.L. Garten, Advanced materials in catalysis, New York: Academic Press, 1977.

[35] J. Hwang, R.R. Rao, L. Giordano, Y. Katayama, Y. Yu, Y. Shao-Horn, Perovskites in catalysis and electrocatalysis, Science. 358 (2017) 751-756. https://doi.org/10.1126/science.aam7092.

[36] F. Basile, M. Campanati, E. Serwicka, A. Vaccari, Hydrotalcites '99. Selected papers from Euroclay 1999, Appl. Clay Sci. 18 (2001) 1.

[37] U. Costantino, M. Nocchetti, G. Gorrasi, L. Tammaro, Hydrotalcites in nanobiocomposites, in: Multifunct. Nanoreinforced Polym. Food Packag., 2011. https://doi.org/10.1533/9780857092786.

[38] J.B. Moffat, Metal-oxygen clusters: The surface and catalytic properties of heteropoly oxometalates, New York: Kluwer Academic/Plenum Publishers, 2001.

[39] M.S. Wainright, G. Ertl, Knozinger, J. H., Weitkamp, Handbook of heterogeneous catalysis (Vol. 1), Weinheim: Wiley-VCH, 1997.

[40] A. Baiker, G. Ertl, Knozinger, J. H., Weitkamp, Handbook of heterogeneous catalysis (Vol. 2), Weinheim: Wiley-VCH, 1997.

[41] K.J. Smith, Alternative Catalytic materials: carbides, nitrides, phosphides and amorphous boron alloys, Focus Catal. 2018 (2018) 7. https://doi.org/10.1016/j.focat.2018.05.055.

[42] S. Zaman, K.J. Smith, A review of molybdenum catalysts for synthesis gas conversion to alcohols: catalysts, mechanisms and kinetics, Catal. Rev. - Sci. Eng. 54 (2012) 41-132. https://doi.org/10.1080/01614940.2012.627224.

[43] C. Bouchy, C. Pham-Huu, B. Heinrich, C. Chaumont, M.J. Ledoux, Microstructure and characterization of a highly selective catalyst for the isomerization of alkanes: A molybdenum oxycarbide, J. Catal. 190 (2000) 92-103. https://doi.org/10.1006/jcat.1999.2741.

[44] R. Schlögl, Carbon in catalysis, in: Adv. Catal., 2013: pp. 103-185. https://doi.org/10.1016/B978-0-12-420173-6.00002-4.

[45] R. Schlögl, G. Ertl, Knozinger, J. H., Weitkamp, Handbook of heterogeneous catalysis (Vol. 1), Weinheim: Wiley-VCH, 1997.

[46] T. Yoshida, Stimuli-sensitive polymers for drug delivery and diagnostic systems interacting with biosurfaces, in: Switch. Responsive Surfaces Mater. Biomed. Appl., 2015: pp. 235-258. https://doi.org/10.1016/B978-0-85709-713-2.00010-9.

[47] F. De Dardel, T.V. Arden, Ullmann's Encyclopedia of Industrial Chemistry, 5th ed., V, Weinheim: VCH, 1987.

[48] C.G. Wulff, G., Gebelein, Biomimetic polymers, New York: Plenum Press, 1990.

[49] U. Mueller, M. Schubert, F. Teich, H. Puetter, K. Schierle-Arndt, J. Pastré, Metal-organic frameworks - prospective industrial applications, in: J. Mater. Chem., 2006: pp. 626-636. https://doi.org/10.1039/b511962f.

[50] S. Zhou, K. You, Z. Yi, P. Liu, H. Luo, Metal salts with highly electronegative cations as efficient catalysts for the liquid-phase nitration of benzene by NO_2 to nitrobenzene, Front. Chem. Sci. Eng. 11 (2017) 1-6. https://doi.org/10.1007/s11705-017-1625-3.

[51] X. Yu, X. Gao, R. Tao, L. Peng, Insights into the metal salt catalyzed 5-ethoxymethylfurfural synthesis from carbohydrates, Catalysts. 7 (2017). https://doi.org/10.3390/catal7060182.

[52] Q. Zhang, H.Y. Yuan, N. Fukaya, J.C. Choi, Alkali metal salt as catalyst for direct synthesis of carbamate from carbon dioxide, ACS Sustain. Chem. Eng. 6 (2018) 6675-6681. https://doi.org/10.1021/acssuschemeng.8b00449.

[53] M.J. Ledoux, C. Pham-Huu, Silicon carbide a novel catalyst support for heterogeneous catalysis, CATTECH. 5 (2001) 226-246. https://doi.org/10.1023/A:1014092930183.

[54] H. Sieber, C. Hoffmann, A. Kaindl, P. Greil, Biomorphic cellular ceramics, Adv. Eng. Mater. 2 (2000) 105-109. https://doi.org/10.1002/(SICI)1527-2648(200003)2:3<105::AID-ADEM105>3.0.CO;2-P.

[55] J.L. Williams, Monolith structures, materials, properties and uses, Catal. Today. 69 (2001) 3-9. https://doi.org/10.1016/S0920-5861(01)00348-0.

[56] M. Valentini, G. Groppi, C. Cristiani, M. Levi, E. Tronconi, P. Forzatti, The deposition of γ-Al_2O_3 layers on ceramic and metallic supports for the preparation of structured catalysts, Catal. Today. 69 (2001) 307-314. https://doi.org/10.1016/S0920-5861(01)00383-2.

[57] M.B. Gawande, R.K. Pandey, R. V. Jayaram, Role of mixed metal oxides in catalysis science - versatile applications in organic synthesis, Catal. Sci. Technol. 2 (2012) 1113-1125. https://doi.org/10.1039/c2cy00490a.

[58] A.S. Kulkarni, R.V. Jayaram, Liquid phase catalytic transfer hydrogenation of aromatic nitro compounds on $La_{1-x}Sr_xFeO_3$ perovskites prepared by microwave irradiation, in: J. Mol. Catal. A Chem., 2004: pp. 107-110. https://doi.org/10.1016/j.molcata.2003.12.042.

[59] J. Sarabut, S. Charojrochkul, T. Sornchamni, N. Laosiripojana, S. Assabumrungrat, U. Wetwattana-Hartely, P. Kim-Lohsoontorn, Effect of strontium and zirconium doped barium cerate on the performance of proton ceramic electrolyser cell for syngas production from carbon dioxide and steam, Int. J. Hydrogen Energy. (2019) 20634-20640. https://doi.org/10.1016/j.ijhydene.2018.07.121.

[60] J.J. Yu, X.P. Wang, L.D. Li, Z.P. Hao, Z.P. Xu, G.Q. Lu, Novel multi-functional mixed-oxide catalysts for effective NO_x capture, decomposition, and reduction, Adv. Funct. Mater. 17 (2007) 3598-3606. https://doi.org/10.1002/adfm.200700334.

[61] C. Lucarelli, P. Moggi, F. Cavani, M. Devillers, Sol-gel synthesis and characterization of transition metal based mixed oxides and their application as catalysts in selective oxidation of propane, Appl. Catal. A Gen. 325 (2007) 244-250. https://doi.org/10.1016/j.apcata.2007.02.034.

[62] L.J.I. Coleman, W. Epling, R.R. Hudgins, E. Croiset, Ni/Mg-Al mixed oxide catalyst for the steam reforming of ethanol, Appl. Catal. A Gen. 363 (2009) 52-63. https://doi.org/10.1016/j.apcata.2009.04.032.

[63] S. Blanco, S.R.G. Carrazán, V. Rives, Oxidative dehydrogenation of propane on Mg-V-Al mixed oxides, Appl. Catal. A Gen. 342 (2008) 93-98. https://doi.org/10.1016/j.apcata.2008.03.002.

[64] C. Liu, Z. Zhao, X. Yang, X. Ye, Y. Wu, Superconductor mixed oxides $La_{2-X}Sr_xCuO_{4\pm\lambda}$ for catalytic hydroxylation of phenol in the liquid-solid phase, Chem. Commun. (1996) 1019-1020. https://doi.org/10.1039/CC9960001019.

[65] C.H. Wang, H.S. Weng, Al_2O_3-Supported mixed-metal oxides for destructive oxidation of $(CH_3)_2S_2$, Ind. Eng. Chem. Res. 36 (1997) 2537-2542. https://doi.org/10.1021/ie960787v.

[66] S. Thongkumkoon, W. Kiatkittipong, U.W. Hartley, N. Laosiripojana, P. Daorattanachai, Catalytic activity of trimetallic sulfided Re-Ni-Mo/γ-Al_2O_3 toward deoxygenation of palm feedstocks, Renew. Energy. 140 (2019) 111-123. https://doi.org/10.1016/j.renene.2019.03.039.

[67] T. Li, M.F. Rabuni, L. Kleiminger, B. Wang, G.H. Kelsall, U.W. Hartley, K. Li, A highly-robust solid oxide fuel cell (SOFC): simultaneous greenhouse gas treatment and clean energy generation, Energy Environ. Sci. 9 (2016) 3682-3686. https://doi.org/10.1039/c6ee02562e.

[68] U.W. Hartley, S. Amornraksa, P. Kim-Lohsoontorn, N. Laosiripojana, Thermodynamic analysis and experimental study of hydrogen production from oxidative reforming of n-butanol, Chem. Eng. J. 278 (2015) 2-12.https://doi.org/10.1016/j.cej.2015.02.016.

[69] K. Krekkeitsakul, T. Utistham, U.W. Hartley, Methanol synthesis in a slurry phase reactor over $Cu/ZnO/Al_2O_3$ catalyst, in: Adv. Mater. Res., 2014: pp. 27-31. https://doi.org/10.4028/www.scientific.net/AMR.931-932.27.

[70] S. Puangubol, T. Utistham, U. Wetwatana, Production of bio-oil by hydrothermal pyrolysis of food waste over ceria catalyst, Curr. Opin. Biotechnol. 22 (2011) S49. https://doi.org/10.1016/j.copbio.2011.05.128.

[71] U. Wetwatana, P. Kim-Lohsoontorn, S. Assabumrungrat, N. Laosiripojana, Catalytic steam and autothermal reforming of used lubricating oil (ULO) over Rh- and Ni-based catalysts, Ind. Eng. Chem. Res. 49 (2010) 10981-10985. https://doi.org/10.1021/ie1004288.

[72] Y. Ono, T. Baba, Catalysis (Vol. 15), Cambridge: The Royal Society of Chemistry, n.d.

[73] K. Tanabe, H. Hattori, G. Ertl, H. Knozinger, J. Weitkamp, Handbook of heterogeneous catalysis (Vol. 1), Weinheim: Wiley-VCH, 1997.

[74] K. Foger, J.R. Anderson, M. Boudart, Catalysis: science and technology (Vol. 6), Berlin: Springer, 1984.

[75] B.C. Gates, Supported metal clusters: synthesis, structure, and catalysis, Chem. Rev. 95 (1995) 511-522. https://doi.org/10.1021/cr00035a003.

[76] E.S.J. Lox, B.H. Engler, G. Ertl, H. Knozinger, J. Weitkamp, Handbook of heterogeneous catalysis (Vol. 4), Weinheim: Wiley-VCH, 1997.

[77] R. Prins, Catalytic hydrodenitrogenation, Adv. Catal. 46 (2001) 399-464. https://doi.org/10.1016/s0360-0564(02)46025-7.

[78] D.E. De Vos, I.F.J. Vankelecom, P.A. Jacobs, Chiral catalyst immobilization and recycling, 2000. https://doi.org/10.1002/9783527613144.

[79] D.E. De Vos, S. De Wildeman, B.F. Sels, P.J. Grobet, P.A. Jacobs, Selective alkene oxidation with H_2O_2 and a heterogenized Mn catalyst: epoxidation and a new entry to vicinal cis-diols, Angew. Chemie - Int. Ed. 38 (1999) 980-983. https://doi.org/10.1002/(SICI)1521-3773(19990401)38:7<980::AID-ANIE980>3.0.CO;2-W.

[80] O. Zaushitsyna, D. Berillo, H. Kirsebom, B. Mattiasson, Cryostructured and crosslinked viable cells forming monoliths suitable for bioreactor applications, Top. Catal. 57 (2014) 339-348. https://doi.org/10.1007/s11244-013-0189-9.

[81] K. Engelmark Cassimjee, M. Kadow, Y. Wikmark, M. Svedendahl Humble, M.L. Rothstein, D.M. Rothstein, J.E. Bäckvall, A general protein purification and immobilization method on controlled porosity glass: biocatalytic applications, Chem. Commun. 50 (2014) 9134-9137. https://doi.org/10.1039/c4cc02605e.

[82] P. Zucca, E. Sanjust, Inorganic materials as supports for covalent enzyme immobilization: methods and mechanisms, molecules. 19 (2014) 14139-14194. https://doi.org/10.3390/molecules190914139.

[83] H. Brunner, Dendrizymes: Expanded ligands for enantioselective catalysis, J. Organomet. Chem. 500 (1995) 39-46.https://doi.org/10.1016/0022-328X(95)00507-M.

[84] A. Kirschning, H. Monenschein, R. Wittenberg, Functionalized polymers - Emerging versatile tools for solution-phase chemistry and automated parallel synthesis, Angew. Chemie - Int. Ed. 40 (2001) 650-679. https://doi.org/10.1002/1521-3773(20010216)40:4<650::AID-ANIE6500>3.0.CO;2-C.

[85] B. Cornils, W.A. Herrmann, Applied homogeneous catalysis with organometallic compounds, Weinheim: Wiley-VCH, 1996.

[86] J.P. Arhancet, M.E. Davis, J.S. Merola, B.E. Hanson, Hydroformylation by supported aqueous-phase catalysis: a new class of heterogeneous catalysts, Nature. 339 (1989) 454-455. https://doi.org/10.1038/339454a0.

[87] U. Kernchen, B. Etzold, W. Korth, A. Jess, Solid catalyst ionic liquid layer (SCILL) - a new concept to improve selectivity illustrated by hydrogenation of cyclooctadiene, Chem. Eng. Technol. 30 (2007) 985-994. https://doi.org/10.1002/ceat.200700050.

[88] T. Wang, L. Gao, J. Hou, S.J.A. Herou, J.T. Griffiths, W. Li, J. Dong, S. Gao, M.M. Titirici, R.V. Kumar, A.K. Cheetham, X. Bao, Q. Fu, S.K. Smoukov, Rational approach to guest confinement inside MOF cavities for low-temperature catalysis, Nat. Commun. 10 (2019). https://doi.org/10.1038/s41467-019-08972-x.

[89] G. Schulz-Ekloff, S. Ernst, G. Ertl, H. Knozinger, J. Weitkamp, Handbook of heterogeneous catalysis (Vol. 1), Weinheim: Wiley-VCH, 1997.

[90] D.E. De Vos, P.P. Knops-Gerrits, R.F. Parton, B.M. Weckhuysen, P.A. Jacobs, R.A. Schoonheydt, Coordination chemistry in zeolites, J. Incl. Phenom. Mol. Recognit. Chem. 21 (1995) 185-213. https://doi.org/10.1007/BF00709416.

[91] W. Kaminsky, Olefin polymerization catalyzed by metallocenes, Adv. Catal. 46 (2001) 89-159. https://doi.org/10.1016/s0360-0564(02)46022-1.

[92] K. Pangarkar, T.J. Schildhauer, J.R. Van Ommen, J. Nijenhuis, F. Kapteijn, J.A. Moulijn, Structured packings for multiphase catalytic reactors, Ind. Eng. Chem. Res. 47 (2008) 3720-3751. https://doi.org/10.1021/ie800067r.

[93] E. Klemm, H. Döring, A. Geisselmann, S. Schirrmeister, Microstructured reactors in heterogenous catalysis, Chem. Eng. Technol. 30 (2007) 1615-1621. https://doi.org/10.1002/ceat.200700311.

[94] G. Busca, Preparation of solid catalysts, in: Heterog. Catal. Mater., 2014: pp. 9-22. https://doi.org/10.1016/b978-0-444-59524-9.00002-x.

[95] P. Euzen, P. Raybaud, X. Krokidis, H. Toulhoat, J.L. Le Loarer, J.P. Jolivet, F. Schueth, K.S.W. Sing, J. Weitkamp, Handbook of porous solids, Weinheim: Wiley-VCH, 2002.

[96] D.D. Athayde, D.F. Souza, A.M.A. Silva, D. Vasconcelos, E.H.M. Nunes, J.C.D. Da Costa, W.L. Vasconcelos, Review of perovskite ceramic synthesis and membrane preparation methods, Ceram. Int. 42 (2016) 6555-6571. https://doi.org/10.1016/j.ceramint.2016.01.130.

[97] J.C. Védrine, Metal oxides in heterogeneous catalysis, Elsevier, 2018. https://doi.org/10.1016/C2016-0-01790-4.

[98] D.P. Debecker, P.H. Mutin, Non-hydrolytic sol-gel routes to heterogeneous catalysts, Chem. Soc. Rev. 41 (2012) 3624-3650. https://doi.org/10.1039/c2cs15330k.

[99] W. Wan, R. Zhang, M. Ma, Y. Zhou, Monolithic aerogel photocatalysts: a review, J. Mater. Chem. A. 6 (2018) 754-775. https://doi.org/10.1039/c7ta09227j.

[100] T. Fröschl, U. Hörmann, P. Kubiak, G. Kucerová, M. Pfanzelt, C.K. Weiss, R.J. Behm, N. Hüsing, U. Kaiser, K. Landfester, M. Wohlfahrt-Mehrens, High surface area crystalline titanium dioxide: potential and limits in electrochemical energy storage and catalysis, Chem. Soc. Rev. 41 (2012) 5313-5360. https://doi.org/10.1039/c2cs35013k.
[101] M. Signoretto, E. Ghedini, F. Menegazzo, G. Cerrato, V. Crocellà, C.L. Bianchi, Aerogel and xerogel WO_3/ZrO_2 samples for fine chemicals production, Microporous Mesoporous Mater. 165 (2013) 134-141. https://doi.org/10.1016/j.micromeso.2012.08.003.
[102] C. Gannoun, R. Delaigle, P. Eloy, D.P. Debecker, A. Ghorbel, E.M. Gaigneaux, Sol-gel derived V_2O_5-TiO_2 mesoporous materials as catalysts for the total oxidation of chlorobenzene, Catal. Commun. 15 (2011) 1-5. https://doi.org/10.1016/j.catcom.2011.08.001.
[103] A.K. Ganguli, A. Ganguly, S. Vaidya, Microemulsion-based synthesis of nanocrystalline materials, Chem. Soc. Rev. 39 (2010) 474-485. https://doi.org/10.1039/b814613f.
[104] V. Valtchev, L. Tosheva, Porous nanosized particles: preparation, properties, and applications, Chem. Rev. 113 (2013) 6734-6760. https://doi.org/10.1021/cr300439k.
[105] A.M. Dumitrescu, P.M. Samoila, V. Nica, F. Doroftei, A.R. Iordan, M.N. Palamaru, Study of the chelating/fuel agents influence on $NiFe_2O_4$ samples with potential catalytic properties, Powder Technol. 243 (2013) 9-17. https://doi.org/10.1016/j.powtec.2013.03.033.
[106] J.R.H. Ross, Contemporary Catalysis: fundamentals and current applications, focus catal. 2019 (2019) 7. https://doi.org/10.1016/j.focat.2019.01.054.
[107] B. Stiles, T.A. Koch, Catalyst manufacture, 2nd ed., New York: M. Dekker, 1995.
[108] J.F.L. Page, G. Ertl, H. Knozinger, J. Weitkamp, Handbook of heterogeneous catalysis (Vol. 1), Weinheim: Wiley-VCH, 1997.

ABBRIVIATIONS AND ACRONYM

HTE	*high-throughput experimentation*
IRT	*infrared thermography*
GC	*gas chromatography*
M	*metal*
O	*oxygen*
TPD	*temperature-programmed desorption*

SOFCs	*solid oxide fuel cells*
WGS	*water gas shift reaction*
T atoms	*tetrahedral centers*
TS1	*titanium-silicate-1*
AIPO	*aluminum phosphates*
MAPOs	*metal alumino phosphates*
SAPO	*silico alumino phosphates*
BMO	*bismuth molybdates*
HTlc	*hydrotalcite-like compounds*
LDH	*layered double hydroxides*
SCA	*synthetic carbon allotropes*
CNT	*carbon nanotubes*
CNF	*carbon nanofibers*
PEMFCs	*proton exchange membrane fuel cells*
DMFCs	*direct methanol fuel cells*
MOFs	*metal-organic frameworks*
HMF	*5-hydroxymethylfurfural*
SA	*surface area in* m^2/g
cat/cats	*catalyst/catalysts*
SiC	*silicon carbide*
YSZ	*yttria-stabilized zirconia*
ULO	*used lubricating oil*
SLPC	*supported (solid) liquid-phase catalysis*
SAPC	*supported (solid) aqueous-phase catalysis*
SCILL	*solid catalysts with ionic liquid layer*

PEGS	*pourbaix-enabled guest synthesis*
MAO	*methyl-laluminoxane*
SC	*super critical*
SCFs	*supercritical fluids*
SDAs	*structure directing agents*
PZC	*point of zero charge*
CVD	*chemical vapor deposition*
PVD	*physical vapor deposition*

CHAPTER 4
CATALYST CHARACTERIZATION

4.1 DEFINITION OF CATALYST CHARACTERIZATION

The prepared catalysts have their own characteristics that need measured or proven. These characteristics include both physical and chemical properties of the catalysts in detail because they are more or less responsible for their catalytic performances. Some of the major characteristics of the catalysts are listed below [1]:

1. The nature of its smallest units i.e. chemical composition of catalyst's bulk and surface.
2. The arrangement or alignment or architecture of these smallest units, observed in terms of bulk or solid structure, crystallite size, crystallite size distribution, crystallite morphology, porousity (micro-, meso-, and macro-), and surface area.
3. Chemical properties of the catalyst's surface such as valence state, acidity, reactivity with difference molecules, surface energy, and surface electronic states.
4. The cluster properties or the aggregate properties of the catalyst i.e. particle size, magnetic properties, density of bulk (or of particle or of skeletal), mechanical strength, and attrition resistance.
5. Catalytic properties or catalytic performances i.e. activity, selectivity, and stability. This is sometimes not considered truly characterization, but called 'the catalytic performance test' in which it requires a design of reactors for testing.

4.2 LIST OF TECHNIQUES FOR CATALYST CHARACTERIZATION

The following list collects most common techniques that are applied for the catalyst's characterizations.

1. **X-ray diffraction (XRD):** This technique is often applied to characterize the bulk crystal structure and chemical phase composition using diffraction of an X-ray beam as a function of the angle of the incident beam. The broadening of the diffraction peaks can be interpreted as diameter of the crystallites. The crystal domains that are larger than 3 to 5 nm should be detectable by XRD.
2. **X-ray fluorescent spectroscopy (XRF):** XRF is normally used as a quantitative analysis to determine composition of containing elements in the catalyst using incident X-ray radiation to eject electrons from inner levels of the atoms.

3. **Brunauer, Emmett and Teller method (BET):** BET is a widely accepted method used for analysis of specific surface area and distribution of mesopore sizes of the catalyst. The method relies on multi-layer physisorption isotherms of inert gases.
4. **Scanning electron microscopy (SEM):** Using backscattered or secondary electrons to observe images of the topology of the catalyst's surface.
5. **Transmission electron microscopy (TEM):** This method will determine micro-texture and microstructure of electron transparent samples by transmission of a focused parallel electron beam to a fluorescent screen, with a resolution presently better than 0.2 nm.
6. **X-ray photoelectron spectroscopy (XPS):** UV photons (generally higher than 1 keV) assisted with detection of photoelectrons emitted from atomic core levels as a function of their energy is utilized to create the excitation of surfaces. The shifts in core-level energies give information on surface chemical states e.g. oxidation states.
7. **Fourier transform infrared spectroscopy (FTIR):** This technique uses high speed infrared spectroscopy where the laser beam is split by a moving interferometer (Michelson type) in order to produce an interferogram. The interferogram will be digitally transformed into an entire set of spectrum. By this method, the structures of adsorbed molecules on the catalyst's surface will be investigated, under the controlled conditions. FTIR can be also applied in kinetic studies due to its rapid scanning resonance ranging from 1 ms to 1 s.
8. **Inductive coupled plasma (ICP):** This is used for chemical analysis of either solid or liquid samples by vaporizing them in a plasma heater.
9. **Nuclear magnetic resonance (NMR):** This technique allows possibility to study chemical environment of nuclei having a magnetic moment due to splitting of the nuclear spins by an external magnetic field. NMR is applied for study adsorbed or solid compounds of carbon, hydrogen and aluminum.
10. **Thermogravimetric analysis (TG or TGA):** This is a measurement of weight loss or weight gain as a function of temperature change. This technique is performed under a controlled gaseous surrounding environment. This technique is widely applied for study of gas-solid reactions.
11. **Temperature-programmed desorption (TPD):** The determination of desorption rate of adsorbed molecules as a function of temperature (ramping linearly). By this technique, the adsorption states, binding energies, surface concentrations and desorption kinetics of the interested catalyst will be obtained.

12. **Temperature-programmed reduction (TPR):** This is also measured as a function of temperature. The rate of reduction will be investigated, offering more information in terms of oxidation states of either the surface or the bulk of the studied catalyst.
13. **Temperature-programmed surface reaction (TPSR):** As mentioned as 'temperature-programmed', this techniques is to measure rate of reaction of a gaseous species with an adsorbed species as a function of temperature (changing proportionally). The reactivity of different surface species, their reaction states (paths), relatively unsteady state reaction rates or even brief mechanism can be achieved using this technique.
14. **Transient kinetic method (TKM):** Mechanism of the reactions can be gained using this method. The flow of one of the reactants is suddenly stopped or switched to one having a different isotopic label; products are analyzed as a function of time using a fast and responsive mass spectrometer (gas analyser) which connected online to the testing system or the rig. By quantitative and qualitative analysis of the product distribution as a function of time after the interruption, this method of course can conclude either mechanism pathways or intermediates of the reactions.
15. **Scanning transmission electron microscopy (STEM):** A transmission of highly focused electron probe to a CRT is used to determine nanotexture and nanostructure of the catalyst, over a small area where the diameter is larger than 3nm.
16. **Ultraviolet-visible spectroscopy (UV-VIS):** The adsorption edge and band-gap energies of the surface species of the catalyst will be observed using conventional UV-VIS (tungsten and deuterium light sources) coupled with diffuse reflectance.
17. **Infrared spectroscopy (IR):** A technique used to analyze chemical structure of gas, liquid or solid molecules. In this method, the incident IR radiation will be absorbed by a molecule causing excitation of molecular vibration modes. The frequency of these vibrations depend on the nature and binding of the molecules.
18. **Atomic absorption spectroscopy (AAS):** Quantitative analysis used to measure atomic composition based on photon absorption of a vaporized aqueous solution preferably from the starting material.
19. **Energy dispersive X-ray spectroscopy (EDX):** Low resolution, high efficiency X-ray diffraction of thin specimens in transmission electron microscopy.

20. **Field emission microscopy (FEM):** Giving an image of the atomic arrangement at the surface of the tip of a material through projection of ions in the intense electrical field generated at the tip.
21. **Extended X-ray absorption fine structure (EXAFS):** This technique uses a high energy X-ray source transmitting through a sample, giving structural information regarding surface in an atomic-scale. The EXAFS is normally applied to study supported catalyst by in situ technique.

The other associated or less frequent used techniques/equipment include: adsorption (ADS), atomic force microscopy (AFM), Auger electron spectroscopy (AES), controlled-atmospheric electron microscopy (CAEM), computer-controlled scanning electron microscopy (CCSEM), electron energy loss spectroscopy (EELS), electron probe micro-analysis (EPMA), electron paramagnetic resonance (EPR), high-resolution electron energy loss spectroscopy (HREELS), ion microprobe (IMP), ion scattering spectroscopy (ISS), low-energy electron diffraction (LEED), low-energy ion scattering (LEIS), laser microprobe mass spectrometry (LMMS), magnetic susceptibility measurement (MS), Mossbauer absorption spectroscopy (MAbS), magic angle spinning (MAS), molecular beam scattering (MBS), Mossbauer emission spectroscopy (MES), neutron scattering (NS), proton-induced X-ray emission (PIXE), Rutherford backscattering (RBS), sum frequency generation (SFG), secondary ion mass spectrometry (SIMS), secondary neutral mass spectroscopy (SNMS), scanning tunneling microscopy (STM), time of flight secondary ion mass spectrometry (TOF-SIMS), ultraviolet photoelectron spectroscopy (UPS) and wavelength dispersive spectroscopy (WDS). These techniques are applied in industry and laboratory for catalyst development and characterization. The following sections will describe important physical, chemical, mechanical and thermal characteristics, in correspondence to their relevant techniques.

4.3 WHY WE CHARACTERIZE

The objectives of catalyst characterization include: (1) to understand relationships among physical, chemical and catalytic properties, for instance, to relate the catalyst's structure and its function; (2) to clarify apparent phenomenon or behavior of the catalyst such as deactivation – knowing the causes behind phenomenon helps engineers to design the catalytic process better; (3) to determine the catalyst's physical and chemical properties e.g. composition, pore size, specific surface area, particle size or even mechanical strength – these information are useful for techno-economic analysis, reactor design, modeling and process optimization; (4) to control the quality of the prepared catalyst in the manufacturing level – the physical and chemical properties of the catalysts can be monitored.

The principle of catalyst characterization is simple, to understand the relationship between the catalyst's characteristics and its catalytic performance. This in-depth information render a development of the most promising catalysts which are tailor-made to needs. Table 4.1 summarizes catalyst characteristics and relevant characterization techniques which are often utilized for such properties. The techniques are reported with the corresponding the American society for testing materials (ASTM), which is an organization in the United States, which has adopted standard procedures to test various materials. The standardized methods are utilized widely around the world including industries, governments, academics, scientists and engineers.

Table 4.1: Catalyst characteristics with their relevant techniques and ASTMs [1].

Characteristics	**Techniques**	**ASTM**
Physical properties		
Surface area	Adsorption of N_2 or CO_2, microscopy, CCSEM	D-3663-84, D-4567-86
Pore size, and its size distribution	Extended N_2 and CO_2 adsorptions, Hg porosimetry, NMR spin relaxation of H_2O	D-4641-87, D-4284-83
Density, skeletal (solid)	He displacement or pycnometry	n/a
Density, apparent (particle)	He displacement	n/a
Density, bulk (tap)	Tapping pack density	D-4164-88
Catalyst particle size, and its size distribution	Sieving, electronic counting, laser light scattering, SEM, TEM, optical imaging	D-4513, 4438, 4464
Single pellet crush strength	Crushing test in hydraulic press	D-4179-82
Bulk crushing strength	Crushing test in hydraulic system	n/a
Attrition and abrasion resistance	Rotating drum, air jet, and ultrasonic test	D-4058-87
Chemical properties		
Chemical state, bulk	TG, TPR, MAbS, FTIR, EPR, NS, NMR	n/a
Chemical state, surface	XPS, TPSR, EXAFS, MAbS, FTIR, NMR	n/a
Chemical state, surface additives	XPS, FTIR, Raman, NMR, EELS, HREELS, TPD, TPSR, MBS	n/a

(Continued)

Table 4.1: *(Continued)*

Characteristics	Techniques	ASTM
Chemical properties		
Composition, bulk	AAS, ICP, XRF/XRD, SEM, TEM, MAS, TG, FTIR, NMR	D-3610-83, D-4481-85, D-4642-86
Composition surface	AES, XPS, SIMS, EXAFS, ISS	n/a
Homogeneity	EPMA, IMP, LMMS, PIXE, SEM, TEM	n/a
Morphology/structure, bulk	XRD, SEM, TEM, STEM, MAbS	n/a
Morphology/structure, surface	LEED, EXAFS, TEM, STEM, STM, FEM	n/a
Dispersion or percentage exposed	TEM, XRD	D-3908-82
Surface acidity	TPD (of bases), IR, NMR	D-4824-88
Surface reactivity, active sites concentration	TPD, TPSR, TKM, calorimeter	n/a

Most physical techniques in Table 4.1 is to have a probe incident beam which hits a solid surface and to analyze the resulting probe beam, which has taken a kind of finger print of the material [2]. The concept is illustrated as shown in Figure 4.1.

Often that one particular technique cannot clarify one characteristic. Sometimes, it needs a sophisticated set of techniques to clarify one data. For the concept of catalyst characterization, the following principles could be a good guides for researchers/ developers: (1) all tools are not equal, each of them has different limitations and advantages; (2) the use of more than one tool is generally more capable to give the stronger evidence; (3) the most accurate and productive techniques are often those applied to the working surface where they are characterized in situ.

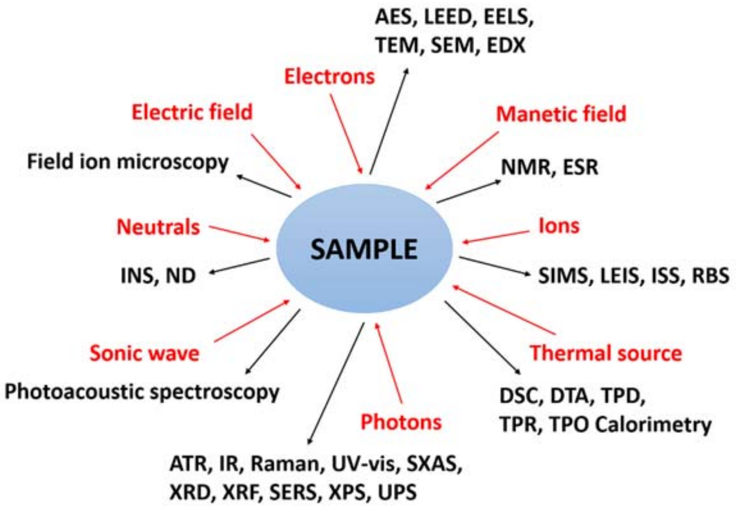

Figure 4.1: Major physical characteristics and techniques for catalyst characterization, using incident beams (oriented towards the catalyst sample) and reflected or emitted beam (oriented away from the catalyst sample) [2].

4.4 CATALYST PHYSICAL PROPERTIES

4.4.1 SURFACE AREA, PORE SIZE AND PORE VOLUME

One of the most important characteristics of the solid catalysts is the surface area, pore size and pore volume as these parameters are ones that determine the internal surface that can accommodate the active sites and facilitate the accessibility of the active sites to the reactants, and control the extent of the surface-to-bulk transportation [1]. Some of the catalysts; e.g. carbons, zeolites, kieselguhr; have natural pores, otherwise, the pores can be created by drying or calcination of the precipitates of hydrous oxides. For example, the porosity of Raney nickel catalysts are formed by selective leaching of an alloy constituent such as aluminum. Pores of ceramics can be created by burning out the combustible incorporated substances. Besides, the pores sometimes can be formed in situ during the catalytic reactions due to volatilization, re-crystallization.

The high surface area (high density of small pores) generally advantages the catalyst's catalytic performance as it can maximize the dispersion of the active sites on the catalyst's surface, however, if the reactive molecules are relative large (such as those contained in the heavy petroleum or coal-derived feedstock), the small pores would give the negative effect as they inhibit the accessibility of the large molecules. Thus, the size and the number of pore, determine the surface area, should be tailor made to the size of the reactants too.

Gas adsorption to measure the surface area and pore size

This is usually the gas adsorption and condensation of N_2 at liquid N_2 temperature using static vacuum procedures to determine the internal surface area of a mesoporous materials which have surface area more than 1 to 1,200 m^2/g. This method has been standardized by ASTM: D3663-84, 1988 [3]. By This Method, The Sample enclosed in a glass chamber will be purged by inert gas while heated up to 100 to 400 °C, then cooled to -196 °C using a liquid N_2. The increased partial pressure of the N_2 above the sample's surface is recorded, together with the amount of N_2 adsorbed at each pressure. Sufficient time of these procedure should be allowed to assure the equilibrium adsorption is reached. The process is afterwards reversed by reducing the pressure in which it should create another curve. Example is shown in Figure 4.2 (a) where monolayer coverage and pore structure are investigated. Each adsorbed molecule occupies an area of the surface equivalent to its cross-sectional area (0.162 nm^2), thus the overall coverage surface area should be determined by the number of N_2 molecules which are adsorbed at monolayer coverage. However, the coverage beyond the monolayer occurs in practical. In fact, when the N_2 partial pressures are relatively high, the liquid N_2 is condensed inside the pores. The Brunauer, Emmett and Teller (BET) equation is well-known to describe the relationship between (1) the volume adsorbed at a given partial pressure and (2) the volume adsorbed at monolayer coverage as follow:

$$\frac{x}{V(1-x)} = \frac{1}{cV_m} + \frac{(c-1)x}{cV_m} \tag{4.1}$$

Where $x = \frac{P}{P_0}$, P = partial pressure of N_2, P_0 = saturation pressure at the experiment temperature, V = volume adsorbed at P, V_m = volume adsorbed at monolayer coverage, and c = constant. Equation (4.1) can be linearized from $y = mx + b$ where $x = \frac{P}{P_0}$ and $y = \frac{x}{V(1-x)}$, obtaining a linear curve as shown in Figure 4.2 (b). Its intercept, b, is equal to $\frac{1}{cV_m}$ and the slope m is equal to $\frac{c-1}{cV_m}$. The results of a certain catalyst will be most accurate when the relative pressure $\left(\frac{P}{P_0}\right)$ is set between 0.05 and 0.3. The surface area can be determined using this linear plot shown as Figure 4.2 (b).

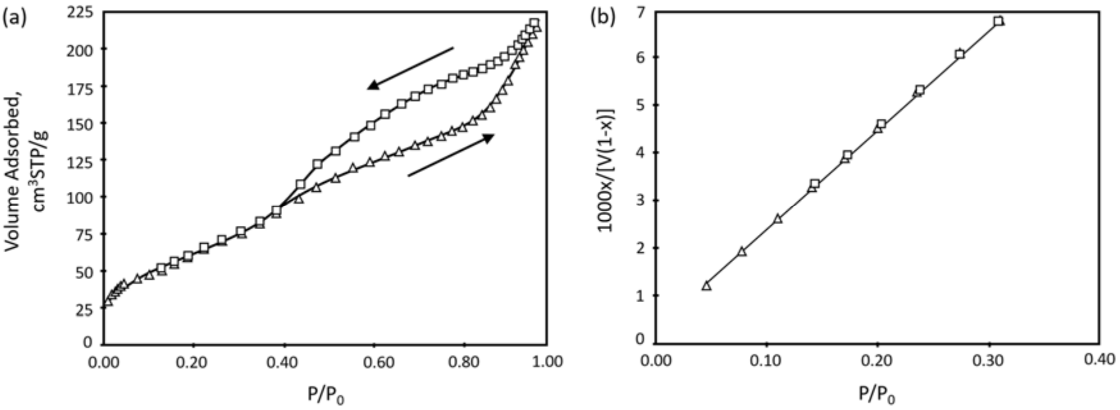

Figure 4.2: (a) N_2 adsorption and desorption isotherms at -196 °C for Bayerite Al_2O_3, and (b) linearized BET plot of the N_2 adsorption data for Bayerite Al_2O_3 from (a). The triangle symbol presents adsorption data while square symbol represents desorption [1].

***Example 4.1**: Calculation of BET surface area from N_2 adsorption data.*

Uptake versus partial pressure data obtained for N_2 adsorption at -196 °C on a Bayerite alumina are listed in Table 4.2. A plot of these data in the form of volume adsorbed versus partial pressure was shown earlier in Figure 4.2 (a). There are two isotherm branches, one for adsorption and another one for desorption, for which a hysteresis is observed.

Table 4.2: N_2 adsorption data at -196 °C for Bayerite alumina [1].

Adsorption		***Desorption***	
$x = P/P_0$	*Volume (STP)/g*	$x = P/P_0$	*Volume (STP)/g*
0.010	*31.0*	*0.992*	*200.0*
0.020	*34.4*	*0.990*	*198.7*
0.031	*36.6*	*0.987*	*196.1*
0.040	*38.2*	*0.981*	*192.1*
0.049	*39.7*	*0.975*	*188.8*
0.079	*43.6*	*0.968*	*185.7*
0.109	*47.1*	*0.957*	*182.0*
0.138	*50.2*	*0.942*	*178.3*
0.168	*53.2*	*0.924*	*175.0*

(Continued)

Table 4.2: *(Continued)*

Adsorption		*Desorption*	
$x = P/P_0$	*Volume (STP)/g*	$x = P/P_0$	*Volume (STP)/g*
0.198	*56.3*	*0.905*	*172.2*
0.243	*61.0*	*0.890*	*170.2*
0.283	*65.5*	*0.868*	*167.6*
0.327	*70.7*	*0.846*	*165.5*
0.369	*76.4*	*0.822*	*163.1*
0.414	*83.3*	*0.795*	*160.5*
0.459	*90.6*	*0.766*	*157.6*
0.501	*97.2*	*0.735*	*153.9*
0.546	*103.1*	*0.701*	*149.1*
0.587	*107.6*	*0.666*	*143.5*
0.630	*111.5*	*0.628*	*136.8*
0.667	*114.8*	*0.590*	*129.2*
0.698	*117.4*	*0.545*	*120.1*
0.732	*120.2*	*0.503*	*112.7*
0.764	*123.0*	*0.460*	*99.4*
0.793	*125.7*	*0.408*	*82.4*
0.818	*128.3*	*0.371*	*76.5*
0.844	*131.4*	*0.324*	*70.0*
0.866	*134.7*	*0.279*	*64.7*
0.887	*138.6*	*0.243*	*60.7*
0.906	*143.4*	*0.202*	*56.4*
0.923	*149.3*	*0.171*	*53.3*
0.938	*155.9*	*0.141*	*50.2*

(Continued)

Table 4.2: *(Continued)*

Adsorption		***Desorption***	
$x = P/P_0$	***Volume (STP)/g***	$x = P/P_0$	***Volume (STP)/g***
0.946	*159.7*		
0.965	*172.7*		
0.973	*178.2*		
0.978	*182.2*		
0.984	*187.3*		
0.987	*190.8*		
0.992	*196.6*		
0.995	*201.1*		

From the data set in Table 4.3, we select only those data in the P/P_0 *range of 0.05 to 0.30, the appropriate monolayer/multilayer region for determining surface area using the BET equation (Table 4.3). Both adsorption and desorption data may be used, since there is no hysteresis in the low partial pressure range.*

Table 4.3: Selected N_2 adsorption data for BET analysis [1].

$x = P/P_0$	V	$1000x/V(1-x)^2$
0.0493	*39.7047*	*1.306*
0.0789	*43.6222*	*1.964*
0.1091	*47.0630*	*2.602*
0.1382	*50.1667*	*3.197*
0.1678	*53.2163*	*3.789*
0.1978	*56.2752*	*4.382*
0.2429	*60.9763*	*5.262*
0.2832	*65.4621*	*6.035*
0.3265	*70.6871*	*6.858*

(Continued)

Table 4.3: *(Continued)*

$x = P/P_0$	V	$1000x/V(1-x)^2$
0.3325	*70.0441*	*6.827*
0.2794	*64.7470*	*5.988*
0.2426	*60.6871*	*5.278*
0.2017	*56.3898*	*4.481*
0.1709	*53.2518*	*3.871*
0.1408	*50.1597*	*3.267*

The BET method involves plotting $\frac{x}{V(1-x)}$ *versus* x *(where* $x = \frac{P}{P_0}$ *and* V *is the volume adsorbed) to obtain a straight line having a slope of* $\frac{c-1}{cV_m}$ *and an intercept* $\frac{1}{cV_m}$ *(where* V_m *is the volume adsorbed at the monolayer coverage and c is a constant). The selected data are plotted in Figure 4.2 (a). A linear least squares fit yields a slope of 0.0199 and an intercept of 4.25 x* 10^{-4}*. The slope/intercept ratio* $c-1$ *is 46.86. The monolayer volume* V_m *is calculated from the relationship:*

$$V_m = \frac{1}{(c \times intercept)} \tag{4.2}$$

to be 49.22 cm^3 *(STP)/g. The BET surface area is obtained using the widely accepted assumption that each* N_2 *molecule occupies an area of 0.162* nm^2 *and the following equation:*

$$SA\left(\frac{m^2}{g}\right) = \frac{V_m \times 6.02 \times 10^{23}\frac{molecule}{mole} \times 16.2 \times 10^{-20}\frac{m^2}{molecule}}{22{,}400\frac{cm^3}{mole}} \tag{4.3}$$

Applying equation (4.3), a value of V_m *= 49.22* cm^3 *(STP)/g corresponds to a SA of 214.3* m^2/g*.*

The example above is relied on multi-point BET method combined with classical adsorption methods in which its procedures take a long time. Thus, a single point method (which is more rapid, but not as accurate) was developed afterwards and standardized by ASTM: D-4567-86, 1988 [4]. Interpretation method of the multi-point and single point BET surface area was later improved by a developments in adsorption technology [5] in order to shorten the analytical time down to only 15 to 30 minutes after outgassing which takes around 30-60 minutes approximately. This commercial technology relies on the flow rate of the adsorbate gas into the tube (containing sample) at relatively high pressure (10-500 Torr). The high rate of adsorption is therefore maintained throughout the isotherm measurement. An accurate mass flow meter/ controller is used to monitor/adjust inlet gaseous flow rate, in order to raise the base pressure gently.

The gas adsorption isotherms can give physical informations of porous materials such as total surface area (sum of the internal and the external surface areas), porous structure, specific pore volume, pore width and pore-size distribution for micropores and mesopores. Pore size is classified as micropores (pore width < 2 nm), mesopores (pore width = 2 to 50 nm) and macropores (pore width > 50 nm), according to IUPAC [6].

For the micropores, interactions of adsorbate molecules with adsorbent pore walls are generally strong molecular forces of the nearest and the closest neighbors of the nearest i.e. of adsorbed monolayers. The gas will be condensed in micropores at relatively low pressure, leading to a fill below the region of BET monolayer (volume adsorbed at P/P_0 less than 0.05 in Figure 4.2 (a). In this case, that volume of the condensed gas is measured as the volume of the micropores. This can also be calculated as an equivalent surface area and sometimes considered as micropore surface area. In the micropore range where the pore dimensions are comparable to molecular dimensions, pore filling rather occurs instead of the condensation. The pore dimensions from physical data is then estimated using the Dubinin-Ra-dushkevich and the Dubilin-Stoeckli theories. Although low temperature N_2 adsorption can be practically used to measure micropore volume, however, it may still takes hours or days to fill the micropores especially for the high surface area materials such as carbons, activated carbons, coals and coal chars [7]. CO_2 adsorption at 0 to 25 °C is considered reliable and convenient to measure micropore volume and equivalent surface area. Since the adsorption of CO_2 under these conditions occur at low partial pressure (P/P_0 < 0.2) and low coverage, an appropriate equation to describe the isotherms is the Dubinin-Polanyi equation is as follow [8]:

$$\ln(q_i) = \ln(q_{io}) - D[ln\frac{P}{P_0}]^2 \tag{4.4}$$

Where q_i is the amount adsorbed at a given pressure, q_{io} is the micropore capacity, and $D = \left(\frac{T}{\beta E_0}\right)^2$ in which β is a similarity coefficient related to the adsorbate to a standard adsorbate (benzene) and E_0 is the energy of adsorption of the standard adsorbate. Apparent surface areas of carbons can be calculated using an equivalent area for the CO_2 molecule of 0.201 nm^2.

For the mesopores, the difference is capillary condensation which occurs above $\frac{P}{P_0}$ = 0.05. The mesopore surface area, determined by Kelvin equation [8]:

$$\ln\frac{P}{P_0} = \frac{V}{RT}\left(\frac{2\sigma\cos\Theta}{r_\kappa}\right) \tag{4.5}$$

Where P/P_0 = pressure/saturated pressure, V is the molar volume, σ is the surface tension of the liquid adsorbate, Θ = the contact angle between adsorbate and adsorption later on pore walls (thus, Θ is generally assumed 0) and r_κ = Kelvin radius of a pore assuming cylindrical shape. The geometric radius r_p of a pore given by the sum of the Kelvin radius r_κ and the thickness of the adsorption layer (t) where $r_p = r_\kappa + t$, since an adsorption layer is typically formed before the capillary occurs [9]. The mesopore surface area is generally called the matrix, relating to a measurement of surface area of cracking catalysts (ASTM-D-4365-85, 1988) [9], which is widely utilized in the fluid catalytic cracking (FCC) process. This technique is adapted by extending the pressure range used in ASTM-D-3663, 1988 [3].

Pore size by mercury intrusion

The pore volume, surface area and the pore size distribution of the macropores cannot be measured by the adsorption of N_2 because the Kelvin equation's parameter $\ln\left(\frac{P}{P_0}\right)$ becomes relatively too small at large r_p, thus the changes in pore diameter with $\frac{P}{P_0}$ cannot be experimentally determined.

To estimate the macropore volume and macropore size distribution, the mercury intrusion method, based on ASTM-D-4284-83, 1988 [10], is applied. The penetration of mercury into the macropore is a function of applied pressure. The voids between particles in the material will be filled by the penetration of mercury at low pressure, ranging from 0 to 2 atm. The large macropores will be penetrated by the mercury at moderate pressure, around 3 to 500 atm, whereas the small macropores and large mesopores will be filled at high pressure from 500 to 2000 atm. The penetration of mercury is also related to the material's resistant, due to the non-wetting nature of the mercury. The Washburn equation is described as shown in equation (4.6), representing the relation between pore radius (r_p) and the applied pressure (P).

$$r_p = \frac{-2\gamma\cos\theta}{P} \tag{4.6}$$

Where angle θ is the wetting or contact angle between mercury and the solid, averagely values from 130 to 140°; γ is the surface tension of the mercury, around 0.48 N/m; P is pressure at atmosphere; and r_p is pore radius in nm. This technique is suitable for pores sizing from 3 to 5 nm in diameter, however, this also depends on the instrument's capability which is generally capable with maximum diameter of 10^5 nm. Typical mercury porosimetry data for a γ-Al_2O_3 carrier are illustrated in Figure 4.3 where the integral penetration of mercury into the pores is plotted against the applied pressure.

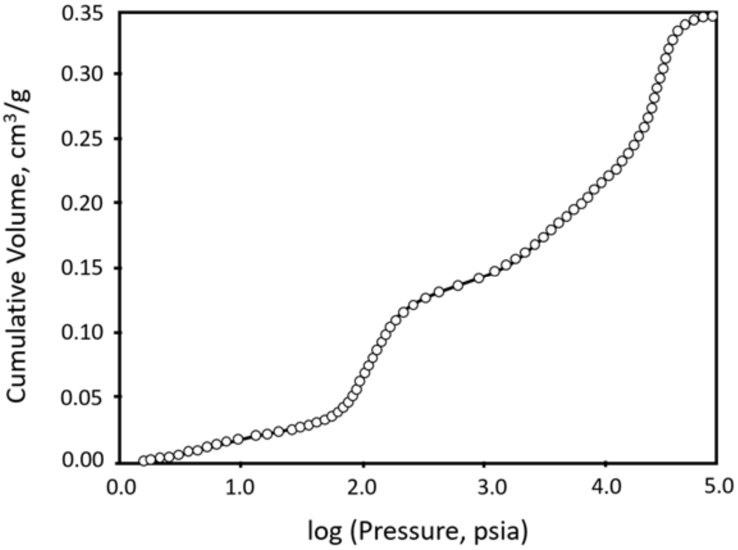

Figure 4.3: Integral penetration volume of mercury into γ-Al_2O_3 versus log applied pressure [1].

4.4.2 PARTICLE SIZE, SIZE DISTRIBUTION AND DISPERSION

Powders

This kind of catalysts is normally used in liquid-phase slurry reactors; e.g. in Fischer-Tropsch synthesis, liquid phase hydrogenations or fluidized bed reactors. The particle size of powders are largely varied, depending on their origin. Small particle size is commonly preferred as it provides more specific surface area, thus higher reactivity. The particles size range can be determined/classified using sieves of various mesh sizes (ASTM D-4513, 1988) [11] by noting the weight percentage of material that passes through one mesh size but is retained on the next finer screen. The sieves will be stacked up in layers with the coarsest on top while the underlying screens become progressively finer. A precise weight of catalyst with no more than 50% humidity will be added on top of the most upper sieve. The whole stack of a series of sieves will be then vibrated allowing the finer particles to pass through coarser screen until retained by those screens finer in opening than the particle size of the material of interest. Each fraction will be precisely weighted and a size distribution is then determined. This method is only applicable for the particles larger than 40 µm.

An electronic counter is a more sophisticated analyzer for particle size and size distribution of the finer particles. The method is standardized by ASTM D-4438-85, 1988 [12] where a suspended particles pass through an orifice while its change in resistance is measured. The powder is suspended in an electrolyte and pump through a tube containing a small orifice. An electric current will pass through this tube, as individual particles pass through the orifice, a fraction of the current is interrupt. The fraction of current's change is a measure of particle size. The magnitude of the change in current flow is subdivided over the range of sizes limited by the size of the orifice. The equivalent sphere of the excluded volume, assuming constant density for the particles, will be used to calculate the particle diameter. The results are normally recorded as weight percentage as a function of incremental particle size. Irregular size materials such as carbon carrier will bring the deviation to the analysis and interpretation, which is based on the spherical particle model.

Another method is when a He-Ne laser for sizing fine particles, according to ASTM D-4464-85, 1988 [13]. The laser beam will be diffracted in proportion to the radius of the particles as it passes through an aqueous solution containing the particles. An electric current will be generated from a photo detector and before being processed.

Other techniques are just as equal in terms of the sensitivity to the particle's shape. The empirical correlation, to standardize the shape to be near-spherical, is normally applied since a universal measurement of particle size is not yet developed.

Particulates

Powder catalysts are sometimes fabricated into particulates (pelletized/cracked/sieved) using a compressing machine, e.g. pelletizer, to get the optimal size of the catalysts. This is useful for the packed-bed or fixed-bed reactor because either too small or too big particles could have a large effect on key parameter of the reaction; such as pressure drop, flow rate, contact between catalyst and reactant, temperature control. These parameters indeed influence the catalytic performance e.g. product distribution, conversion, yield and the process economic. The optimal size of particulates will maximize the process performance.

Wash-coat thickness

The catalyst layer that is coated inside the reactor's wall works the same way as powder or particulates catalysts. The reactants need to penetrate through the pores to reach the active site, before release the product and diffuse out again into the bulk fluid. However, these can occur only one side of the layer (one next to the bulk, not one attached to the wall). The thickness of the wash-coat catalyst is frequently measured by optical microscopic method.

Dispersion

Dispersion of the metal active sites is completely related to the particle size and its distribution. The surface area and particle size of the metal are quantities, determining the overall catalytic properties of the catalyst system. The metal dispersion (D) is equal to N_S/N_T where N_S is the number of metal atoms exposed at the surface and N_T is the total number of metal atoms in a giving amount of catalyst. In this case, the fraction of surface atoms D can be obtained if the N_S is experimentally available. The N_S can be determined by chemisorption measurements. The N_S can be determined by measuring the chemisorption of the adsorbent which strongly binds to the metal but barely interact with the support at the selected temperatures and pressures. H_2, CO, NO and N_2O; with steady-state, transient or temperature program methods; have been widely applied as the adsorbent [14]. By assuming an appropriate shape of the metal particles, the chemisorption data can give the average particle sizes.

4.4.3 MECHANICAL STRENGTH

Crush strength

The particulates of packed catalyst needs to be able to stand the crushing due to the static pressure of the bed height. When using a monolith especially in stacked mode, it should be able to resist the crushing axially. In automotive applications, the vibration resistance as well as the radial strength is also concerned. For spheres, the crush strength is measured, according to ASTM D-4179-82, 1988 [15], by crushing a single particle or representative of several particles between parallel plates of a device capable of exerting compressive stress, while recording for force necessary to crush the material. The similar procedure is applicable for catalysts fabricated in other shapes e.g. tablets, extrudates and monoliths. This method is not feasible for irregular-shaped materials.

Attrition and abrasion

For the moving catalysts such as those applied in fluid-bed or slurry-bed reactor are subjected to the abrasion by physical collisions. In this case, the abrasion resistance is the desired characteristic. To test the abrasion resistance, the catalysts in the interested shape/form (spheres, tablets etc.) will be introduced into a rotating drum, ASTM D-4058-87, 1988 [16]. After a certain time, the fines produced are measured. The drum normally has just one baffle with smooth inner surface. The erosion of the wash-coated monolith is tested by introducing high gaseous flow rates through the material. The high gaseous flow rate could be a jet of gas simulating the linear velocities used in the operation. The weight loss of catalyst due to the erosion will be recorded.

Thermal strength

The monolith catalyst will be subjected to the rapid thermal changes (thermal shocks) which could occur in real operation during the start-up and shutdown. The wash-coated material tends to be lost after frequent thermal shocking due to the different thermal expansion between the wall of the reactor (coated on) and the wash-coated catalyst (coating on). The weight loss is measured.

4.4.4 DENSITY

Packing or bulk density

Density is an important specification of the catalyst as the catalysts (mainly particulates) are sold by weight, but typically charged into the packed-bed reactor by volume. The density of catalyst is also crucial for the system that operated in fluidization and slurry reactor. Besides, the density of the powdered catalysts decide whether it should be used suspended or settled. The fabricated catalysts come in various shapes such as pellets, spheres or extrudates. These catalysts are first dried at a certain temperature (normally around 400 to 450 °C) to eliminate remaining water, organic solvent and other impurities. This step is normally done for at least 3 hours, according to the standard ASTM D-4164-88, 1988 [17]. The material will be cooled in air and afterwards be vibrated while being poured into a cylinder of known volume and weight. Then the volume occupied by the catalysts and its weight is measured and recorded. The apparent packing density of the catalyst is the measured weight of the catalyst divided by its volume. A tapping device can be used instead of the vibrator, to obtain the apparent tapped packing density.

Skeletal or solid density

Skeletal density is the density of the material without void/pores. Thus, skeletal (solid) volume is catalyst volume in bulk excluding its pore volume and the inter-particle void space between discrete particles. The skeletal density can be calculated using the following equation:

$$\rho_{skeletal} = \frac{M}{V_{solid}} \tag{4.7}$$

$$V_{solid} = V_{bulk} - V_{pore} - V_{void} \tag{4.8}$$

When V_{solid} stands for the solid volume, $\rho_{skeletal}$ is the skeletal density, M = mass whereas the void volume is represented by V_{void}, in which it can be calculated by mercury displacement at about 2 atm and the used to calculate the V_{solid} further if V_{bulk} and V_{pore} are known. V_{solid} can be determined from He gas displacement techniques using pycnometry.

4.5 CATALYST CHEMICAL PROPERTIES

The catalytic characteristics of catalysts; i.e. activity, selectivity and stability; are greatly influenced by chemical properties of the materials in the atom/molecule level. The chemical properties rely mainly on the catalyst structure, morphology, dispersion, acidity and chemical composition. However, the impurities in the bulk catalysts also effect the catalytic properties, especially if they can immigrate to the surface. Most chemical properties are determined in a spectroscopic scale, thus, they often analyzed by spectroscopic methods. The fundamental of spectroscopic techniques are based on the excitation of the material using electromagnetic radiation, ions, neutral particles or heat; and followed by the analysis of the resulting emission as demonstrated in Figure 4.4. Photon sources may range in energy from 0.01 eV for infrared to 100,000 eV for EXAFS and Mossbauer spectroscopies.

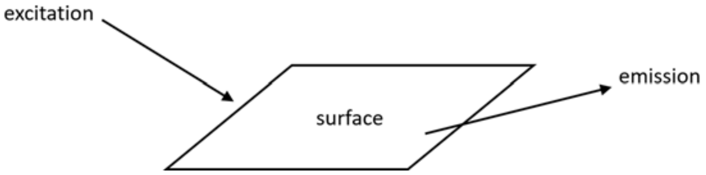

Figure 4.4: Principle of spectroscopy [1].

Commercially produced multi-phase catalysts can be analyzed by some spectroscopic methods. However, most methods are for well-defined single crystal surfaces. A few methods can be applied for in situ experimentations, while some others are utilized only under high vacuum conditions. Table 4.4 tabulates various spectroscopic methods according to sample type. Some of the methods are advantaged for surface studies, while some are rather for the bulk studies.

Table 4.4: Classification of spectroscopic methods, based on type of samples and the condition of study [18].

Analysis environment	Study of real catalysts	Study of single crystal surface
In situ reaction conditions	XRD	IR spectroscopy
	Temperature programmed techniques	Temperature programmed techniques
	IR and Raman spectroscopies	STM
	EXAFS	AFM
	Mossbauer spectroscopy	SFG
	ESR	
	UV-VIS	
	NMR	
	CAEM	
	AFM	
	calorimetry	
In vacuo	XPS	Most surface science techniques
	SIMS	
	SNMS	
	LEIS	
	TEM	
	SEM	

4.5.1 CHEMICAL COMPOSITION

Elemental analysis

The appropriated composition of the chemical elements; i.e. active phases, promoters and supports; are crucial for the catalyst's optimal catalytic performance. Thus, precise analysis of element composition is very important in research and development. For example, the impurities; i.e. alkaline or alkaline earth; containing in the Al_2O_3 based catalysts can act 2 ways, either to inhibit or to enhance the catalytic performance of the catalyst system. This is not the question of the type of impurities solely, but also the concentrations. Excessive amount of the impurity will act as fluxes, leading to unwanted sintering and loss of the specific surface area. However, the just-right amount of the same kind of the impurity can enhance the catalyst's stability against the sintering and/or improve the product selectivity. Therefore, the element composition is an importance factor.

To analyze the bulk composition, many techniques can be utilized such as AAS and ICP. Quite often that the catalysts need pre-treatment process such as dissolving before being analyzed by these techniques. Some well-known standards: i.e. ASTM D-3610-83, 1988 [19]; ASTM D-4481-85, 1988 [20]; ASTM D-4642-86, 1988 [21]: are commonly followed to investigate the composition of $CoMo/Al_2O_3$, Ni/Al_2O_3 and Pt/Al_2O_3, respectively.

Phase analysis by X-ray diffraction

This technique is suitable for materials that have sufficient crystallinity (>1% approximately), with crystallites sizing from 3 to 5 nm, to diffract X-rays. XRD can be used for both qualitative and quantitative analysis of chemical phase. The theory of this technique is based on the principle of X-ray diffraction which responses differently when scattering on the different kind of materials because each materials has a certain pattern of crystal structures consisting certain pattern of planes formed by repetitive arrangements of atoms where these atoms are responsible for diffracting the X-ray. The angles of diffraction differ for the various planes within the crystal. Every single materials therefore has its own distinctive diffraction pattern which is beneficial for classify the catalyst's structure. The example of the use in XRD is to compare the pre- and post-exposure of $NaCl\text{-}Mn_2O_3/SiO_2$ and $Na_2WO_4\text{-}Mn_2O_3/SiO_2$ at several calcination temperatures [22], in order to observe if there are some changes in phases or crystallinity of the catalysts. XRD has also been used in observation of contamination as minor crystalline phase that could be formed via precursor's choice, preparation method or calcination's condition and its atmosphere [23].

4.5.2 CHEMICAL STRUCTURE AND MORPHOLOGY

Surface texture, morphology and crystallite size via electron microscopy and STM

Chemical structure, surface structure, morphology and crystallite size can be identified by the electron microscopy. It can analyze over a wild range of size resolutions, starting from atomic dimensions (0.2-0.3 nm) to several hundred microns. In this matter, 2 main techniques are being applied: (1) TEM; which is an analysis of transparent films to a resolution of 0.2 to 0.3 nm The sample that is prepared for TEM needs to be thin, as TEM analyses by focusing and transmitting electron through the sample, on a conducting grid to form high resolution images of the sample; (2) SEM; which involves an analysis of surfaces at a resolution of 10 nm. The electron beam will be focused on the specimen and is scanned by a set of deflection coils. Backscattered electrons or secondary electrons emitted from the sample are detected. As the electron beam passes over the surface of the sample, variations in composition and topology produce variations in the intensity of the secondary electrons.

Nanostructure of nanophase materials; for instance, materials with 1-2 nm of regular variations; can be analyzed by HR-TEM with a resolution of less than 0.2 nm. This technique allows researchers to see molecular layers and surface layers. Besides, electron microscopy can predict the origin or source of the catalyst materials such as whether carbon materials are derived from wood, peat or other sources of carbon. TEM can determine the shape, morphology and composition of a specific carbon of the interested specimen.

In addition, SEM can be applied to observe edges or surface irregularities of the particulates which were used in fluidized-bed reactor or slurry reactor, in order to investigate their resistance to attrition/erosion. SEM can be utilized in comparing the catalyst's morphology between pre- and post-exposure. Figure 4.5 represents morphology of the catalyst which was wash-coated in a microchannel reactor [24].

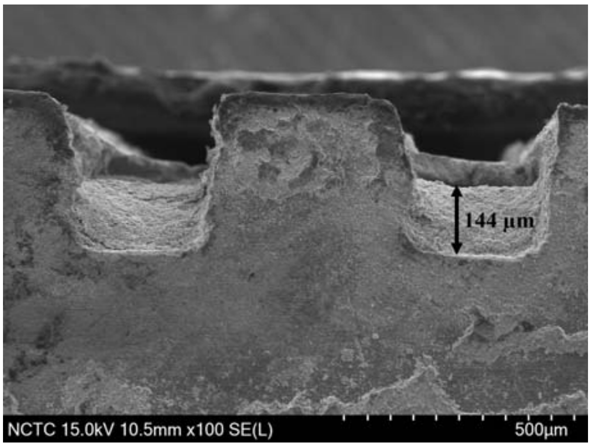

Figure 4.5: Surface morphology of the microchannel plates analyzed using SEM technique after the catalyst coating process [24].

When the energy dispersive technique was assisted with X-ray spectroscopy, the method is called EDX (energy-dispersive X-ray spectroscopy). One of the example is the comparison of surface morphography of stainless steel substrates (316L) before and after annealing at different temperatures [25], which the results are shown as Figure 4.6

[25], whereas Figure 4.7 [26], Figure 4.8 [27] and Figure 4.9 [28] illustrate other 3 examples of SEM images of: 6-channel micromonolith made of $La_{0.3}Sr_{0.7}Co_{0.7}Fe_{0.3}O_{3-\delta}$ (Figure 4.7); SEM micrographs of Zn/ZnO at different magnifications (Figure 4.8); and SEM images of cross-section of LSM/YSZ (lanthanum-strontium/yttria-stabilized-zirconia) anode (Figure 4.9); respectively.

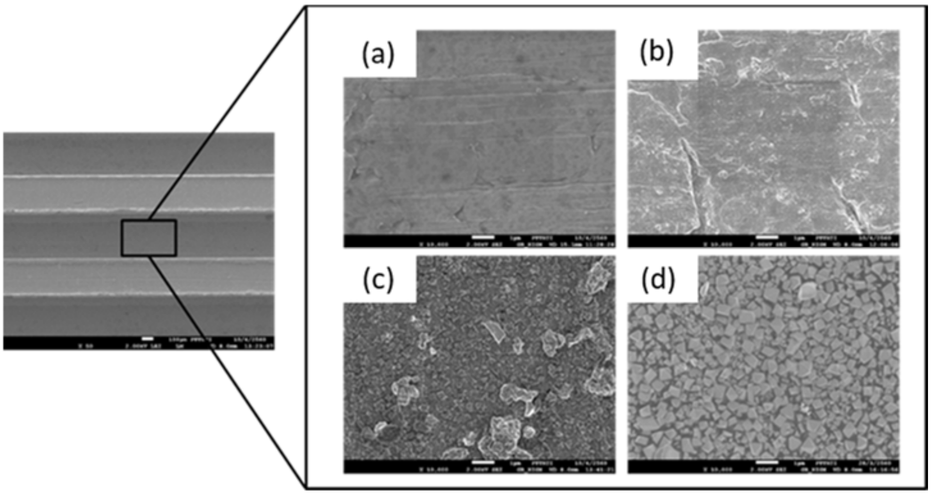

Figure 4.6: Morphology of surface substrates, analyzed using EDX technique (a) before annealing, and after annealing at (b) 600, (c) 700, and (d) 800 °C [25].

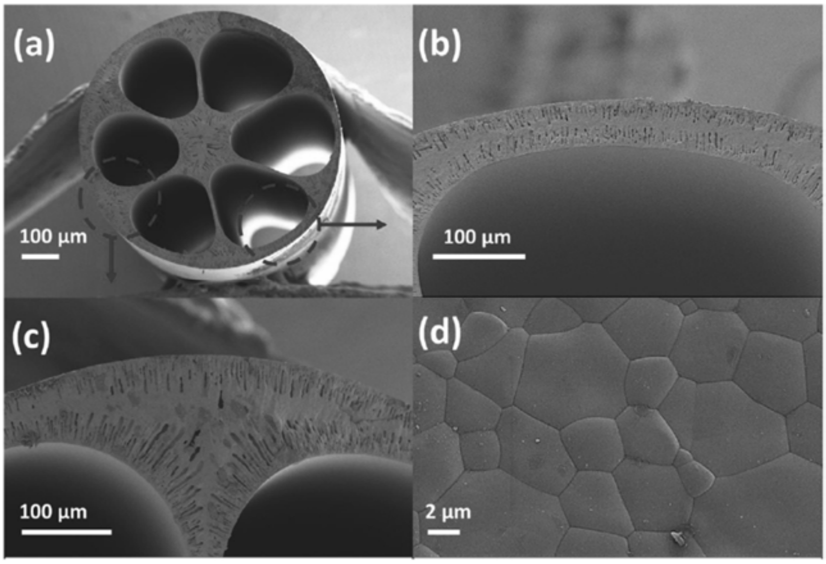

Figure 4.7: Morphology, by SEM, of sintered $La_{0.3}Sr_{0.7}Co_{0.7}Fe_{0.3}O_{3-\delta}$ micromonolith membrane with bio-inspired design: (a) overall image; (b) active region for oxygen permeation with relatively uniform thickness; (c) cross sectional image of wall, between the shell and two bores and; (d) outer surface of the membranes [26].

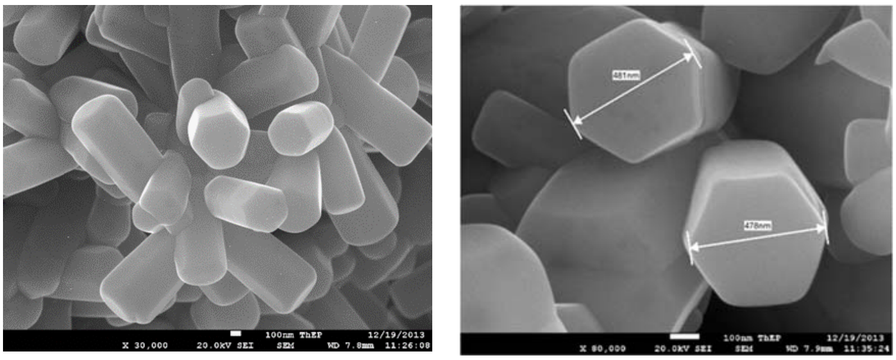

Figure 4.8: SEM micrographs of Zn/ZnO at different magnification [27].

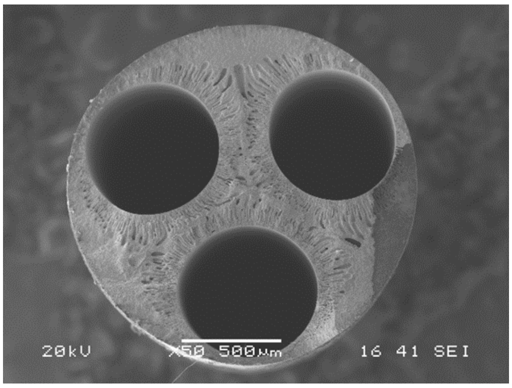

Figure 4.9: Morphology of the anode cross sectional image, made of LSM-YSZ [28].

The more fine atomic resolution of analyzer for surface morphology and structure is possibly STM or AFM. This technique has 0.1 Å resolution and is able to resolve atoms at the surface of materials [29]. This technique is based on the principle of quantum tunneling of electrons between a sharp metal tip and the sample surface. The tip will be brought within atomic distance, which is around 2 Å, of the surface and then kept stable there at the exact distance by a fast-response electronic control. It is possible to move the tip along the sample's surface as it is mounted on a piezoelectric ($BaTiO_3$) holder, which expands in a range of angstroms under the operating potential. The atom-size bumps will be detected easily from fluctuation in the tunnel current due to the fact that the tunnel current varies exponentially with the separation from the surface.

Other properties that can be obtained from STM are; (1) the arrangement of atoms on the surface of supported metal clusters and, (2) defect sites on single-crystal surfaces.

Location and chemical analysis of species within the catalyst

This is called a spot analysis or an area analysis where the electron microscope is assisted with an energy dispersive spectrometer (EDS) or wavelength dispersive spectroscopy (WDS). The unique X-ray patterns of the sample will be created by electrons bombarding the sample. While the composition of any portion of the sample can be determined by EDS, the mapping of the location of the species can be achieved by WDS. EDS and WDS can be assisted with computerized automation system to be applied for this scanning and transmission electron microscope. These computer-modified tools can be incredibly beneficial for catalyst optimization or design a highly tailor-made catalyst for a specific application.

Crystallinity

LEED and XRDboth can be applied to determine the crystallinity of the materials, with a little bit of differences in purposes and applications. LEED is used to examine the crystalline structure of the surface of well-defined single crystals, while XRD is rather used for investigating the bulk crystallinity of catalytic phases and catalyst carriers such as supports, catalyst system includes active site, support and the promoter.

Oxidation state

Because the oxidation state is about oxygen gain or loss, thus, one of the easiest method to determine the oxidation state is to measure the weight change during reduction or oxidation of the sample in a controlled environment. The weight change measurement can be carried out by microbalance techniques, in which one of the most popular method is thermal gravimetric analysis (TGA). To perform this, the catalyst (weight around 50 to 100 mg) will be equilibrated at a certain temperature in a stream of inert gas. H_2 for the reduction and O_2 for the oxidation will be co-fed with the inert carrier gas while the weight change is measured and monitored. The weight change can give information regarding the valence state of the catalyst component or the quantity of catalyst which is reduced/oxidized during a known change in valence state. The fraction of reduced species can be calculated from the measured increase in mass relative to the total during oxidation of the previously reduced sample, assuming the total quantity of active catalyst component is known from bulk chemical analysis.

Another method that is equivalently reliable is probably the temperature programmed method, in this case, consists of 2 steps which are (1) temperature-programmed reduction (TPR) and (2) temperature-programmed oxidation (TPO). The 2 steps are generally combined together as a redox reaction. While the TPR is for measuring H_2 consumption, the TPO is to measure O_2 consumption, rather than weighing the weight change caused by the change in number of oxygen atoms. The oxidation state can be determined based on stoichiometry of the reaction. To perform the TPR or TPO, the relevant reactant (H_2 for reduction and O_2 for oxidation) will be flowing through the packed catalyst while the reactor temperature is raised proportionally. The gaseous product will be analyzed real-time using either gas chromatography or mass spectrometer. Quantitative interpretation of TPR and TPO spectrum can provide (1) reduction/oxidation temperature for various phases, (2) reduction/oxidation stoichiometry and (3) information of the redox mechanism.

4.5.3 DISPERSION OR CRYSTALLITE SIZE OF CATALYTIC SPECIES

Dispersion, measured by chemisorption

In general, the highly active and selective catalysts are either amorphous or having relatively very small crystallites. The crystallite size of these materials are not obtainable by XRD. If these catalysts are well-dispersed, their crystallite size and its distribution can be achieved via TEM. Apart from its high cost, the procedure of using TEM can be quite tedious and requiring a sophisticated skill of the user. A selective gas chemisorption can be instead used as a probe reaction. This method is supposed to be less tedious, inexpensive and less complicated. The chemisorption, in this matter, can be used for: (1) estimation of amount of active sites towards a specific reaction, thus, the TOF determination is achievable; (2) catalyst optimization and quality control. For example, the change of available active sites number at the surface area, caused by sintering or different preparation methods; (3) understanding in basic information of the catalyst's reactivity by its metal structure and/or support. The metal surface area, average crystallite diameter and the number of potential catalytic sites can estimated by a measurement of monolayer hydrogen adsorption capacity. Commercially, it has been used in optimizing surface area during the preparation process and in estimating the extent of deactivations.

Chemisorption of H_2 on metals

To measure the monolayer of H_2 adsorption of any supported metals, the procedure should be reproducible, convenient and responsive using an apparatus that is easy to use and inexpensive. This method will account both reversible and irreversible hydrogen chemisorbed on the metal while excluding chemical and physical adsorption on the support. Kinetic limitation of the highly activated adsorption should be concerned. There is currently no universal standardized adsorption methods for metal dispersion measurement, however, some internationally accepted standards have been developed around the world.

Other chemisorbates

The adsorption stoichiometries for other gases; i.e. CO and O_2; are not as consistent as H_2. Normally, several layers of metal oxides will be formed when the adsorption of oxygen is applied, especially in base metals. The stoichiometry of CO adsorption on metals is highly variable because of the possibility of each CO adsorbing either in the hollows of 3 or 4-fold sites such as one molecule of CO is binding with 2 to 4 metal atoms, or sometimes, 2 or 3 molecules of CO can be adsorbed on 1 single metal atom. However, CO chemisorption is still currently used by many researchers despite not quite being reliable as a method for determination of surface metal area. H_2 chemisorption is not applicable to investigate metal oxides or sulfides as it binds weakly with those materials. Besides, it's only either specific or nonspecific to a few sites. Sometimes, NO and O_2 are used to determine catalytic are of metal oxides, but the applications are very limited due to the lack of data in adsorption stoichiometries.

Table 4.5: Comparison of ASTM standard volumetric test method and proposed volumetric test method by Japan Catalysis Society, for measuring H_2 uptake of Pt/alumina catalysts [30].

Equipment/procedure	**ASTM D-3908-82 method** [31]	**Proposed method (Japan)**
Equipment specification		
Gas handling vacuum system	Glass or metal, $P < 10^{-5}$ Torr	Glass, $P < 10^{-6}$ Torr
Pressure-measuring device	0-500 Torr (with 0.1 Torr error)	0-100 Torr to 0.08%
Calibration bulb	Volume calibrated to 0.1%	
Catalyst sample	>1 g of > 20 mesh, 0-5%Pt	0.1 to 0.5 g, 0.5%Pt
Procedure		
Pretreatment	Air calcination at 450 °C, 1 h	Evacuation at 450 °C and heating in 50 Torr; O_2 at 450 °C for 1h
Reduction	450 °C in 1 atm H_2, 1-2 h	300 °C in 50 Torr H_2, 1 h
H_2 uptake	20-25 °C, 30-60 min each point	25 °C, 1 h at each point

(Continued)

Table 4.5: *(Continued)*

Equipment/procedure	**ASTM D-3908-82 method** [31]	**Proposed method (Japan)**
Results		
Measured uptake	0.122 (with 0.003 error)cm^3(STP)/ g$_{cat}$ average of determination form 5 different laboratories.	0.335, 0.360 cm^3(STP)/g$_{cat}$ for 2 different catalysts
Repeatability	13% of average value	
Reproducibility	<16% of the average value	

The hydrogen-oxygen titration

This technique was originally developed by Benson and Boudart (1965) and well-known for it's user-friendly. This method is sensitive for measuring Pt surface area. The following chemical reaction was proposed for the hydrogen titration of an oxygen-covered Pt surface.

$$\mathrm{Pt-O} + \left(\frac{3}{2}\right)\mathrm{H_2} \rightarrow \mathrm{Pt-H} + \mathrm{H_2O} \tag{4.9}$$

Because the H_2 uptake is 3 times higher for each Pt surface atom than that for dissociative H_2 adsorption, thus, the sensitivity is also 3 times higher. This technique had been later developed with a more precise handling procedure [32,33], concluding that the number of H and O atoms adsorbed per 1 Pt atom are 1.1 and 0.71, respectively. The developed procedure [32] includes: (1) evacuation of the sample at 25 °C for 30 min to remove air; (2) evacuation at 125 °C for 30 min to remove water; (3) reduction in flowing hydrogen (30 cm^3/min) while heating up in 502 °C and holding at 502 °C for 1 h; (4) evacuation for 1 h at 502 °C to remove gas phase and adsorbed hydrogen followed by cooling *in vacuo*; (5) exposure to 160 Torr of O_2 at 225 °C to oxidize the surface followed by evacuation for 15 min at 225 °C to remove the gas phase O_2; and (6) measurement of H_2 uptake. This the Pt dispersion can be calculated through the following equation:

$$E\ (\%\text{metal exposed}) = \frac{1.95\ HT}{[(2x+y)w]} \tag{4.10}$$

Where HT is the hydrogen uptake in the titration in μmol/g, x and y are the stoichiometric ratios of chemisorbed oxygen and hydrogen, and w is the weight percentage of the platinum in the sample.

Palladium catalyst can be also applied for this very similar procedure, except that the hydrogen titration is carried out at 100 °C and under pressure less than 345 Torr to avoid bulk Pd hydride formation. This method is known to be handy and useful, therefore, generating accurate measurement of dispersion agreeing with those performed via H_2 adsorption, CO adsorption and TEM.

Flow chemisorption method

Apart from the above mentioned time-consuming static vacuum techniques, there is the better way to convey this dispersion measurement – the dynamic flow technique in which a pulse of adsorbate such as H_2 or CO is injected into a stream of inert gas and passed through a bed of catalyst maintained at the constant temperature. The amount of the gas injected will be compared with amount of the gas that passes through the bed without adsorbing. This term of measurement will be equivalent to the amount of gas adsorbed. No gaseous adsorption is expected to occur once the monolayer coverage is reached (saturation). The main difference between the static and dynamic method is that the dynamic transient method is measuring the species that are strongly adsorbed while the static is to measure all chemisorbed species (both strong and weak) at their equilibriums. Therefore, the static method normally provide a significantly higher amount of measured monolayer adsorbed species than that measured by the transient dynamic method. The condition of irreversible adsorption is normally opted for since it is difficult to predict the degree of reversibility for different catalysts. The transient dynamic method involves [34]: (1) cooling the reduce catalyst in hydrogen to around -73 °C; (2) before starting, purging Ar at 200 ml/min in order to remove gaseous H_2 and; (3) continuing the purging while increasing the temperature to 400 °C to remove adsorbed hydrogen. The area of the desorption peak, provided by a gas chromatography (GC) coupled with thermal conductivity detector (TCD) is considered as the amount of desorbed hydrogen from the surface. This technique provides an accurate measurement of the monolayer capacity (as the hydrogen adsorption on metal is generally irreversible at -73 °C), yet it is a rapid test which could be completed within a few hours using affordable equipment.

Chemisorption and active sites

This methodology is to measure the amount of the metal atoms laid on the surface (both active and inactive ones) as not all the metal atoms are reactive to one particular catalytic reaction. For example, in the supported metals, the active sites are usually a collection or ensemble of metal atoms; in the oxide or sulfide catalysts, the active sites can be vacancies or metal ions of a specific oxidation state. However, the number of active sites are not the only parameter that influences the catalyst activity and/or selectivity. The supports and promoters play a role as well because their appearance can change the electronic configuration of overall property of the catalyst system. Therefore, the adsorption capacity may not be always directly related to the catalytic performance. Although knowing the number of surface atoms is beneficial for developing initial conceptual understanding towards the nature of the active sites.

Crystallite size from transmission spectroscopy

TEM and STEM is techniques where a thin sample is prepared by either microtome slicing or mounting on a carbon grid before being subjected to an electron beam. The transmitted electron beams will be further projected on a film as a two dimensional image. The dense area of the sample, which inhibit the transmission of the electrons, will be shown as dark spots on the bright film image. The outline of the metal particles or crystallite will be formed by these dark spots. Thus, their sizes can be estimated. This technique nowadays can provide as high as 0.2 nm resolution with 10^6 magnification. The dispersion or ratio of surface atoms to total atoms in the crystallite can be determined via assuming a shape of the crystallites. This technique investigates only small amount of sample, thus, it would be difficult to claim that all the sizes is uniformly distributed in that small portion of sampling. To solve this, many different area of the materials should be sampled before being statistically analyzed afterwards.

Crystallite size from X-ray diffractions

The width of X-ray diffraction peak is inversely related to the crystallite size of the interested phase, meaning that the breadth of the peak is also implying the crystallite size. The Scherrer equation relates to the peak's breadth (B) and the half-peak height of an XRD line due to a specific crystalline plane to the size of the crystallites (d):

$$B = \frac{\kappa\lambda}{d \cos \theta} \tag{4.11}$$

Where λ is the X-ray wavelength, θ is the diffraction angle, κ is a constant (usually equal to 1). When the crystallite size increases, the line breadth (B) decreases. By this methodology, a brief estimation of the crystallite size can be figured out. For example, the crystallite size of CeO_2 and CeO_2/ZrO_2 were compared using the Scherrer equation. It was found that the Zr addition reduced the crystallite size of the overall catalyst system [25]. Figure 4.10 showed the diffractogram patterns of studied catalysts. As well as Figure 4.11, which proved that the prepared perovskite is single crystalline phase with no detection of impurities. Fourier analysis of the data can give the better precision of the crystallite size [35].

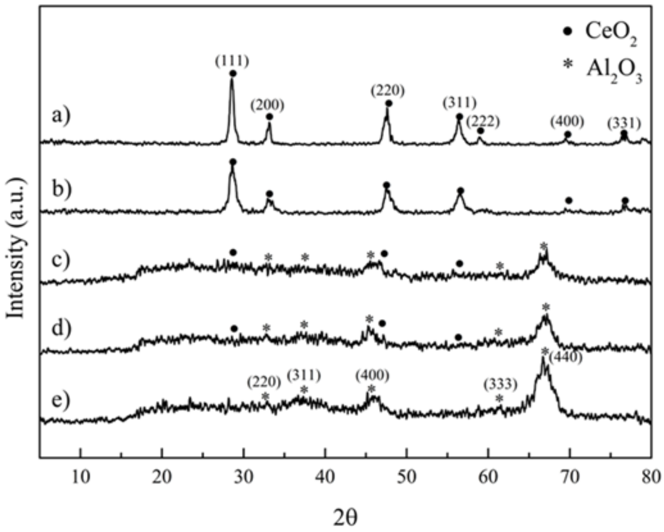

Figure 4.10: XRDpatterns of (a) CeO_2, (b) CeO_2/ZrO_2(3:1), (c) 10%CeO_2-Al_2O_3, (d) 10%CeO_2/ZrO_2(3:1)-Al_2O_3 and (e) pure alumina [25].

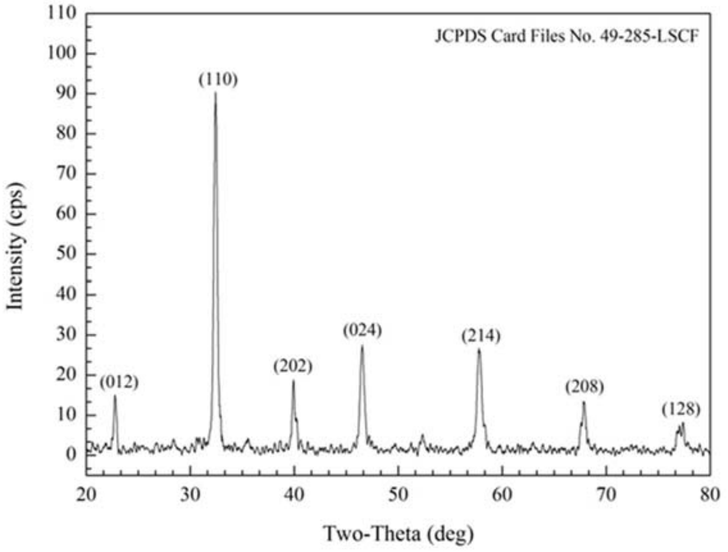

Figure 4.11: XRDdiffractograms of $La_{0.3}Sr_{0.7}Co_{0.7}Fe_{0.3}O_{3-\delta}$, after calcination at 800 °C [36].

The crystallite size achieved from the above mentioned method is not always comparable. Chemisorption is biased towards a smaller average crystallite size and line broadening towards a larger size. To be precise, the line broadening and chemisorption method is not comparable because the former is a volume-averaged measurement while the latter is surface area-averaged measurement. However, the chemisorption and TEM are comparable if only the surface-averaged size distribution is calculated from the TEM data.

4.5.4 SURFACE ACIDITY

Acidity of the active sites are requited in many chemical reactions such as polymerization, isomerization, aromatization or a simple cracking. This reaction can be catalyzed by Lewis and/or Brønsted acid sites. The acid properties include the nature of surface acidity, its strength and its number [37]. The Brønsted acid sites can be titrated using alkaline materials while the acid strength can be measured using acid indicators (e.g. Hammet) and calorimetric methods. More sophisticated analysis includes TPD of chemisorbed-bases (e.g. ammonia), calorimetry, FTIR and NMR.

Gas adsorption

To measure the acidity, ammonia and/or pyridine can be used as an alkaline to perform the adsorption of acid gas, following the ASTM D-4824-88, 1988 [38]. Ammonia-TPD is one of the most common method to measure the acidity of zeolites and other acidic solids. However, its downsides/limitations include: (1) the lack of specificity (i.e. being dependent on experimental conditions and bed depth, desorption of non-protonic binding sites, Lewis sites can take place in a wild range of temperature from 100 to 325 °C which is a region where Brønsted sites are assumed to adsorbed); (2) inaccuracy in acid strength measurement, in the case of ammonia desorption; (3) inconsistency results can be expected, for instance, higher desorption temperature is evidenced for CaO than for the classical zeolites.

TPD can be carried out using various amines such as ethylamine, n-propylamine, isopropylamine or t-butylamine, for the Brønsted acidity measurement [39]. These amine will be adsorbed with a coverage of one molecule per Al site and decomposing to alkenes and ammonia at a certain temperature which only depends on the alkyl group. Besides, this techniques is advantageous in defining the type of the acid sites as the decomposition will occur only on the Brønsted acid and not the Lewis acid.

Infrared and NMR analysis

The relative amount of Lewis and Brønsted acid sites presenting in a catalyst can be determined using an infrared adsorption. Each site has distinctive and well-resolved IR bands. For example, pyridines forms a complex with Lewis acid sites, and produces an IR adsorption band at around 1,450 cm^{-1} while pyridinium ions form at Brønsted acid sites will release the IR band at approximately 1,550 cm^{-1}. Thus, the ratio between the 2 kinds of acids can be calculated using the relative intensities of the 2 IR bands [37,40].

In addition, IR, NMR and calorimetric study can be utilized together to gain both qualitative and quantitative information on the number and strength of the Brønsted acid and Lewis acid sites in aluminas and zeolites [41-43]. In details, the zeolites will be heated at high temperature in steam. After that, the aluminum atoms will be eliminated from the zeolite's framework. However, the non-framework aluminum is remained in the zeolites as tiny amorphous alumina clusters and is responsible for Lewis acidity of the steam-pretreated zeolites. Informative structure and number of 2 different kinds of Lewis acid sites presented in de-aluminated mordenite can be obtained via a high resolution NMR and FTIR of adsorbed CO [40-43]. In addition, the Lewis acid sites are often considered the higher acid strength, compared to the Brønsted sites, determined by calorimetric measurements.

4.5.5 SURFACE REACTIVITY

In this matter, the kinetics of molecule-surface interactions are investigated qualitatively and quantitatively. The following characteristics can be defined by this surface reactivity measurement methodology: (1) kinetics of adsorption/desorption of H_2 or CO or other reactant probe molecules; (2) reaction with hydrogen, oxygen or water of reactive surface intermediates and fouling agents such as carbons and cokes; (3) bond strength and concentration of the different surface species. This methodology allows researchers to investigate microkinetics data, which often predicts the reaction mechanism. The characterization techniques which rely on this principle include TGA, DTA, TPD, TPR, TPSR, TPO and TPS. While TPR and TPO were explained earlier in the reducibility and oxidation state determination, the TPD and TPSR will be described in this section in terms of adsorption, desorption, reaction kinetics, mechanism, population of active sites and the activity of the active sites. Some methodologies also involve applications of microcalorimetry.

Temperature-programmed desorption (TPD)

TPD, including flash desorption, thermal desorption spectroscopy (TDS), is initially developed to observe the kinetics of desorption of molecules from well-defined single crystal surfaces in high vacuum [18]. The procedure includes exposing the single crystal surfaces to the adsorbate gas under a certain condition. After that, the gas is flashed from the surface at a high linear heating rate (from 0.5 to 50 °C/s), then the pressure of the desorbing versus time is monitored throughout the experimentation. The reaction orders, Arrhenius parameters and saturated surface coverage of desorption can be obtained by varying the initial coverage if the adsorbate and the ramp rate of heating. According to these data, the heats of adsorption, the binding energies of various adsorbates on different type of the single crystal materials can be determined as a function of coverage [44,45]. Parameters such as re-adsorption, pore diffusion, bed height of the catalyst (differential catalyst, usually set by 0.1 g of catalyst) and the heating rate (around 0.2-0.8 °C/s) are the key component to achieve the meaningful data. The experiment should ideally have no influences from limitation of mass and heat transfers. For example, TPD result revealed that H_2 desorption from supported noble metal catalysts indicated that binding energies are about the same as for the single crystals and are independent from the support. In contrast, the H_2 desorption released from supported base metals; i.e. Co, Fe and Ni; showed that the binding energies are highly influenced by the support, by the unreduced metal oxides and by the promoters. Another example is O_2-TPD, carried out to determine the oxygen lattice/oxygen vacancy, which are available at the surface of the metal-doped oxygen carriers such as NaCl-Mn_2O_3/SiO_2, comparing with Na_2WO_4-Mn_2O_3/SiO_2 [22]. The achievable information from TPD is illustrated in Table 4.6.

Table 4.6: Temperature-programmed desorption and its interpreted information.

Process	Variations and influences	Interpreted information
H_2 on single crystal noble and base metals, focusing on Ni and Pt	Binding energy, adsorption kinetics, saturation coverage as function of geometry	Binding energy and kinetics are effectively independent of surface plane for a given metal: binding energy decreases significantly with increasing coverage [30,45,46]
H_2 adsorption on supported noble metal catalysts	Binding energy, adsorption kinetics, effects of support	The gas pressure must be much higher than for single crystal study because of support porosity and diffusional restriction, coupling between re-adsorption and pore diffusion decreases desorption rates by several orders of magnitude relative to single crystals, binding energies are about the same as for single crystals and not affected by support [30,47-52]
H_2 on supported Co, Ni, Fe	Effects of coverage, support and promoter on binding energy and adsorption kinetics	Kinetics and binding energy are generally influenced by supports and promoters, activation energy of the adsorption increases with increasing surface K_2O or MOx concentration, metal surface on the support generates new adsorption states of high binding and activation energy [30,46,53,54]

(Continued)

Table 4.6: *(Continued)*

Process	Variations and influences	Interpreted information
CO on Co/Al_2O_3	Effects of loading, extent of reduction, decoration	Adsorption of weakly reduced $1\%Co/Al_2O_3$ involves one molecular state at low binding energy, desorption from 3 to 15%Co includes additional states of high binding energy corresponding to C+O recombination, adsorption of CO on strongly reduced and higher loading catalysts is dissociative, ability to dissociate CO correlates with high activity for CO hydrogenation [1]
CO on Co/W (100) and Co/W (110)	Effects of surface and electronic structure on adsorption mechanism	CO adsorption on monolayer Co/W (100) occurs dissociatively at 27 °C but at higher temperature on Ni/W (100), a structural homolog, and Co/W (110), which has a very different structure, results are explained mainly by differences in electronic structure between Co and Ni surfaces, which affect the ability of highly open M/W (100) structure to dissociate CO [55]
O_2 on NaCl-Mn_2O_3/SiO_2, comparing with Na_2WO_4-Mn_2O_3/SiO_2	Effect t of Na precursor when being doped on the same support/oxygen carrier (in this case, it's the Mn_2O_3/SiO_2 catalyst system)	The active surface oxygen (Os) of NaCl-Mn_2O_3/SiO_2 and Na_2WO_4-Mn_2O_3/SiO_2 was created at temperature of 400 and 500 °C with the amount of surface oxygen lattice at 278 and 213 µmol/g, respectively [22]

Temperature-programmed surface reaction (TPSR)

This technique is a transient experiment that measures the changes and behavior of the reaction when the temperature is continuously changed, as a function of time. The common reactive gases can be H_2, O_2 or H_2O with: (1) previously adsorbed species such as CO; (2) surface carbon or coke; (3) previously reduced catalyst i.e. during the calcination. The typical online analyzer that is most commonly used in this technique is mass spectrometer and/or gas chromatography. The results are representing peaks in correspondence to the reaction states i.e. temperature at which the reaction rate passes through a maximum. From the results, unsteady-state reaction rates, relative reactivities, of surface species and activation energy of the reaction can be determined by the result's interpretation. Table 4.7 presents some of the TPSR studies and interpreted information received from this experimentation.

Table 4.7: Examples of information available from TPSR.

Method	Process	Variations and influences	Interpreted information
TPSR	Reaction of H_2 with CO_2 adsorbed on $Co/A_{l2}O_3$, Ni/Al_2O_3 and Pt/Al_2O_3	Effects of metal, metal loading, extent of reduction; role of support in CO hydrogenation	These catalysts were evidenced to have 2 different reaction pathways for CO hydrogenation which are (1) dissociation of Co on metal followed by hydrogenation of carbon atoms to methane, and (2) spillover of H and CO from the surface to the support, migration the acid sites, methoxy intermediate formation and its diffusion to the metal where it further decomposes to methane [56,57]
TPSR	Reaction between H_2 and C, caused by dissociation of CO in the presence of Ni/Al_2O_3	Carbon forms deposited during CO dissociation at 250 °C on Ni/Al_2O_3	3 types of carbon are formed: (1) C_α' which is very active with approximately maximum reaction rate at 77 °C when assigned to the surface of CH_x species; (2) active C_α with its maximum rate at 177 °C when exposed to the surface carbon; (3) C_β being reactive at around 402 °C if assigned to a film of polymeric carbon [58]
TPSR	Reaction between C and H_2, resulted from FT synthesis over unsupported Fe/Al_2O_3 and $Fe/K/Al_2O_3$	Carbon and carbide species observed as a function of reaction temperature and K promoter	Lower C reactivity for Fe/K relative to Fe; C reactivity decreases with increasing reaction temperature from 215 to 245 °C; deactivation at higher reaction temperature is due to graphitic film poisoning [59]

(Continued)

Table 4.7: *(Continued)*

Method	Process	Variations and influences	Interpreted information
TPO	Reaction of oxygen with coke formed on Pt, Re, Pt-Re on Al_2O_3 and SiO_2	Effects of metal, support, and sulfidation on coke level and H and H to C ratio in coke	Small amount of coke is formed in absent of acidic support, soft coke is predicted as H to C ratio is high, most of the coke is hard and is formed on alumina, sulfiding decreases the coke formation and increases H to C ratio; less amount of coke is formed on sulfide PtRe/Al_2O_3 relative to sulfided bometallic and sulfide Pt/Al_2O_3 [60]
TPSR	Reaction of methane in the presence of NaCl-Mn_2O_3/SiO_2 and Na_2WO_4-Mn_2O_3/SiO_2	Effect of Na precursors on mechanism of oxidative coupling of methane (OCM) using oxygen lattice within the catalysts as an oxidant source	Both catalysts showed similar mechanistic pathways, however, C_2H_6 and C_2H_4 occurred at the same temperature via OCM over NaCl-Mn_2O_3/SiO_2 whereas C_2H_6 occurred first then further followed by C_2H_4 in the presence of Na_2WO_4-Mn_2O_3/SiO_2. The results suggested that at temperature higher than 850 °C, the solid-gas mechanism of the 2 catalysts might follow different mechanistic pathways [22]
TPSR	Reaction of oxygen in the presence of the post-exposure NaCl-Mn_2O_3/SiO_2 and post-exposure Na_2WO_4-Mn_2O_3/SiO_2	To investigate the coke formation and its amount which were occurred via the OCM reaction	TPSR spectra of CO_2 and CO formation via coke combustion over the 2 catalysts were reported for comparison purpose. 0.1 µmol/h.hr of CO_2 was detected when NaCl-Mn_2O_3/SiO_2 was used as a catalyst. No coke formation was observed for Na_2WO_4-Mn_2O_3/SiO_2 [22]

(Continued)

Table 4.7: *(Continued)*

Method	Process	Variations and influences	Interpreted information
TPSR	Reaction between H_2 and surface of $La_{0.3}Sr_{0.7}Co_{0.7}Fe_{0.3}O_{3-\delta}$	Effect of temperature on oxygen release and its amount over $La_{0.3}Sr_{0.7}Co_{0.7}Fe_{0.3}O_{3-\delta}$	Overall oxygen storage capacity (OSC) of the catalyst was calculated at 4,072 µmol/g.cat which was released by 3 different peaks at 3 different temperatures at below 530 °C, between 530 and 750 °C and above 750 °C [61]
TPSR	Reaction between H_2 and solid oxygen lattice within $BaFeO_{3-\delta}$ (BF) based perovskites	Effects of Ba substitutes in $BaFeO_{3-\delta}$ based perovskites on their reducibility	At temperature higher than 800 °C, BF showed the highest number of OSC, followed by BLF ($Ba_{0.95}La_{0.05}FeO_{3-\delta}$), then BFG ($BaFe_{0.975}Gd_{0.025}O_{3-\delta}$), at 560, 236 and 216 µmol/g, respectively [62].
TPSR	Methane reacting with surface active sites of 10%NiO-$La_{0.3}Sr_{0.7}Co_{0.7}Fe_{0.3}O_{3-\delta}$	How CH_4 is reacted with 10%NiO-$La_{0.3}Sr_{0.7}Co_{0.7}Fe_{0.3}O_{3-\delta}$	The mechanism of methane partial oxidation was predicted when oxygen lattice worked as an oxidant [63]

Figure 4.12 shows the CH_4-TPSR over $La_{0.3}Sr_{0.7}Co_{0.7}Fe_{0.3}O_{3-\delta}$. The mechanism can be predicted by product calculation and calculation.

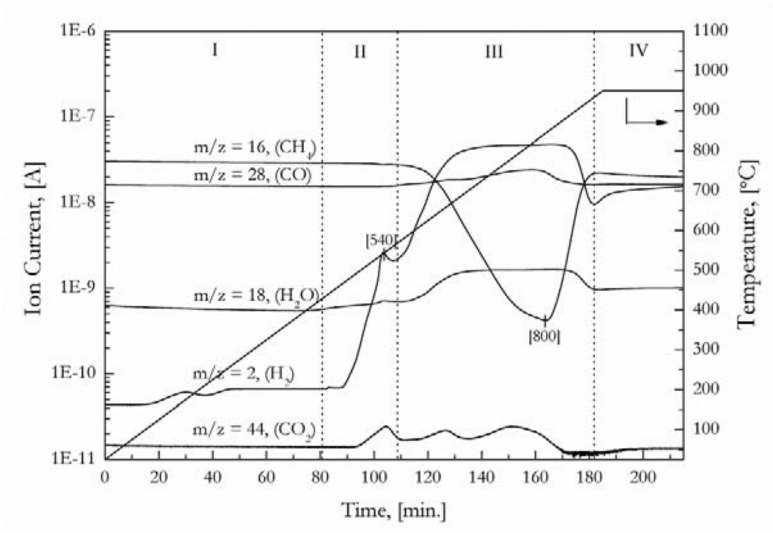

Figure 4.12: CH_4-TPSR over $La_{0.3}Sr_{0.7}Co_{0.7}Fe_{0.3}O_{3-\delta}$ [63].

CH_4-TPSR can be used with TG, TEM, XRD and Mossbauer spectroscopy to achieve more information of the formed intermediates in the reactions.

Calorimetry

Heats of adsorption and surface reaction can be measured/investigated précising using a microcalorimetry, which is normally performed with a heat-flow operation. In this operational manner, the heat generated during the adsorption or reaction will be measured as the heat flow between the catalyst sample and a heat sink controlled at a precise temperature. There is a thermopile setting around the sample, acting as a detector and heat conductor between the sample and the heat sink. This method is not applicable for kinetics measurement/study as it involves heat flow and occurs slowly. However, this is one of the best simple direct methods to measure the heat of adsorption as a function of coverage under the actual reaction operating condition.

Besides, distribution of acidic and basic sites of zeolites and other metal oxides and their strength can be directly measured using the calorimetry too. Another use of calorimeter includes to study changes in heat of adsorption e.g. to observe alloying or metals segregation in bimetallic catalysts. In addition, calorimetry has been also applied in surface reaction science, including investigation of oxidation and reduction of metal oxides, oxidation of adsorbed hydrocarbons or hydrogen and decomposition reactions.

4.5.6 SURFACE CHEMISTRY, STRUCTURE AND COMPOSITION

The surface composition of a catalyst may be determined by the equipment that used for the bulk composition i.e. XRD or Mossbauer too, if only the dispersion of the material is uniform. However, the dispersion degree in the materials is not always ideal, thus, the composition of the material at the surface can be very different to that in the bulk. This is when the surface chemistry and apparatus for such science is heavily involved in catalysis since heterogeneous reactions initially start from surface in which it accommodate active sites and interact with reactive substances. Some of the surface characterization techniques are designed for only the well-defined single crystals as models of catalytic surfaces. However, there are some other techniques; i.e. XPS, AES, SIMS, STM or TPD/TPSR; that are designed for investigate surface structure, composition and morphology of the catalysts. The in situ techniques are normally applied with FTIR, EXAFS, NMR, UV-VIS and Mossbauer, to study the catalyst's behavior in real-time under the operational condition of the reactions. Bear in mind that the NMR and Mossbauer methods are based in bulk transmission, therefore, are able to be utilized to well-dispersed surface which accommodates large amount of atoms, relatively.

Surface science techniques

These techniques are sophisticated and well-developed. They are designed to observe the surface of large single crystals, metal films or foils in ultra-high vacuum environment. Some previous works reported successes in its application in catalyst powder too. In general. This kind of techniques provides an insight understanding towards the surface's function how the surface structure relates to the overall performance of the catalysts. The knowledge gained in this helps researchers to design the more active, more selective and more stable catalysts for specific reactions. Surface science's fundamental in all apparatus/techniques are quite similar in common. It starts with the excitation of the sample using photon or particle bombardment. This causes the emission of photons/particles which are detected/analyzed. This technique allows researchers to define symmetry, geometry, composition, electronic structure and vibrational spectrum of the surface using the tools like XPS, AES, SIMS, ISS and STM as surface spectroscopies. In addition, HREELS is able to give information on structure of molecules adsorbed on planar (single crystals and polycrystalline) solid surfaces. Many of these apparatuses are to operate under ultra-high vacuum atmosphere. The criteria for choosing appropriate tools depend on various factors such as: (1) the number of monolayer analyzed; (2) sensitivity; (3) the capability to analyze the surface quantitatively; (4) the possibility to analyze the chemical states of the surface; (5) the acceptable level of damaged surface by the incident radiation; (6) the extent of charging problem; (7) resolution; (8) cost; (9) strength; (10) specific limitations; (11) nature of the sample; e.g. whether if it's amorphous or poly crystalline or well-defined single crystals; and others.

X-Ray photoelectron spectroscopy (XPS)

In this technique, surface of the sample will be bombarded with X-ray photons where the emission of photoelectrons will be measured as a function of electron energy. The emission pattern of each element and its oxidation state is unique and specific, thus, the chemical analysis can be carried out using these information [18]. The depth or the thickness of the surface that is applicable for the analysis is around 1 to 20 Å, due to the relatively weak energy of the emitted photoelectrons. However, this thickness is varied, depending on the element at the surface. The composition of a thin surface layer as a function of depth can be achieved by sputtering away the layers of surface where the underlying surface can be analyzed. By this technique, in-depth surface information; i.e. oxidation state of the active sites, metal-oxide interaction, changes in the element's oxidation state by the reaction progress and surface impurities; can be obtained. XPS can be applied for oxide phase dispersion measurement which are difficult to be measured by chemisorption or other conventional methods.

Auger electron spectroscopy (AES)

AES is a highly specific-to-element spectroscopy. An electron beam of 1 to 10 keV will be directed at a conducting metal (single crystal) or foil surface [1]. The resulting secondary Auger electrons will be emitted from the surface for measurement and analysis. Auger electrons are created by relaxation of core electron holes in which they were previously excited by high energy electrons or X-rays, e.g. XPS. Thus, the relaxation occurs by filling the core hole with an electron from a higher-energy shell. The energy released from this transition movement can be considered as either an X-ray photon (X-ray fluorescent) or by emission of a second Auger electron of the interested element. AES is very useful for providing information on surface impurities. There are 2 advantages of using AES in relation to XPS: (1) it has higher lateral resolution; (2) its surface selectivity for various significant elements.

Ion scattering spectroscopy (ISS)

This method consists of a beam of ions scattering elastically by atoms in solid, mechanically. There are 2 kinds of ion scattering which are Rutherford backscattering spectrometer (RBS) and Low energy ion scattering (LEIS). In the RBS, the mono-energetic beam of He^+ ions (2 to 4 MeV) will be directed from an accelerator to a surface of the sample from which they are elastically scattered in a surface layer of a few microns of thickness. Afterwards, the backscattered ions will be detected with an energy resolution around 10 to 20 keV. Therefore, the RBS is feasible for identifying isotopes up to atomic mass of 40, however, it is not applicable for determine heavy catalytic elements such as Ir, Pt and Au. In addition, the RBS analysis towards the mixed supports catalyst system; i.e. Rh/Al_2O_3 or ZrO_2/SiO_2; will produce peaks due to the heavier elements on a near zero background, since the intensity is lower for the lighter elements. RBS is considered a bulk analysis, compared with the LEIS, due to the fact that the thick later is analyzed [18]. On the other hand, LEIS, also referred to as ISS, is commonly used for the surface analysis. The incident of the lower energy ion beam (0.1 to 10 keV) that manage to reach the detector has been scattered by the outermost layers. LEIS is regarded as one of the most powerful tools for quantitative analysis of the exposed surface layer's composition. LEIS can be applied in study of adsorbate orientation and bond length in order to investigate surface impurities. Besides, it can be also utilized in measurement of surface composition in supported metals, metal oxides and complex multi-metallic catalysts.

Secondary ion mass spectroscopy (SIMS)

SIMS is well-known for its high sensitivity to analyze surface composition, however, it is one of the most difficult techniques for quantitative analysis [64]. A primary beam of Ar^+ ions will be directed at surface of the sample with energy ranging from 0.5 to 5 keV. This will sputter the atoms, ions, and molecular fragments from the surface for further analysis of the ions by a mass spectrometer. During the transient operation, a few tens of monolayers will be removed and recorded as per minute. This allows depth profiling. In contrast, during its steady-state operation, the rate of removal is on the order of on monolayer which recorded by hours, in fact, several hours, due to the low primary particle flux. This allows chemical mapping of the surface in a non-destructive analysis. SIMS's advantages include high sensitivity for light elements and the ability to produce and analyze fragments of molecules which are the representative of the parent surface reaction. On the other hand, its downsides include large variations in sensitivity with matrix composition, a 5-orders of magnitude variation in elemental sensitivity across the periodic table, and inhomogeneous of sample charging which makes the quantitative analysis very complicated or even impossible. In general, secondary ion yield in SIMS decreases when molecular weight of the element increases and ionization potential increases. The SIMS sensitivity is not useful when the mass range is high.

Secondary neutral mass spectroscopy (SNMS)

This technique is adapted from SIMS and designed to solve the previous problem. SNMS is designed to improve the sensitivity (to under ppt level) especially those with high mass range. SNMS can be assisted with laser-post ionization (LP), however, the technology is still expensive due to its initial stage of development [65].

High resolution electron energy loss spectroscopy (HREELS)

This involves dipole and impact scattering of low energy electrons by atoms or molecules adsorbed on the surface under high vacuum atmosphere [18,65]. The former exciting vibrations normal to the surface while the latter vibrations parallel to the surface. The extent of energy loss due to these vibrational excitations is represented by an energy spectrum of the scattered electrons. HREELS is able to detect energy losses over the full vibrational spectrum ranging from 800 to 4,000 cm^{-1}, with 0.8 cm^{-1} resolution approximately. This method is sensitive to sub-monolayer amounts of adsorbates possessing weak dynamic dipoles and has been utilized widely in study of adsorbed molecule's orientation.

Reflection adsorption infrared spectroscopy (RAIRS)

RAIRS when compared to HREELS is limited by a range of 1,000 to 3,000 cm^{-1}. This technique is used to study the molecules with large dynamic dipoles moments such as CO, NO and other gaseous compounds. However, its energy resolution of 0.5 cm^{-1} is better than that of the HREELS.

In situ method for catalyst characterization

1. *Infrared spectroscopy (IR)*

This was possible the first spectroscopy applied in catalysis science [18, 65] and yet still continues to be applied widely in catalytic surface studies nowadays. IR can be utilized to: (1) identify adsorbed species/intermediates, to observe their structures on the surface of well-dispersed catalysts; (2) provide information in terms of chemistry of the active sites during either preparation or reaction i.e. oxidation state, acidity, number of atoms aka site molecularity. The in situ spectra of supported catalysts can be obtained using a special flow cells under the operation temperature up to 500 °C and pressure of 1 to 2 atm. Apart from the IR, EELS and RS are the other kinds of vibrational spectroscopy. The vibrations in these techniques are excited by absorption and scattering of photons and scattering of electrons. For IR, the infrared radiation generally in the range of 4,000 to 400 cm^{-1}, which further utilized to excite molecular vibrations of stretching, bending in one plane, bending our of plane, and torsional. Normally, the vibrations of stretching are the highest frequency and most relevant to catalysis field of study. Species with polar bonds such as CO, NO and OH give strong IR bands, whereas the compounds with covalent bond such as those containing C-C, N=N, H_2 and N_2 will absorb IT either weakly or none; since absorption of an IR photon occurs only if a dipole moment changes during the vibrations. The IR region can be classified to 5 regions [18]:

i. The X-H stretch region (4,000 to 2,500 cm^{-1}) such as strong bands for OH, CH and SH.
ii. The triple bond region (2,500 to 2,000 cm^{-1}) for instance, gaseous CO and linearly adsorbed CO (2,200 to 2,000 cm^{-1}).
iii. The double-bond region (2,000 to 1,500 cm^{-1}) e.g. bridge-bonded CO, carbonyls (approximately 1,700 cm^{-1}).
iv. The fingerprint region (1,500 to 500 cm^{-1}) i.e. single bonds between C and N, O, S and halogens.
v. The metal-adsorbate region (450 to 200 cm^{-1}) for example, M-X where X is C, O and N.

IR can be divided to 3 sub-categories based on experimentation procedures: (1) transmission IR or FTIR to a thin wafer to a detector; (2) diffuse reflectance IR spectroscopy (DRIFTS) which involves reflectance of IR radiation from a powder to an ellipsoidal mirror, which will be collected after focused on the detector; (3) reflection IR from a flat metal surface.

2. ***Mossbauer spectroscopy (MAbS)***

   MAbS aka gamma-ray resonance spectroscopy [66,67] is known for its high sensitivity to measure chemical oxidation state, electronic and magnetic properties of atoms of a specific isotope on the surface or in the bulk of a solid. During the test, gamma radiation will be created and emitted from a radioactive source such as ^{57}Co which later undergoes nuclear decay to the excited state of the related Mossbauer atom such as ^{57}Fe. The gamma radiation can be absorbed by the nucleus in the same Mossbauer isotope in catalyst's absorber. The energy levels of absorbed nucleus in the catalyst will be altered by the chemical and magnetic environment of that atom such as oxidation state or ferromagnetism [1]. The energy of the absorbing atom has to capable/match with that of the emitting atom, in order to allow resonant absorption to occur. This specific condition can be created by modulation of energy of the source by the 'Doppler Effect' which is – the source will be accelerated via a range of velocities where one of these will match with the difference in energy between the source and absorber. Therefore, the spectra of MAbS are a plot between percentage of gamma rays absorbed and the velocity of the source.

   Some of the most outstanding insights that were previously achieved using MAbS are [66,68] include: (1) chemical phases in both surface and bulk are likely to be responsible for the catalytic performance of iron catalysts which were utilized in ammonia synthesis, Fischer-Tropsch synthesis, water gas shift (WGS) reaction, and selective catalytic reduction of NO; (2) surface and bulk chemistries of supported Pt-Fe, Pd-Fe and Pt-Ir-Fe alloys; (3) properties of surface and lattice of small metal and metal-oxide clusters in supported Fe and Co catalysts and their interactions with supports; (4) the chemistry of iron exchanged in various types of zeolites.

3. ***Nuclear magnetic resonance spectroscopy (NMR)***

   Nuclear particles (such as electrons) will undergo spin. The spinning of charged particles (such as protons) create a magnetic moment or dipole along the spin's axis. The nucleus can either have a net dipole (i.e. ^{1}H, ^{13}C, ^{27}Al and ^{29}Si or not have, depending on the number and alignment of its particle dipoles. If a nuclear dipole is placed in an external magnetic field, it would align with the field. However, if sufficient electromagnetic energy in the radio frequency (RF) range is provided, the dipole would change its orientation to a higher energy state aligning against the magnetic field. During the relaxation period of the applied RF energy, the excited nuclear spin state decays to the more stable (less excited) ground state, which re-emits RF radiation at the excitation frequency. Emission or absorption of the unique excitation energy constitutes the condition for nuclear magnetic resonance. For the practical procedure, a sample will be put inside a large homogeneous magnetic field where a broad-band pulsed RF field of a high frequency at a certain angle is applied. Nuclei in different environments will be excited and then de-excited, Afterwards the re-emitted RF signals will be detected by electromagnetic induction and Fourier transformed to give a graphical relationship between intensity and frequency. NMR can be applied to observe many catalytic phenomenon, for example: (1) bonding and mobility of adsorbed hydrogen species on noble metals; (2) structure of coke formation which could be responsible for catalyst's deactivation; (3) kinetics of exchange reactions between physicsorbed and chemisorbed species; (4) reactions of short-lived transition metal complexes on the catalytic oxides; (5) structures of the adsorbed species; (6) acidity of the materials and their structures; (7) identification of framework and no- framework aluminas in zeolites.

4. ***Electron spin resonance (ESR) or electron paramagnetic resonance (EPR)***
This method is usually used for measurement the types and concentrations of paramagnetic ions and radicals in solid catalysts, due to its high sensitivity for detection of unpaired electrons [69] which is acceptably assumed for all elements. These species compose of active sites or intermediates. Principle of ESR involves placing a solid sample (crystalline or powder) with its weight from 10 to 1,000 mg, into as cell inside an external magnetic field that splits the energy levels of the unpaired electrons. Resonance is a must to create, in the same way as in NMR. In this case, a microwave source of 9,000 MHz will be applied to the magnetic field which will be later swept away until the resonance condition for a change in electron spin is fulfilled, leading to absorption of energy. The resonance absorption will be measured using a crystal-magnetic T detector located in one of the 3 arms. Based on the theory of the Wheatstone bridge, a current variation will occur in crystal detector when the circuit balance is interrupted by the resonance in T-arm housing the sample. This offers an absorption plotted against field curve. Modulation of the magnetic field at low frequency (around 100 kHz) will result in an increase in the intensity of the absorption curve, gaining the distinctive derivative curve. The experimentation is normally carried out as in situ test in various atmosphere at relatively moderate to high temperatures. The resulting spectrum are collected generally at -193 to 27 °C. The catalytic characteristics that can be obtained via ESR are: adsorbed paramagnetic species, non-paramagnetic materials doped with paramagnetic materials, properties of surface using charge-transfer-surface complexes, properties of bulk by ionization of materials using UV radiation or

gamma ray and, paramagnetic transition metal ions within or at the surface of material.

5. ***Extended X-ray adsorption fine structure (EXAFS)***
   This sophisticated technique is used to clarify detailed local structures of solids and local structures of surface of mono-dispersed catalysts [1,18]. Photoelectrons will be firstly created during X-ray absorption which results in formation of fine structure as interference fringes in the X-ray absorption spectrum, when scattered by neighbor atoms. The frequency of EXAFS can refer to the inter-atomic distance between the absorbing and the neighboring atoms, while its amplitude can indicate the number, type and order of the neighboring atoms. When handled as an in situ operation, this technique can be very useful for giving information on the structure of coordination of atoms on the surface of a well-dispersed catalysts [18].
6. ***Ultraviolet-visible spectrometry (UV-VIS)***
   This method is used to study electronic structures and chemistries of the surface species, normally oxides. To start with, the visible and UV radiation, released from Tungsten and deuterium, reflected from the powdered sample will be collected by hemispherical mirrors and directed towards the detector. The absorption spectra are concerted from the reflectance data through a mathematical function where the absorption edges are estimated by comparing to the standards. The changes in the absorption edge of surface species can reveal the changes of surface concentrations, the size of cluster, thus, indicating charge transfer and oxidation state [70].

4.6 CATALYST SELECTION AND ITS CRITERIA

Despite various nature of each individual catalysts and its specific function, there are several main criteria in the catalyst selection that can be described in common which are; activity, selectivity, stability, mechanical strength and cost. Maximizing the catalyst's activity is crucial as it has a direct influence on the reactor sizing, thus, resulting in the reactor and process's cost. High selectivity is also desirable due to the high cost of separation. Stability and mechanical strength also play a role in the cost directly. Please see Figure 3.1 for the evolution of the catalyst selection and design.

Question 4.1
4.1.1 Summarize and give examples of physical and chemical characteristics of a catalyst, and how can they be measured correspondingly? 4.1.2 Can you classify; 4.1.2.1 Characterizations that require heavy machinery? 4.1.2.2 Characterizations that applied real-time or in situ? And what could be the advantages of the in situ characterizations?

4.7 SUMMARY AND PERSPECTIVES

This chapter includes details on catalyst's characterization. The characterization techniques can be performed by either transient or steady state experiment, in order to address physical or chemical characteristics of the catalysts. Physical properties such as surface area, pore size, particle size, mechanical strength and density can be achieved using BET method, XRD method and tapped packing density. These techniques can be standardized using international accepted ASTM standards. Similarly, chemical properties of the catalysts such as chemical composition, chemical structural and morphology, surface acidity and basicity, and surface reactivity can be investigated using XRF, or any other probe reactions, both transient and steady state experimentation. Catalyst's characterization helps researchers to select the best catalyst prior the experimental tests. Catalyst characterization is important for determining the catalyst's properties, therefore it can predict the catalyst performance towards an interest reaction or process.

REFERENCES

[1] C.H. Bartholomew, R.J. Farrauto, Fundamentals of industrial catalytic processes, AIChE, Wiley. (2006).

[2] J.C. Védrine, Metal oxides in heterogeneous oxidation catalysis: state of the art and challenges for a more sustainable world, ChemSusChem. 12 (2019) 577-588. https://doi.org/10.1002/cssc.201802248.

[3] ASTM D-3663-84, Standard test method (STM) for surface area of catalysts, 3-6 (1988).

[4] ASTM D-4567-86, STM for single point determination of specific surface area of catalysts using nitrogen adsorption by continuous flow method, 37-40 (1988).

[5] The micro report, Micromeritics Instrum. Corp. 14 (2003).

[6] J. Rouquerol, D. AVNIR, C.W. Fairbridge, D.H. Everett, J.H. Haynes, N. Pernicone, J.D.F. Ramsay, K.S.W. Sing, K.K. Unger, Recommendations for the characterization of porous solids (Technical Report), Pure Appl. Chem. 66 (1994) 1739-1758. https://doi.org/10.1351/pac199466081739.

[7] W.E. White, C.H. Bartholomew, W.C. Hecker, D.M. Smith, Changes in surface area, pore structure and density during formation of high-temperature chars from representative U.S. coals, Adsorpt. Sci. Technol. 7 (1990) 180-209. https://doi.org/10.1177/026361749000700401.

[8] O. Deutschmann, H. Knozinger, K.Kochloefl, T. Turek, Heterogeneous catalysis and solid catalysts, Wiley-VCH Verlag GmbH Co. KGaA, Weinheim. (2009). https://doi.org/10.1002/14356007.a05_313.

[9] ASTM D-4365-85, STM for determining zeolite area of a catalyst, 32-36 (1988).

[10] ASTM D-4284-83, STM for determining pore volume distribution of catalysts by mercury porosimetry, (1988).

[11] ASTM D-4513, STM for particle size distribution of catalytic materials by sieving, 71-72 (1988).

[12] ASTM D-4438-85, STM for particle size distribution of catalytic materials by electronic counting, 63-65 (1988).

[13] ASTM D-4464-85, STM for particle size distribution by laser light scattering ASTM D-4464-85, 66-67 (1988).

[14] G. Bergeret, P. Gallezot, Handbook of heterogeneous catalysis, Wiley-VCH Verlag GmbH & Co. KGaA, 1997.

[15] ASTM D-4179-82, STM for single pellet crush strength of formed catalyst spheres, 57-59 (1988).

[16] ASTM D-4058-87, STM for attrition and abrasion of catalysts and catalyst carriers, 53-54 (1988).

[17] ASTM D-4164-88, STM for tapping pack density of formed catalysts and catalyst carriers, 55-56 (1988).

[18] J.W. Niemantsverdriet, Spectroscopy in catalysis. New York: VCH., 1993.

[19] ASTM D-3610-83, STM for chemical analysis of Co, Mo/Al_2O_3 catalysts, (1988).

[20] ASTM D-4481-85, STM for chemical analysis of Ni/Al_2O_3 catalysts., (1988).

[21] ASTM D-4642-86, STM for chemical analysis of Pt/Al_2O_3 catalysts, (1988).

[22] P. Saychu, M. Thanasiriruk, C. Khajonvittayakul, R. Viratikul, V. Tongnan, M. Hartley, S. Wongsakulphasatch, N. Laosiripojana, U.W. Hartley, Catalytic performance of Na-Mn_2O_3-based catalysts towards oxidative coupling of methane, Catal. Today. 375 (2021) 225-233. https://doi.org/10.1016/j.cattod.2020.12.024.

[23] N. Ngoenthong, V. Tongnan, T. Sornchamni, Application of a micro-channel reactor for process intensification in high purity syngas production via, Int. J. Hydrogen Energy. (2019). https://doi.org/10.1016/j.ijhydene.2019.11.240.

[24] C. Wongsartsai, V. Tongnan, T. Sornchamni, N. Siri-nguan, N. Laosiripojana, M. Hartley, U.W. Hartley, CO_2 utilization via methanation using 40%Ni/$Ce_xCr_{1-x}O_2$ as a novel catalyst: a comparative study of packed-bed and micro-channel reactors, React. Kinet. Mech. Catal. 131 (2020) 101-117. https://doi.org/10.1007/s11144-020-01853-1.

[25] N. Ngoenthong, M. Hartley, T. Sornchamni, N. Siri-nguan, N. Laosiripojana, U.W. Hartley, Comparison of packed-bed and micro-channel reactors for hydrogen production via thermochemical cycles of water splitting in the presence of ceria-based catalysts, Processes. 7 (2019) 1-12. https://doi.org/10.3390/pr7100767.

[26] T. Li, T. Kamhangdatepon, B. Wang, U.W. Hartley, K. Li, New bio-inspired design for high-performance and highly robust $La_{0.6}Sr_{0.4}Co_{0.2}Fe_{0.8}O_{3-\delta}$ membranes for oxygen permeation, J. Memb. Sci. 578 (2019) 203-208. https://doi.org/10.1016/j.memsci.2019.02.042.

[27] V. Tongnan, T. Sornchamni, N. Laosiripojana, U.W. Hartley, Study of crystal growth and kinetic parameters of Zn/ZnO oxidation in the presence of H_2O and CO_2, React. Kinet. Mech. Catal. 125 (2018) 99-110. https://doi.org/10.1007/s11144-18-1411-3.

[28] T. Li, M.F. Rabuni, L. Kleiminger, B. Wang, G.H. Kelsall, U.W. Hartley, K. Li, A highly-robust solid oxide fuel cell (SOFC): Simultaneous greenhouse gas treatment and clean energy generation, Energy Environ. Sci. 9 (2016) 3682-3686. https://doi.org/10.1039/c6ee02562e.

[29] D.M. Bonnell, Scanning probe microscopy and electroscopy: Theory, techniques, and applications (2nd ed.), NY: Wiley-VCH, 2001.

[30] C.H. Bartholomew, H_2 chemisorption on supported noble metals and its use in determining metal dispersion, Catalysis Cambridge: Royal Society of Chemistry, 1994.

[31] ASTM D-3908-82, STM for hydrogen chemisorption on supported platinum on alumina catalysts by volumetric vacuum method, 13-16 (1988).

[32] D.J. O'Rear, D.G. Löffler, M. Boudart, Stoichiometry of the titration by dihydrogen of oxygen adsorbed on platinum, J. Catal. 121 (1990) 131-140. https://doi.org/10.1016/0021-9517(90)90223-7.

[33] J.E. Benson, M. Boudart, Hydrogen-oxygen titration method for the measurement of supported platinum surface areas, J. Catal. 4 (1965) 704-710. https://doi.org/10.1016/0021-9517(65)90271-X.

[34] R. D. Jones, C. H. Bartholomew, Improved flow technique for measurement of hydrogen chemisorption on metal catalysts, Appl. Catal. 39 (1988) 77-88. https://doi.org/10.1016/S0166-9834(00)80940-9.

[35] S.R. Sashital, J.B. Cohen, R.L. Burwell, J.B. Butt, Pt SiO_2. II. Characterization of the gel and the platinum particles by X-Ray diffraction, J. Catal. 50 (1977) 479-493. https://doi.org/10.1016/0021-9517(77)90060-4.

[36] U.W. Hartley, V. Tongnan, N. Laosiripojana, P. Kim-Lohsoontorn, K. Li, Nitrous oxide decomposition over $La_{0.3}Sr_{0.7}Co_{0.7}Fe_{0.3}O_{3-\delta}$ catalyst, React. Kinet. Mech. Catal. 125 (2018) 85-97. https://doi.org/10.1007/s11144-018-1398-9.

[37] P. Jacobs, The measurement of surface acidity, characterization of heterogeneous catalysis, Amsterdam: Marcel Dekker, 1984.

[38] ASTM D-4824-88, STM for determination of catalyst acidity by ammonia chemisorption, (1988).

[39] W.E. Farneth, R.J. Gorte, Methods for Characterizing Zeolite Acidity, Chem. Rev. 95 (1995) 615-635. https://doi.org/10.1021/cr00035a007.

[40] R.B. Michael, Infrared spectra of adsorbed molecules, Appl. Spectrosc. Rev. 1 (1968) 289-378. https://doi.org/10.1080/05704926808547587.

[41] A. Auroux, M. Muscas, D.J. Coster, J.J. Fripiat, Distribution of acid sites and differential heat of NH_3 chemisorption on some aluminas and zeolites, Catal. Letters. 28 (1994) 179-186. https://doi.org/10.1007/BF00806047.

[42] D. Coster, A.L. Blumenfeld, J.J. Fripiat, Lewis acid sites and surface aluminum in aluminas and zeolites: a high-resolution NMR study, J. Phys. Chem. 98 (1994) 6201-6211. https://doi.org/10.1021/j100075a024.

[43] D. Coster, A.L. Blumenfeld, J.J. Fripiat, Lewis acid sites and surface aluminum in aluminas and mordenites: an infrared study of co chemisorption, J. Phys. Chem. 98 (1994) 8549-8554. https://doi.org/10.1021/j100075a024.

[44] G.A.Somorjai, Chemistry in two dimensions : surfaces, Ithaca : Cornell University Press, 1981.

[45] G.A. Somorjai, Surface chemistry and catalysis, NY: Wiley interscience, 1994.

[46] C.H. Bartholomew, hydrogen adsorption on supported cobalt, iron, and nickel, Catal. Letters. 7 (1990) 27-52. https://doi.org/10.1190/1.9781560802440.ch1.

[47] R.J. Gorte, Design parameters for temperature programmed porous catalyst, J. Catal. 75 (1982) 164-174.

[48] J.S. Rieck, A.T. Bell, Studies of the interactions of H_2 and CO with silica- and lanthana-supported palladium, J. Catal. 96 (1985) 88-105. https://doi.org/10.1016/0021-9517(85)90363-X.

[49] J.S. Rieck, A.T. Bell, Studies of the interactions of H_2 and CO with Pd TiO_2 and TiO_2-promoted Pd SiO_2, J. Catal. 99 (1986) 262-277. https://doi.org/10.1016/0021-9517(86)90352-0.

[50] R.P. Underwood, A.T. Bell, Lanthana-promoted Rh SiO_2. I. studies of CO and H_2 adsorption and desorption, J. Catal. 109 (1988) 61-75. https://doi.org/10.1016/0021-9517(88)90185-6.

[51] J.W. Gues, Energetics of hydrogen adsorption on porous and supported metals, Hydrogen effects in catalysis, NY: Marcel Dekker, 1988.

[52] P.G. Menon, Hydrogen as a tool for characterization of catalyst surfaces by chemisorption, gas titration, and temperature programmed techniques, Hydrogen effects in catalysis, NY: Marcel Dekker, 1988.

[53] S.A. Stevenson, J.A. Dumesic, R.T.K. Baker, E. Ruckennstein, Metal-support interactions in catalysis, sintering and redispersion, NY: Van Nostrand Reinhold, 1987.

[54] G.B. Raupp, J.A. Dumesic, Effect of varying titania surface coverage on the chemisorptive behavior of nickel, J. Catal. 95 (1985) 587-601. https://doi.org/10.1016/0021-9517(85)90137-X.

[55] B.G. Johnson, P.J. Berlowitz, D. Wayne Goodman, C.H. Bartholomew, The structural and chemisorptive properties of ultrathin cobalt overlayers on W(110) and W(100), Surf. Sci. 217 (1989) 13-37. https://doi.org/10.1016/0039-6028(89)90532-3.

[56] P.G. Glugla, K.M. Bailey, J.L. Falconer, Activated formation of a HCO complex on Ni Al_2O_3 catalysts, J. Catal. 115 (1989) 24-33. https://doi.org/10.1016/0021-9517(89) 90004-3.

[57] B. Sen, J.L. Falconer, T.F. Mao, M. Yu, R.L. Flesner, Spillover of CO and H_2 onto Al_2O_3 surfaces, J. Catal. 126 (1990) 465-476. https://doi.org/10.1016/00219517(90)90013-A.

[58] J.G. McCarty, H. Wise, Hydrogenation of surface carbon on alumina-supported nickel, J. Catal. 57 (1979) 406-416. https://doi.org/10.1016/0021-9517(79)90007-1.

[59] S.A. Eliason, C.H. Bartholomew, Reaction and deactivation kinetics for Fischer-Tropsch synthesis on unpromoted and potassium-promoted iron catalysts, Appl. Catal. A Gen. 186 (1999) 229-243. https://doi.org/10.1016/S0926-860X(99)00146-5.

[60] S.M. Augustine, G.N. Alameddin, W.M.H. Sachtler, The effect of Re, S, and Cl on the deactivation of Pt γ-Al_2O_3 reforming catalysts, J. Catal. 115 (1989) 217-232. https://doi.org/10.1016/0021-9517(89)90020-1.

[61] T. Khamhangdatepon, V. Tongnan, M. Hartley, T. Sornchamni, N. Siri-Nguan, N. Laosiripojana, K. Li, U.W. Hartley, Mechanisms of synthesis gas production via thermochemical cycles over $La_{0\cdot3}Sr_{0\cdot7}Co_{0\cdot7}Fe_{0\cdot3}O_3$, Int. J. Hydrogen Energy. (2020). https://doi.org/10.1016/j.ijhydene.2019.12.148.

[62] U.W. Hartley, A. Ngoensawat, V. Tongnan, N. Laosiripojana, P. KimLohsoontorn, Effect of La and Gd substitution in $BaFeO_{3-\delta}$ perovskite structure on its catalytic performance for thermochemical water splitting.pdf, Catal. Commun. 135 (2020) 105901.

[63] C. Khajonvittayakul, V. Tongnan, T. Kangsadan, N. Laosiripojana, S. Jindasuwan, U.W. Hartley, Thermodynamic and mechanism study of syngas production via integration of nitrous oxide decomposition and methane partial oxidation in the presence of 10%NiO-$La_{0.3}Sr_{0.7}Co_{0.7}Fe_{0.3}O_{3-\delta}$, React. Kinet. Mech. Catal. 127 (2019) 839-855. https://doi.org/10.1007/s11144-019-01600-1.

[64] J.C. Vickerman, S. A.J, Secondary ion mass spectrometry – the surface mass spectrometry, in surface analysis: The principal techniques, Chichester: Wiley, 1997.

[65] P. M.J., W. F.C., Veryovkin I. V., Laser-point ionization for quantitative elemental analysis in TOF-SIMS: surface analysis by mass spectrometry, 2001.

[66] H. Topsøe, S. Mørup, Applications of mössbauer spectroscopy to surface science and catalysis, mössbauer spectroscopy applications 2, R. L. Cohe, Academic Press, New York, 1980.

[67] A.G. Maddock, Mossbauer spectroscopy: Principles and applications, Chichester: Horwood, 1997.

[68] A.J. Dumesic, Mössbauer spectroscopy applications to heterogeneous catalysis, Adv. Catal. 26 (1977) 121-246.

[69] J.C. Vedrine, Electron spin resonance, in characterization of heterogeneous catalysts, F. Delanna, New York, 1984.
[70] B.M. Weckhuysen, Snapshots of a working catalyst: Possibilities and limitations of in situ spectroscopy in the field of heterogeneous catalysis, Chem. Commun. 2 (2002) 97-110. https://doi.org/10.1039/b107686h.

ABBRIVIATIONS AND ACRONYM

XRD	*X-ray diffraction*
XRF	*X-ray fluorescent spectroscopy*
BET	*Brunauer, Emmett and Teller method*
SEM	*scanning electron microscopy*
TEM	*transmission electron microscopy*
XPS	*X-ray photoelectron spectroscopy*
FTIR	*Fourier transform infrared spectroscopy*
ICP	*inductive coupled plasma*
NMR	*nuclear magnetic resonance*
TG, TGA	*thermogravimetric analysis*
TPD	*temperature-programmed desorption*
TPR	*temperature-programmed reduction*
TPSR	*temperature-programmed surface reaction*
TKM	*transient kinetic method*
STEM	*scanning transmission electron microscopy*
UV-VIS	*ultraviolet-visible spectroscopy*
IR	*infrared spectroscopy*
AAS	*atomic absorption spectroscopy*
EDX	*energy dispersive X-ray spectroscopy*
FEM	*field emission microscopy*

EXAFS	*extended x-ray absorption fine structure*
ADS	*adsorption*
AFM	*atomic force microscopy*
AES	*Auger electron spectroscopy*
CAEM	*controlled-atmospheric electron microscopy*
CCSEM	*computer-controlled scanning electron microscopy*
EELS	*electron energy loss spectroscopy*
EPMA	*electron probe micro-analysis*
HREELS	*high-resolution electron energy loss spectroscopy*
IMP	*ion microprobe*
ISS	*ion scattering spectroscopy*
LEED	*low-energy electron diffraction*
LEIS	*low-energy ion scattering*
LMMS	*laser microprobe mass spectrometry*
MS	*magnetic susceptibility measurement*
MAbs	*mossbauer absorption spectroscopy*
MAS	*magic angle spinning*
MBS	*molecular beam scattering*
MES	*Mossbauer emission spectroscopy*
NS	*neutron scattering*
PIXE	*proton-induced x-ray emission*
RBS	*Rutherford backscattering*
SFG	*sum frequency generation spectroscopy*
SIMS	*secondary ion mass spectrometry*
SNMS	*secondary neutral mass spectroscopy*

STM	*scanning tunneling microscopy*
TOF-SIMS	*time of flight secondary ion mass spectrometry*
UPS	*ultraviolet photoelectron spectroscopy*
WDS	*wavelength dispersive spectroscopy*
ASTM	*American society for testing materials*
FCC	*fluid catalytic cracking*
EDS	*energy dispersive spectrometer*
TPO	*temperature-programmed oxidation*
HT	*hydrogen uptake in the titration*
GC	*gas chromatography*
TCD	*thermal conductivity detector*
TPS	*temperature-programmed sulfidation*
TDS	*thermal desorption spectroscopy*
LP	*laser-post organization*
RAIRS	*reflection adsorption infrared spectroscopy*
ESR	*electron spin resonance*
EPR	*electron paramagnetic resonance*
FT	*Fischer-Trosch synthesis*
WGS	*water gas shift reaction*
RF	*radio frequency*
OCM	*oxidative coupling of methane*
OSC	*oxygen storage capacity*
LSM/YSZ	*lanthanum-strontium/yttria-stabilized-zirconia*

CHAPTER 5
CATALYTIC APPLICATIONS OF METAL OXIDES

5.1 INTRODUCTION

Metal oxides have been utilized in either non-catalytic or catalytic applications widely during the development of mankind. Metal oxide's structures, components, preparation methods, characterizations have been also well observed all around the world. This chapter, the applications of metal oxides in energy technologies will be focused, due to the rapid demand of chemistry/petrochemical processes that have been increasing dramatically recently from sudden economic development.

Preparation methods of metal oxides and energy technologies

As previously mentioned in Chapter 3, metal oxides can be synthesized using several methods such as high-temperature solid-state (ceramic) method, hydrothermal method, templating method, sol-gel method, electro-deposition, chemical vapor deposition and the most popular method – the precipitation. Properties of the synthesized catalysts are different depending on the selected preparation method, and can be even tailor made to desire. Metal oxides are applied massively in energy technology due to its ability to generate charge carriers when the energy is applied [1]. Metal oxides are excellent as an electrode materials because they have a large variety of oxidation states, rendering for redox charge transfer. Ceria is one of the metal oxides that is outstanding for hydrocarbon reforming reactions due to its high resistance to coke deposition. Many metal oxides: such as spinels (e.g. $ZnAl_2O_4$ and $CuFe_2O_4$); perovskites (e.g. LSCF or $SrTiO_3$); transition metal oxides (TMO_x) where M is, for example, Mn, Cu, Co, Ti, Zr and Ce) and mixed metal oxides: will be described in this chapter. Figure 5.1 presented applications of metal oxides in energy technologies.

Energy generation

Metal oxides are one of the solutions to produce green energy to prevent environmental degrading worldwide. The applications of energy generation includes solar cells, fuel cells, thermoelectric generators, nuclear reactors, motion energy harvesting and combustion.

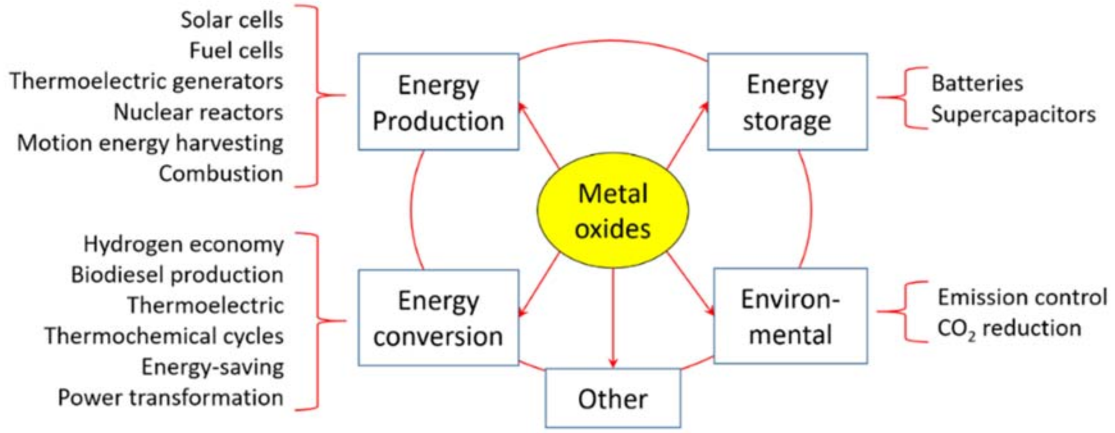

Figure 5.1: Schematic diagram presenting possible applications of metal oxides in energy technologies.

Energy storage

This field focuses on development of materials and technologies to store sustainable or renewable or clean energies. One of the promising materials in this area is nickel metal hydride battery, which was firstly developed in 1960s. This material has been utilized widely in battery development. Besides, lithium-ion battery will most likely to become the high potential energy storage device in the future, especially in electric vehicles (Evs). Post-lithium-ion batteries i.e. Na, K, Zn, Mg and Al-ion; have been also studied for this kind of application due to its natural abundant, low cost and environmental friendliness. Another application apart from batteries is the production of super-capacitors which was explored since 1970s. The super-capacitors have higher power density than rechargeable batteries and higher energy densities than conventional dielectric capacitors and longer life cycles.

Energy conversion

Metal oxides can be used for energy productions such as hydrogen, liquid fuels and bio-diesel. This technologies are beneficial for low carbon industry and sometimes called hydrogen economy, which is a part of Thailand 4.0 policy, based on BCG (Bio-circular-green economy) model. Thermochemical cycles, energy-saving smart windows, super-conductors in AC power transportation and transformation are considered a part of energy conversion technologies.

Energy and environment

The most popular metal oxide in this field is perhaps precious metal i.e. Pt and support such as TiO_2. CO_2 as a by-product of combustion of organic molecules is increasing lately up to 410 ppm which is the highest record so far. CO_2 has been captured and converted to more valuable chemicals using various metal oxides as catalysts. Metal oxides for energy and environment technologies include emission control and CO_2 reduction.

5.2 SOLAR-DRIVEN FUEL PRODUCTION BY METAL-OXIDE THERMOCHEMICAL CYCLES

Thermochemical cycles process is somehow similar to chemical-looping process where they rely on the redox properties of the metal oxides. While chemical looping focuses on combustion process, thermochemical cycles process is based on any redox reaction where the reduction and oxidation step of the oxygen carriers, in this case, metal oxides, occurred in series. This process allows conversion of CO_2 and/or H_2O to syngas or H_2 production. However, the reaction is strongly exothermic, thus, often the process will be proposed by associating with solar thermal technology. With the solar thermal technology, the process can be economy-feasible and environmentally friendly. The reaction temperature can be as high as 900 to 1,500 °C, during the reduction step, and slightly lower during the oxidation step, depending on the selected metal oxides. Thermochemical cycles assisted by nuclear heat source was firstly invented in 1960s [2]. During the reduction step, the oxygen in metal oxides will be released, activating the metal oxides to be readily active for the oxidation step. During the oxidation step, the oxygen from reactive gases will be taken onto the metal oxides lattice will be recycled back to its original form. Many redox pairs i.e. Fe_3O_4/FeO, Mn_3O_4/MnO, Co_3O_4/CoO, Nb_2O_5/NbO_2, In_2O_3/In, WO_3/W, CdO/Cd and ZnO/Zn had been researched during the last few decades [3-6]. Some recent materials such as SnO_2/SnO, CeO_2/Ce_2O_3, GeO_2/GeO and MgO/Mg has been studied [7]. Non-stoichiometric redox materials such as perovskites (e.g. $La_{0.3}Sr_{0.7}Co_{0.7}Fe_{0.3}O_{3-\delta}$ or $BaFeO_{3-\delta}$), CeO_{2-x} and CeO_{2-x}/ZrO_{2-y} are drawing attentions due to its phase stability [8-12].

5.2.1 REACTION PRINCIPLES OF THE TWO-STEP THERMOCHEMICAL CYCLES OVER METAL OXIDES

One of the good examples to explain thermochemical cycles is water splitting (WS) and/or CO_2 splitting (CDS). The two steps involve an endothermic reduction and an exothermic oxidation processes, occurred in series. During the reduction step, the metal oxides will be reduced by thermal or chemical process. The reduced materials will be re-oxidized, in this case by H_2O and CO_2, and recycling back to its original form. The solar thermal technology is usually applied for at least the reduction step, if not both reduction and oxidation.

Reduction step [12]:

$$M_xO_{y(s)} \rightarrow M_xO_{y-\delta(s)} + \frac{\delta}{2}O_{2(g)} \tag{5.1}$$

Where M is metal, O is oxygen and δ is the stoichiometric oxygen atom that is release per molecule. During this step, the active oxygen vacancies are created in the metal oxide's lattice. The gaseous oxygen is therefore released.

Oxidation step:

$$M_xO_{y-\delta(s)} + \delta CO_{2(g)} \rightarrow M_xO_{y(s)} + \delta CO_{(g)} \tag{5.2}$$

$$M_xO_{y-\delta(s)} + \delta H_2O_{(g)} \rightarrow M_xO_{y(s)} + \delta H_{2(g)} \tag{5.3}$$

Where equations (5.2) and (5.3) illustrate the metal oxides oxidation by CO_2 and H_2O, respectively. During these (separate or co-occurring) oxidation steps, CO_2 and H_2O are decomposed on the material's surface, giving syngas or pure hydrogen as product. The process is also considered a recycle process to re-generate the original form of the metal oxides. The overall process is shown as Figure 5.2. The suitable operating temperature depends on many factors such as type of metal oxides, oxygen partial pressure and the reducing gas. Right temperature of each step will maximize yield of the desire product. Some researchers chose to run both steps at the same temperature, in order to minimize time required for switching temperature between low and high [10,12]. The overall efficiency was reported at only 13-22% with temperature switching [13].

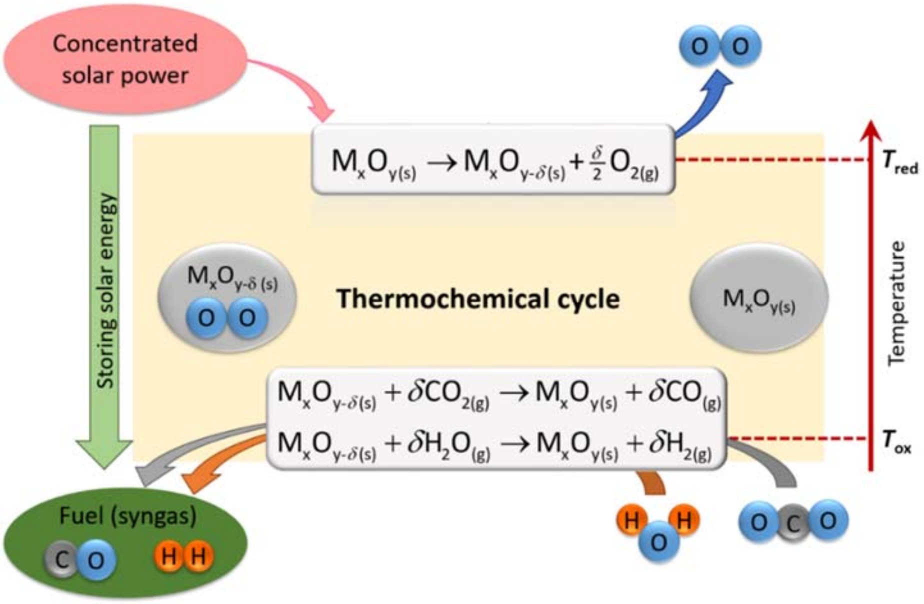

Figure 5.2: Metal oxide as an oxygen carrier applied in the thermochemical cycles of CO_2 and H_2O co-splitting [14].

Metal oxides for this application can be categorized into 2 main groups which are non-volatile and volatile materials. Volatile compounds are the materials that change phase e.g. ZnO/Zn, mainly gas-solid, during the redox reaction due to the loss of oxygen. Volatile materials generally have higher oxygen exchange capacity (O_2 release/uptake) than the non-volatile. Therefore, the fuel production of H_2 production can be more thermodynamically favorable because of the increased entropy which is generated by phase-changing. However, the volatile products have disadvantages. One of those is that the system requires quenching process where the gas phase materials will be condensed back into its original solid form. In addition, the separation could be quite complicated and expensive [15], yet the operation mode could be very limited to only fluidization, for example. On the other hand, the phase of non-volatile materials, e.g. Fe_3O_4/FeO, are not changing during the reaction. There are also 2 types of the non-volatile materials, the stoichiometric and non-stoichiometric materials. The stoichiometric materials will release/uptake oxygen where there no vacancy of the oxygen is left in the lattice, meaning that the molecular formula of the material is changed during the redox reaction e.g. Fe_3O_4/FeO. For the non-stoichiometric materials, the molecular formula of materials remain the same e.g. CeO_2/CeO_{2-x}, because the oxygen release/uptake occurs in the lattice level, leaving oxygen vacancies inside the material's crystallography. The stoichiometric materials normally offer higher yield of product per gram catalyst, however, they tend to not be as mechanically stable as the non-stoichiometric materials. Although the non-stoichiometric materials provide much lower yield of product in general. To increase the oxygen vacancies, which lead to the higher yield of product, the materials are usually doped with other metal oxides e.g. ZrO_2 or Cr_2O_3 [8-12]. Some of the materials can be problematic due to its melting point. For example, the optimal operating temperature of Fe_2O_3/Fe_3O_4 and Co_3O_4/CoO is higher than its melting point. In this case, sometimes (1) a use of reducing agent such as CH_4 or (2) the adjusted partial pressure of oxygen would be assisted, in order to lower the operating temperature. There are 2 commonly methods to lower oxygen partial pressure in the system: (1) sweep out the gaseous reactants/products by flowing an inert carrier gas through the system at the high flow rate and; (2) to run the reaction in a vacuum. These methods will increase the driving force between the oxygen in the solid materials and the oxygen in the gaseous bulk.

5.2.2 REACTION AND PROCESS DESIGNS

Various physical and chemical phenomena and the reaction parameters; i.e. thermodynamics, kinetics, phase change, transport phenomena, mechanical and thermal stability; highly influence selection of materials [16].

Reaction thermodynamics

When it comes to a design of reaction and reactor, the first issue that should probably be concerned is the thermodynamics. The thermodynamics phenomena of the reaction can be investigated based on equations (5.1), (5.2) and (5.3). The possible maximum efficiency (η_{max}) can be defined in terms of reduction temperature (T_{re}), oxidation temperature (T_{ox}) and thermolysis temperature (T_{th}). These temperatures are the temperature where $\Delta G^0 = 0$ (noted that $T_{ox} \geq 298\ \mathrm{K}$ and $T_{re} \leq T_{th}$) for the equation (5.1); the sum of equations (5.2) and (5.3); and the sum of equations (5.1), (5.2) and (5.3); respectively. The following equation describes η_{max} in terms of the mentioned temperatures:

$$\eta_{max} = \frac{[1-298/T_{th}]}{[1-T_{ox}/T_{th}]}\left[1-\frac{T_{ox}}{T_{re}}\right] \tag{5.4}$$

The thermodynamics of thermolysis and (line 3) and a hypothetical two-step thermochemical cycles (line 1 and 2) can be plotted as shown in Figure 5.3.

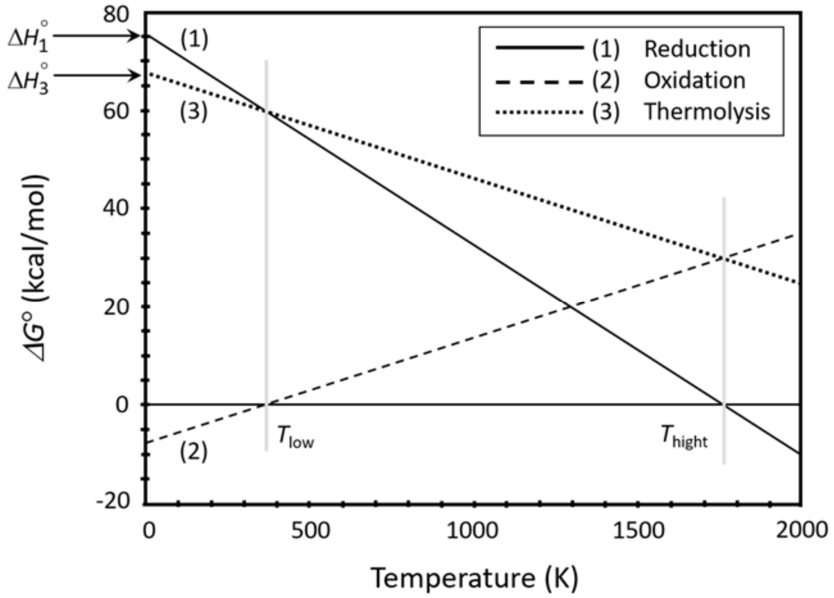

Figure 5.3: Simplified plot of the thermodynamics of CO_2/H_2O co-splitting via two-step thermochemical cycles process.

The thermodynamics of the net reaction can also be investigated using Gibbs free energy minimization method [9], considering each gaseous elementary reactions. For example, the elementary reactions of integration of nitrous oxide decomposition and syngas production in a membrane reactor are described as shown in Table 5.1. Table 5.2 illustrates the selected equations to estimate to changes of standard Gibbs free energy.

Table 5.1: The possible reactions in a membrane reactor [9].

Reaction	Reaction
Feed side	
$N_2O \rightleftharpoons N_2 + \frac{1}{2}O_2$	(1)
$N_2O + \frac{3}{2}O_2 \rightleftharpoons 2NO_2$	(2)
Membrane	
$ABO_{3-\delta} + \frac{\delta}{2}O_2 \rightleftharpoons ABO_{3,(s)}$	(3)
Permeate side	
$CH_4 + \frac{1}{2}O_2 \rightleftharpoons 2H_2 + CO$	(4)
$C_2H_6 + O_2 \rightleftharpoons 3H_2 + CO$	(5)
$C_3H_8 + \frac{3}{2}O_2 \rightleftharpoons 4H_2 + 3CO$	(6)
$C_2H_4 + O_2 \rightleftharpoons 2H_2 + 2CO$	(7)
$C_3H_6 + \frac{3}{2}O_2 \rightleftharpoons 3H_2 + 3CO$	(8)
$CH_4 \rightleftharpoons C_{(s)} + 2H_2$	(9)
$CO + \frac{1}{2}O_2 \rightleftharpoons CO_2$	(10)
$H_2 + \frac{1}{2}O_2 \rightleftharpoons H_2O$	(11)

*non-subscripted compound are in gas phase.

Table 5.2: Equations for calculation of the changes of the standard Gibbs free energy [9]**.**

Equation	**Reaction**
$Cp^\circ = A + BT + CT^2 + DT^3 + ET^4$	(12)
$\Delta_r H^\circ = \Delta_r H_0^\circ + \int_{T_0}^{T} \Delta Cp^\circ dT$	(13)
$\Delta_r H^\circ = \Delta_r H_0^\circ + \left[\begin{array}{c} \Delta A(T - T_0) + \frac{\Delta B}{2}(T^2 - T_0^2) + \frac{\Delta C}{3}(T^3 - T_0^3) \\ + \frac{\Delta D}{4}(T^4 - T_0^4) + \frac{\Delta E}{5}(T^5 - T_0^5) \end{array} \right]$	(14)
$\Delta_r S^\circ = \Delta_r S_0^\circ + \int_{T_0}^{T} \frac{\Delta Cp^\circ}{T} dT$	(15)
$\Delta_r S^\circ = \Delta_r S_0^\circ + \left[\begin{array}{c} \Delta A \cdot ln\left(\frac{T}{T_0}\right) + \Delta B(T - T_0) + \frac{\Delta C}{2}(T^2 - T_0^2) \\ + \frac{\Delta D}{3}(T^3 - T_0^3) + \frac{\Delta E}{4}(T^4 - T_0^4) \end{array} \right]$	(16)
$\Delta_r S^\circ = \frac{\Delta_r H_0^\circ - \Delta_r G_0^\circ}{T_0}$	(17)
$\Delta Cp^\circ = \sum_i \gamma_i \, (Cp^\circ)$	(18)
$\Delta_r H_0^\circ = \sum_i \gamma_i \left(\Delta_f H_0^\circ\right)$	(19)
$\Delta_r G_0^\circ = \sum_i \gamma_i \left(\Delta_f G_0^\circ\right)_i$	(20)
$\Delta_r G^\circ = \Delta_r H^\circ - T \cdot \Delta_r S^\circ$	(21)

The calculation can be done using computational programme i.e. Aspen Plus. The chemical equilibrium and effect of operating temperature towards such reaction can be therefore estimated. In this case, the changes in standard Gibbs free energy of each reactions were plotted during temperature varying from 500 to 1,000 °C, as shown in

Figure 5.4 [9]. The thermodynamic study helps investigation if one certain reaction can occur or not. In this case, it showed that the NO_2 formation is not theoretically possible to occur at temperature higher than 700 °C, where the combustion of methane will be noticed during 500 to 600 °C (reaction 4, 10 and 11). Coke formation will be occurred at temperature higher than 700 °C.

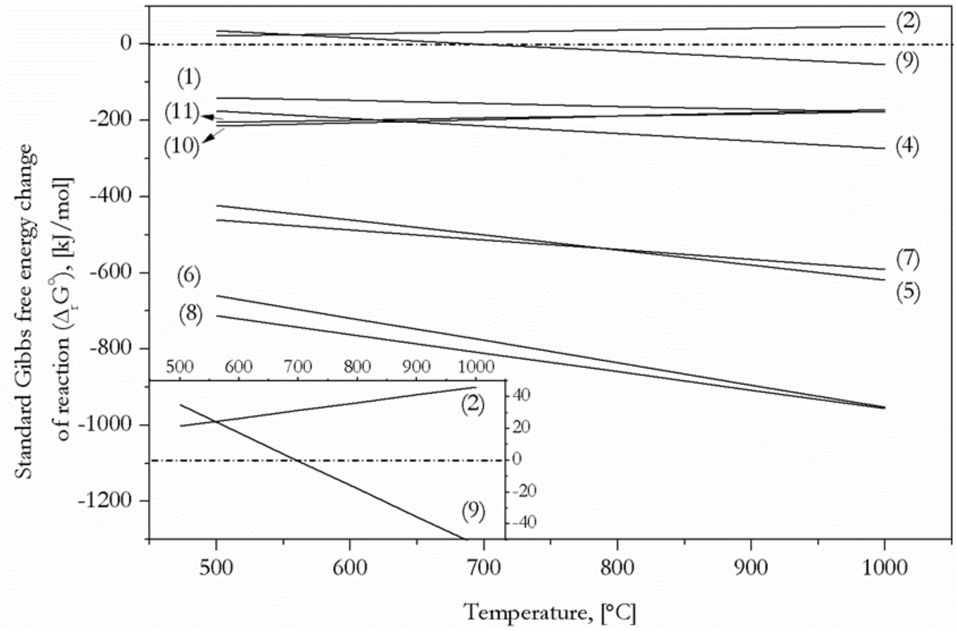

Figure 5.4: Changes in standard Gibbs free energy of each reactions [9].

Vaporization losses

Often, the metal oxides will be run under high operating temperature, sometimes even higher than their melting point, bubble point or decomposition temperature. Vaporization of the material will of course reduce its lifespan, causing an increase in capital investment, maintenance, and operational cost. Besides, the condensation of the vaporized material can lead to equipment failure too. An upper limit to the rate of mass loss (M_e) can be calculated using Langmuir sublimation model if the vapor pressure (P, Torr) and molecular weight (MW) of the evaporating material are known at a certain temperature. The mass loss can be estimated using the below equation.

$$M_e = 5.85 \times 10^2 P \left(\frac{MW}{T}\right) \frac{g}{cm^2 S} \qquad (5.5)$$

This model is based on the assumptions of non-equilibrium evaporation-condensation, meaning that the evaporation occurs in vacuum. Mass loss of the vaporizable materials can be minimized at the cost of lower yield, resulted from the lower operating temperatures.

Microstructural stability

Dense form of morphologies is generally desired when it comes to implementation for thermochemical cycles, perhaps for both structural and chemical reasons. For example, if the reaction kinetics are limited by surface or interfacial area, the meso- or microporous materials could be one of the solutions to obtain sufficient rates. On the other hand, if the kinetics rate is limited by bulk diffusion, the process may require a microstructure in which its grain size is small enough, thus, the diffusion rate becomes relatively fast. The working materials or the active species are often supported on the mechanically stronger materials, in increase the overall material's strength. Sintering from high operating temperature and interfacial degradation of the materials are normally taken to consideration [17].

Reaction kinetics

Reaction kinetics is often studied to identify the extent of reaction and efficiency. Kinetics can predict how fast the reaction occurs, leading to the time requirement for temperature switching between the reduction and oxidation step. Yet, it can optimize the concentration of the reactants, operating temperature, ratio of feed and other important parameters [12]. Reaction kinetics can be used for reactor design too. For example, a microchannel reactor has been applied for the thermochemical cycles of CO_2/H_2O co-splitting for intensifying the previous process which used a bulky packed-bed reactor [11]. The Arrhenius plot can be achieved via experimentations. Figure 5.5 presented Arrhenius plots of H_2 and CO production at different operating temperatures.

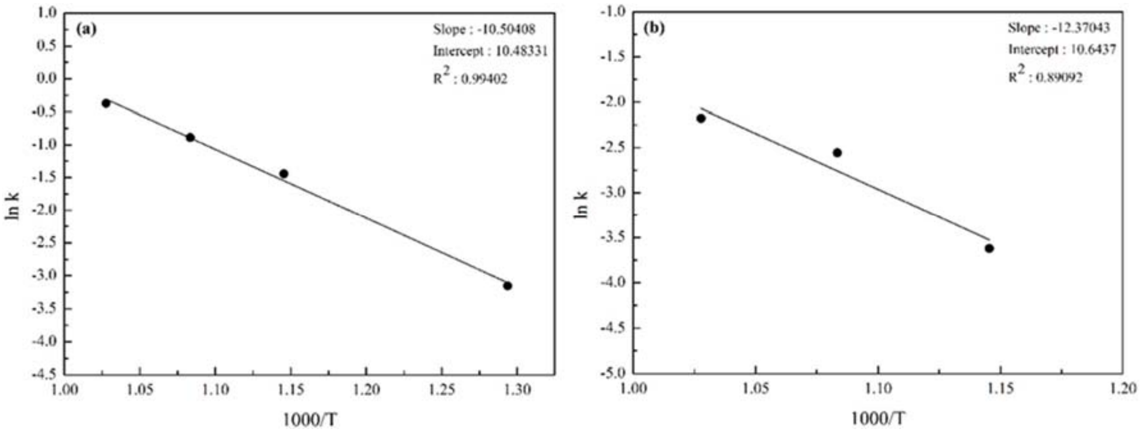

Figure 5.5: Arrhenius plots for H_2 (a); and CO (b); production in the presence of LSCF ($La_{0.3}Sr_{0.7}Co_{0.7}Fe_{0.3}O_3$), at operating temperature of 500, 600, 650 and 700 °C [11].

The kinetics study allows researchers to compare which type of reactor is more desirable by considering the activation energy (E_a) and pre-exponential factor (k_0). From this example, the E_a and k_0 of H_2 production was reported at 87.33 kJ/mol and 595.24 s^{-1}, respectively, whereas those of CO production was calculated at 102.85 kJ/mol and 698.79 s^{-1}, respectively [11]. Transport phenomena is very important when it comes to kinetics study. To be able to achieve the intrinsic kinetic rate, the system needs to be free of transport limitation.

5.2.3 METAL OXIDES FOR TWO-STEP THERMOCHEMICAL METAL-OXIDE CYCLES

5.2.3.1 SYNTHESIS AND CHARACTERIZATION OF METAL-OXIDE MATERIALS

Physical and chemical characteristics of the materials play a big part in catalytic performance towards the thermochemical cycles. The challenge is not only about to prepare the materials with high surface area, high porosity or high redox capability, but also about being tolerance such ultra-high operating temperature and severe condition change i.e. switching temperatures between reduction and oxidation step.

5.2.3.2 MATERIALS

ZnO

ZnO is one of the first materials to be utilized in chemical looping since 1970s, then further applied in thermochemical cycles. ZnO is volatile under the reaction condition, thus, the process needs quenching process which is more complicated in terms of separation and also more expensive. ZnO however is advantaged in high oxygen exchange capacity (compared to the non-volatile materials), non-precious and high energy content per mass [6,18]. The reduction and oxidation step of H_2O/CO_2 splitting in the presence of ZnO/Zn are presented as shown below.

Thermal reduction of ZnO:

$$\mathrm{ZnO_{s(s)}} \rightarrow \mathrm{Zn_{(g)}} + \frac{1}{2}\mathrm{O_{2(g)}}; \qquad \text{where } T > 1727\ °\text{C};\ \Delta H = 456 \text{ kJ/mol} \quad (5.6)$$

Oxidation of Zn by H_2O and CO_2, respectively:

$$\mathrm{Zn_{(g)}} + \mathrm{H_2O_{(g)}} \rightarrow \mathrm{ZnO_{s(s)}} + \mathrm{H_{2(g)}}; \quad \text{where } T < 1027\ °\text{C};\ \Delta H = -104 \text{ kJ/mol} \quad (5.7)$$

$$\mathrm{Zn_{(g)}} + \mathrm{CO_{2(g)}} \rightarrow \mathrm{ZnO_{s(s)}} + \mathrm{CO_{(g)}}; \quad \text{where } T < 1027\ °\text{C};\ \Delta H = -67 \text{ kJ/mol} \quad (5.8)$$

During the reduction process, one of the most challenging part is to quench the product mixture to avoid recombination. The quenching efficiency depends on the dilution ratio between $Zn_{(g)}$ in an inert gas and to the temperature of the surface where the quenching takes place. Therefore, the inlet of the oxidation step chamber is likely to be always containing a substantial amount of ZnO, varying from 6 to 85%mol. During the lab-scaled oxidation step, a flow of steam will be introduced and bubbling through the molten Zn at temperature around 450 to 500 °C [19]. Usually ZnO will be added into the Zn system, to avoid sintering and allow complete recovery of ZnO particles for recycling to the reduction step.

Ferrites

The redox pair of Fe_3O_4/FeO can be reacted with H_2O in a process of water splitting. The reactions are shown below:

$$\mathrm{Fe_3O_4} \rightarrow \mathrm{3FeO} + \frac{1}{2}\mathrm{O_2} \tag{5.9}$$

$$\mathrm{H_2O} + \mathrm{3FeO} \rightarrow \mathrm{Fe_3O_4} + \mathrm{H_2} \tag{5.10}$$

Thermal reduction of magnetite (Fe_3O_4) to wustite (FeO) generally occurs at temperature higher than 2227 °C, which is higher than the melting point of magnetite at 1535 °C and wustite at 1370 °C. This results in a liquid Fe_3O_4 and FeO phase, causing a rapid decrease of the iron oxide surface area and a deactivation of the material. To achieve lower operating temperature, one of the inexpensive solution is to add metal substitute into the ferrite redox pair system. The metals can be either transition metals or alkaline earth metals i.e. Mn, Co, Ni, Zn. In addition, another problem of the ferrite system is sintering and melting. The particle size of the materials will be then increased as a result, after a few cycles of operation. This leads to a lower product yield eventually. To improve such problem, the ferrites can be stabilized by mixing with an inert material such as YSZ (Yttria-stabilized-zirconia). After being stabilized, the reduce phase Fe^{2+} will be dissolved in YSZ lattice, avoiding the melting.

Hercynites

Another spinel structural material, that is beneficial for thermochemical cycles process, apart from ferrite is the hercynites which are the doped aluminum spinels of $(\mathrm{A_xB_{1-x}})^{+2}\mathrm{Al_2^{+3}O_4}$with cations A and B being Fe and/or Cu. This will allow combination of great redox capability from iron oxides and high thermal stability from aluminum oxides. The hercynites can be synthesized from a reaction between $CoFe_2O_4$ and Al_2O_3 (where the ferrite was deposited on the Al_2O_3 support), at high temperature during the experiments [20].

Ceria

Ceria can be considered either stoichiometric reducible material or non-stoichiometric reducible material. In 2006, a stoichiometric CeO_2/Ce_2O_3 redox pair was first demonstrated in a solar reactor under 100 to 200 mbar at 2000 °C, where the CeO_2 is already in a molten state [21]. Similarly, the non-stoichiometric CeO_2/CeO_{2-x} was later proposed as it does not require such ultra-high reduction temperature, although the oxygen exchange capacity is relatively less [22]. Ceria generally has fluorite structure for a wide range of oxygen stoichiometry, ranging from $x = 0$ to 0.24 at temperature of 1500 °C. The oxygen vacancies can be formed and the oxygen atom transportation can be promoted throughout the material. Ceria has relatively high melting point, compared to other materials, thus the sintering is not a concern for ceria. Addition of other metal oxide into the ceria system is therefore not for avoiding sintering, but mostly to enhance the oxygen vacancies. The thermodynamics and kinetics properties of ceria can be adjusted by adding its fluorite structure with other alkaline earth metal or transition metal and lanthanide oxides such as; Ca, Sr, Li for 2+ dopants; Sm, Gd, Y, Cr, Pt, La, Sc for 3+ dopants; and Zr and Hf for 4+ dopants [23]. The addition of 2+ and 3+ dopants will establish stable intrinsic oxygen vacancies, leading to an increase in electronic mobility within the ceria lattice [24-26]. The addition of intrinsic vacancies results in higher oxygen diffusion coefficients compared to pure ceria, due to the fact that diffusion of oxygen in ceria occurs via ambipolar diffusion of both electrons and ions [27]. Besides, the introduction of La^{3+} was reported to improve the thermal stability upon repetitive cycling [28]. However, the addition of +2 and +3 dopants have not been proven to improve the reduction extents, thus no thermodynamics benefit, compared to the un-doped ceria under the same condition [29,30]. On the other hand, +4 dopants such as Zr4+ and Hf4+ was reported to enhance the reduction extents. With the addition of +4 dopants, the reducibility of Ce4+ was shown to increase, due to a decrease in the partial oxygen molar enthalpy. However, the oxidation of Zr-doped catalyst system was observed to be more difficult, compare to the un-doped. Thus, this evidence could be either the cause of thermodynamic phenomenon or kinetic limitation [31]. Study of entropy change (ΔS_{re}) study revealed that the doping shifts entropy to a more negative value at a certain composition for some dopants, i.e. lanthanide and alkaline earth, because the number of reducible oxygen atoms decreases as the result of vacancy creation. However, the addition of Zr into ceria-based catalyst was found to increase the overall reducibility from 585 to 1,700 $\mu mol/g_{cat}$ [10]. Two types of reactors, which are microchannel reactor and packed-bed reactor, were also compared in this work. The microchannel reactor was found to have the better performance compared to the packed-bed reactor. However, $Ce_{0.75}Zr_{0.25}O_2$ showed the better catalytic performance than CeO_2 in both type of reactors [10]. Figure 5.6 illustrate reducibility of both catalysts using TPR (temperature-programmed reduction) technique, whereas and H_2 productivity of the catalysts in packed-bed and microchannel reactors are shown as Figures 5.7 and 5.8.

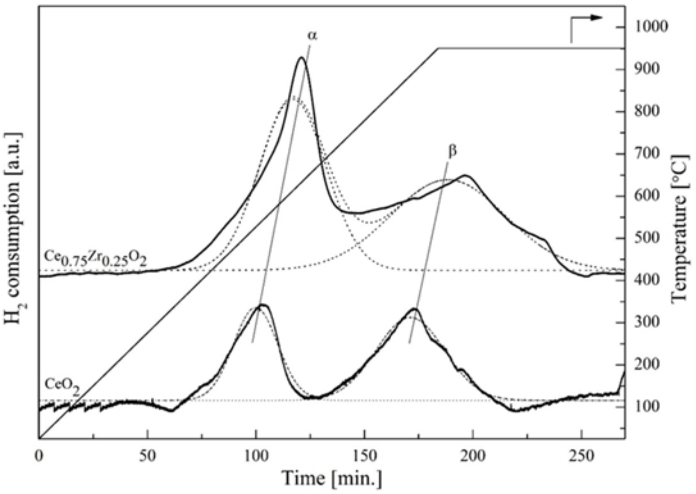

Figure 5.6: Reducibility of pure CeO_2 and CeO_2/ZrO_2 (3:1) via TPR [10].

The first peaks (α) of the 2 catalysts were due to the surface reduction, seen at around 300 °C, whereas the second peaks (β), noticed at 650 °C, were reported to be the result of bulk reduction.

The degree of reduction was calculated and tabulated as shown in Table 5.3.

Table 5.3: Reducibility of CeO_2 and CeO_2/ZrO_2 (3:1) reported in OSC and %reduction [10].

Catalysts	**Peak α**			**Peak β**			**Total**	**Total %**
	T_{red} (˚C)	**OSC (µmol/g)**	**%reduction (δ)**	**T_{red} (˚C)**	**OSC (µmol/g)**	**%reduction (δ)**	**OSC (µmol/g)**	**reduction (δ)**
$CeO_{2-\delta}$	545	585	9.34% (δ=0.046)	900	915	14.64% (δ=0.074)	1500	23.98% (δ=0.12)
CeO_2/ZrO_2 (3:1)	680	1700	547.40% (δ=0.272)	950	1390	44346% (δ=0.222)	3090	98.86% (δ=0.49)

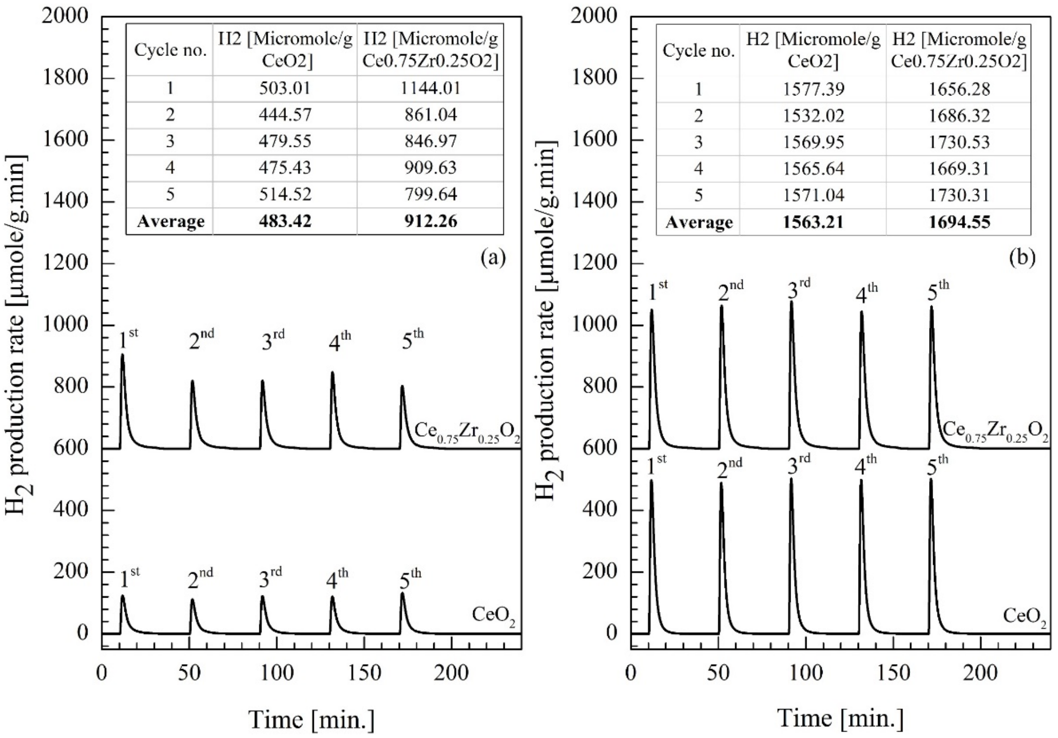

(a)

Cycle no.	H2 [Micromole/g CeO2]	H2 [Micromole/g Ce0.75Zr0.25O2]
1	503.01	1144.01
2	444.57	861.04
3	479.55	846.97
4	475.43	909.63
5	514.52	799.64
Average	**483.42**	**912.26**

(b)

Cycle no.	H2 [Micromole/g CeO2]	H2 [Micromole/g Ce0.75Zr0.25O2]
1	1577.39	1656.28
2	1532.02	1686.32
3	1569.95	1730.53
4	1565.64	1669.31
5	1571.04	1730.31
Average	**1563.21**	**1694.55**

Figure 5.7: H_2 productivity over CeO_2 and $Ce_{0.75}Zr_{0.25}O_2$ in a packed-bed reactor, at the same reduction/oxidation temperature a) 700/700 °C and b) 900/900 °C [10].

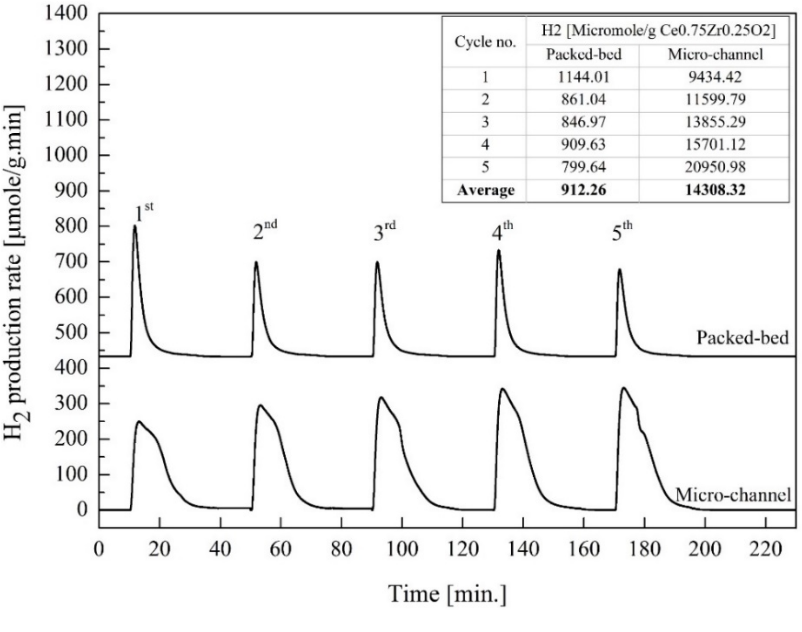

Cycle no.	H2 [Micromole/g Ce0.75Zr0.25O2]	
	Packed-bed	Micro-channel
1	1144.01	9434.42
2	861.04	11599.79
3	846.97	13855.29
4	909.63	15701.12
5	799.64	20950.98
Average	**912.26**	**14308.32**

Figure 5.8: Comparison of H_2 productivity over $Ce_{0.75}Zr_{0.25}O_2$ received from the microchannel reactor and the packed-bed reactor at reduction/oxidation temperature at 700/700 °C [10].

In conclusion, the addition of Zr in the ceria-based material was reported to increase the catalytic performance of the thermochemical cycles of water splitting, due to its increased oxygen storage capacity (OSC). Effective radius of the cations are an important factor to define the oxygen mobility in the lattice. In this case, the substitution of Zr^{4+} (smaller ionic radius of 0.84 Å) into Ce^{4+} (larger ionic radius of 0.97 Å) created a smaller unit cell volume and larger channel radius in the lattice, while the material's structure was remained fluorite as desired [10]. Since the smaller cell volume requires less energy for oxygen ions to mobile, therefore the active oxygen could migrated from one vacancy to another throughout the lattice via the radius channel.

Perovskites

Perovskites are a type of mixed metal oxides that have general molecular formula as $ABO_{3-\delta}$, where A and B can be substituted by other dopants, i.e. A´ and B´. The number of potential material configurations is therefore larger than the ceria-based materials. From thermodynamic analysis, LSM perovskites ($La_{1+x}Sr_xMnO_{3-\delta}$) was found to have higher oxygen exchange capacity compared to pure ceria [13]. Its reducibility of the material was shown to be around 2 times higher than ceria, however, the oxidation step was thermodynamically less favorable, leading to an incomplete oxidation but still more than ceria can offer [32]. LSCF ($La_{0.3}Sr_{0.7}Co_{0.7}Fe_{0.3}O_3$) was utilized in syngas production process via thermochemical cycles of H_2O/CO_2 co-splitting [12]. LSCF was reported to possess a pure cubic structure where 110 and 100 plane diffractions were active for CO_2 splitting, while 111 was more favored by H_2O splitting. OSC of LSCF was estimated at 4,072 µmol/g_{cat} using TPR as shown in Figure 5.9.

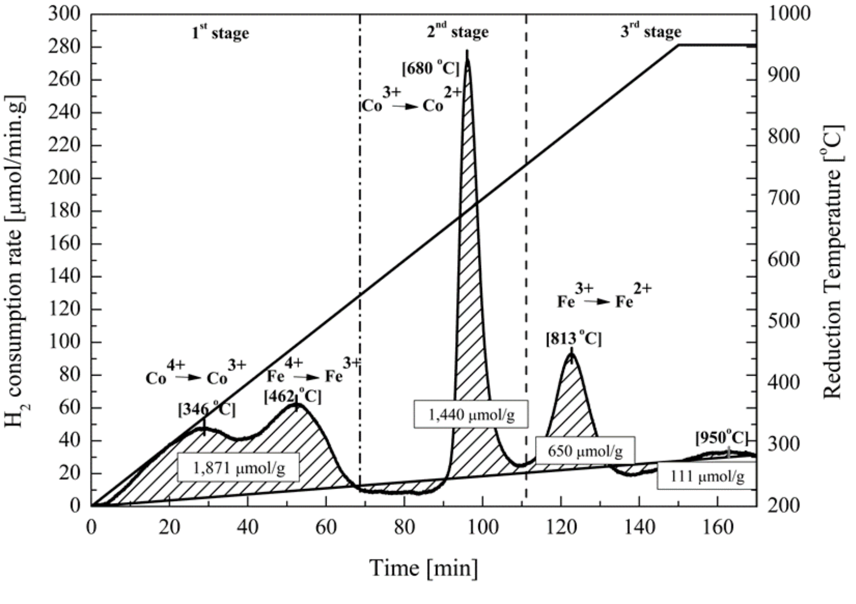

Figure 5.9: Rate of H_2 consumption and oxygen released, in the presence of LSCF [12].

Surface reaction:

$$2\dot{O}H_{o(s)} + 2LSC'''F_{LSCF(s)} \leftrightarrow 2O^{\times}_{O(s)} + 2LSCF^{\times}_{LSCF(s)} + H_{2(g)} \tag{5.12}$$

$$2\dot{O}H_{o(s)} + 2LSCF'''_{LSCF(s)} \leftrightarrow 2O^{\times}_{O(s)} + 2LSCF''''_{LSCF(s)} + H_{2(g)} \tag{5.13}$$

$$2\dot{O}H_{o(s)} + 2LSC''F_{LSCF(s)} \leftrightarrow 2O^{\times}_{O(s)} + 2LSC'''F_{LSCF(s)} + H_{2(g)} \tag{5.14}$$

$$2\dot{O}H_{o(s)} + 2LSCF''_{LSCF(s)} \leftrightarrow 2O^{\times}_{O(s)} + 2LSCF'''_{LSCF(s)} + H_{2(g)} \tag{5.15}$$

Where $LSCF^{\times}_{LSCF}$ denotes the regular LSCF, $LSC'''F_{LSCF(s)}$ is a polaron cation if Co^{3+}, $LSCF'''_{LSCF(s)}$ is a polaron cation of Fe^{3+}, $LSC''F_{LSCF(s)}$ is a localized electron of Co^{2+}, and $LSCF''_{LSCF(s)}$ is a localized electron of Fe^{2+}. During the H_2O splitting. A hydroxyl ion group is able to incorporate with the excited localized (Co^{+2}, Fe^{+2}) electrons of LSCF to form gaseous hydrogen and revert to extra proton for B-site cation to be a regular (Co^{+3}, Fe^{+3}) cation and return the available active site on the surface. The H_2O splitting pathways were showed on Figure 5.10.

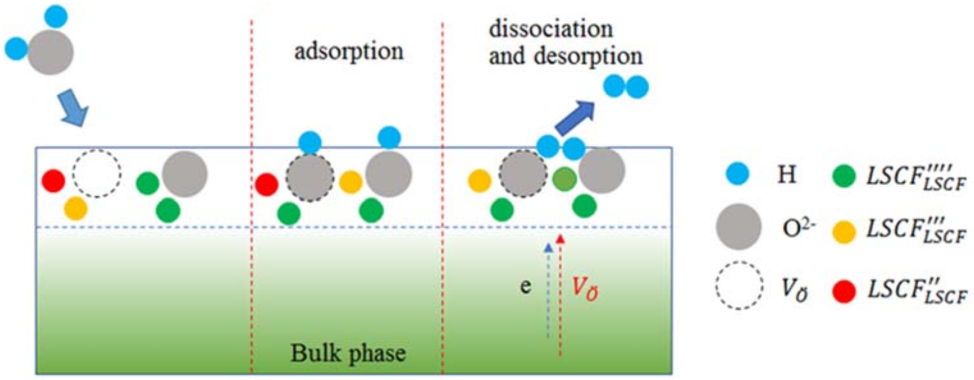

Figure 5.10: Schematics of H_2O splitting possible pathways [12].

Carbon dioxide splitting mechanism was also predicted as shown below:

Adsorption of CO_2 species:

$$CO_{2(g)} + V_{ö(s)} + O^{\times}_{o(s)} \leftrightarrow (CO)_{ö(s)} \tag{5.16}$$

Thus, the surface reactions were proposed:

$$(CO_3)_{ö(s)} + 2LSC''F_{LSCF(s)} \leftrightarrow 2O^{\times}_{O(s)} + 2LSC'''F_{LSCF(s)} + CO_{(g)} \tag{5.17}$$

$$(CO_3)_{ö\,(s)} + 2LSCF''_{LSCF(s)} \leftrightarrow 2O^{\times}_{O(s)} + 2LSCF'''_{LSCF(s)} + CO_{(g)} \tag{5.18}$$

Where $(\mathrm{CO}_3)_{\ddot{o}\,(s)}$ is an adsorbed carbonyl ion group, which would be reacted further during the surface reaction step, shown in Figure 5.11. In addition, 110 and 100 plane diffractions were found to be active for CO_2 splitting, while 111 plane diffraction was more favoured by H_2O splitting. Besides, the carbonyl ion was believed to be competing with hydroxyl ion during the surface adsorption process on localized Co^{2+}, Fe^{2+} of the LSCF.

Carbon dioxide adsorption:

$$\mathrm{CO}_{2(g)} + 2\mathrm{LSC}'''\mathrm{F}_{\mathrm{LSCF}(s)} + \mathrm{V}_{\ddot{o}(s)} + \mathrm{O}^{\times}_{o(s)} \leftrightarrow 2\mathrm{LSCF}^{\times}_{\mathrm{LSCF}(s)} + (\mathrm{CO}_3)_{\ddot{o}(s)} \quad (5.19)$$

$$\mathrm{CO}_{2(g)} + 2\mathrm{LSCF}'''_{\mathrm{LSCF}(s)} + \mathrm{V}_{\ddot{o}(s)} + \mathrm{O}^{\times}_{o(s)} \leftrightarrow 2\mathrm{LSCF}^{\times}_{\mathrm{LSCF}(s)} + (\mathrm{CO}_3)_{\ddot{o}(s)} \quad (5.20)$$

Equations (5.19) and (5.20) expressed the mechanism pathway of surface CO_2, also illustrated in Figure 5.11. CO_2 molecules diffused from the bulk steam to the available active site on the surface of LSCF and incorporate with the lowest stage of polaron cation (Co^{3+}, Fe^{3+}) with O^{2-} ion. The carbonyl ion (CO_3^{2-}) was generated and adsorbed on the surface, blocking the surface to react with H_2O and CO_2. The proposed mechanism was well agreed with other works, reporting that high amount of alkaline earth metals (such as Ba or Sr), as an A site substitution in perovskite (ABO_3), tended to incorporate with carbonyl ions, creating a layer of such compound and covering the surface of the perovskite. In conclusion, the CO_2 adsorption could poison the catalyst and lower the productivity of syngas.

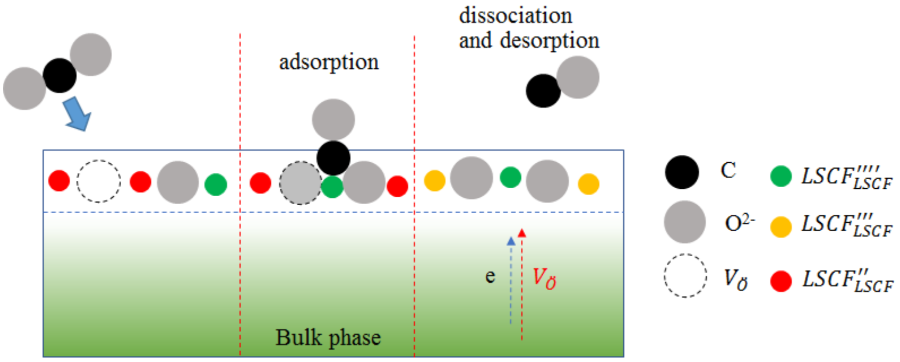

Figure 5.11: Schematics of CO_2 splitting possible pathways [12].

The LSCF was also applied in the same reaction, although the study focused on process intensification using a microchannel reactor [11]. The OSC of LSCF was determined at 4,465 $\mu mol/g_{cat}$ which is slightly higher than one used previously in the packed-bed study, at 4,072 $\mu mol/g_{cat}$ [12]. This could be due to the influence of mass and/or heat transfer limitation occurring in the testing system. Temperature-programmed surface reaction (TPSR) was performed for both H_2O splitting and CO_2 splitting to investigate the catalytic behavior of LSCF. The surface hydroxyl group was suggested to be the cause of H_2O splitting. This work also studied the reaction at the same reduction and oxidation temperature. It was found that the optimal temperature was 700 °C, giving 2,266 μmol/g_{cat} of H_2, 705 μmol/g_{cat} of CO and 67% of solid conversion [11]. The activation energy (E_a) and pre-exponential factor (k_0) of H_2O splitting were reported at 87.33 kJ/mol and 595.24 s^{-1}, respectively. Those of the CO_2 splitting were estimated at 102.85 kJ/mol and 698.79 s^{-1}, respectively [11]. Figures 5.12 and 5.13 demonstrate H_2-TPR of LSCF, under temperature ranging from room temperature to 950 °C; and comparison between experimental and model data of H_2 and CO production over LSCF.

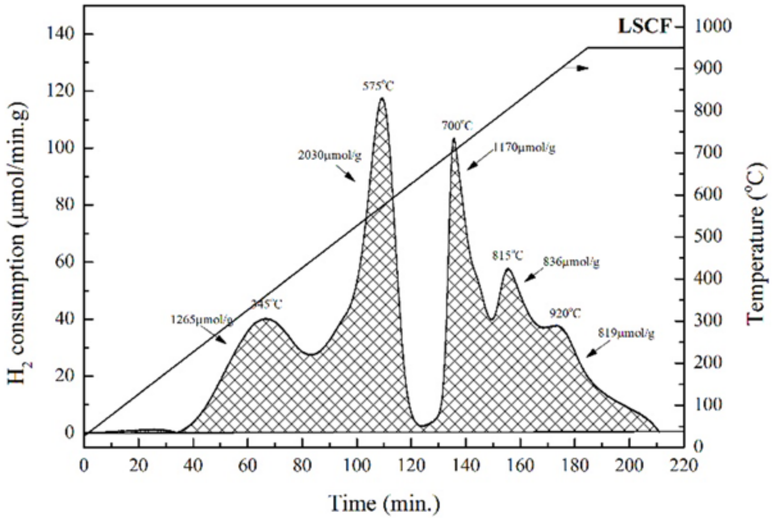

Figure 5.12: Temperature programed reduction of LSCF [11].

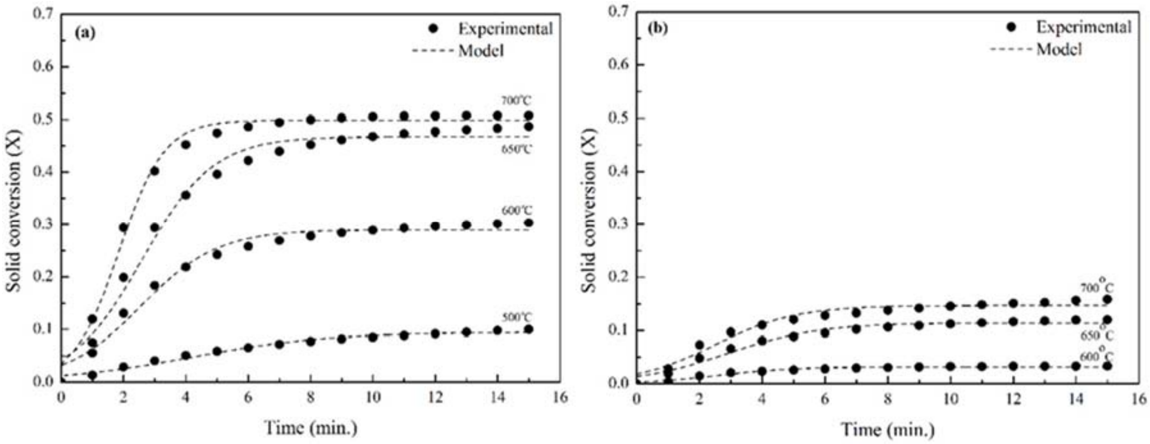

Figure 5.13: Experimental and solid conversion model [11] of LSCF for H_2 (a) and CO (b) production at 500, 600, 650 and 700 °C.

Effect of La and Gd substitution in $BaFeO_{3-\delta}$ (BF) perovskites structure on its performance towards thermochemical cycles of water splitting was also studied [8]. The reduction and oxidation temperature in this work was paired at the same temperature of 500/500, 700/700 and 900/900 °C. Amongst all the interested catalysts, $Ba_{0.95}La_{0.05}FeO_{3-\delta}$ (BLF) showed the best catalytic performance, giving the highest H_2 yield at 1,310 µmol/g_{cat} at 900 °C. The E_a and k_0 of BLF was determined at 47.4 kJ/mol and 0.18 s^{-1}, respectively. TPR study, as presented in Figure 5.14, revealed that the addition of La^{3+} has a greater advantage for the BF-based perovskites than the addition of Gd^{3+}, with respect to oxygen mobility [8].

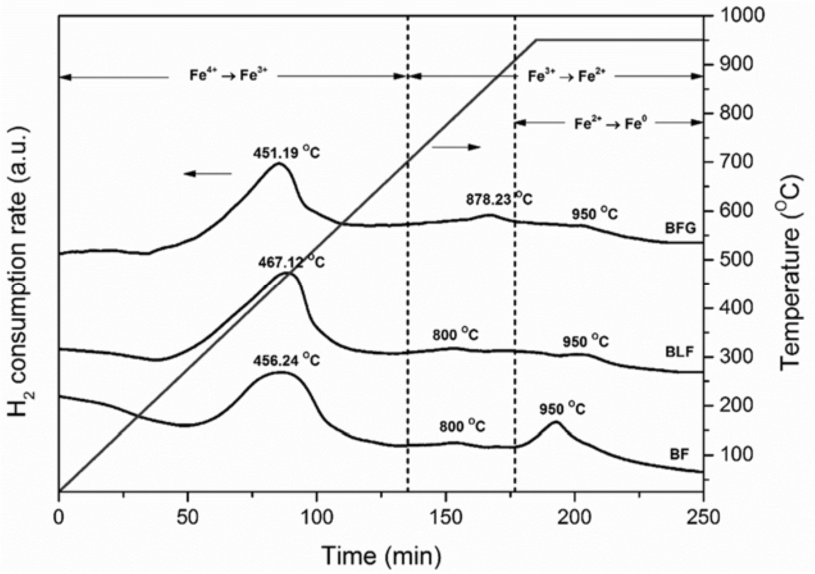

Figure 5.14: Temperature programmed reduction of BF, BLF and BFG ($BaFe_{0.975}Gd_{0.025}O_{3-\delta}$), studied in the range of temperature from ambient to 950 °C [8].

5.2.4 NEW CONCEPTS TO FURTHER IMPROVE THE TWO-STEP THERMOCHEMICAL METAL-OXIDE CYCLES

Isothermal thermochemical cycles

One of the thermochemical cycles process's challenge is the complication caused by the need of temperature swing, between the reduction and oxidation step [8,11,12]. This includes: (1) thermodynamic inefficiency, resulted by the irreversible heat losses incurred upon cooling of the active material to the oxidation temperature and the heat required for activation of the materials during the reduction step; (2) thermal stress, caused by the continuous rapid changes of operating temperatures. For these reasons, an isothermal pressure swing cycling was proposed [33,34], in order to prevent (1) the unnecessary loss of efficiency, (2) maximize the product yield per cycle and (3) obtain longer lifespan of the solid materials. Nevertheless, the concept's implementation in a real-scale solar-fuel production reactor experienced another challenge which is the competition between reduction step and oxidation step, to occur at a given temperature and pressure. This means that local oxygen evolution will co-exist with hydrogen evolution, at least at some regions of the reactor – and that is enough to paint the worst case scenario – which is the explosive mixture, and the less worrying problem is the recombination of the desired products. A combination of well-targeted pressure and temperature swing, rather than each individually, was proposed to avoid such problems. This operational concept could allow the most efficient mode of operation for the two-step thermochemical cycles process. To achieve this, the difference of the optimal temperature of each step should be determined [35].

Chemical-looping thermochemical metal-oxide cycles

To help lowering the temperature difference between the reduction and oxidation step, a gaseous reducing agent, i.e. coke or methane, can be fed during the reduction step. Thus, this operation is not solely thermal reduction. This can be considered as 'carbothermal reduction' which allows the reduction occurs at lower temperature as oxygen will be easier to be released by the existence of carbon source [6,8-12,36]. In case of introducing methane, metal oxide cycle with the partial oxidation of methane coupled with reduction of metal oxide can be illustrated as:

$$\mathrm{MO_x + yCH_4 \rightarrow MO_{x-y} + y(CO + 2H_2)} \tag{5.21}$$

This application also increases the amount of oxygen uptake/release at the same operating temperature, compared to the solely thermal reduction. With this method, the isothermal or near-isothermal operation could be achieved while the products yield is maintained [37]. In addition, the by-products, in this case are H_2 and CO, during the reduction step can be useful.

Spontaneous membrane assisted thermochemical cycles

The two steps of reduction and oxidation process can be designed to take place at two separated sides of a membrane. This enables the two steps to occur at the same time from both sides. The challenges of the membrane assisted thermochemical cycles include: (1) fabrication of the membrane, as the nature of metal oxides is a hard material although fragile; (2) the membrane needs to be sintered as dense membrane, as the other gases permeation is unwanted. The only element that can transfer through will be only oxygen, through solid state diffusion within the material's lattice; (3) the catalyst coating process, in some case, the 2 reactions need different catalysts. This leads to the concept of coating 2 different catalysts on 2 sides of the membrane; (4) the stoichiometric redox materials should not be used as a membrane because the oxygen release/uptake can alter the crystallography of the material, causing them severe structural collapses. For example, 10%NiO-$La_{0.3}Sr_{0.7}Co_{0.7}Fe_{0.3}O_{3-\delta}$ (10%NiO-LSCF) was applied as an oxygen carrier/redox material for an integration of 2 reactions which are methane partial oxidation and nitrous oxide decomposition [9]. The former reaction is the reduction process, whereas the latter acts as the oxidation process. The mechanism of the reactions was determined using temperature-programmed reaction (TPR) and temperature-programmed surface reaction (TPSR) of CH_4 techniques, as shown in Figures 5.15 and 5.16, and Gibbs free energy minimization method (Aspen Plus assisted), as described previously in Tables 5.1 and 5.2. The reactions were suggested to occur following Eley-Rideal surface reaction. The optimal temperature was at 800 °C under atmospheric pressure; where (1) NO_2 formation was not detected, (2) no production of C^{2+} and C^{3+} were observed, (3) complete conversion of N_2O, CH_4 and O_2 were obtained, (4) high purity syngas was achieved with non-detectable amount of any by-products and (5) readily utilizable syngas at the desired ratio of 2 was gained [9].

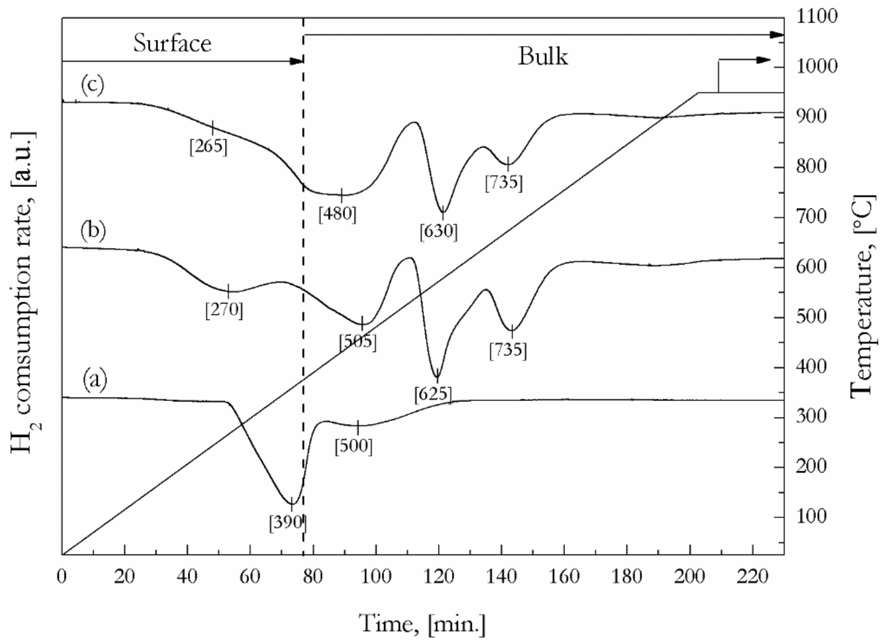

Figure 5.15: H_2-TPR of (a) NiO, (b) LSCF and (c) 10%NiO-LSCF [9].

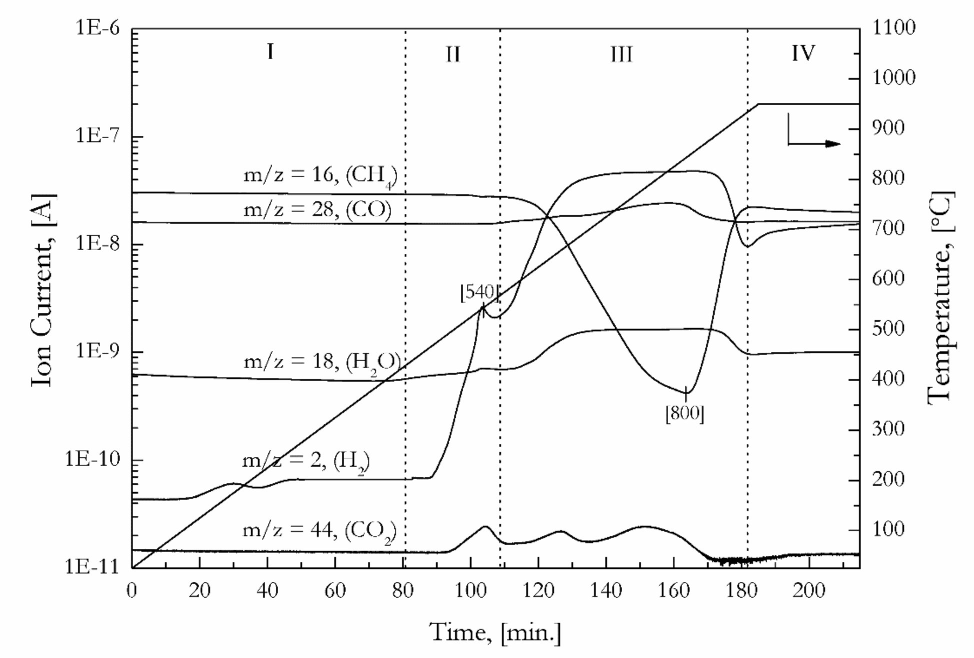

Figure 5.16: CH$_4$-TPSR profile of 10%NiO-LSCF [9].

Photo-thermochemical cycles (PTC)

In this process, the photochemical method was applied to the thermochemical cycles process to avoid the temperature limitation. The cycling reactions can be described as below:

Photochemical process (> 27 °C)

$$MO \rightarrow MO_{1-\delta} + \frac{1}{2}O_{2(g)} \tag{5.22}$$

Thermochemical process (> 300 °C)

$$MO_{1-\delta} + (\delta - \gamma)H_2O_{(g)} + \gamma CO_{2(g)} \rightarrow MO + (\delta - \gamma)H_{2(g)} + \gamma CO_{(g)} \tag{5.23}$$

Figure 5.17 illustrated the schematic diagram of the two-step photochemical reduction and thermochemical oxidation for syngas production in the presence of metal oxide (MO).

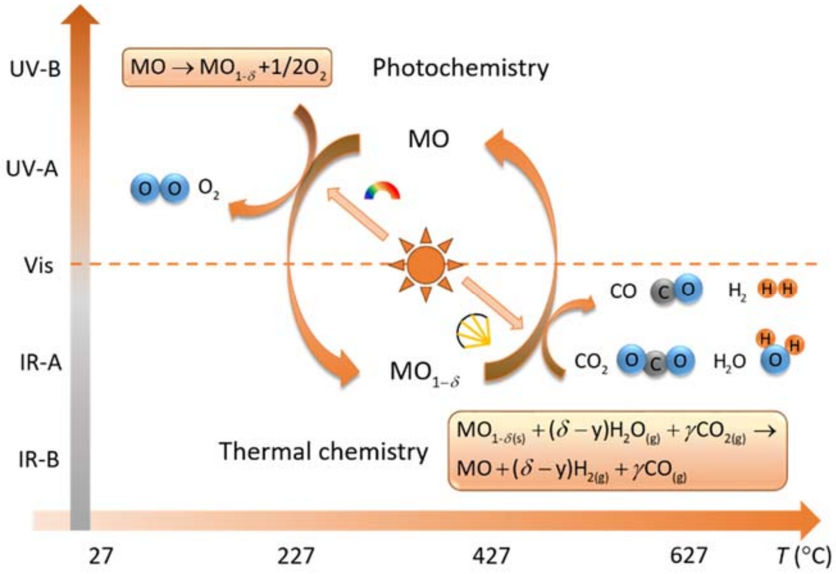

Figure 5.17: Photo-thermochemical cycles of syngas production [38].

During the reduction step, photo-induced V_O will be created on the surface of photochemical materials such as TiO_2 under UV. Afterwards they will be re-oxidized by H_2O and CO_2 at temperature lower than 600 °C during the oxidation step. This helps reducing the massive external heat requirement, thus, it allows the process to be performed even without the integration of solar thermal technology [38].

5.3 METAL OXIDES FOR EMISSION CONTROL

Amongst all the pollutants and emissions, the engine emissions are the majority of outdoor air pollutions. This includes sulfur dioxide (SO_2), volatile organic compounds (VOCs), nitrogen oxides (NO_x), and particulate matter (PM), consisting of solid carbon (soot) and unburned carbonaceous compounds i.e. hydrocarbon (HC) [39]. One absolute way to reduce SO_2, which is solely released from sulfur-mixed fuels, is to limit to eliminate the sulfur use in fuels [40]. The emissions of HC and CO can be simultaneously abated using three-way catalysts (TWCs) and diesel oxidation catalysts (DOCs) [41,42]. However, the most problematic pollutants are PM and NO_x because they are not yet well-controlled by public. Generally, PM and NO_x can be controlled by separated after treatment systems [43]. PM from the combustion chamber can be trapped by a combination of diesel particulate filters (DPFs) and DOCs. The trapped pollutants will be further oxidized by noble metals i.e. Pt catalyst to regenerate the DPFs. The most promising NO_x removal technologies are the (1) selective catalytic reduction (SCR) where either ammonia or urea will be used as a reducing reactant and (2) lean NO_x trapping (LNT) The conventional after-treatment processes to reduce both NO_x and PM at the same time include continuous regeneration traps (CRTs), DPFs systems and, diesel particulate NO_x reduction (DPNR) systems [42,43]. The main challenge of the technology development in this area is to develop low cost and high efficiency metal oxides (rather than precious metals that are generally have better catalytic performance but at higher cost). Recently, many oxides have been proven to exhibit high catalytic performance towards the emission control reactions i.e. spinels (such as $ZnAl_2O_4$ and $CuFe_2O_4$), perovskites (e.g. $SrTiO_3$ or $MgTiO_3$), transition metal oxides (such as Mn, Cu, Co, Ti, Zr, and Ce oxides), and mixed metal oxides (MMOs) (for instance MnO_x-CeO_2, CoO_x-CeO_2, CuO-CeO_2 and $Ce_{0.5}Pr_{0.5}O_2$) [44]. The later sections will focus on diesel emission control using metal oxide catalysts.

Question 5.1
5.1.1 What are the main challenge of thermochemical reactions? (especially when the green technology is aimed) 5.1.2 Thermochemical-cycle reactions are quite similar to chemical looping system. Can you define the differences and the similarities between the two?

5.3.1 EMISSION CONTROL TECHNOLOGIES USING METAL OXIDE CATALYSTS

5.3.1.1 TWC TECHNOLOGY

The removal of pollutants i.e. HC, CO and NO can be together removed using a single bed of TWCs. In the reactor, HC and CO will be converted to CO_2 and water by oxidation whereas NO will be converted to N_2 by reduction, as shown below:

Oxidation:

$$\mathrm{C_yH_n} + \left(1+\frac{\mathrm{n}}{4}\right)\mathrm{O_2} \rightarrow \mathrm{yCO_2} = \frac{\mathrm{n}}{2}\mathrm{H_2O} \tag{5.24}$$

$$\mathrm{CO} + \frac{1}{2}\mathrm{O_2} \rightarrow \mathrm{CO_2} \tag{5.25}$$

$$\mathrm{CO} + \mathrm{H_2O} \rightarrow \mathrm{CO_2} + \mathrm{H_2} \tag{5.26}$$

Reduction:

$$\mathrm{NO\ (or\ NO_2)} + \mathrm{CO} \rightarrow \frac{1}{2}\mathrm{N_2} + \mathrm{CO_2} \tag{5.27}$$

$$\mathrm{NO\ (or\ NO_2)} + \mathrm{H_2} \rightarrow \frac{1}{2}\mathrm{N_2} + \mathrm{H_2O}(2+\frac{\mathrm{n}}{2}) \tag{5.28}$$

$$\mathrm{NO\ (or\ NO_2)} + \mathrm{C_yH_n} \rightarrow \left(1+\frac{\mathrm{n}}{4}\right)\mathrm{N_2} + \mathrm{yCO_2} + \frac{\mathrm{n}}{2}\mathrm{H_2O} \tag{5.29}$$

In terms of the catalysts, TWCs generally contain 2 components which are substrate, support and active species. Typically the substrates are fabricated as monolith, produced by cordierite and metal foil. Support materials are based on high temperature metal oxides such as alumina and ceria-based materials. The active species will be coated at the outer layer of all the components and are traditionally noble metals such as Pt, Pd and Rh. Recently, the active phases are also made of the more economic materials i.e. perovskites and oxides of transition metal (e.g. Cu, Ni, Mn, Co).

Metal oxides as support materials for TWCs

1. ***Alumina***

   Alumina has overall 7 crystal structures which are α-, γ-, δ-,κ-, η-, θ-, and χ-Al_2O_3. In catalysis, the most common form of alumina is γ-Al_2O_3 because it is versatile and has a rich catalytic properties. The γ-Al_2O_3 has been widely utilized in automobile exhaust control application because of its high specific surface area, high porosity and high structural/mechanical/thermal stability. The γ-Al_2O_3 is an octahedral cubic crystallite, meaning that it has both octahedral and tetragonal Al. Its structure is pseudo-spinel, differing only in oxide anion packing density. In addition, its surface possesses both Brønsted and Lewis acid sites which are desired in catalysis field [45,46]. The γ-Al_2O_3 offers surface area of around 300 m^2/g or more, in general, where its pore size varying from 30 to 120 Å with pore volume of 0.5 to 1.0 cm^3/g in terms of structure, the γ-Al_2O_3 has single layers of close-packed spheres in which the layers have O^{2-} ion at position. The spheres of the second layers are located at 50% of the hollows of the first layer. The third layer can be distributed in the remaining hollows of the first layer. The small Al^{3+} cation is sit in the space between these layers of oxide anion packing.

2. ***$Ce_xZr_{1-x}O_2$***

   Ceria is an oxygen carrier material, having high OSC. This enables the possibility of effective and efficient operation of the reaction that has fluctuating oxygen concentration. CeO_2 can be either stoichiometric or non-stoichiometric material. When prepared and operated as non-stoichiometric material, Ce^{4+} in the CeO_2 will be readily converted to Ce^{3+}. CeO_2 was reported to enhance dynamic performance in purification of CO, NO_x and HC under conditions of rich to lean air to fuel (A/F) ratios in automotive exhausts. The addition of Zr was reported to increase both OSC, oxygen mobility and thermal stability of the CeO_2-based catalysts [47]. High specific surface area Al_2O_3 was found to improve thermal stability of the CeO_2/ZrO_2-based catalyst systems to be even higher. Besides, the addition of La^{3+} can restrict the phase transformation of γ-Al_2O_3 to α-Al_2O_3

at high temperature, leading to a higher catalytic properties; i.e. thermal stability, oxygen mobility or ionic conductivity; of the CeO_2/ZrO_2-based catalysts.

Metal oxides as TWCs

Because of the high price of noble metals and its sensitivity to be poisoned by chloride/chlorine products, mixed metal oxides are recently developed to be applied as TWCs individually.

1. ***Perovskites***
   Perovskites (ABO_3 or A_2BO_4) are one of the interesting materials for TWCs as they have high thermal stability and are inexpensive. They have been widely applied in oxidations of HC and VOCs. Co- and Mn-based catalysts were previously proposed as absolute alternatives to noble metal supported catalysts as they have comparable activities towards the oxidations of HC and VOCs. High temperature calcined perovskites can have relatively low specific surface area, which is somehow remained a challenge [48].
2. ***Transition metal oxides***
   Transition metal oxides are good candidates as noble metals substitutes in complete oxidation reaction. Despite being less active at lower temperature, compared to the noble metals, they are very much comparable at higher operating temperatures. Oxides of Cu, Co, Mn and Ni are some of the most active materials for VOCs combustion process. Mn and Co are drawing attentions from researchers lately due to their low cost, environmentally friendliness and high activity. In addition, Mn-based oxides are becoming more attractive in catalysis due to their various oxidation states and their high OSC [49].

5.3.1.2 THE DOCs

Catalysts for diesel combustion should be able to oxidize CO, unburnt HCs and NO_x. The DOCs are typically made of ceramics and fabricated as honeycomb monoliths. Figure 5.18 presents monolith made of LSCF.

Ceramic monolith has outstanding mechanical strength because it has low porosity, however, its major downside includes a difficulty to disperse the active-catalyst on. For this reason, often the active species will be coated on the ceramic support using wash-coat method where the active catalysts will be disperse in the wash-coat solution. A high surface area wash-coat solution can provide highly dispersed precious metal sites which (1) increase the accessibility of the active species for the reactants and (2) lower the amount of the precious metals needed, resulted in lower operational cost. The choice of support highly effects catalytic performance of the overall catalyst system, including thermal stability, surface area, pore volume and surface reactivity. Al_2O_3, ZrO_2 and La_2O_3 were applied as wash-coat solution materials [10,11]. Precious metals such as Pt and Pd had been largely applied as DOCs in the past decades [51].

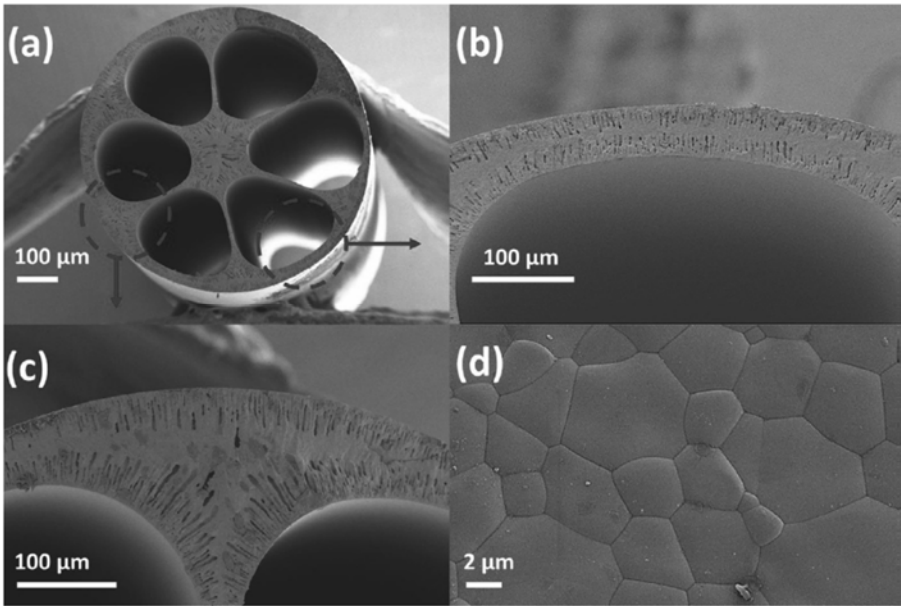

Figure 5.18: Morphological images via SEM of sintered LSCF micromonolith: (a) whole view, (b) active region, (c) cross sectional area of wall, and (d) outer surface of the ceramic monolith [50].

Metal oxides as wash coat material for DOCs

Alumina is a common wash-coat material, offering higher specific surface area and thermal stability. Zirconia is another option, providing high crystallinity although lower surface area compared to the alumina [52]. An acidic (or electrophilic) wash-coat support such as Al_2O_3 and SiO_2 results in a lower electron density on Pt particles, when compared with less acidic materials i.e. ZrO_2 or La_2O_3 [53]. The acid strength was reported to increase along with the changes in oxidation state of Pt. The acidic supports were found to provide greater resistance to Pt oxidation which is undesired. This resistance towards Pt oxidation is also increased because the catalyst has electronegative additives incorporated into the formulation. Moderate strength of acidity of supports was found to enhance catalytic performance of Pd towards methane combustion, even if PdO was formed. This is because PdO is considered active for such reaction.

5.3.1.3 DIESEL NO_x REMOVAL CATALYST TECHNOLOGY

Nitrogen oxides (NO_x), include NO, NO_2 or N_2O, are the cause of acid rain, photochemical smog, ozone depletion and the greenhouse effect. One of the most efficient methods to abate NO_x is SCR with ammonia; i.e. $4NO + 4NH_3 + O_2 \rightarrow 4N_2 + 6O_2$; for NO removal [54,55]. Metal oxides such as V_2O_5 (+WO_3 or MoO_3)/TiO_2 catalysts were recently explored as the SCR catalysts, to replace the expensive, poison sensitive, and high operating temperature required Pt. Such metal oxides offer lower cost and more tolerance to poisons, especially to SO_2 [54]. However, the operating temperature can still be as high as 250 °C [55]. Such temperature is considered slightly too high because the downstream temperature is generally below 200 uch temperature is considered slightly too high because the downstream temperature is generally below 200 °C, thus the development of low-temperature SCR is crucial, to avoid unnecessarily reheating the flue gas by more than 50 °C. Recently, researchers developed transition metal oxides; such as $NiSO_4/Al_2O_3$, MnO_x/Al_2O_3, V_2O_5/activated carbon, and MnO_x/TiO_2, to lower the operating temperature of the current SCRs [55].

Reaction mechanism of metal oxide-based catalysis for ammonia-SCR of NO_x

There are extensive amount of previous works that investigated gas-solid mechanistic reactions between the metal oxides and NO_x. These works include the predicted mechanism of (1) reaction between ammonium ion and adsorbed NO_2, (2) reaction between an amide and gaseous NO, and (3) reaction between coordinated ammonia and a species generated by spillover of NO on the support [56-58]. A mechanism of low temperature ammonia SCR of NO_x in the presence of MnO_x/Al_2O_3 had been determined [56]. The adsorption of NH_3 on a Lewis acid sites was proposed to be initially occurred and afterwards oxidized to an NH_2 function in which it reacted with gaseous NO via Eley-Rideal mechanism partway (ER), simultaneously with nitrite intermediates on the surface through Langmuir-Hinshelwood mechanism pathway (LH). Mechanistic pathway in the presence of MnO_x/CeO_2 catalyst was reported to be comparably similar [57].

$$\frac{1}{2}O_{2(g)} \rightarrow O_{(a)} \tag{5.30}$$

$$2NH_{3(g)} \rightarrow 2NH_{3(a)} \tag{5.31}$$

$$NH_{3(a)} + O_{(a)} \rightarrow NH_{2(a)} + OH_{(a)} \tag{5.32}$$

$$NO_{(g)} + O_{(a)} \rightarrow NO_{2(a)} \tag{5.33}$$

$$NH_{2(a)} + NO_{(g)} \rightarrow NH_2NO_{(a)} \rightarrow N_{2(g)} + H_2O_{(g)} \tag{5.34}$$

$$NH_{3(a)} + NO_{2(a)} \rightarrow N_{2(g)} + H_2O_{(g)} + OH_{(a)} + (a) \tag{5.35}$$

$$2OH_{(a)} \rightarrow H_2O_{(g)} + O_{(a)} \tag{5.36}$$

Where (a) represents acid sites of the solid catalyst. These reaction of NH_2 and NO, and the formation of NH_2NO are the typical SCR mechanistic pathways which were reported for other metal oxides such as V_2O_5/TiO_2, V_2O_5-WO_3/TiO_2 and Mn-based oxides [59]. The low temperature SCR over a commercial V_2O_5-WO_3/TiO_2 was proposed as illustrated in Figure 5.19 [59].

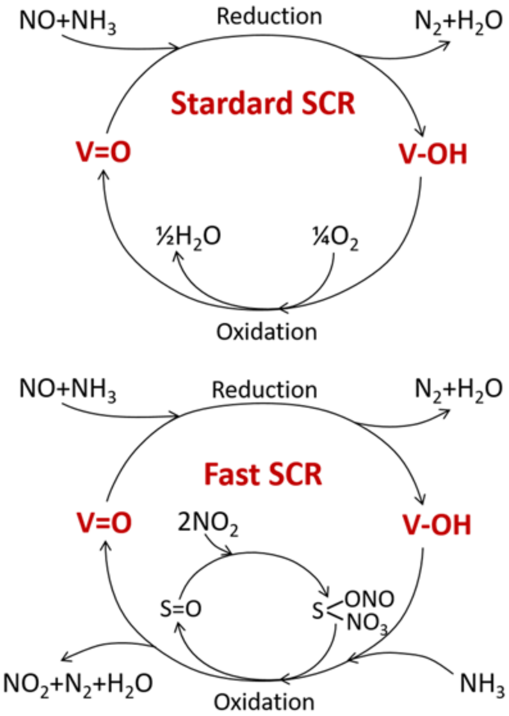

Figure 5.19: Comparison between the redox cycles of the standard SCR and fast SCR, in the presence of V_2O_5-WO_3/TiO_2 [59].

From Figure 5.19, the vanadium sites were reduced by reaction between NO and NH_3 before being re-oxidized either by oxygen (for the standard SCR) or nitrates (for the fast SCR, where the dis-proportionation of NO_2 was observed) [59].

<u>Metal oxide-based catalysts for ammonia-SCR of NO_x</u>

1. ***Single metal oxide-based catalysts***
   Oxides of transition metals; i.e. Fe, Mn, Cr, Cu, V, Cr, and Co; were reported to show excellent activities towards the low temperature SCR. Nano-MnO_x was reported to be one of the most promising amongst these catalysts, due to its outstanding catalytic performance [60-62]. Like every other catalysts, the physical and chemical properties of MnO_x; such as high specific surface area,

crystallinity or oxidation state of the MnO_x; have a strong influence on its overall catalytic performance. Various oxidation state of Mn allows the compounds to be formed in many stable forms of oxides in which their reduction temperatures are ordered as $Mn_3O_4 > Mn_2O_3 > Mn_5O_8 > MnO_2$. At low temperature, MnO_2 showed the highest catalytic activity whereas Mn_2O_3 offered the highest N_2 selectivity [63]. It can be concluded that the NO conversion was usually increased when the Mn^{4+}/Mn^{3+} ratio was increased. In addition, N_2 selectivity decreased when the temperature was increased. When the temperature was fixed constant, N_2 selectivity was found to decrease with increasing NO conversion [64].

2. ***Mixed oxide-based catalysts***

   While MnO_x is undoubtedly one of the best metal oxide compounds for SCR, however, its main disadvantages are its low specific surface area and low thermal stability (leads to sintering and even lower surface area). The addition of other metals has been reported to improve such problems [65]. Amongst all the Mn-based mixed oxides, CeO_2/MnO_x was reported to show the best performance, providing 100% N_2 selectivity at 100 to 150 °C [66]. One remaining challenge of the MnO_x/CeO_2 application in SCR is its low activity and lower temperature, and intolerance to SO_2 poisoning [67]. Partial substitution of Sn to the MnO_x/CeO_2 was found to ease such problem, even in the presence of H_2O [68]. The addition of Sn was believed to increase the oxygen vacancy concentration in which it probably facilitates NO oxidation to NO_2, yet enhances Lewis acid sites, created by surface sulfation during SCR in the presence of SO_2.

3. ***Supported metal oxide-based catalysts***

   Supports such as Al_2O_3 and TiO_2 had been excessively applied for SCR, as well as the supported transition metal oxides in which its catalytic performance, when doped on TiO_2 are ordered as: Mn > Cu ≥ Cr ≥ Co > Fe ≥ V >>> Ni. The activity of Mn-based materials are proportionally related to the level of Mn loading and the reaction temperature [69]. Mn species was proven to play an important role in SCR as TiO_2 alone did not show any significant NO conversion. A model, as shown in Figure 5.20, was proposed to interpret the effect of transition metals on the activity of MnO_x/TiO_2 [70]. The addition of transition metals can segregate the manganese oxides and titania particles. These particles were prevented from sintering so that the MnO_x was remained amorphous, leading to an increase in catalytic activity of the overall catalyst system.

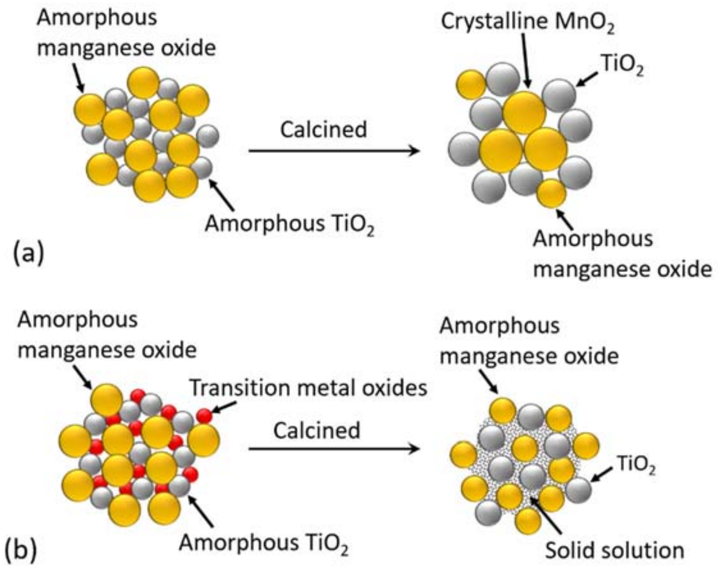

Figure 5.20: Modeled illustrations for (a) Mn/TiO_2 and (b) metal-Mn/TiO_2 structures before and after calcination [70].

5.3.1.4 SIMULTANEOUS CONTROL OF DIESEL SOOT AND NO_X EMISSIONS

One of the major challenges of DPFs is the back pressure in the system, created by a blocked DPF. This therefore requires routine re-generation process to avoid to engine's damage. The trapped materials in the filter are generally consisted of carbon particles, with some amount of adsorbed HCs. These particles can be removed from the filter using 2 techniques [71]:

(1) O_2 combustion:

$$[C] + O_2 \rightarrow CO_2 \tag{5.37}$$

(2) NO_2 combustion:

$$[C] + NO_2 \rightarrow CO_2 + NO \tag{5.38}$$

NO_2 combustion regeneration is a popular technique, recently. It is called continuous regenerating trap (CRT), where Pt-doped catalysts are placed upstream in the filter. The catalysts will oxidize the emitted NO to NO_2 which is the better oxidant compared to O_2 and can be utilized for PM oxidation with a DOC at exhaust temperature (200 to 500 °C) without having to reach the classical optimal temperature of soot combustion (600 °C or more). One of the CRT's downsides is the loss of NO_2 from the filter, thus the total NO_x removal efficiency is relatively low [45]. Both NO_x and the diesel soot can be eliminated simultaneously in a single catalyst bed using DPNR technology [72,73].

The DPNR is a technology which combines the (1) NO_x storage reduction (NSR) for NOx removal with (2) combustion of soot; over the same type of catalyst in one reactor. The schematic structure of DPNR can be illustrated as shown in Figure 5.21 [73].

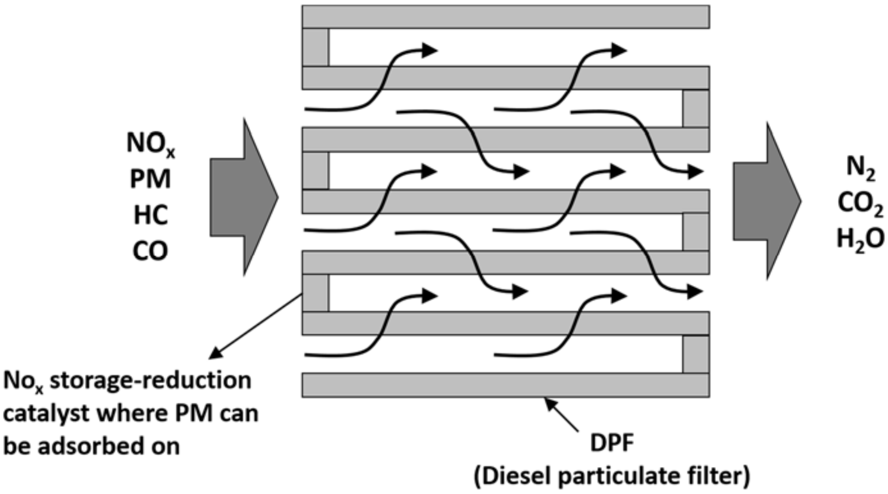

Figure 5.21: DPNR catalyst system and its configuration [73].

From Figure 5.21, the internal porous surface of the DPF's cell walls were coated with the NSR catalyst. Under lean conditions, the NO is oxidized to NO_2 while the adsorbed oxygen atoms were activated on the Pt active sites. Majority of NO_2 will be converted to nitrate and/or nitrite species on the surface of the catalyst, whereas the residual NO_2 and activated oxygen atoms will be reacted directly with the diesel soot. Nitrates and/or nitrite species can be decomposed to NO_2 which will be further reduced by soot to N_2, HC and CO on the Pt sites, in an enriched atmosphere. In order to improve the efficiency of NO_x and soot conversion, operating conditions and reaction designs are crucial. One of the first DPNR catalysts is CuO-based materials. Afterwards, more metal oxides such as perovskites, spinel-type oxides and hydrotalcite-derived oxides have been being applied as DPNR catalysts [74-78].

Contact conditions between soot and catalyst

The kinetics of soot oxidation depends on very much the degree of contact between the soot cake and the catalyst [79]. The interaction between the two solids (soot and catalyst) and the gas (NO_x) strongly affects the catalytic activities of the whole process. Two type of the contacts between soot and catalyst had been modeled to investigate their possible mechanisms/behaviors. The two assumptions are [80]:

1. ***A loose contact condition***:
   This type of contact was experimented by gently mixing the catalyst and soot together and stirred until sufficiently homogeneous. The mixture showed the reproducible catalytic results, despite having been under this short procedure of 1 to 2 minutes. The surface oxygen species were reported to exist under this loose contact conditions. The example of the materials include perovskites, spinels and other mixed oxides.
2. ***A tight contact condition***:
   This type of contact was mimicked by ball milling the soot and catalyst together. This method resulted in close contact between the soot and catalyst. It was found that the number of contact points was maximized, enabling better differentiation of the morphologies. However, this kind of contact may be less representative of the actual contact conditions occurring during the real reaction. Surface oxygen species over alkaline (Na, K, Cs) and alkaline earth metal (Ca, Ba, Mg) oxides are categorized under this tight contact conditions.

Mechanism of oxygen transport

The following parameters are considered important to understand the behavior and determine the performance of the catalyst for soot oxidation at lower temperature. Oxygen transportation from the catalyst's lattice to the soot is one of the key parameters is one of the parameters that controls the intrinsic activity of the catalyst [81]. Figure 5.22 illustrates the basic oxygen transport phenomena of reaction between the metal oxides and soot [52].

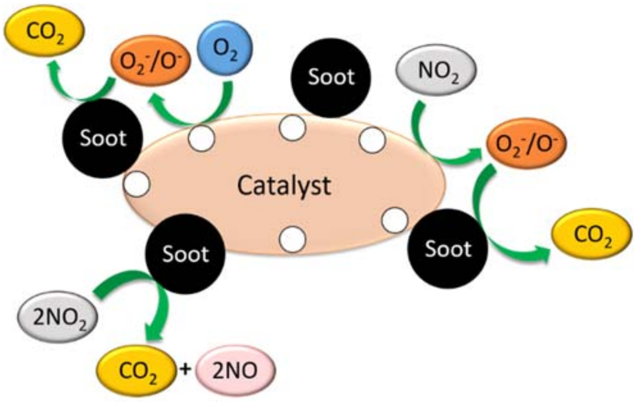

Figure 5.22: Illustration of basic oxygen transportation mechanisms between the metal oxides and the soot [52].

The three mechanism of the oxygen transfer were proposed as follows [52,81]:

1. ***Surface redox mechanism:***
   Surface oxygen of the catalyst will be transferred to the surface of the soot at the soot-catalyst interface, where the gaseous oxygen can be filled the resulting oxygen vacancies [82,83]. Example of the metal oxides that follow this mechanism is Co_3O_4.
2. ***Spill-over mechanism***
   In this case, the oxygen is initially absorbed and dissociated onto the surface of the catalyst, generating active oxygen species. This gaseous oxygen species will be further transferred to the surface of the soot. For this particular case, the catalyst-soot contact is not necessarily required [83]. CeO_2 and Cr_2O_3 are considered having spill-over mechanism.
3. ***Redox mechanism***
   This mechanism is suggested when the catalyst was reduced by transferring bulk oxygen to soot which was oxidized. Examples of the metal oxides are V_2O_5 and Fe_2O_3 [83].

Mechanism for simultaneous NO_x and soot removal

The idea of simultaneously soot and NO_x removal was firstly proposed in 1989. The widely accepted mechanism of such are divided into 2 main parts [84]: The predicted mechanisms are illustrated as shown in Figure 5.23 [85].

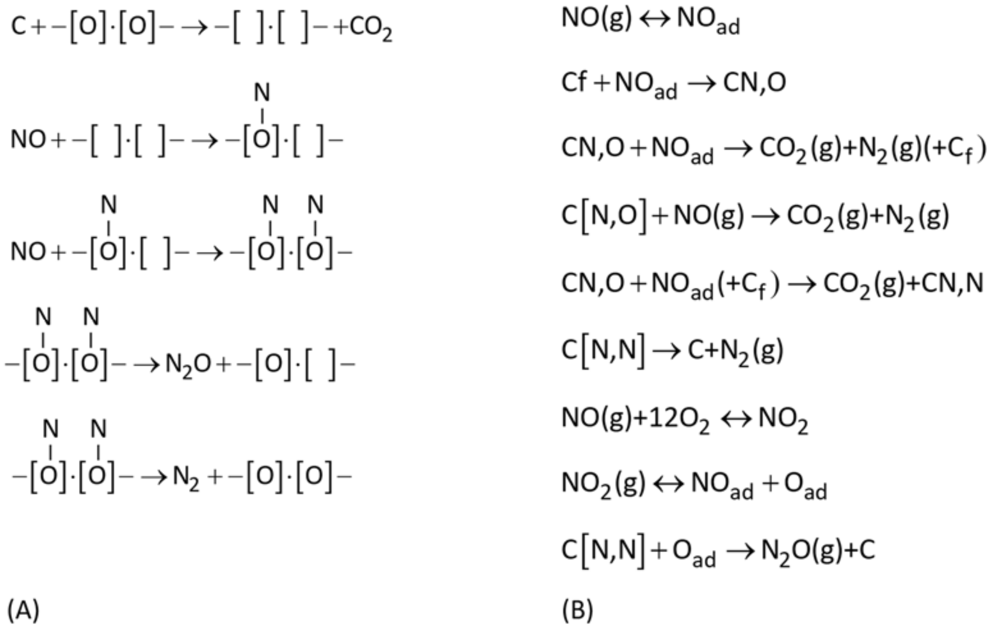

$$C + -[O]\cdot[O]- \rightarrow -[\ ]\cdot[\ ]- + CO_2$$

$$NO + -[\ ]\cdot[\ ]- \rightarrow -[\overset{N}{O}]\cdot[\ ]-$$

$$NO + -[\overset{N}{O}]\cdot[\ ]- \rightarrow -[\overset{N}{O}]\cdot[\overset{N}{O}]-$$

$$-[\overset{N}{O}]\cdot[\overset{N}{O}]- \rightarrow N_2O + -[O]\cdot[\ ]-$$

$$-[\overset{N}{O}]\cdot[\overset{N}{O}]- \rightarrow N_2 + -[O]\cdot[O]-$$

(A)

$$NO(g) \leftrightarrow NO_{ad}$$

$$Cf + NO_{ad} \rightarrow CN,O$$

$$CN,O + NO_{ad} \rightarrow CO_2(g)+N_2(g)(+C_f)$$

$$C[N,O] + NO(g) \rightarrow CO_2(g)+N_2(g)$$

$$CN,O + NO_{ad}(+C_f) \rightarrow CO_2(g)+CN,N$$

$$C[N,N] \rightarrow C+N_2(g)$$

$$NO(g)+12O_2 \leftrightarrow NO_2$$

$$NO_2(g) \leftrightarrow NO_{ad} + O_{ad}$$

$$C[N,N] + O_{ad} \rightarrow N_2O(g)+C$$

(B)

Figure 5.23: Two different mechanisms proposed for simultaneous NO_x and soot removal [85].

The mechanism demonstrated in Figure 5.23 can be detailed as described below:

1. ***Mechanism A:***
   Two adjacent oxygen vacancies will be created on the catalyst surface by soot combustion before developing active sites for the chemisorption of two NO molecules. The adsorbed NO will be dissociated to $N_{(ad)}$ and $O_{(ad)}$, which will generate further N_2O or N_2. However, these mechanism are not explaining the positive effect of the oxygen because the oxygen would be expected to fill the oxygen vacancies on the catalyst surface, leading to a lower reaction rate.
2. ***Mechanism B:***
   The positive effect of oxygen was included in this mechanism. Initially, C[N,O] will be formed by the combustion of reactive free carbon (C_f) and adsorbed NO molecules. The C[N,O] can be converted to N_2 by 2 possible pathways: (i) C[N,O] reacts with another $NO_{(ad)}$ or gaseous NO molecule or, (ii) C[N,O] is converted to another reaction intermediate C[N,N], which afterwards decomposes into N_2. The promoting effect of oxygen can be attributed to the formation of active sites for NO chemisorption on C_f as a consequence of carbon combustion, or to easier formation of NO_2, which is more active than NO in the reaction with soot. .

<u>Criteria of the catalyst materials</u>

The best catalyst should provide a high rate of soot oxidation and NO_x reduction at relatively low temperature. Thus, the material should possess an excellent redox property and allow establishment of good contact between the catalyst and solid reactant, in this case, soot. The textural structure of the catalyst should be feasible to capture soot particles, with its size larger than 25 nm [86].

<u>Metal oxides as soot oxidation catalysts</u>

Many of metal oxides have been found beneficial for soot combustion such as mono-basic metal oxides, ceria-based catalysts, mixed metal oxide (MMO) catalysts, and perovskites [87,88].

1. ***Monobasic metal oxide catalysts***
   This category of metal oxides include single metal oxide compounds i.e. CeO_2, SiO_2, Al_2O_3, TiO_2 and ZrO_2. Amongst these materials, only ceria can generate highly active oxygen species, resulted in its knowingly high OSC [52].
2. ***Ceria-based catalysts***
   Ceria has excellent redox property in which Ce^{3+} and Ce^{4+} oxidation states allows high capacity of atomic oxygen release/uptake. Foreign elements such as; Zr, La,

Pr, Sm, K, Co, Ba-K, Cu-V, Ag or Cu; can be doped into the ceria, in order to enhance its OSC, redox properties and thermal stability [89].

3. ***Alkali-metal oxides***

   One of the most popular alkali oxides is K-based oxide catalysts as they exhibit relatively high activity towards the soot oxidation. This advantage is the result of its ability to form low-melting point compounds with other catalyst components, leading to improvement of surface mobility of the active species and thus favoring the soot-catalyst contact [90,91]. $K_2Ti_2O_5$ is one of the best candidates for the soot oxidation due to its high activity. Some metals i.e. Pt, Cu, Co or Ce were doped into the $K_2Ti_2O_5$ catalyst system in which its synergistic effect on its catalytic performance towards the soot oxidation had been being researched [91-93].

4. ***Mixed metal oxides (MMOs)***

   MMOs are generally the oxides of rare earth, alkali, alkaline-earth and noble metals; which possess layered double hydroxides (LDHs).LDHs are a class of ionic lamellar compounds consisting of positively charged brucite-like layers with an interlayer region containing charge-compensating anions and solvation molecules. LDHs can be illustrated as shown in Figure 5.24 [40]. The general formula of LDHs can be written as $[\mathrm{M}^{2+}_{1-x}\mathrm{M}^{3+}_{x}(\mathrm{OH})_2]^{x+}(\mathrm{A}^{n-})_{x/n}\cdot y\mathrm{H_2O}$, where M^{2+} and M^{3+} are di- and tri-valent cations, respectively. The value of x is equal to the molar ratio of $M^{2+}/(M^{2+}+M^{3+})$ which is generally varied from 0.2 to 0.4, A^{n-} represents an anion. The chemical and physical properties of LDHs can be tailored by changing the molar ratios of M^{2+}/M^{3+} and the type of interlayer anions.

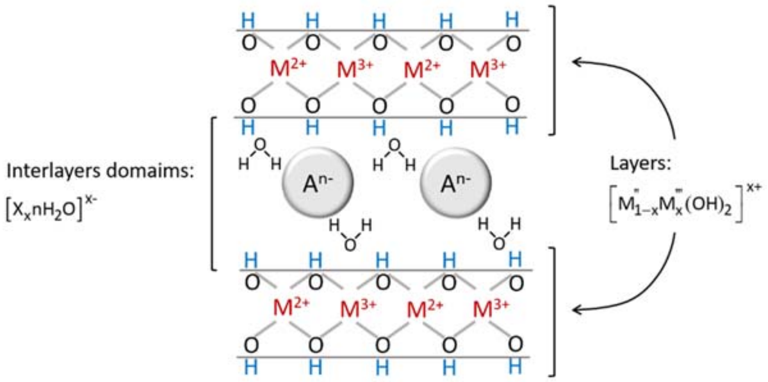

Figure 5.24: Molecular structure of LHDs [40].

Various composition of LDHs and their structural properties make them versatile and suitable for application in catalysis and adsorption. LDHs have (1) high specific surface area, even with high temperature calcination, (2) good basic properties, (3) high metal dispersion and, (4) high thermal stability. Binary LDH derived catalysts (such as CuAl or CoAl), ternary LDH-derived catalysts (i.e. MnMgAl, CoMgAl and CuMgAl) and quaternary LDH-derived catalysts (i.e. CoMgAlCe) have been applied into the process of soot oxidation integrated with NO_x reduction [94-99].

5. ***Spinel-type oxides***

   Co-based spinel oxides are one of the best catalysts for simultaneous removal of NO and soot, due to their high catalytic performance, their abundant and their cost [100,101]. Addition of Ce in the spinel oxides i.e. $Ce_{0.1}Co_{0.9}Cr_2O_4$ were reported to improve the catalytic activity; giving 90% soot conversion and 69.8% NO conversion, at 446 °C [102]. The addition of foreign elements was believed to cause deformation of the spinel structure, leading to crystal defects which are desirable as they increase the concentration of the oxygen vacancies. This enhances oxygen mobility and the redox behavior of the cerium-modified cobalt chromite catalysts.

6. ***Perovskite-type oxides***

   Perovskites have their advantages in cost, high OSC, high flexibility to be adjusted and high thermal stability. The molecular structure of perovskites is illustrated as shown in Figure 5.25, where A and B are two cations having very different sizes, O is oxygen anion that bonds to both A and B.

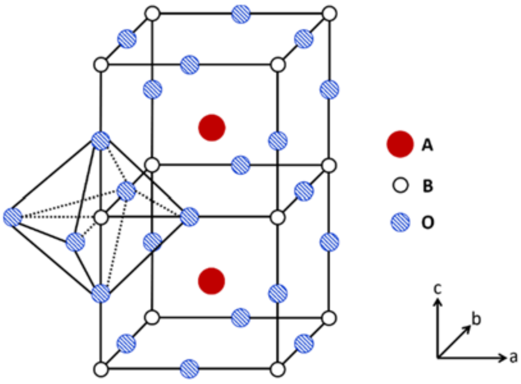

Figure 5.25: ABO_3 representing ideal cubic structure and framework [40].

La-based perovskites are one of the most popular recipe which are widely applied into redox reactions [103-105].Co and K containing La-based perovskites were found to have an improved mobility of the surface lattice oxygen, which helps reducing the operating temperature of soot oxidation/combustion. However, one of its downsides is its low surface area, ranging from 5 to 50 m^2/g, which often limits the choice of applications. Thus, one possible future improvement for perovskites is to increase their specific surface area, perhaps by inventing a novel preparation method. Success so far was only to coat perovskites on high surface area supports such as alumina or silica. Macro-porous perovskites (pore size > 50 nm); e.g. three-dimensional ordered macro-porous (3DOM) $LaMn_{1-x}Fe_xO_3$; were found to have higher catalytic performance towards soot oxidation/combustion, compared to the nanoporous perovskites (10 nm of pore size). This is due to the mass transfer limitation due to the size of the soot (particle size > 25 nm).

<u>Pathways to further improve the catalysis of soot combustion</u>

Because the soot combustion is a reaction that occurs by 3 interfacial contacts between the gaseous reactant (O_2, air, NO_x), solid catalyst (MMOs, perovskites or others) and solid soot (in form of particles or cake); thus not only the intrinsic kinetics is determining the activity/performance of the overall process, but also the contact efficiency between these phases. The well-ordered interpenetrating macro-porous structure allows soot to go through the catalyst without having too much resistance, enabling easy access to all the active species within the pores [106-111].

5.3.2 SPECIFIC CATALYST PREPARATION FOR EMISSION CONTROL TECHNOLOGIES

The following methods are generally applied for metal oxides that are utilized in emission control: (1) solution combustion synthesis (SCS) method, (2) reactive grinding method, (3) sol-gel method, (4) co-precipitation method, (5) incipient wetness impregnation method, (6) ligated method, (7) impregnation method, (8) solid-state reaction method, (9) complex combustion method, (10) colloidal crystal templating method.

5.3.2.1 PREPARATION OF METAL OXIDE CATALYSTS WITH NANOSIZED STRUCTURE

Common preparation techniques for soot oxidation/NO_x reduction include solution combustion synthesis (SCS), reactive grinding and complex combustion because these methods can provide nanosized catalysts [112-114]. Amongst these techniques, the reactive grinding provides room temperature synthesis of pure perovskite-phase materials without thermal treatment, thus, is considered as a high-energy mechanical synthesis or mechanochemical synthesis. Besides, the mechanical abrasion reduces the crystallite size to nanoscale, offering homogeneous mixture with excellent solid-state diffusion [115]. When prepared using various grinding additives, perovskites can have surface area as high as 150 m^2/g, after calcination at 202 °C. For example, specific surface area of $LaCoO_3$, $LaGaO_3$, $LaCoO_3$ and $SrCoO_3$ was reported at 100, 98, 110 and 150 m^2/g, respectively [116-118].

5.3.2.2 PREPARATION OF METAL OXIDE CATALYSTS WITH HIGH SURFACE AREA

The most popular methods for high surface area materials include sol-gel method, co-precipitation method, microemulsion method, impregnation method and solution combustion method. For example, 3DOM structured catalysts can be successfully prepared using the following methods: (1) colloidal crystal templating method, (2) a modified emulsifier-free emulsion polymerization method and (3) combination of ethylene glycol ligation, solution combustion and calcination of LDHs. While the impregnation method is well-known in catalysis, the calcination LDHs is much more specific. The layered double oxides (LDOs) can be synthesized using calcination process of LHDs, providing large surface area, high thermal stability and high catalytic activity. When being heated, the water contained within the interlayer will be lost, accompanied to a large extent by dehydroxylation and decarbonation, resulting in the formation of hybrid oxides and three-dimensional (3D) networks [119].

Question 5.2
Why are researchers still developing catalytic converters when there are some commercialized one already?

5.4 METAL OXIDES IN FUEL CELLS

Fuel cells are one of the most promising technologies to produce efficient, clean and reliable energy, due to their high-energy conversion efficacy and their pollution free emission. They can be considered as energy generation, energy storage and energy delivery [120]. Within the fuel cells, the chemical energy, which stored in various fuels combined with oxygen from the air, will be converted directly to electrical power by electrochemical reactions occurring on electrodes. Fuel cells can provide high theoretical/practical efficiencies compared to the conventional heat conversion engines. Main components of fuel cells consist of 2 similar parts which are anode, cathode and electrolyte. During the operation, fuels will be transported to anode and oxidized, while the oxidant; i.e. oxygen or air; will be transported to the cathode to be reduced. These phenomena occur under a certain conditions, with electrons being transferred from the anode to the cathode while anions from the cathode to the anode, as shown in Figure 5.26.

The overall reaction of a fuel cells which uses hydrogen and methane as a fuel was shown as equations (5.39) and (5.40), respectively.

$$\mathrm{H_2} + \frac{1}{2}\mathrm{O_2} \rightarrow \mathrm{H_2O} \tag{5.39}$$

$$\mathrm{CH_4} + 2\mathrm{O_2} \rightarrow \mathrm{CO_2} + \mathrm{H_2O} \tag{5.40}$$

The fuels, which was hydrogen and methane, are oxidized to H_2O and CO, respectively. These reactions involves release and translation of electrons, releasing electrical energy instead of heat. There are various type of fuel cells which are alkaline fuel cells (AFCs), direct methanol fuel cells (DMFCs), proton exchange membrane fuel cells (PEMFCs), phosphoric acid fuel cells (PAFCs), molten carbonate fuel cells (MCFCs) and solid oxide fuel cells (SOFCs). These fuel cells have different operating temperature and different type of ions released. Figure 5.27 demonstrates operating temperatures/reactions/ processes occurring in different type of fuel cells.

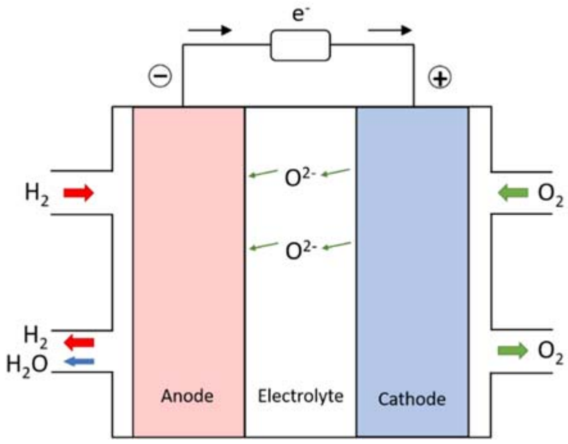

Figure 5.26: Schematic of solid oxide fuel cells (SOFCs) using hydrogen as fuel and oxygen as oxidant [121].

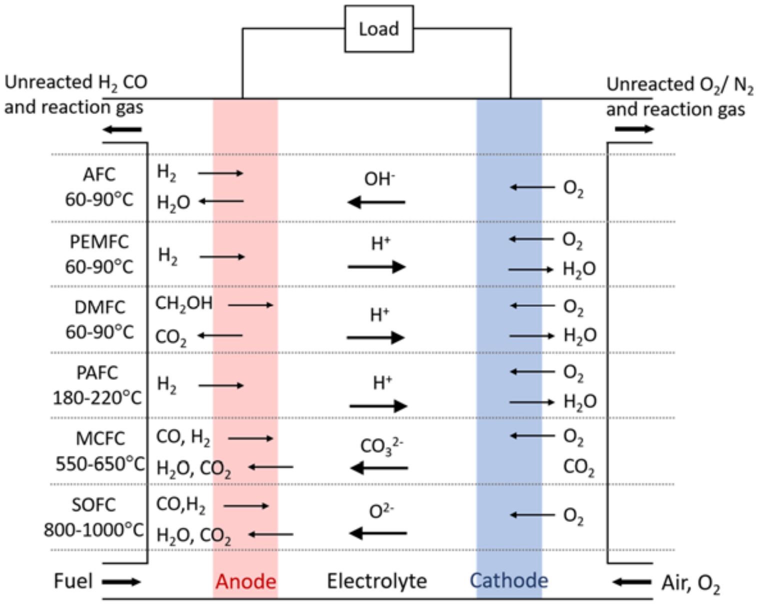

Figure 5.27: Different operating temperatures, reactions and processes of each type of fuel cells [122].

5.4.1 METAL OXIDES IN SOLID OXIDE FUEL CELLS

5.4.1.1 ANODE MATERIALS

Anode can be also called the fuel electrode. It acts both as reaction sites and a catalyst for electrochemical oxidation of fuels. Anode is initially fabricated from precious metals (such as Pt, Ag) or transition metals (Fe, Co, Ni). However, these materials are easily degraded by negligible ion conductivity, incapability of thermal expansion and low porosity. During the past few decades, ceria and other high temperature metal oxides i.e. perovskite have been utilized in fuel cells applications for catalytic performance improvement.

Ni and its modifications

There are many advantages of using Ni as an active species for SOFCs such as its low cost, high activity, and high stability even under reducing condition and/or high temperature (as high as 1,000 °C). To prevent sintering or coagulation of Ni particles at high temperature, Ni is normally dispersed on high surface area materials i.e. yttria-stabilized zirconia (YSZ) [123-125]. YSZ is not only to support and spread the Ni particles, but also to keep the thermal expansion coefficient compatible with cathode and electrolyte. The catalytic performance and electric properties of Ni/YSZ depend on microstructure and distribution of Ni and YSZ phases [126-128]. It was reported that the higher surface area of NiO is responsible for the higher shrinkage and the lower sintering starting temperature [129]. The conductivity of Ni-YSZ is mostly ionic if the concentration of Ni is lower than 30% by volume. In contrast, the conductivity of the overall catalyst system is electronic when the concentration of Ni is higher than 30% by volume, due to the fact that the metallic character of Ni becomes more dominant. The electrical conductivity of the Ni/YSZ anode was reported to be maximized at 30% by volume of Ni [130].

CeO_2 and its modifications

Many HCs reforming catalysts are capable for applications in fuel cells due to their mixed ionic and electronic conductivity (MIEC) properties [131-133]. Ceria is an outstanding catalyst for this matter. It also has high resistance towards coke formation, allowing the option of direct introduction of dry hydrocarbon fuels to the anode. Despite having high activity and high conductivity, however, ceria has low electrical conductivity which results in lower performance of the SOFCs. Thus, other metals; e.g. Ni, Co and Pt; can be doped onto the ceria. This enables the C-H bonds in HCs to be easily broken [134-137]. Doping 40% of an equimolar Cu and Co into the ceria was reported to increase coke formation, when methane was used as a fuel [138,139], in an intermediate temperature

SOFCs. Besides, this bimetallic Cu-Co formation was proven to show higher catalytic activity for methane oxidation, favoring charge transfer on the triple phase boundary, yet presenting high potential sulfur resistance in which it is often contained in the methane or biogas feed stream. Yttria and gadolinium were also found their uses in mixing with ceria for fuel cell's applications, due to their high ionic conductivity under oxidizing conditions and sufficient MIEC under reducing conditions. These anodes can be fabricated via spray coating with co-precipitation nanopowders. The anodes demonstrated good structural stability in direct carbon fuel cells (DCFCs) [140].

Perovskites and their composites

One of the limitation of Ni is that it cannot tolerate much of the carbon deposition, especially when the SOFCs is operated using dry HCs as fuel. The perovskites can ease the problem because of its OSC which is beneficial for combusting coke, thus, regenerating the material's surface. Structure of perovskite, ABO_3, can be schematically demonstrated as shown in Figure 5.28.

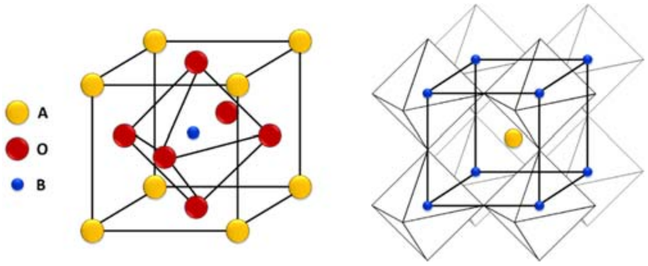

Figure 5.28: Molecular structure of a general perovskite (ABO_3) [121].

In general, the total charge of A and B is +6. The A-site cations; e.g. La, Sr, Ca and Pb; normally have lower valences, thus are larger and coordinated to 12 oxide anions. The B-sites cations; such as Ti, Cr, Ni, Fe, Co and Zr; would occupy much less space and are coordinated to 6 oxide anions. $PrBaCo_2O_5$ (PBCO) displayed excellent MIEC and fast oxygen kinetics when applied as an oxygen electrode in SOFCs [141]. $PrBaMn_2O_{5+\delta}$ (PBMO) was as well reported to be successfully fabricated by in situ annealing of $Pr_{0.5}Ba_{0.5}MnO_{3-\delta}$ under fuel conditions. The material showed high redox stability, high coke resistance and high sulfur tolerance. $Sr_2Fe_{1.5}Mo_{0.5}O_{6-\delta}/Gd_{0.1}Ce_{0.9}O_{2-\delta}$ (SFM-GDC), synthesized using low-temperature sintering assisted with wet-impregnation method, was reported to demonstrate an excellent resistance towards the sulfur poisoning. It can stand up to 100 ppm H_2S [142]. $La_{0.75}Sr_{0.25}Cr_{0.5}Mn_{0.5}O_3$ (LSCM) was found to possess an excellent resistance towards coke deposition, as an anode in SOFCs, even when operated under low moisture content (around 3%H_2O) using CH_4 as a fuel [143]. $La_{0.75}Sr_{0.25}Cr_{0.5}Fe_{0.5}O_{3-\delta}$ (LSCrF) showed high activity towards methane steam reforming, thus, was also applicable for SOFCs, which catalyzes stoichiometric methane oxidation and partial oxidation with its high OSC [144]. In terms of the importance of A or B substitution degree, A-site deficiency can enhance the valence charge of B-site metals and the formation of additional OSC. For instance, A-site deficient $SrTiO_3$-based perovskite with donor doping on Sr- or Ti- site could result in an increase of the electronic and ionic conductivity [145]. $La_xSr_{1-x}MnO_3$ (LSM) was doped on YSZ and utilized as a bi-layer structure cathode of a microtubular SOFCs whereas the anode and electrolyte was made of Ni-YSZ and pure YSZ, respectively. The overall system was fabricated and schematicalized as shown in Figure 5.29.

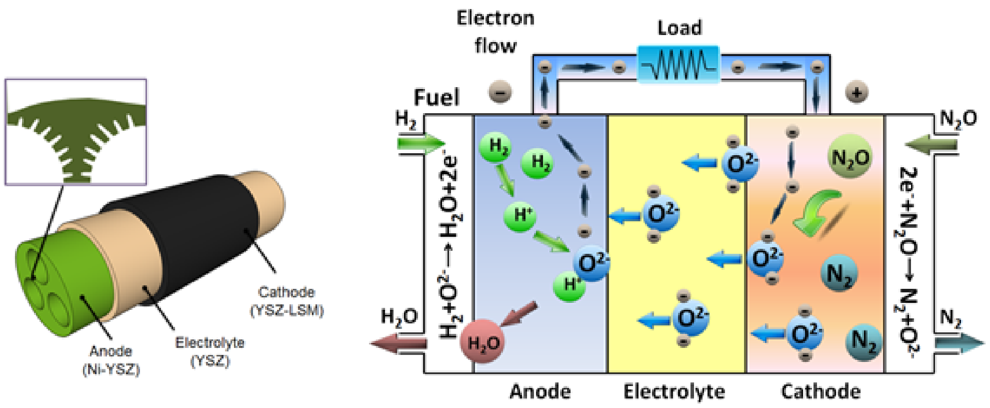

Figure 5.29: An illustration of materials used as different component in a microtubular SOFCs (a) and a schematic diagram of the SOFCs reactions and configurations when having N_2O as a source of oxidant [146].

The SOFCs's performance was reported to be improved by 50% when using N_2O as oxidant, instead of air [146]. The high power output was produced by N_2O decomposition at moderate temperature of 750 °C, indicating a successful integration between renewable energy production and greenhouse gas abatements. The morphological images of multi-channel anode and electrolyte were illustrated as shown in Figure 5.30.

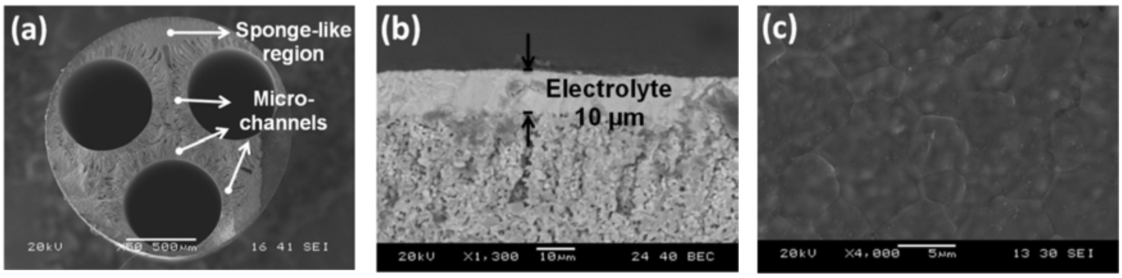

Figure 5.30: SEM images of (a) cross sectional anode, (b) cross-sectional electrolyte and (c) outer surface of the electrolyte [146].

The uniform channels of the anode were synthesized using an in-house designed spinneret where the internal coagulant was split into three streams, several phase inversion processes occurred simultaneously, leading to the formation of hierarchical asymmetric structure possessing both microchannels and high porosity region. Figure 5.31 shows the spinneret or the extruder used to fabricate this microtubular fuel cells.

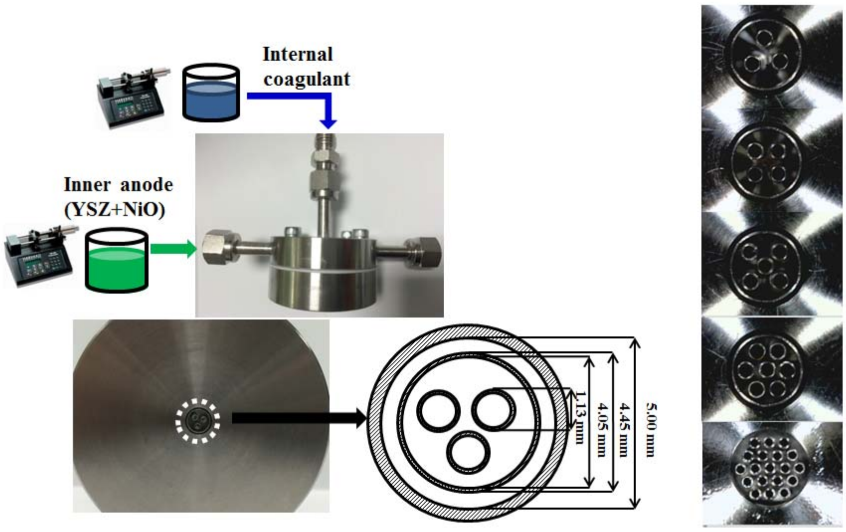

Figure 5.31: Schematic diagrams and images of the extrusion process of multi-nozzle spinneret [146].

The electrochemical performance of the microtubular SOFCs was tested using 30 ml/min of H_2 as the fuel, and 50 ml/min of N_2O as the oxidant, where the results from open-circuit potential differences (OCPDs) for various oxidant ranging from 1.15 to 1.17 V (set as near-theoretical values) were obtained. The highest power density of 0.31 W/cm^2 was achieved under operating temperature of 750 °C using N_2O as the oxidant. $La_{0.6}Sr_{0.4}Co_{0.2}Fe_{0.8}O_{3-\delta}$ (LSCF) was prepared as an orange-like ceramic-based membrane (OPM) which could be applied in SOFCs or oxygen separation, illustrated as Figure 5.32 [50].

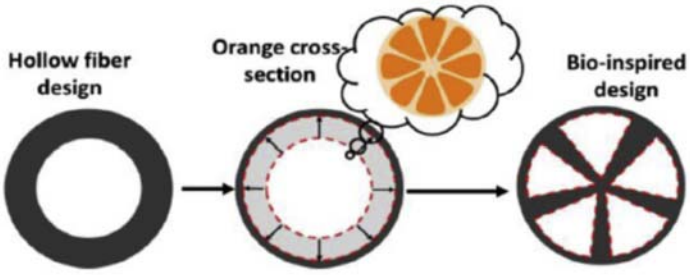

Figure 5.32: Schematic diagram of the bio-inspired design of LSCF fabrication [50].

5.4.1.2 ELECTROLYTE MATERIALS

Electrolyte is responsible for transportation of oxide ions from the cathode to the anode where the oxygen can react with the fuel. The oxide ions are conducted by a thermally activated oxygen vacancy hopping process. The crystal structure of a good solid electrolyte should have large available interionic spaces to attain a high level of point defect disorder and low migration enthalpy (normally < 1eV), to achieve high ionic conductivity. Besides, the electrolyte needs to be dense, to sufficiently avoid the gas permeation, yet has high chemical stability. Some high-temperature metal oxides i.e. ZrO_2, CeO_2, Bi_2O_3-based oxides and $LaGaO_3$-based perovskites are considered to be capable with the high operating temperature [147].

<u>ZrO_2 and its composites</u>

Zr-based materials are widely utilized as ion-conducting electrolytes in SOFCs because of its high thermal stability. At ambient temperature, the pure ZrO_2 is a monoclinic crystal which will be converted to tetragonal crystal at temperature above 1,170 °C, before finally changed to cubic fluorite structure at 2,370 °C and remained stable in such phase until up to its melting point at around 2,680 °C [148]. These structural phase changes are reversible when the temperature is reduced, resulting in a large volume change correspondingly. This dramatic change in volume causes material's cracking due to its low thermal shock resistance. Addition of Zr^{4+} ions with acceptor dopant cations will stabilize tetragonal or cubic phase of ZrO_2 at room temperature. Y_2O_3 can as well stabilize the cubic phase of ZrO_2 at temperature as high as 2,500 °C, as the valence of Y^{3+} dopant is relatively smaller than that of Zr^{4+}, thus, the oxygen vacancies are generated. These oxygen vacancies not only stabilize the cubic phase of ZrO_2, but also enhance the ion conductivity [149]. 8% by mole of Y_2O_3-ZrO_2 (8YSZ) was reported to have the highest ionic conductivity of 0.1 S/cm at 1,000 °C which is the minimum ionic conductivity required for a good electrolyte. Anodes of SOFCs, that use YSZ as an electrolyte, are often made of Ni-base materials because of their thermal compatibility. $La_{0.75}Sr_{0.25}Cr_{0.5}Mn_{0.5}O_{3-\delta}$ was found its use as an anode to match the YSZ electrolyte in SOFCs. YSZ is the most popular commercial electrolyte for SOFCs due to its high stability under reducing condition, low cost, simple handling process (e.g. spin coating), although it has relatively low electric conductivity when operated under low or intermediate temperature ranges [150]. For its applications in SOFCs, at least more than 95% of theoretical density should be achieved, thus the YSZ electrolyte can be considered as dense. This dense YSZ demands high temperature sintering process, up to 1,400 °C [151]. The high temperature sintering is not always desired, as such high temperature could encourage an unwanted reactions between the YSZ electrolyte and the cathode (e.g. LSM or LSCF), producing undesired resistive compounds (e.g. $La_2Zr_2O_7$ or $SrZrO_3$). The addition of sintering acids such as strontium gallate, copper and manganese can lower the sintering temperature down to 1,200 °C [152-157]. Sc_2O_3 doped ZrO_2 (ScSZ) is one of the most promising candidates for electrolyte in SOFCs. 11% by mole of Sc_2O_3 doped ZrO_2 was reported to have the ionic conductivity at 1.5 and 3 times higher than 8YSZ, at 850 and 1,000 °C, respectively [158], as shown in Table 5.4. In addition, ScSZ can offer the lower operating temperature of SOFCs because it has high ionic transference (under various temperatures and oxygen partial pressures) and excellent thermochemical properties. Its downsides, however, include complex phase assembly, conductivity degradation by time at high temperatures and poor accessibility [158].

Table 5.4: Properties of ZrO_2 based materials as electrolytes [158].

Composition (%by mole)	**Expansion coefficient (10^{-6} K^{-1})**	**Bend strength at 300 K (MPa)**	**Conductivity at 1,000 °C ($S.cm^{-1}$)**
3%Y_2O_3-ZrO_2	10.8	1200	0.05
8%Y_2O_3-ZrO_2	10.5	230	0.09
11%Sc_2O_3-ZrO_2	10.0	255	0.30

<u>CeO_2 based materials</u>

Despite having high OSC and large unoccupied octahedral sites (that provides a route for rapid diffusion of oxide ions), ceria itself does not possess sufficient ionic conductivity. To improve its ionic conductivity, additional oxygen vacancies can be established into the structure by substitution of the host Ce^{4+} with acceptor cations such as Gd^{3+}, Sm^{3+}, or Y^{3+} [159-163]. Gd was found to increase the ionic conductivity of the nanocrystalline CeO_2 thin film with a decreased activation energy due to its decreased grain size [164]. Sm and La doped similarly showed positive effects on ionic conductivity of the CeO_2-based catalyst system. $Ce_{0.9}Mo_{0.1}O_{2+\delta}$ demonstrated the highest electrical conductivity amongst all the other different ratios of Ce to Mo [165]. Ce^{4+} in the doped-ceria tends to be reduced to Ce^{3+} under reducing condition or low partial pressure of oxygen over a large range of operating temperatures. Despite having high ion conductivity, high phase stability and high electronic conductivity; the doped ceria materials exhibit poor mechanical properties, caused by the structure expansion (which is the result of increased size of the Ce^{3+} ions).

<u>Bi_2O_3 and its composites</u>

Pure bismuth oxide (Bi_2O_3) has various phases including α β, γ, and δ [166]. Amongst these phases, probably the face-centered cubic δ-Bi_2O_3 possesses the highest ion conductivity. The high-temperature fluorite structure of δ-Bi_2O_3 provides a high concentration of intrinsic oxygen vacancies (25% of the oxygen sub-lattice site), thus indeed offers high ionic conductivity. During a cooling down to 700 °C, from the higher temperatures, Bi_2O_3's phase will be transformed from the cubic (δ) to the monoclinic (α) phase and negatively influence its ionic conductivity, volume and structure. To maintain the cubic phase, even at low temperature, metal oxide dopants i.e. CaO, Y_2O_3, WO_3 can be partly substituted into the Bi_2O_3 catalyst system [167].

LaGaO$_3$ and its composites

For the $LaGdO_3$ electrolyte, substantial gallium deficits were commonly found on the surface, when operated under reducing condition at high temperature. This was the cause of high partial pressure of Ga oxides such as Ga_2O. Sr was reported to enhance the Ga depletion when added to the lanthanum sites, however, adding Mg to Ga sites showed no changes. When doping the $LaGaO_3$ with Mg, the vapor pressure of metal dopant i.e. Cr or Ga will not change the metal-deficient side. On the other hand, when doping $LaGaO_3$ with Ca or Sr, the vapor pressure of M will change noticeably. The correlation of actual diffusion coefficient and oxygen non-stoichiometry was tabulated as shown in Table 5.5 [168].

Table 5.5: Compositional dependence of D and α [168].

Composition	**D (cm^2/s)**	**A (cm/s)**
$LaGaO_3$	1.9×10^{-16}	1.5×10^{-10}
$LaGa_{0.9}Mg_{0.1}O_{2.95}$	2.6×10^{-16}	1.3×10^{-10}
$La_{0.9}Sr_{0.1}Ga_{0.8}Mg_{0.2}O_{2.85}$	1.3×10^{-15}	6.2×10^{-10}

Nevertheless, Ga ions tend to be lost under reducing condition for all the above materials. This results in the formation of new phases [169].

Oxyapatite and its composites

The general formula of oxypatite can be written as $A_{10-x}(MO_4)_6O_{2\pm\delta}$, where A stands for rare earth or alkaline earth, M represents Si or Ge. It is considered as an interesting family of oxide conducting solid electrolytes as its conductivity is comparable to the popular YSZ, when operated under medium temperature. One of the example for oxyapatite is $La_{9.33-0.67}(SiO_4)_6O_2$. The A-site deficiency has an effect on relaxation of SiO_4 tetrahedral and resulted in a displacement of the anions from the channels to new interstitial sites, therefore generating vacancies with stable oxygen content [170]. For example, the ionic conductivity of $La_{9.33+x/3}Si_{6-x}Al_xO_{26}$ will be enhanced when aluminum doping is balanced by A-site vacancies without a change in the oxygen content The conductivity was found to be maximized at $x = 1.5$. Some dense ceramics of apatite demonstrate number of oxygen ion transference higher than 0.995.

5.4.1.3 CATHODE MATERIALS

Cathode is responsible for electrochemical reduction of oxygen where it should accept electrons from the current collector. Cathode should have high electronic conductivity, sufficient porosity, high catalytic activity, high stability under oxidizing condition, and matching thermal expansion between electrolyte and the interconnect materials [171]. Perovskites were one of the first compounds finding their applications in fuel cells as cathodes since 1960s. Afterwards, the doped lanthanum cobaltites and lanthanum manganites were following the perovskites footstep in 1970s.

$LaMnO_3$ and its modifications

$LaMnO_3$ or lanthanum manganites has great compatibility with YSZ electrolytes [172]. Small amount of A site cations such as Sr^{2+} or Ca^{2+} into the $LaMnO_3$ improves performance of the overall catalyst system. Sr^{2+} was reported to be the most commonly used for doping the $LaMnO_3$, the compound is regarded as lanthanum strontium manganite (LSM). Like other high potential materials, the LSM has high electrical conductivity, high electrochemical activity, high thermal stability, and high compatibility with YSZ, GDC and LSGM. These reasons made LSM one of the most common cathode material with long durability.

$LaCoO_3$ and its modifications

Co-based perovskites have excellent electrochemical activity in oxygen reduction reaction and, just like most mixed metal oxides described here, have high mixed electronic and ionic conductivities. However, their major problem is that they have high thermal expansion with coefficient values of more than $20 \times 10^{-6}\ K^{-1}$, plus, they can interact with the YSZ (as an electrolyte) at temperature as low as 700 °C, leading to formation of undesired products which act as insulators. To minimize the effect of their thermal expansion, ceria can be doped into the catalyst system. Sr and/or Fe can be also partly substituted into the $LaCoO_3$ to improve its ion/electronic conductivity [9,11,12, 173]. The ratio between A-sites and B-sites, together with optimal operating conditions had been studied excessively.

A_2BO_4 and its modifications

A_2BO_4; e.g. $Mn_{1.5}Co_{1.5}O_4$, $CoFe_2O_4$, $LiNi_{0.5}Mn_{1.5}O_4$, and $Cu_{1.25}Mn_{1.75}O_4$; works as a cost-effective spinel-structured oxide protection layers to prevent Cr poisoning in the Cr-containing catalysts such as LaCr-based perovskites, which has its major advantage in being able to be operated under temperature ranging from 600 to 800 °C [174-178]. For example, $Mn_{1.5}Co_{1.5}O_4$ can lower the contact resistance between the cathode and stainless steel interconnect and simultaneously work as a mass barrier to hinder scale growth on the stainless steel, yet to prevent the segregation of Cr through the outer layer of coating [174-176]. $CoFe_2O_4$ was reported to have electrical conductivity of 0.85 $S.cm^{-1}$ whereas its thermal expansion's average coefficient was determined at 11.80×10^{-6} K^{-1}, from ambient to 800 °C. The dense and Cr-free $CoFe_2O_4$ spinel layer could help eliminate the Cr segregation, leading to an improvement in cell performance stability.

5.4.2 METAL OXIDES IN OTHER FUEL CELLS

The major role of metal oxides in other types of fuel cells relies on its ability to improve the mechanical properties when added as an additive/support of such fuel cell's components, electrodes and electrolyte.

TiO_2 and its composites

TiO_2 is beneficial for PEMFCs. Addition of TiO_2 into Nafion membrane was reported to increase its hydration performance which is helpful for high kinetics reactions occurring within the PEMFCs. The high kinetics reactions occur when the PEMFCs are operated at high temperature, resulting in a decrease in CO poisoning and increase the overall efficiency of fuel cells. Nafion-Pt-TiO_2 membranes were reported to exhibit higher water uptake and lower fuel crossover than the un-doped Nafion [179]. Pt nanoparticles doped TiO_2 were found to improve carbon stability and cathode performance of the PEMFCs due to the reduced contact between Pt and C. TiO_2 can also be utilized in DMFCs as an anode via photo-electro catalytic reaction. Ni doped TiO_2 showed good electro-catalysis behavior, giving a maximum power of 48 µW using methanol as a fuel source [180].

SiO_2 and its composites

SiO_2 works the same way as TiO_2 described in the previous section. SiO can be impregnated onto the Nafion via sol-gel processing of tetraethoxysilane and by preparing a recast film. The synthesized material showed the excellent wettability at 80 to 140 °C [181]. SiO_2 is a hydrophilic compound that has an excellent application in DMFCs. SiO_2 combined with sulfonated poly (arylene ether sulfone) exhibited high proton conductivity, long membrane life time under oxidative conditions, good dimensional stability, high single cell performance and minimized the methanol crossover [182].

WO_3 and its composites

One of the unique properties of WO_3 is its electro-chromic properties and its electro-catalytic activities. WO_3 will be intercalating and de-intercalating ions i.e. H^+ into its structure in the formation of tungsten bronzes such as H_xWO_3 where x is more than 0 and less than 1 [183,184]. Pt doped on WO_x were successfully applied in PEMFCs. It was reported that Pt in the WO_x system would increase the CO tolerance of the anode catalyst [185]. When applied as cathode, Pt-WO_3 demonstrated high stability and good response in single cells during the testing duration of up to 1,500 h. Pt-WO_3 can be combined with C and utilized in electro-catalytic and electro-oxidation of methanol in DMFCs. WO_3 can be also fabricated as mesoporous WO_3 microspheres with their sizes averaging around 5 nm, using spray drying method. The Pt-WO_3 based-materials were reported to establish hood electro-catalytic activity and good stability during the methanol oxidation [186].

Question 5.3
5.3.1 Give examples of businesses that use fuel cells in their applications 5.3.2 What are the challenges of fuel cells?

5.5 METAL OXIDES FOR HYDROGEN STORAGE

Most of the renewable and green energies are produced based on natural resources i.e. wind, solar and water, which are abundant but somehow can be very inconsistent. As the renewable energies are becoming more and more practical in the past decades, the energy storage technologies are then required to handle the unpredictable availability of the renewable energies correspondingly. When it comes to utilizing the renewable energy, there is always the incompatible and unpredictable mismatch between the renewable power generation and the load demand. Many energy storage applications have been being researched excessively, including batteries, capacitors, compressed air, flywheels, pumped hydro and many more [187]. Hydrogen storage is one of the most attractive technologies as it has high efficiency and is environmentally friendly. Hydrogen is not only well-known as a chemical feedstock which can be utilized further to many chemicals such as ammonia or methanol, but also is a clean energy resource that can provide low carbon industry, so called the hydrogen economy. One of the main challenges in hydrogen storage technology is that hydrogen has a high gravimetric energy density and a low volumetric energy density. It is light and it is large, under ambient temperature and pressure. The selection criteria of choosing the right hydrogen storage technology depends very much on its applications. For instance, in transportation application, hydrogen storage will be preferably stored at high density in a safe and light container. In contrast, if applied in a stationary applications, a high volumetric density will be finely accepted as it does not affect the efficiency of the system.

Hydrogen can be stored using 2 basic approaches as (1) stored as a compressed gas, (2) stored as a cryogenic liquid hydrogen and (3) stored as solid using advanced adsorption materials. The first two methods are quite well-explored, whereas the third method is still under research and development. The US Department of Energy (US DoE) has gathered information regarding current status of the hydrogen storage technologies, as tabulated in Table 5.6 [188].

Table 5.6: Targets and current status of H_2 storage technologies [188].

Storage targets	**Gravimetric kWh/kg (kgH_2/kg system)**	**Volumetric kWh/L (kgH_2/L system)**	**Cost USD/kWh (USD/kgH_2)**
2017	1.8 (0.055)	1.3 (0.040)	12 (400)
Ultimate	205 (0.075)	2.3 (0.070)	8 (266)
700 bar compressed (type IV)*	1.5	0.8	17
350 bar compressed (type IV)*	1.8	0.6	13
Metal hydride ($NaAlH_4$)	0.4	0.4	n/a
Sorbent (MOF-5, 100 bar)	1.1	0.7	16

*Projected H_2 storage system performance

The volumetric hydrogen storage capacity can be improved using the solid-state hydrogen storage, thus, it is considered as a sustainable solution according to it thermodynamic filling requirement time. The principle of this solid-state hydrogen storage is based on either (1) physisorption, involving weak binder energies of 4 to 10 kJ/mol (found in porous materials) or (2) chemisorption where the binder energies are estimated around 50 to 100 kJ/mol (in metal hydrides). For the chemisorption process over metal hydrides or complex hydrides, the gaseous hydrogen molecules will be dissociated on the surface of the solid material before the hydrogen atoms will be diffusing through the lattice of the metal [189]. Physisorption hydrogen storage is easier to process, comparing to the chemisorption, due to its reversible reaction and fast adsorption/desorption kinetics [190]. During the physisorption, the gaseous hydrogen will be physisorbed on the surface of the pores of the high porous materials such as zeolites, porous carbon structures and metal-organic frameworks (MOFs). The degree of physisorption thus relies almost solely on the specific surface area, pore volume, operating temperature and operating pressure. The physisorption hydrogen storage generally provides low hydrogen storage capacity (as low as 1 wt%) when operated under ambient temperature and pressure of 50 to 100 bar. However, when the physisorption hydrogen storage is operated under cryogenic operation (temperature of -196 °C under high pressure), its hydrogen capacity becomes more acceptable. The requirement for operating under the cryogenic temperature is not helpful as it needs to be maintained using liquid nitrogen, causing unnecessarily difficulties to practically process. Chemisorption is more straightforward. Hydrogen compounds occurred under elevated pressure, releasing heat as it is an exothermic reaction. The pressure will be reduced while the external heat will be applied, to release the gaseous hydrogen. When operating under ambient temperature, some metal hydrides can be operated reversibly, although offering only around 3 wt% of gravimetric hydrogen storage capacity [191]. However, 7 to 18 wt% of the gravimetric hydrogen storage capacity can be achieved using MgH_2 and $LiBH_4$, respectively, if operated under relatively high temperature [192]. MgH_2 is considered one of the most popular materials for hydrogen storage technology because it has high gravimetric hydrogen storage capacity, it is reversible and it is inexpensive [193]. It disadvantages include its high decomposition/desorption temperature and its low adsorption/desorption kinetics. Alloys, metal oxides, metal halides, carbon materials, metal hydrides and transition metal oxides (TMOs) can be mechanically milled with MgH_2, in order to increase the hydrogen adsorption kinetics [194-206]. Amongst these foreign compounds to be added, the TMOs was reported to be the most effective because TMOs are able to encourage the dissociation/recombination of hydrogen molecules and atoms, respectively. The oxygen in oxides is probably contributed to improve the reaction kinetics by eliminating the resistance of MgO layer formed on the surface of MgH_2 particles [192,207-209]. TMOs are interesting foreign compounds to be add in MgH_2 system, due to its good electrical and ionic conductivity, reversible capacity and mechanical stability. Nanostructured TMOs such as TiO_2, ZnO, SnO_2, $Zn_2V_2O_7$ hierarchical nanostructures (HNs) and hollow microflowers (HMFs) are good candidates for hydrogen storage advanced materials [210].

In principle, hydrogen will react with some metals and alloys to form metal hydrides, which has higher hydrogen storage capacity (6.5 H atoms/cm^3 for MgH_2) than gaseous hydrogen (0.99 H atom/cm^3) or liquid hydrogen (4.2 H atoms/cm^3) [211]. Thus, metal hydride-based hydrogen storage is considered safe, volume efficient, and suitable for on-board vehicle applications.

The hydration of metals could be categorized into 2 pathways: (1) direct dissociative chemisorption and (2) electrochemical water splitting. The two reactions are described as shown below.

Chemisorption of direct dissociation:

$$\mathrm{M} + \frac{x}{2}\mathrm{H_2} \leftrightarrow \mathrm{MH_x} \tag{5.41}$$

Electrochemical splitting of water:

$$\mathrm{M} + \frac{x}{2}\mathrm{H_2O} + \frac{x}{2}\mathrm{e^-} \leftrightarrow \mathrm{MH_x} + \frac{x}{2}\mathrm{OH^-} \tag{5.42}$$

There M stands for a metal.

Metal hydrides are made of metal atoms that possess a host lattice and hydrogen atoms. Two different kind of hydrides are normally formed within the metal hydride compounds which are: (1) α-phase where only some hydrogen is being adsorbed and, (2) β-phase at which hydride is fully formed. Performance of hydrogen storage depends on many parameters i.e. type of metals, metal's surface structure, metal's purity or the operating conditions [211]. Criteria for hydrogen storage material's selection includes: (1) high hydrogen capacity per unit mass and unit volume (depending on the applications), (2) low dissociation temperature, (3) moderate dissociation pressure, (4) low heat of formation in order to minimize the energy necessary for hydrogen release, (5) low heat dissipation during the exothermic hydride formation, (6) reversibility, (7) limited energy loss during charge and discharge of hydrogen, (8) fast kinetics, (9) high stability against O_2 and moisture for long cycle span, (10) cyclibility, (11) low cost of recycling and (12) high safety [189]. The light metals such as Li, Be, Na, Mg, B and Al, are especially interesting because of its light weight and number of hydrogen atoms per metal it can take, which is normally set around H/M = 2.

5.5.1 Mg-BASED METAL HYDRIDES

Mg and its alloy have been researched widely due to their high hydrogen storage capacity by weight and low cost. Magnesium hydride, MgH_2, is one of the most promising materials because it has the highest energy density at 9 MJ/kg Mg. in addition, it has high heat resistance, vibration adsorbing, reversibility and recyclability. The main downside of MgH_2 is the high temperature of hydrogen discharge/desorption (at 300 °C under 1 bar of hydrogen) [212-214], slow desorption kinetics and a high reactivity towards air and oxygen. Its optimal operating temperature is still too high to be practically applied on-board [215-217]. As mentioned earlier, adding small amount of foreign compounds can improve the overall catalytic properties of the MgH_2. For example, MgH_2-ZrO_2 was reported to be successfully prepared by high power ball milling [218] at the ratio of MgH_2 to ZrO_2 equaled to 99:1 and 95:5, respectively. ZrO_2 was reported to be uniformly distributed within the materials with less than 2 µm of particle size. Grain size of the materials with the 2 different ratios of MgH_2 to ZrO_2 were revealed by TEM. The results concluded that the 5 mol% ZrO_2 addition gave the smaller grain size (71.2 nm), compared to the one with 1 mol% (87.6 nm). Other TMOs; i.e. Nb_2O_5, V_2O_5, TiO_2, Sc_2O_3, Cr_2O_3, Mn_2O_3 and Fe_2O_3; also have the same influence on grain size similarly to the ZrO_2. In addition, ZrO_2 was found to be evenly distributed throughout the Mg matrix, leading to a near-ideal hydrogenation catalyst. ZrO_2 was found to increase the kinetic rate efficiently. The use of nanoparticles was reported to be more thermodynamically beneficial, than the bulk particles. Its thermodynamics are dominated by the energy differences between the metal and its hydrides. Its grain size also plays importance role in its efficiency. Table 5.7 demonstrates recent studies on Mg-based hydrides by properties of hydrogen adsorption/desorption [189].

Table 5.7: Hydrogen adsorption and adsorption properties of Mg-based hydrides [189].

Materials	Method	T (°C)		P (bar)		Kinetics (min)		Cycling ability	Max wt% H_2	Ref.
		T_{abs}	T_{des}	P_{abs}	P_{des}	T_{abs}	T_{des}			
MgH_2–5mol% Fe_2O_3	BM	300		2-15		20		n/a	1.37	[196]
30wt%Mg–M mNi$_{5}$–*x* *(*CoAlMn*)$_x$*	BM	15		6		83		n/a	2.30	[219]
Mg–5wt%$FeTi_{1.2}$	BM	400	400	30	1	n/a	n/a	9 cyc, stable after 4th	2.70	[220]
MgH_2–5mol% V_2O_5	BM	250		15		1.6		n/a	3.20	[196]
90Mg–10Al	BM	400	400	15	12	2.7-19	0.5-5.8	n/a	3.30	[221, 222]
Mg–50wt% $ZrFe_{1.4}Cr_{0.6}$	BM	250-350	300-350	20	1	1	5	2 cyc, stable	3.40	[223]
Mg–10wt% CeO_2	BM	300	300	11	0.5	60	60	5 cyc, unstable	3.43	[224]
Mg–20wt%Mm (La, Nd, Ce)	BM (pellet)	300	480	10	1	10	5	n/a	3.50	[225]
Mg–40wt% $ZrFe_{1.4}Cr_{0.6}$	BM		270-280		1		15	2 cyc, stable	3.60	[226]
La_2Mg_{17}–40wt% $LaNi_5$	BM	250-303	250-303	4-7	4-7	0.45	4	20 cyc, unstable	3.70	[227, 228]
$La_{0.5}Ni_{1.5}Mg_{17}$	Hydriding combustion	280-400	280-400	2.2-11.3	1.6-15.5	15	5	Unstable	4.03	[229]

(Continued)

Table 5.7: *(Continued)*

Materials	**Method**	**T (°C)**		**P (bar)**		**Kinetics (min)**		**Cycling ability**	**Max wt% H_2**	**Ref.**
		T_{abs}	T_{des}	P_{abs}	P_{des}	T_{abs}	T_{des}			
Mg–50wt% $LaNi_5$	BM		250-300	10-15	10-15	3.33		Unstable	4.10	[230]
MgH_2–2$LiNH_2$	BM	200	200	50	10		60	4 cyc, stable after 2nd	4.30	[231, 232]
Mg_2CoH_5	Mixing	450-550		17-25		n/a	n/a	1,000 cyc, stable	4.48	[233]
MgH_2–5mol% Al_2O_3	BM	300		15		67		n/a	4.49	[218]
1.1MgH_2–2$LiNH_2$	BM	200		30		30		9 cyc, stable	4.50	[234, 235]
Mg–20wt%TiO_2	BM	350	330-350	20	1	2	10	n/a	4.70	[236]
Mg–30wt% $MmNi_{4.6}Fe_{0.4}$	BM (hexane medium)		300-550		2		30	n/a	5.00	[237]
MgH_2–5wt%V	BM	300	300	1-3	1-3	2	10	2,000 cyc, stable	5.00	[238]
Mg–Fe–Mg_2FeH_6	Mixing	473-552		77-85		90		600 cyc, stable	5.00	[233]
MgH_2–Mg_2FeH_6	Mixing	350-525	350-525	3.6-93.7	3.6-93.7	90-1,440		600 cyc, stable	5.00	[239]
MgH_2–5wt%Ti	BM	200	300	10	0.15	0.83	3.33	n/a	5.00	[193]
MgH_2–5wt%Ni	BM	200	300	10	0.15	16.7	5	n/a	5.00	[193]
Mg–30wt% $LaNi_{2.28}$	BM	280		30		1.6		3 cyc, stable	5.40	[240]
MgH_2–5wt%V	BM	200	300	10	0.15	1.66	3.33	n/a	5.50	[193]
Mg–10wt% Fe_2O_3	BM	320		12		n/a	n/a	3 cyc, stable	5.56	[241]
Mg–30wt% $CFMmNi_5$	Mixing and encapsulation	500	500	3-10	3-10		40	n/a	5.60	[242]
Mg–10wt% Al_2O_3	BM	300	300	11	0.5	60	60	5 cyc, unstable	5.66	[224]
MgH_2–5wt%V	BM	200	300	10	0.15	4.2	33	n/a	5.80	[243]

(Continued)

Table 5.7: *(Continued)*

Materials	Method	T (°C)		P (bar)		Kinetics (min)		Cycling ability	Max wt% H_2	Ref.
		T_{abs}	T_{des}	P_{abs}	P_{des}	T_{abs}	T_{des}			
Mg–10wt% Cr_2O_3	BM	300	300	11	0.5	60	60	5 cyc, unstable	5.87	[224]
Mg/MgH_2–5wt% Ni	Wet-chemical method	230-370		4.0-1.4	4.0-1.4	90		800 cyc, stable	6.00	[233]
MgH_2–5wt%Mn	BM	200	300	10	0.15	13.33	8.33	n/a	6.00	[193]
MgH_2–0.2mol% Cr_2O_3	BM	300	300	1-2	1-2	6	10-35	1,000 cyc, stable	6.40	[244]
MgH_2–2mol%Ni	BM		150-250		1		150	2 cyc, unstable	6.50	[245]
MgH_2–1mol% Cr_2O_3	BM	300	300	8.4	Vac.	2	6	n/a	6.70	[192]
MgH_2	BM	300	350	3-10	0.15		12.5-50	n/a	7.00	[246]
$3Mg(NH_2)_2$–8LiH	BM		140-190		1	n/a	n/a	n/a	7.00	[247]
Mg–0.5wt% Nb_2O_5	Mixing	300	300	8.4	Vac.	1	1.5	n/a	7.00	[235]
MgH_2–1wt%Al	BM	180	335-347	0.6	n/a	420		n/a	7.30	[248]
MgH_2–5wt%Ge	BM		50-150		n/a	n/a	n/a	n/a	≤7.60	[249]

Most researches on Mg-based hydrides are based on minimizing the desorption temperature and increasing the rates of hydrogenation/dehydrogenation reactions on the surface. The ball-milling (which is a mechanical alloying) described earlier, is one of the method to mix the microstructure of the hydride with other metal compounds, in order to improve the adsorption/desorption kinetics [250].

5.5.1.1 IMPROVEMENT ON SURFACE PROPERTIES AND MECHANICAL BALL-MILLING

Surface is the key factor for hydrogen adsorption by metals. Hydrogen molecules will be dissociated on the surface of metal before the dissociated hydrogen atoms can be transferred via solid-state diffusion within the bulk metal. For pure Mg, at the beginning the chemisorption rate is the limiting step as it is slower than the diffusion rate, which has no obstacle because no reactions occur in the first place, thus, no product layers to be formed and acting as a diffusion resistance [251,252]. After a certain time of reaction, the hydride layer grows and becomes almost a near-impermeable layer. At this point, the diffusion then becomes the limiting step during the hydride formation process.

Ball milling

The ball-milling process establishes new surface with rich properties [212]. The objectives of ball-milling process is to increase the specific surface area, to form micro and nanostructure, and to generate the desired lattice defects both at the surface and within the bulk/interior. The defects are believed to ease the diffusion of hydrogen by providing more sites with low activation energy of diffusion. The induced microstrain helps diffusion by reducing the hysteresis of hydrogen adsorption and desorption [220]. The increased surface area enhances the kinetics rate of hydrogen transformation. The properties of the storage solid material can be tailored to a specific requirement by adjusting the composition of the alloys, altering the surface properties, adapting the microstructure, nanocrystalline and grain size of the materials; using ball-miller. This technique is affordable while minimizing the loss of storage capacity. The structural differences between milled and un-milled crystalline MgH_2 were observed [246]. The specific surface area of MgH_2 was reported to increase 10 times if milled. The milled MgH_2 exhibited faster hydrogen desorption kinetics, reduced the activation energy compared to the un-milled sample, as presented in Figure 5.33.

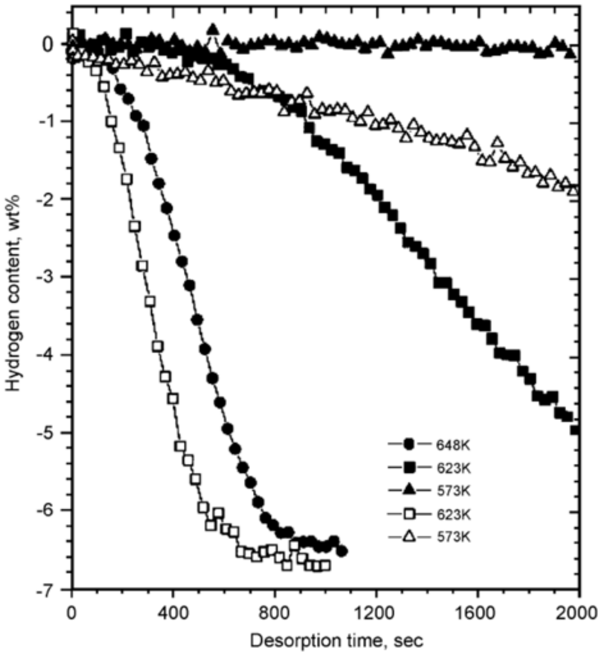

Figure 5.33: Desorption of hydrogen compared between milled and un-milled MgH_2 under a hydrogen pressure of 0.15 bar [246].

The activation energies for desorption were determined at 156 and 123 kJ/mol for the un-milled and milled MgH_2 powders, respectively. The ball-milled Mg_2NiH_4 thus showed lower desorption temperature. The reduction of desorption temperature can be as significant as 100 °C for MgH_2 and 40 °C for Mg_2NiH_4, depending on the ball-milling conditions [253]. The ball-mill powders was reported to be readily active, meaning that the activation process is not required, unlike the conventional ones. The pressure-composition (P-C) isotherms was not much affected by the grain boundary. This thermodynamic aspects of hydrides formulation can be more visible using Van't Hoff plot, demonstrating the relationship between equilibrium pressure and changes in enthalpy and entropy, as shown in Figure 5.34. The pressure of hydrogen desorption of the un-milled MgH_2 was lower than that of the milled one.

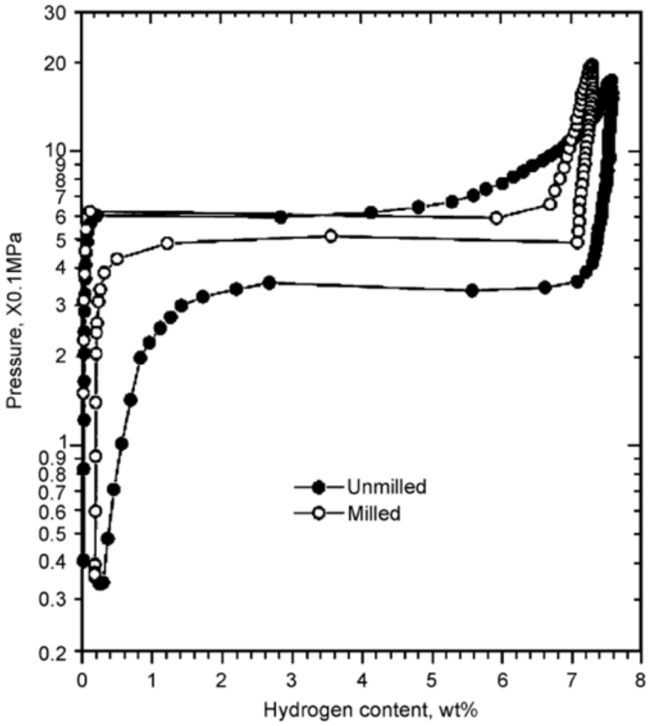

Figure 5.34: Pressure-concentration-temperature plots of the un-milled and milled MgH_2 at 350 °C [246].

Performing the ball-milling procedure in an inert atmosphere was reported to reduce the particle size of the alloys, and create fresh new surfaces, which leads to an increase in hydrogen absorption rate. Besides, the hydrogen absorption rate was found to increase when the milling time is increased [220], due to the large amount of phase boundaries and the porous surface structure [230]. Nanocrystalline hydrides were reported to increase the hydrogenation kinetics even at low temperature. The nanoscrystalline hydrides can be created by means of local change in the stable atomic positions into the metastable configuration. $LiNH_2/MgH_2$ was reported to have low dehydrogenation at 200 °C, although it has low kinetic rate and low yield of hydrogen uptake [231]. Smaller clusters of MgH_2 showed much lower desorption energy than bulk MgH_2, leading to a lower temperature of hydrogen desorption. The hydrogen desorption energy was found to decreased when the crystal grain size was decreased, especially if it is lower than 1.3 nm. For example, MgH_2 with its crystallite size of 0.9 nm would have the hydrogen desorption temperature of 200 °C, approximately. Nanocrystalline particles with grain size smaller than 10 nm normally increase the density of grain boundaries, resulted in easier activation [254,255]. The hydrogenation process was found to be able to occur during the ball-mill process [256-258], which enhanced the kinetics of formation of high hydrogen-content hydrides.

<u>Adding foreign metals</u>

Mg-10wt%Fe_2O_3 can also be synthesized using the mechanical grinding method under H_2 rich atmosphere [241]. The hydrogen absorption rate was found to increase, because the increased surface defects (of Mg) are facilitating nucleation. Mg particle size was also reduced, resulted in a shorter distance for hydrogen atoms to diffuse.

The addition of Ni demonstrated similar effects on MgH_2 performance. Ni was found to lower the hydrogen desorption temperature of MgH_2 to 225 °C by ball-milling under hydrogen atmosphere [257]. The alloying time had a significant effect on absorption capacity of the hydrides. The reaction kinetics was improved when the milling time was increased [258-262], as shown in Figure 5.35.

In research, the metal hydrides are generally fabricated as bulk materials, rather than thin films. Although the thin film hydride gives much better performance. Pure Mg was research on this fabrication choice, it was concluded that the thinner Mg sheet provided faster kinetics of hydrogenation (completed MgH_2 formation). Hydrogen was found to be able to transport within the solid material for around 30 µm before it was stopped [263]. Ball-milling process can generate powders in the range of 60 to 100 µm in size [262]. The smaller particle size of metal hydrides can eliminate the formation of hydride layers that are thicker than 50 µm [215]. Thus, thin film fabrication is useful as it can ease the complication of transporting hydrogen over the thick layers of the already-formed hydrides. Mg was found to be totally converted to MgH_2 at temperature lower than 200 °C [264].

Nanocomposite three-layered Pd/Mg/Pd films were researched [261]. Pd layers was found to accommodate only 0.15 to 0.30 wt% of hydrogen, whereas Mg films contain 5.0 wt% of hydrogen, post exposure under H_2 atmosphere at 1 bar at 100 °C. Desorption temperature was decreased when the degree of crystallization of Mg layer (in Pd/Mg films) decreased. The degree of crystallization of Mg layer in Pd/Mg films can be achieved by different sputtering conditions. The minimal crystallization of the film was found to absorb 5.6 wt% of hydrogen and all the hydrogen was fully desorbed at temperature lower than 190 °C in vacuum.

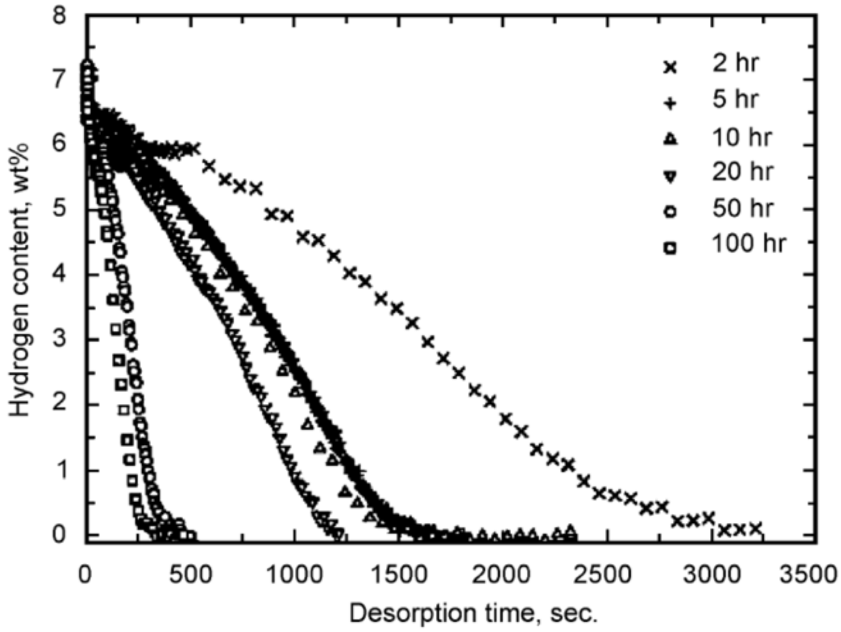

Figure 5.35: Desorption profiles of Mg-0.1mol%Nb_2O_5 when milled for 2, 5, 10, 20, 50 and 100 h at 300 °C and vacuum [261].

Organic solvent mechanical alloying

Organic solvents such as benzene, cyclohexane or carbon materials; can be introduced during the ball-milling process [265,266], to improve the solid-material's performance. Benzene assisted ball-milled MgH_2 showed reversible hydriding/re-hydriding capacity under 1 bar of hydrogen. Organic additives were proposed to be necessary for the production of nanosize magnesium with high dispersion. Wet milling with toluene seemed to pick up hydrogen and carbon, and also requiring much longer milling time [267].

Ni addition

$MgNiH_4$ is a promising material for solid-state hydrogen storage because it possesses high capacity and unusual structural/bonding properties, yet is low cost, light weight and low-toxicity [268-270]. Table 5.8 shows kinetics of hydrogen absorption/desorption in the presence of Mg-Ni-based hydrides over various conditions.

Table 5.8: Hydrogen absorption/desorption kinetics of Mg-Ni-based hydrides [189].

Material	Method	Temperature (°C)		Pressure (bar)		Kinetics (min)		Cycling stability	Max. weight of H_2	Ref.
		T_{abs}	T_{des}	P_{abs}	P_{des}	T_{abs}	T_{des}			
Mg_2Ni–1wt% Pd	BM	200		15		27		4 cyc, stable	2.50	[271]
Mg_2Ni	BM	300		29		n/a		5 cyc, unstable	3.20	[272]
Mg_2Ni	BM	300		11.6		10		4 cyc, stable	3.50	[271]
Mg_2Ni	BM	280	280		1-2	n/a		n/a	3.53	[273]
Mg–Mg_2Ni	BM	300		12		83		2 cyc, unstable	3.60	[274]
Mg_2Ni	BM	280-330	280-330	1-15	1-2	1	1	n/a	4.10	[267]
70wt%Mg–30wt%$LaNi_5$	BM	350	350	10	1.5	30	10	10 cyc, stable	4.66	[275, 276]
65wt% MgH_2–35wt% Mg_2NiH_4	BM	220-240	220-240		0.5	10		20 cyc, stable	5.00	[253]

Mg_2NiH_4 was formed by hydrogenation of Mg_2Ni [277]. Its chemical reaction can be written as:

$$\mathrm{Mg_2Ni{+}2H_2 \rightarrow Mg_2NiH_4} \tag{5.43}$$

During the hydrogenation process, the Mg_2Ni will react with 3.6 wt% of hydrogen and becoming the Mg_2NiH_4. De-hydriding temperature was observed at 350-300 °C, at desorption pressure of 2.1 to 3.0 bar [253,260,269,273]. Mg_2Ni is advantaged over other magnesium hydrides because of its high hydrogen capacity of 4 hydrogen atoms per Mg_2Ni and its light specific weight [278]. Nanostructure Mg_2Ni can react with hydrogen at room temperature whereas polycrystalline $MgNi_2$ needs the hydrogenation temperature to be as high as 250 to 350 °C, under 15 to 50 bar [269].

5.5.1.2 CYCLIC ABILITY

Cyclic ability can be defined as how efficient/how much performances of the solid materials are when being treated under cycling condition. Cyclic ability depends on many factors i.e. its nature, additives, cycling temperatures, starting microstructure and its intermediate phases. Mixed oxides; e.g. Cr_2O_3, Al_2O_3 and CeO_2; were added into magnesium hydrides as additives. All the compounds were found to lose its performance after the 5th cycle, due to the agglomeration of the particles during the process [224]. Misch metals (Mm); such as Ce, La, Nd and Pr; had been applied to increase to cyclic ability [279]. However, the addition of Mm can have an adverse effect on hydrogen storage capacity and its reaction rate [225]. Formation of the phase changes, segregation, and disintegration can be observed in La_2Mg_{17}+40wt%$LaNi_5$ during the cycling process at temperature of 350 °C. The hydrogen capacity of $La_{0.5}Ni_{1.5}Mg_{17}$ was decreased as the cycling proceeded [229].

Number of cycling as high as 1,000 or 2,000 cycles were researched [233,238] over metal compounds-doped magnesium hydrides. Ni-doped Mg and Mg_2CoH_5 were reported near-stable even after 800 cycles with only small fluctuations in hydrogen capacity, as shown in Figure 5.36 [233].

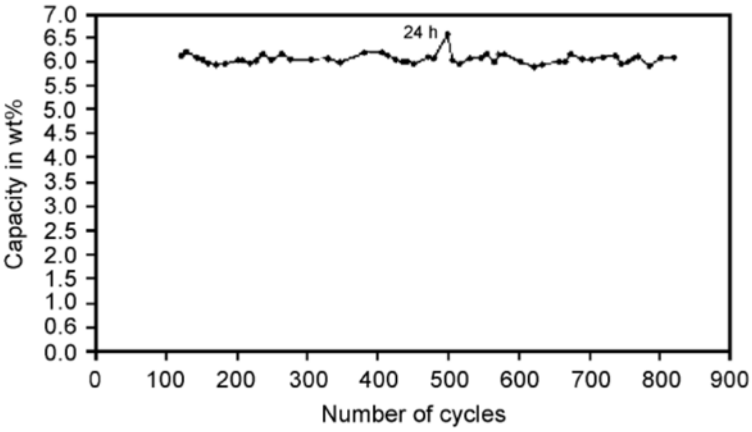

Figure 5.36: Cyclic stability of Ni-Mg at 230-370 °C, under 4 bar, experimenting over 3 h [233].

MgH_2-5wt%V was studied over 2,000 cycles [238]. The material was reported stable even when the hydrogen capacity reached 5 wt%. No change in isotherms or disintegration was detected. For MgH_2+0.2mol%Cr_2O_3, the hydrogen capacity/hydrogen storage of the material was found to even increase during the cycling process by 8%, approximately, This was concluded to be the cause of structural relaxation and crystallite growth [244]. Mg-2wt%Ni alloy was found to be losing its kinetics of hydrogenation/dehydrogenation during its 4,300 cycles test, however, its hydrogen capacity was found to remain the same, although it needs higher operating temperature to reach the same level of uptake/release [280]. The nanocrystalline Mg_2Ni showed a decrease in hydrogen capacity by 15% after 2,100 cycles, due to the formation of non-hydride phases [281].

Feed impurities

The impurity tolerance is one of the main criteria for selection of solid-state hydrogen storage materials. The influence of gaseous N_2, O_2, CO_2, and CO were investigated on a pure magnesium powder [282]. O_2 and N_2 was found to slow down the hydrogen absorption, whereas CO and CO_2 inhibited the hydrogen uptake. H_2O was reported to increase the hydrogen storage capacity by 5% over MgH_2-V-Ti, however, it desorption characteristic was worsen due to the surface deterioration of the particles [283,284].

Question 5.4
5.4.1 What are the difficulties of H_2 storage? 5.4.2 Name techniques that are recently used/being developed for higher efficiency of storing H_2

5.5.1.3 CATALYST EFFECT

The intrinsic rate of hydrogen absorption in the solid-state hydrogen storage is governed by (1) the rate of hydrogen dissociation on the surface, (2) the solid-diffusion of hydrogen from the surface (covered by oxide layers) to the bulk solid metal, (3) the rate of solid-diffusion of hydrogen from the surface (where hydride layers already formed) to the bulk solid metal. Catalyst is therefore taken into account, as the effective catalysts can encourage the formation of hydride in significant content.

Pd, Ni, Ge and V were applied into the magnesium hydrides. Amongst these catalysts, Ni was probably showing the most impressive improvement by (1) increasing 50% hydrogen storage capacity of the solid material, (2) yet decreasing the temperature of the hydrogenation process from 275 to 175 °C [262], and (3) decreasing the temperature of de-hydrogenation from 350 to 275 °C. Pd was also a good catalyst. Despite its cost, the specialty includes oxygen tolerance, as palladium oxide, if formed, can be easily decomposed afterwards. Pd was added into Mg_2Ni, $LaNi_5$, and FeTi solid materials [271]. Pd was concluded to enhance the absorption rates at lower temperature and resistance to air or oxygen exposure. The addition of Ge was found to decrease the hydrogen desorption temperature, ranging from 50 to 150 °C, depending on the catalyst level. Nevertheless, the performance of Ge-based material was reduced after a few cycles of hydrogenation/de-hydrogenation [249]. V can increased the hydrogen storage capacity by 5.8 wt% while the thermodynamics parameters of the process was maintained [243], as illustrated in Figure 5.37.

Ti and V are useful for preventing the oxidation of the alloy surface, thus increase desorption capacity over cycling process [284]. The addition of some metal oxides; e.g. V_2O_5, Cr_2O_3, Fe_3O_4 were found to improve the kinetics of MgH_2. Amongst these metal oxides, Cr_2O_3 was outstanding for fast hydrogen absorption, while V_2O_5 and Fe_3O_4 render rapid hydrogen release [192,196,224,244].

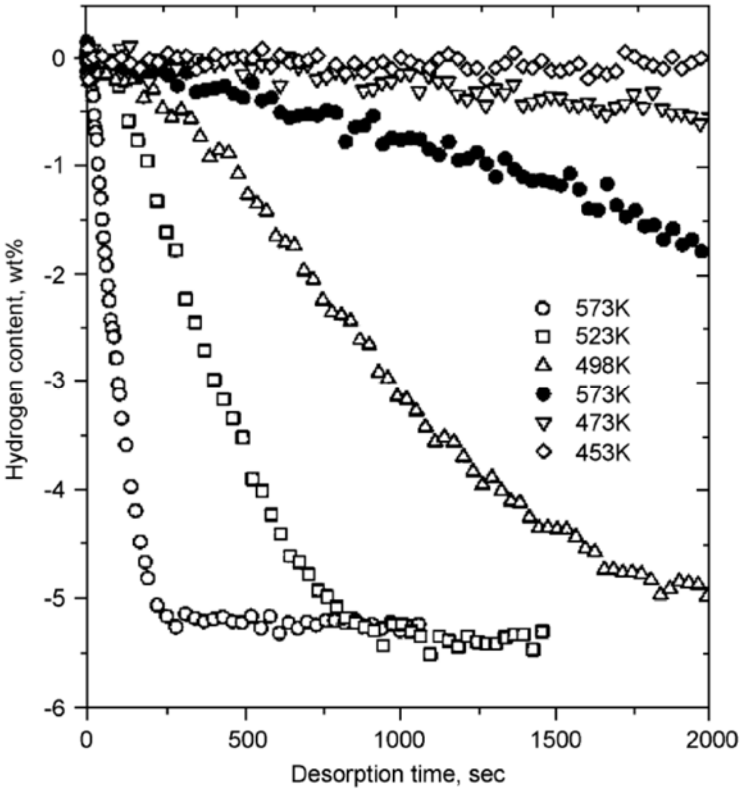

Figure 5.37: Hydrogen desorption profiles of ball-milled MgH_2-5wt%V (hollow) and MgH_2 (solid) under operating pressure of 0.15 bar [243].

In summary, efficient and inexpensive catalysts are still being searched for. New type of compounds such as solium alanates and magnesium alanates have been demonstrated in this application, as well as hydrogen generation/storage by hydrolysis [285].

5.5.1.4 CHEMICAL COMPOSITION

Composition has influences on properties of solid materials towards the hydrogen storage performance. In the Mg/Al alloys, the hydrogen capacity was found to decrease when Al level was decreased, although the kinetics was improved. The ball-milling process allows combination of two or more phases having different hydrogenation characteristics [221]. The ball-milling process enables an increase in solubility limit of the foreign compound in the host material. Mg_2FeH_6-MgH_2 can have the maximum amount of stored hydrogen of 5.0 wt% (around 30% less than the iconic MgH_2 which that of was 7.7 wt%) Mg_2FeH_6-MgH_2 has low price of precursors, constancy of the heat delivery temperature by controlling the applied hydrogen pressure and absence of heat losses with time. The intermetallic hydride, Mg_2FeH_6 exhibits the high volumetric hydrogen density of 150 kgH_2/m^3, more than 2 times of that provided by the liquid hydrogen [221].

5.5.2 COMPLEX HYDRIDES

Complex hydrides are known as one-pass hydrogen storage system where hydrogen is created by contact with water. Na, Li and Be are the only elements that are lighter than magnesium and are able to form solid-state compounds with hydrogen [189]. The hydrogen content can be as high as 18 wt% for $LiBH_4$, although all the complex hydrides have one common challenge – both thermodynamic and kinetic limitations. The complex hydrides such as alanates $(AlH_4)^-$, amides $(NH_2)^-$ and borohydrides $(BH_4)^-$ were studied. The hydrogen is generally located at the corners of a tetrahedron. Borates are considered stable and decomposed only at high temperatures. Alanates have excellent hydrogen storage capacity, although they are decomposed in 2 steps upon dehydriding [286].

5.5.2.1 SODIUM ALANATES

Sodium alanates are the complex hydrides which are formed by sodium and aluminum. Complex aluminum hydrides without other metal are not considered rechargeable hydrogen carriers due to its irreversibility and low kinetics. However, when doped with other transition metals or rare-earth metals, i.e. sodium, such complex hydrides become reversible. Doping Ti compounds into the aluminum hydrides was reported to enhance the reaction's kinetics, reversibility under moderate conditions [287,288]. Sodium aluminum hydrides ($NaAlH_4$) is a good candidate for hydrogen storage application because it has theoretically reversible hydrogen capacity of 5.6 wt%, is low cost and is abundant. These complex hydrides release hydrogen via a series of decomposition reactions. Such reactions in the presence of $NaAlH_4$ is shown below:

$$\mathrm{NaAlH_4} \leftrightarrow \frac{1}{3}\mathrm{Na_3AlH_6} + \frac{2}{3}\mathrm{Al} + \mathrm{H_2} \tag{5.44}$$

$$\mathrm{Na_3AlH_6} \leftrightarrow 3\mathrm{NaH} + \mathrm{Al} + \frac{3}{2}\mathrm{H_2} \tag{5.45}$$

$NaAlH_4$ (sodium tetra-hydro-aluminate) and Na_3AlH_6 (trisodium hexa-hydro-aluminate) contain hydrogen of 7.4 and 5.9 wt%, respectively. During the overall decomposition process, Na_3AlH_6 would be formed in the first step as an intermediate, together with gaseous hydrogen and metallic Al. Afterwards, the Na_3AlH_6 will be further decomposed to NaH, together with another set of metallic Al and gaseous hydrogen. The kinetics of both reactions are relatively slow. These reactions are reversible which should be concerned as the evolved hydrogen could be converted back to the sodium alanates, under severe conditions. By stoichiometric calculation, the hydrogen evolution of equations (5.44) and (5.45) is theoretically estimated at 3.7 and 1.9 wt%, for a theoretical net reaction of 5.6 wt% reversible gravimetric hydrogen storage [288]. The first decomposition step (equation (5.44)) occurs at temperature ranging from 185 to 230 °C, whereas the second step of decomposition takes place at slightly higher temperature of 260 °C, approximately. NaH, in fact, can be further decomposed, however, at temperature as high as 425 °C. Thus, this high temperature decomposition step is not generally taken into account as the reaction temperature is too high for any practical (on-board) storage system. Some catalysts were reported to be added onto the sodium alanates and successfully enhance the overall performance of the materials [289], as demonstrated in Table 5.9.

Table 5.9: Characteristic and properties of sodium alanates when utilized as a solid-state hydrogen storage material [189,289].

Material	Method	Temperature (°C)		Pressure (bar)		Kinetics (min)		Cycling stability	Max. weight of H_2	Ref.
		T_{abs}	T_{des}	P_{abs}	P_{des}	T_{abs}	T_{des}			
Na_3AlH_6	Mechano-chemical synthesis		200		1		150	n/a	2.50	[290]
Na_2LiAlH_6	BM	211		45		100		n/a	2.50	[291]
$NaAlH_4$–2mol%Ti(Obu*n*)$_4$–2mol%Zr(OPr*i*)$_4$	BM	125-165	125-165	101-202	101-202	60	180	5 cyc, unstable	3.00	[292]
$NaAlH_4$–4mol%Ti	BM	120	150	120	1	60	600	8 cyc, unstable	3.30	[293]
$NaAlH_4$–2mol%Ti	BM	25-193	25-160	20-120	1	300-720	40	n/a	3.80	[294]
$NaAlH_4$–2mol%(Ti(Obu*n*)$_4$	Mixing	120	180-260	60-150	60-150	1,020	120-300	25 cyc, unstable	4.00	[288]
$NaAlH_4$–2mol%Ti(Obu*n*)$_4$	Mixing	120-135	160-180	130-150	130-150	330	90	33 cyc, unstable	4.00	[287]
$NaAlH_4$–2mol% $TiCl_3$	BM		100-125		83-91		20	5 cyc, unstable	4.00	[292]
$NaAlH_4$–2mol%Zr(OPr)$_4$	Mixing		200		1		n/a	3 cyc, stable	4.00	[295]
$NaAlH_4$	Mechano-chemical synthesis	80-180	80-180	76-91	76-91	120-300	300	2 cyc, unstable	5.00	[296]

(Continued)

Table 5.9: *(Continued)*

Material	Method	Temperature (°C)		Pressure (bar)		Kinetics (min)		Cycling stability	Max. weight of H_2	Ref.
		T_{abs}	T_{des}	P_{abs}	P_{des}	T_{abs}	T_{des}			
$NaAlH_4$–2mol%(Ti(Obun)$_4$)	Mixing	104		88		1,020		3 cyc, stable	4.00	[289]
$NaAlH_4$–2mol%Ti(Obu*n*)$_{4\text{-C}}$	Mixing		200		1		n/a	Unstable	5.00	[297]
$NaAlH_4$–2mol% TiN	BM	104-170		115-140			30-1,200	25 cyc, stable	5.00	[298]

When adding the liquid alkoxides; such as $Ti(OBu^n)_4$ or $Zr(OPr^i)_4$; into the sodium alanates, the hydrogen release is often contaminated by hydrocarbon. The surface of sodium alanates are also likely to be damaged by such catalysts, causing a decreased number of cycles. On the other hand, $TiCl_3$ catalyst has a positive effect on the sodium alanates [299]. It contributes to a reduced weight of the solid material and an increased hydrogen storage capacity. The hydrogen release/uptake capacity of the $TiCl_3$ doped $NaAlH_4$ was reported to increase around 50 times higher than the un-doped one. TiN and ZrO_2 were also reported to have a positive influence of the overall performance of the materials. Although ZrO_2 has less positive effect on the hydrogen storage capacity and stability, compared to the titanium oxide group, however, it was better at dehydriding the Na_3AlH_6 to NaH and Al. The state of Ti precursor was reported to be have stronger influences in the hydrogen capacity, than the level of Ti. Smaller size of Ti particles is responsible for an increase of the reaction rate [300]. However, Ti is not the best catalyst for improving the kinetics, in some studies, it was reported that the dehydrogenation desorption process could take up to 4,200 min [299]. Mechanical alloyed Na_3AlH_6 was found to exhibit higher kinetics rate than Na_3AlH_6 which obtained from the decomposition of $NaAlH_4$ [301].

5.5.2.2 LITHIUM AND POTASSIUM ALANATES

Lithium alanates has even higher hydrogen storage capacity, compared to the sodium alanates. However, its main drawback is its extremely high equilibrium pressure of hydrogen at room temperature. This made lithium alanates considered as unstable hydrides – meaning that even though desorption of hydrogen can occur easily, but it is almost impossible to be re-absorbed [290]. Desorption of $LiAlH_4$ occurs via 2 minor decomposition steps, similarly to the sodium alanates:

$$3\mathrm{LiAlH_4} \rightarrow \mathrm{Li_3AlH_6} + 2\mathrm{Al} + 3\mathrm{H_2} \tag{5.46}$$

$$\mathrm{Li_3AlH_6} \rightarrow 3\mathrm{LiH} + \mathrm{Al} + \frac{3}{2}\mathrm{H_2} \tag{5.47}$$

The total hydrogen content of $LiAlH_4$ and Li_3AlH_6 is 10.5 and 11.2 wt%, respectively. The hydrogen released during the 2 reactions are calculated at 5.3 and 2.7 wt% at temperature ranging from 160 to 200 °C. Nevertheless, after the reaction is completed, the 2.65 wt% of total hydrogen remained in $LiAlH_4$ was not released, but stayed in the form of LiH. This amount of hydrogen can be only desorbed at high temperature, as high as 680 °C [290]. Its chance of commercialization is therefore limited by its high temperature operation and slow kinetics. The performance of Li-based materials are summarized as shown in Table 5.10 [189].

Table 5.10: Absorption and desorption of hydrogen over the Li-base materials [189].

Material	Method	Temperature (°C)		Pressure (bar)		Kinetics (min)		Cycling stability	Max. weight of H_2	Ref.
		T_{abs}	T_{des}	P_{abs}	P_{des}	T_{abs}	T_{des}			
$LaNi_3BH_3$	Arc melting	25		4		30		2 cyc, unstable	0.84	[302]
Li_2NH	Mixing	200-230	200-230	7	1	10	300	15 cyc, unstable	3.10	[303]
$LiNH_2$–LiH–1mol%$TiCl_3$	BM	180	150-250	30		30		3 cyc, stable	5.00	[304]
Li_2O–Li_3N	Partial oxidation	180		7		3		6 cyc, stable	5.20	[305]
$Li_2MgN_2H_2$	Mixing	180	180	90	1	60	60	n/a	5.50	[232]
Li_3N	Mixing	50	240-270	0.5	1	20		n/a	6.00	[306]
Li_2NH	Mixing	255-285	255-285	10	1.5	n/a	n/a	n/a	6.50	[235]
$Li_3BN_2H_8$	BM		250-364		1		228	n/a	10.00	[307]
$LiBH_4$-1/2MgH_2–2mol%$TiCl_3$	BM	315-450	315-450	4.5-19	2-3	240	240	3 cyc, unstable	10.00	[308]

$KAlH_4$ was also studied [309]. Hydrogen storage capacity was determined at 3.5 wt% at 10 bar of hydrogen at temperature ranging from 250 to 330 °C. In contrast to the $NaAlH_4$ and $LiAlH_4$, $KAlH_4$ offers an easy reversible reaction without any additional catalysts.

5.5.2.3 LITHIUM NITRIDES

Lithium nitrides themselves might not be the best candidate for hydrogen storage material because their operating temperature are normally just too high, under the manageable operating pressure. However, researchers found that the study of lithium nitrides are useful for developing metal-N-H system as they are proven to be a potential pathway for reversible solid-state hydrogen storage material [235]. The reaction between Li and hydrogen was proposed as shown below [189,310,311]:

$$\mathrm{Li_3Ni} + 2\mathrm{H_2} \rightarrow \mathrm{LiNH_2} + 2\mathrm{LiH} \tag{5.48}$$

Li_3N can theoretically store 10.4 wt% of hydrogen. However, it has two plateaus in its P-C isotherm – meaning that desorption isotherm cannot return to its origin. $LiNH_2$ could be further decomposed to Li_2NH, LiH and the evolved hydrogen of 7 wt%:

$$\mathrm{LiNH_2} + 2\mathrm{LiH} \rightarrow \mathrm{Li_2NH} + \mathrm{LiH} + \mathrm{H_2} \tag{5.49}$$

In addition, NH_3 can be produced during the reaction and react with H_2, poisoning the downstream processes. The presence of LiH can ease this situation by capturing the NH_3. This reaction has relatively fast kinetics, therefore, the further damage caused by NH_3 reactions are prohibited, during the hydrogenation of Li_3N [312]. Many recent researches had been reporting that partial substitution of different valence cations with larger electronegativities, e.g. Mg, could help reducing the desorption temperature of hydrogen in the Li-based complex hydrides [313].

5.5.2.4 LITHIUM BORO- AND BERYLLIUM HYDRIDES

$LiBH_4$ provides a gravimetric hydrogen density of 18 wt% and was first synthesized in an organic solvent, however, the hydrogen desorption temperature is as high as 470 °C [314,315]. Its disadvantages include: (1) difficult synthesis, the synthesis of $LiBH_4$ occurs at temperature around 650 °C, under pressure of H_2 at 150 bar; (2) expensive [316]. Small amount of hydrogen (0.3 wt%) evolution occur at low operating temperature whereas the larger amount of hydrogen (13.5 wt%) will be released at higher temperature, with 4.5 wt% of total hydrogen remained as LiH, the final decomposition product. Around 8 to 10 wt% of hydrogen can be reversibly re-stored at temperatures of 315 to 400 °C, by adding MgH_2 and $TiCl_3$. Since Li and Be are the lightest hydride-forming metals, thus their reversible hydrogen capacity are generally higher than other known-hydrides [317]. In addition, $Li_3Be_2H_7$ is highly toxic [212].

5.5.3 INTERMETALLIC COMPOUNDS

Intermetallic compounds are made of combination between an elements forming a stable hydride with an element forming a non-stable hydride. Despite its long term development since 20 years ago, the application of intermetallic compounds in solid-state hydrogen storage is still struggling with their high weight (especially for on-board applications) and low hydrogen storage capacity [318]. Another type of intermetallic compounds are categorized by their crystal structure i.e. AB_2 (Laves phase), AB_5 typed phase, Ti-based body centered cubic phase or BCC (body centered cubic). The properties of these intermetallic compounds are summarized and tabulated as shown in Tables 5.11 and 5.12 [189].

Table 5.11: Absorption and desorption of hydrogen over various intermetallic compounds [189].

Material	Method	Temperature (°C)		Pressure (bar)		Kinetics (min)		Cycling stability	Max. weight of H_2	Ref.
		T_{abs}	T_{des}	P_{abs}	P_{des}	T_{abs}	T_{des}			
MgS	BM	-196		50		n/a		n/a	0.50	[319]
$La_{0.90}Ce_{0.05}Nd_{0.04}Pr_{0.01}Ni_{4.63}Sn_{0.32}$	Melting	100	25	2-10	0.24	6.6	6.6	n/a	0.95	[320]
$Zr(Cr_{0.8}Mo_{0.2})_2$	Induction melting	120		30		n/a		n/a	0.99	[321]
$Ml_{0:85}Ca_{0:15}Ni_5$	RF melting		25		10		60	100 cyc, stable	1.10	[322]
$LaNi_{4.8}Sn_{0.2}$	Arc melting	80	80		3-4		n/a	1,000 cycle, stable	1.16	[323]
$La_{0.55}Y_{0.45}Ni_5$	Induction melting		-20		3.5		n/a	5 cycle, stable	1.30	[324]
$Ti_{0.9}Zr_{0.15}Mn_{1.6}Cr_{0.2}V_{0.2}$	RF melting		25		10		60	100 cyc, stable	1.30	[322]
$MnNi_{4.6}Al_{0.4}$	Melting	25	25		25		5	11 cyc, stable	1.30	[325]
$MnNi_{4.6}Fe_{0.4}$	Melting	25	25	35		15		11 cyc, stable	1.44	[325]
$Ml_{0.75}Ca_{0.25}Ni_5$	RF levitation melting	20		100	6.8		n/a	n/a	1.45	[326]
80wt% $TiCr_{1.1}V_{0.9}$–20wt%$LaNi_5$	Melting + BM	30	30	17	0.5		n/a	n/a	1.50	[327]
$Ti_{0.97}Zr_{0.03}Cr_{1.6}Mn_{0.4}$	RF levitation melting	20		100	81		n/a	n/a	1.55	[326]
$La_{0.7}Mg_{0.3}Ni_{2.65}Mn_{0.1}Co_{0.90}$	Melting	30	30	5	0.33		n/a	n/a	1.56	[328]

(Continued)

Table 5.11: *(Continued)*

Material	Method	Temperature (°C)		Pressure (bar)		Kinetics (min)		Cycling stability	Max. weight of H_2	Ref.
		T_{abs}	T_{des}	P_{abs}	P_{des}	T_{abs}	T_{des}			
$Zr_{0.75}Ti_{0.25}Cr_{1.5}Ni_{0.5}$	Arc melting	40		47		n/a		n/a	1.75	[329]
$Ti_{1.1}CrMn$	Arc melting	23	23	33	1	1	5	1,000 cyc, stable	1.80	[330]
FeTi	BM	25		100		n/a		n/a	1.92	[331]
V–7.4%Zr–7.4%Ti–7.4%Ni	Arc melting	40		10	1	n/a		10 cyc, unstable	2.00	[332]
$V_{0.375}Ti_{0.25}Cr_{0.30}Mn_{0.075}$	Arc melting	30	30	50	0.2	n/a		n/a	2.20	[333]
$Ti_{45}Zr_{38}Ni_{17}$ Quasicrystal powders	BM	300	427	80		1,200		n/a	2.23	[334]
Ti–V–Cr	Arc melting	40	40	100		n/a		n/a	2.80	[335]
Ti–10Cr–18Mn–27V–5Fe	Magnetic levitation melting	60		30	1	8.3		n/a	3.01	[336]
Ti–10Cr–18Mn–32V	Magnetic levitation melting	60		30	1	8.3		n/a	3.36	[336]
$TiCr_{1.1}V_{0.9}$	Melting + BM	30	30	17	0.5	n/a		n/a	3.50	[327]
$Ti_{43.5}V_{49}Fe_{7.5}$	Arc melting	-20	300	100	10	20		50 cyc, stable	3.90	[337]
Ti–V–Cr–Mn	Magnetic levitation melting		247-472	30	0.03	n/a		n/a	3.98	[338]
$La_{1.8}Ca_{0.2}Mg_{14}N_{13}$	BM	27-327	27-327	40	1	15	10	6 cyc, unstable	5.00	[339]

Table 5.12: Hydrogen absorption and desorption properties over $LaNi_5$-based compounds [189].

Material	Method	Temperature (°C)		Pressure (bar)		Kinetics (min)		Cycling stability	Max. weight of H_2	Ref.
		T_{abs}	T_{des}	P_{abs}	P_{des}	T_{abs}	T_{des}			
$LaNi_5$	BM	20		20		1.6		8 cyc, unstable	0.25	[340]
$La_{0.59}Ce_{0.29}Pr_{0.03}Ni_4Co_{0.45}Mn_{0.45}Al_{0.3}$	Twin-rolling	60		10	0.6	n/a		n/a	1.27	[341]
$La_{0.9}Ce_{0.1}Ni_5$	Co surface treatment	0-100	25	50			1.8	20 cyc, stable	1.40	[342]
$LaNi_5$	Co surface treatment	0-100	25	50			13.6	20 cyc, stable	1.44	[342]

When these materials are applied under ambient temperature and pressure, their low energy density per unit weight is very much a disadvantage. For example, the hydrogen storage capacity of the most popular $LaNi_5$-based alloys does not give 1.4 wt%, if operated under moderate temperature. Figure 5.12 represents the major outputs from a number of studies on AB_5 type compounds for their application in solid-state hydrogen storage.

The performance of $LaNi_5$ compounds, in terms of hydrogen storage capacity, was reported to be improved by adding other metals [322]. AB_2 type compounds are derived from the Laves phases crystal structures. One of the high potential materials in this group is Ti and Zr (as A-site) based materials. The B elements can be various 3d atoms such as V, Cr, Mn, and Fe. Most of these materials possess faster kinetics, longer life span, and lower cost; compared to LaNi5 related system. Nevertheless, these materials are too stable at room temperature [343] and more sensitive to gaseous impurities than AB_5 based compounds. BCC based materials were reported to be able to absorb more oxygen than the conventional intermetallic compounds, for instance, Ti-based BCC. However, its downside includes its high cost. The quasicrystals have a new type of translational long-range order, presenting non-crystallographic rotational symmetry. These kind of materials contain high amount of interstitial sites. The absorption of hydrogen between the layers of multi-layered walls of nanotubular TiO_2 was reported to take place at 195 to 200 °C under pressure up to 6 bar, where the hydrogen can be intercalated within [344].

5.6 NANOSTRUCTURED METAL OXIDES IN LITHIUM-ION BATTERIES

Nanoscaled and nanostructured metal oxides are becoming one of the key-component to develop the lithium-ion battery which is becoming more popular for its on-board applications, since its first-time development in 1991 by Sony [345]. The Li-ion had been widely applied in many portable devices e.g. laptops or digital cameras; and expanded its uses in the more modern applications such as aerospace, smart grid system and automotive. Li-ion batteries are advantaged in (1) its highest energy density amongst all types of rechargeable batteries; (2) its low self-discharge rate. Lithium-ion batteries nowadays are being developed based on the following criteria/concerns: (1) energy density, (2) discharging and charging rate (power density), (3) safety feature, and (4) cycle stability. These parameters are governed by characteristics of the selected electrode i.e. its nature and structure. The safety issue can be improved by selecting/developing a non-flammable electrolyte or even solid electrolyte to replace the current liquid electrolyte which mostly contains highly flammable organic solvents. Overall performance of the Li-ion batteries can be enhanced by using nano metal oxides as anode, cathode or electrolyte additives. A lithium ion (Li-ion) battery diagram can be schematically illustrated as shown in Figure 5.38.

The typical cell consists of $LiCoO_2$ as a cathode, graphite as an anode, whereas the electrolyte can be a solution of lithium salts such as $LiPF_6$ or $LiBF_4$ dissolved in an organic solvent such as a mixture of propylene carbonate or diethyl carbonate. During the charging step, Li atoms in $LiCoO_2$ will become ions, transporting to the graphite anode through the electrolyte and intercalate within the gaps between graphene layers. Similarly, the intercalated Li atoms in the graphene layers will be released as ions, migrating back to the $LiCoO_2$ cathode and intercalating within the layers of octahedral lattices formed by Co and oxygen atoms. The intercalation can be defined as lithiation/delithiation mechanism which is referred to all the ‘topotactic reactions’ where the structures are not limited to be layers.

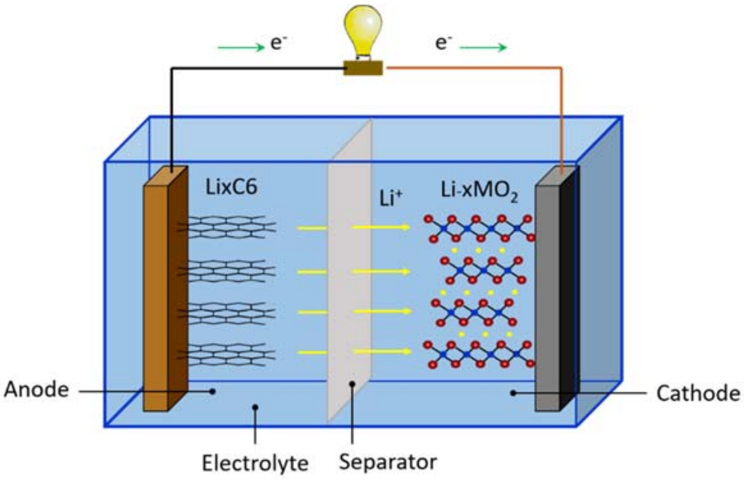

Figure 5.38: Discharging Li-ion battery with a graphite anode, Li_xMO_2 cathode [345].

Reversible redox reaction of metal oxide such as Li/Li^+ is considered another type of lithiation/delithiation and is regarded as ‘conversion reactions’, where the lithiation occur via reduction of the metal oxide by Li to produce metal and lithium while delithiation will take place via the oxidation of the formed metal by lithium oxide. In addition, for the intermetallic AB compounds, Li will reversibly substitute A to form Li_xB in which it has a strong structural relationship with the parent AB compound. This phenomenon is regarded as ‘displacement reactions’. Almost all metal oxide materials can be working as any of these three reactions, except SnO_2-based materials which its lithiation/delithiation combines the conversions and alloying reactions.

Nanoscaled metal oxides have many advantages in Li-ion battery applications: including (1) its smaller size, which could reduce the Li-ion/electron transport pathways and enhance phase transformation; (2) its large surface are, which can increase the charge/discharge kinetic rates, due to the increased contact with the electrolyte; (3) its low density, allowing itself to accommodate the associated volume changes of the transferred species during the lithiation/delithiation process, leading to an improvement in its cycle stability. Nevertheless, its strong points are also the weak points. Its drawbacks include: (1) the nanoscaled and/or nanostructured materials will lower the packing density, causing an increase in the cell's volume, therefore, resulting in a low overall energy density; (2) the large surface area enables higher chances of unwanted reactions between the electrode and electrolyte, due to its larger contact/interface area.

Question 5.5
Li-ION batteries are considered less harmful to our environment. Why?

5.6.1 NANO METAL OXIDES FOR ANODE MATERIALS

5.6.1.1 INTERCALATION METAL OXIDES

Choice for electrodes in Li-ion batteries are generally based on layered materials (e.g. graphite for anode and $LiCoO_2$ for cathode), but not limited to [346]. Tunnel-structured materials such as spinel (AB_2O_4 where A = Li) can find its use in Li-ion battery as Li-storage host with intercalation mechanism. $Li_4Ti_5O_{12}$ and TiO_2 are the most promising anode materials amongst all the metal oxides. $Li_4Ti_5O_{12}$ is a ceramic material which has a defect tunneled structure ($Li_{1/3}Ti_{5/3}O_4$) which can be lithiated over the composition range of $Li_{4+x}Ti_5O_{12}$ ($0 < x < 3$), giving a potential of 1.55 V versus Li/Li^+, approximately, whereas its theoretical lithiation capacity is estimated at 175 mAh/g [347-350]. Although the $Li_4Ti_5O_{12}$ has only moderate lithiation capacity, however, it is considered a zero-strain intercalation material where the defected $Li_{1/3}Ti_{5/3}O_4$ framework exhibits minimum volume change during the intercalation/deintercalation process. This leads to an importance characteristic which is the cycle stability. The potential of 1.55 V of $Li_4Ti_5O_{12}$ is also advantaged for eliminating the formation of solid electrolyte interface (SEI) film, caused loss in efficiency, because the 1.55 V lithiation voltage if higher than the decomposition voltage of the organic solvent in the electrolyte. Yet, the higher lithiation voltage would reduce the chance of lithium metal plating over the anode, resulted in an enhanced safety. On its downside, using $Li_4Ti_5O_{12}$ sacrifices the full cell working voltage due to its higher lithiation voltage compared to graphite which values at 0.1 to 0.2, against Li/Li^+ [345]. The benefit of using nanaoscale $Li_4Ti_5O_{12}$ is that its Li intercalation/deintercalation is significantly increased. The average Li-ion diffusion time

(t) in an ideal anode particle can be described using the below equation, where the Fickian diffusion is assumed:

$$t = \frac{L^2}{2D} \tag{5.50}$$

Where L stands for diffusion distance, D is for the Li-ion diffusivity in the material. This equation clearly illustrates that the shorter distance of diffusion, by the smaller particle size, will result in the shorter diffusion time. Because $Li_4Ti_5O_{12}$ is an electric insulator, its electronic conductivity would be increased during the lithiation reaction from the outer surface directing inward. This problem is not unmanageable as Li^+/e^- transport already occurs at the outer layer. During the delithiation, Li will be released while the conductivity begins to decrease from the outer layer of the $Li_4Ti_5O_{12}$'s particle. This, the kinetics rate of delithiation process will be lower than that of the lithiation. Reducing the Li^+/e^- transport pathway by using nano $Li_4Ti_5O_{12}$ will encourage faster separation of Li^+ and e^-, resulting in the desired high rate of the charge/discharge.

Nanorods $Li_4Ti_5O_{12}$ was successfully prepared for the Li-ion battery [351]. Their diameters were estimated at around 100 nm as shown in Figure 5.39 (a). Its high rate of discharging is very beneficial for the application. Figure 5.39 (b) illustrates that the reversible first discharge capacity was determined at 165 mAh/g under a cycling rate of 0.1 C (16 mA/g), with no noticeable capacity fading up until 30 cycles between 1 and 2.5 V. The initial capacity at 0.5 C was exactly the same as that at 0.1 C. Small capacity was seen to be decreased when the current increased, which were observed at 5 and 10 C (1,600 mA/g) rates. The capacity retention was read at 95 and 93#, respectively, showing 157 and 155 mAh/g. This can be concluded that $Li_4Ti_5O_{12}$ with 700 nm diameter has lower performance. This fact implies that nanoscaled materials will increase the kinetics of charge transfer.

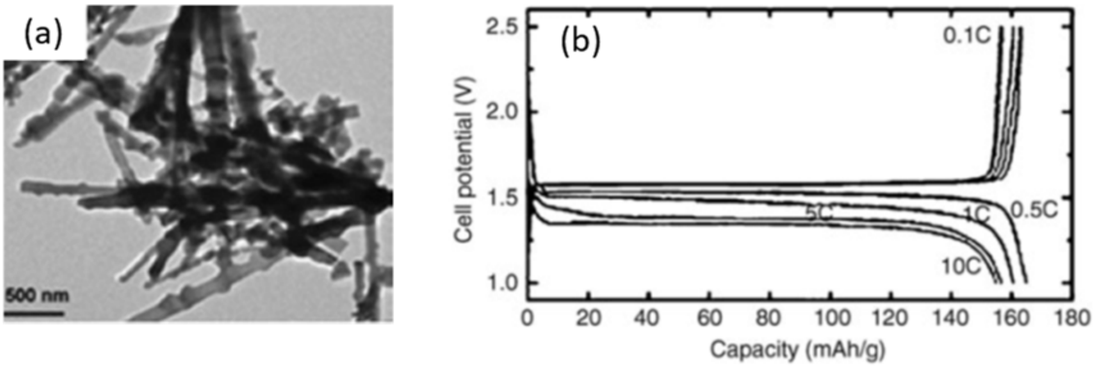

Figure 5.39: (a) TEM image of $Li_4Ti_5O_{12}$ nanorods, (2) rate capacity of the $Li_4Ti_5O_{12}$ at different cycling rate [351].

TiO_2 also has high theoretical lithiation property/capacity, although has slow kinetics. The Li intercalation reaction to TiO_2 can be described as below:

$$\mathrm{xLi^+ + TiO_2 + xe^- \leftrightarrow Li_xTiO_2} \tag{5.51}$$

Full lithiation would result in the formation of $LiTiO_2$ (x = 1) with 335 mAh/g. Because this reaction occurs under the operating voltage of 1.5 to 1.8 V, thus, the anode passivation film (caused by the reaction between the electrode and electrolyte) can be avoided, leading to an increase in the better safety operation. Four types of TiO_2 had been applied in battery applications: rutile, brookite, anatase, and bronz (TiO_2(B)). Amongst these polymorphs, rutile is the most common and that's why it's the most thermodynamically stable form of TiO_2. Anatase and brookite can be converted to rutile by calcination under temperature ranging from 700 to 1,000 °C. The basic physical properties of these TiO_2 are gathered and tabulated as shown in Table 5.13 [352].

The major challenge for using TiO_2 as an anode is its poor Li^+ and its poor electron conductivity. This leads to a prohibited reaction kinetics of Li lithiation/delithiation process [352]. The kinetics of intercalation/deintercalation process was reported to be governed by its structural properties such as site occupation, local coordination and energy [353-355].

Despite all the advantages of nanoscale TiO_2 for improvement of Li-ion batteries, some of their major challenges include the fact that the fuel cells with TiO_2 anode and typical cathode are subjected to lower cell voltages due to its relatively higher lithiation potential versus Li/Li^+ [356].

Other intercalation metal oxides are the oxides of group 5B metals (i.e. V and Nb) and group 6B metals (such as Mo and W) [357]. These oxides are utilized in Li-ion battery applications because of their outstanding layered lattice structures. Binary vanadium oxides with octahedral (or distorted octahedral) coordination have their large variety of oxidation from V^{5+} to V^{2+}. In addition, they are feasible as a cathode due to their high voltage of intercalation/deintercalation, except for VO_2(B) which has monoclinic metastable shear structure which is more likely to be used as an anode (for aqueous electrolyte Li-ion batteries, due to its appropriate electrode potential of 2.5 V versus Li/Li^+ [358]. Flower-like VO_2(B) was successfully synthesized and tested as an anode material when having $LiMn_2O_4$ as a cathode. The flower-like shaped material showed better performance compared to the same materials in the form of nanobelt and carambola-like nanoparticles [359]. Apart from the VO_2(B), other vanadium oxides were also applied in the battery applications such as $LiVO_2$, LiV_3O_8, MnV_2O_6, RVO_4 (when R = In, Cr or Fe) and $LiMVO_4$ (where M = Cd, Co, Zn, Ni, Cu or Mg) [360-364].

Table 5.13: Physical properties of various phases of TiO_2 [352].

Type	Density (g/cm^{-3})	Unit-cell data (nm)	Molecular structure
Rutile	4.13	a = 0.459 c = 0.296	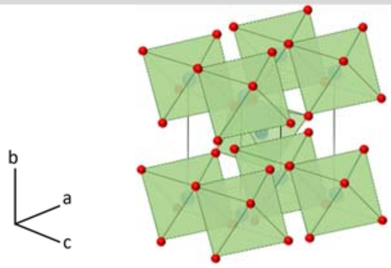
Brookite	3.99	a = 0.917 b = 0.546 c = 0.514	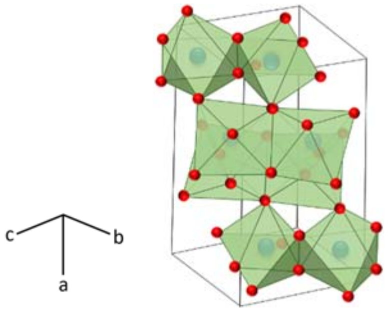
Anatase	3.79	a = 0.379 c = 0.951	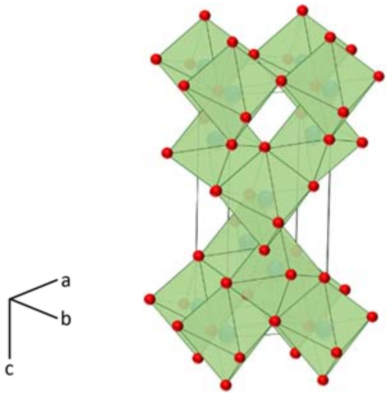
Bronze TiO_2(B)	3.64	a = 1.216 b = 0.374 c = 0.651 β = 107.29°	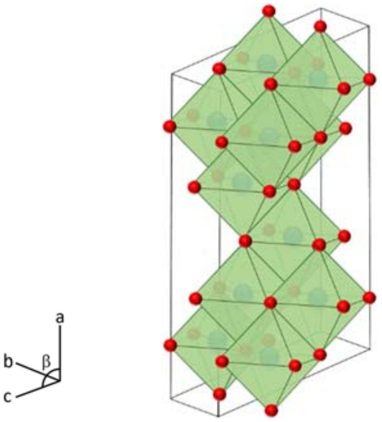

To sum up, these intercalation metal oxides have either layered or tunneled structures which can accommodate lithium ions. These lithiations/delithiations always occur with associated volume expansion which has negative effect on the cycling stability. The lithiation capacity of intercalation metal oxides is limited by the availability of lattice sites and hindered by the redox competition with other phases. One main obstacle for obtaining the full capacity and fast rate of charge/discharge is the slow ion or electron transport kinetics. The nanoscale materials definitely can enhance surface area, thus shorten the transport partway between Li^+ and electron. The capability to store Li in nanoscale materials can be encouraged by increasing the grain interfaces. Main challenge for the intercalation metal oxide anodes is the irreversible capacity – which is currently soothed by coating it with conductive later or doping with conductive composite [345].

5.6.1.2 CONVERSION METAL OXIDES

The new mechanism of lithiation and delithiation was proposed in 2000s [365] for the storage of Li in transition metal oxides. The mechanism is demonstrated in the equation below:

$$2xLi + MO_x \leftrightarrow M + xLi_2O \tag{5.52}$$

Where M can be Fe, Ni, Co, Cu, Mn, Cr, Ru or Zn

In this case, the lithiation process is therefore the chemical reduction reaction of metal oxide by lithium at a particular potential. Similarly, the delithiation process is the chemical oxidation reaction of metal oxide where the metal is oxidized by Li_2O and returned back to its original valence state. This mechanism is referred to as a 'conversion reaction'.

For example, Li and MnO_2 together is acting as a pair of anode/cathode for primary Li battery. The lithiation process of this pair was reported to result on 2 to 5 nm metal grains embedded in an amorphous Li_2O matrix [365]. The transport pathway between the Li^+ and electron is therefore shorten by this nanostructure material while the movement of Li^+ through the Li_2O phase and the movement of electron through the metal phase are also facilitated by nanostructure materials. Such proven phenomena allows the reversible lithiation/delithiation process. However, the fully lithiation/delithiation is not achieved in this case. It was found that the delithiation capacity is mismatch with the lithiation capacity, leading to the conclusion that there is some significant amount of irreversible capacity since during the first cycle. A complexity of this type of metal oxide anode is that it has large voltage profile of hysteresis of charge/discharge while it actually should have as low as possible voltage profile of hysteresis, in order to maximize the energy density efficiency. However, the potential hysteresis can be lowered by making the particle size of the metal oxides smaller [366].

The typical metals in this type of metal oxides include Fe, Co, Ni, Cu, Mn and Cr. Instead of synthesizing these metal oxides as nanospheres, these compounds can be fabricated as other nanoshapes i.e. nanotube, nanowire, nanoflakes, nanospindles, flower-like, hollow-sea-urchin-like nanoparticles and mesoporous structures [367-384]. For example, Mn_2O_3 nanowire could be prepared using a combustion process [385], as shown in Figure 5.40.

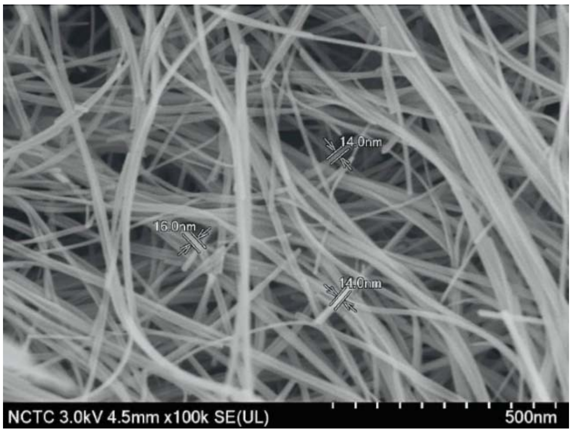

Figure 5.40: Mn_2O_3 prepared using a combustion method assisted an in-house technique [385].

Although these materials have many advantages, their disadvantages include (1) they have high lityhiation potential of above 1 V against Li/Li^+ which results in low overall cell voltage, (2) the delithiation capacities of these metal oxides can be achieved in a wide window of potential, ranging from the lower limit of near-zero to the upper limit of maybe 3 V. These drawbacks are not practically applicable in real-life utilization [386].

5.6.1.3 DISPLACEMENT METAL OXIDES

Displacement mechanism is when one metal A from a binary intermetallic AB by lithium reduction. AP was reported to be a host framework for the lithiation for A and delithiation for Li, respectively. By this method, the extreme change in volume can be limited, resulted in an increase of the battery life cycle. One outstanding metal oxide in this group is $Cu_{2.33}V_4O_{11}$ [387]. During the displacement, Cu is inserted in $(V_4O_{11})_n$ layered structures. Around 5.6 Li per $Cu_{2.33}V_4O_{11}$ would be reversibly substituted and released into the layered structure through the reaction of displacement. $Cu_{2.33}V_4O_{11}$ provides total capacity of around 270 mAh/g, but its lithiation potential is as high as 2.5 V which makes this material more feasible as a cathode [345].

5.6.1.4 TIN DIOXIDES-BASED ANODE MATERIALS

The lithiation and delithiation process of SnO_2 is hard to be categorized as one of the above, as it is a combination of the conversion mechanism and alloying/dealloying mechanism, described by chemical reactions below:

The conversion mechanism: the lithiation reaction where SnO_2 is irreversibly reduced to metallic Sn by Li:

$$4\mathrm{Li}^+ + 4\mathrm{e}^- + \mathrm{SnO}_2 \rightarrow 2\mathrm{Li}_2\mathrm{O} + \mathrm{Sn} \qquad (5.53)$$

The alloying/dealloying mechanism:

$$\mathrm{xLi}^+ + \mathrm{xe}^- + \mathrm{Sn} \leftrightarrow \mathrm{Li}_\mathrm{x}\mathrm{Sn} \qquad (5.54)$$

Sn has high lithiation capacity. 4.4 Li can be inserted in 1 Sn. This property will prevent the pulverization, caused by severe volume change. In addition, Sn is an electronic conductor which can facilitate high capacity and fast rate of charge/discharge process. This, the use of SnO_2 can improve the cycle stability of the anode, but at its cost of one big portion of irreversible capacity during the first cycle. Morphology of SnO_2 synthesized as porous-sphere thin film is presented as shown in Figure 5.41.

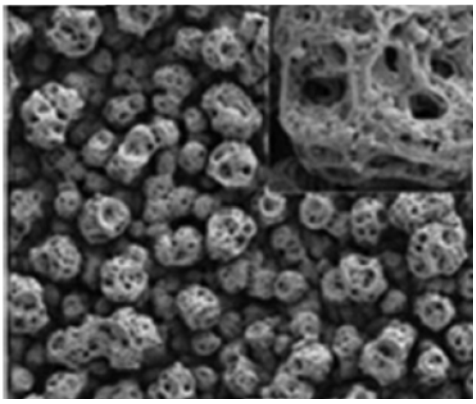

Figure 5.41: Morphology of thin film SnO_2 based porous spheres, captured by SEM technique [345].

5.6.2 NANO METAL OXIDES FOR CATHODE MATERIALS

The most promising cathodes in the Li-ion battery applications are either lithium transition metal oxides or lithium transition metal phosphates. When the lithium metal is applied as an anode in the battery cell, some metal oxides i.e. MnO_2 or V_2O_5 can be utilized as cathodes. By reducing the particle size of the materials by micro- to nano-scale, the power and cycling capability of this low-potention cathodes would be extremely enhanced. This is because of its shorter length of diffusion, high electrode/electrolyte surface contact, and rapid phase transformation. Nevertheless, the high surface contact has its drawback, as the SEI later can be produced via the decomposition of electrolyte, leading to the shorter life cycle of the battery, particularly when used at elevated temperatures. For the cathode that is made of Li-Mn-O, the use of smaller particles results in the higher degree of undesirable dissolution of Mn, In addition, surface coating with nanolayer of inert oxides such as SnO_2, Al_2O_3, MgO or ZrO_2 can ease the Mn dissolution and the minimize the SEI formation, however, it also decreases the rate of reaction [387-389].

5.6.2.1 NANOSCALED CATHODE MATERIALS

Nanotube and nanowire structures of V_2O_5 and $LiCoO_2$ were reported to have a positive influence on the rate, performance and the cycling stability of the Li-ion batteries [390-392]. For example, a high quality single crystalline cubic spinel $LiMn_2O_4$ was synthesized using $Na_{0.44}MnO_2$ nanowire as a self-template [393]. These materials offer high thermal stability, outstanding performance at high rate charge/discharge and excellent cycle stability. Another example is a low-cost nano-$LiFePO_4$ cathode in which it has a gravimetric capacity of 170 mAh/g, plus it has high thermal/chemical stability, less reactivity with electrolyte (due to its low potential), and flat discharge potential profile. These characteristic makes nano-$LiFePO_4$ a good candidate for cathode material, especially for the popular hybrid electric vehicle batteries.

5.6.2.2 NANOSTRUCTURED CATHODE MATERIALS

Despite the fact that the power of cathode is increased when it is made of nanoscale material, the tap density and energy density will decrease dramatically when the particle size decreases [394]. The use of nanoscale materials benefits high power, but leads to low volumetric energy storage. To optimize this, the nanostructured cathode materials can be applied, in order to (1) avoid low volumetric energy density and high reactive surface and (2) to remain all advantages of the nanoscales. For example, nanostructured $LiMnO_2$ cathode was reported to be successfully prepared [395]. It was found that the lattice stress caused by Jahn-Teller distortion can be hosted more easily if it was a nanostructure. The material is able to change between cubic and tetragonal structures instantly during the lithiation/delithiation process.

5.6.3 NANO METAL OXIDES IN ELECTROLYTES

Usually a Li salt solution, as an electrochemical stable organic solvent, will be a perfect electrolyte for Li-ion batteries. It is advantaged in high Li-ion conductivity, but unfortunately is undermined by its flammability, causing a concern for users. Aqueous electrolyte, solid ceramic electrolyte, ionic liquid electrolyte and solid polymeric electrolyte were proposed to sort the problem [396]. Solid polymeric electrolyte is a solvent free membrane, synthesized from Li salts and polymers. The most well-known membranes are generally based on poly (ethylene oxide) (PEO) and some Li salts i.e. $LiPF_6$ and $LiCF_3SO_3$ [397]. The polymeric electrolyte is interesting because it can simplify the manufacturing process, engineering process and transportation process.

The addition of nanosized metal oxides such as TiO_2, Al_2O_3 or SiO_2 was reported to improve the conductivity of PEO, as shown in Figure 5.42 [398]. These metal oxides are believed to act as a plasticizers, leading to the lower degree of the polymer crystallinity.

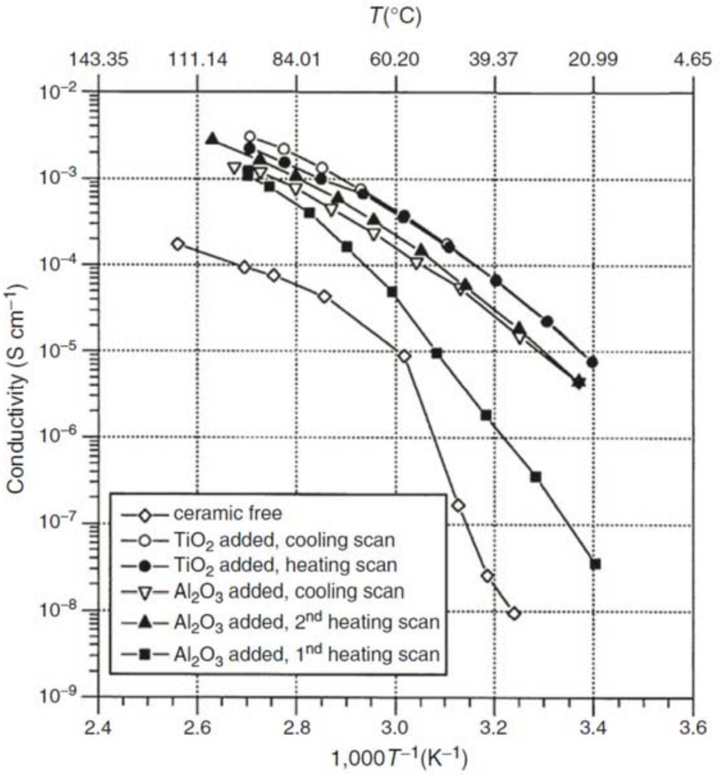

Figure 5.42: Kinetics study presents the Arrhenius plot of the conductivity of non-plasticizers PEO-$LiClO_4$ and of nanocomposite PEO-$LiClO_4$ [398].

5.7 SUMMARY AND PERSPECTIVES

This chapter gathers the important and interesting processes which use metal oxides as the main component of the catalyst system. Most of the processes are the current interest of the world such as thermochemical cycles of water splitting, emission control, fuel cells, and hydrogen storage and lithium ion batteries. All the processes focuses on green technology where the environment impact is strongly considered. The application of metal oxides on the mentioned processes should consider its sustainability, efficiency, and definitely the environmental impacts. However, the challenges and limitations of all the applications are based on economic feasibility, thermodynamic limitations, and regulations for implementation i.e. solar thermal technology is forbidden in some areas such as around airports. To overcome this obstacles, the thermodynamic limitations should be firstly eliminated, by coupling the technologies with green source of energy such as solar energy, wind energy etc. The incentive policies should render the economic feasibility of each technology too. The detailed challenges and scientific limitations of individual technologies were summarized in the context. The current trends in applied heterogeneous catalysis and possible new family of catalysts have been also included in this chapter. Main topics to be studied further in the future include (1) water and temperature tolerant solid-acid catalyst, multifunctional metal oxides with acidic and basic or redox properties, theoretical calculations e.g. DFT of the surface sites and reaction mechanism could be beneficial in searching for appropriate novel catalysts. Application of the metal oxides in heterogeneous catalysis will however definitely extended for future studies.

REFERENCES

[1] Y. Wu, T. V. Ree, Introduction: Energy technologies and their role in our life, Metal Oxides in Energy Technologies, Elsevier, 2018.

[2] J.E. Funk, R.M. Reinstrom, Energy requirements in the production of hydrogen from water, Ind. Eng. Chem. Process Des. Dev. 5 (1966) 336-342. https://doi.org/10.1021/i260019a025.

[3] V.I. Anikeev, A.S. Bobrin, J. Ortner, S. Schmidt, K.H. Funken, N.A. Kuzin, Catalytic thermochemical reactor/receiver for solar reforming of natural gas: Design and performance, Sol. Energy. 63 (1998) 97-104. https://doi.org/10.1016/S0038-092X(98)00050-4.

[4] J.R. Rostrup-Nielsen, J. Sehested, J.K. Noerskov, Hydrogen and Synthesis Gas by Steam- and CO_2 Reforming, ChemInform. 34 (2003). https://doi.org/10.1002/chin.200317288.

[5] S. Koumi Ngoh, D. Njomo, An overview of hydrogen gas production from solar energy, Renew. Sustain. Energy Rev. 16 (2012) 6782-6792. https://doi.org/10.1016/j.rser.2012.07.027.

[6] V. Tongnan, T. Sornchamni, N. Laosiripojana, U.W. Hartley, Study of crystal growth and kinetic parameters of Zn/ZnO oxidation in the presence of H_2O and CO_2, React. Kinet. Mech. Catal. 125 (2018) 99-110. https://doi.org/10.1007/s11144-018-1411-3.

[7] C. Agrafiotis, M. Roeb, C. Sattler, A review on solar thermal syngas production via redox pair-based water/carbon dioxide splitting thermochemical cycles, Renew. Sustain. Energy Rev. 42 (2015) 254-285. https://doi.org/10.1016/j.rser.2014.09.039.

[8] A. Ngoensawat, V. Tongnan, N. Laosiripojana, P. Kim-Lohsoontorn, U.W. Hartley, Effect of La and Gd substitution in $BaFeO_{3-\delta}$ perovskite structure on its catalytic performance for thermochemical water splitting, Catal. Commun. 135 (2020) 105901. https://doi.org/10.1016/j.catcom.2019.105901.

[9] C. Khajonvittayakul, V. Tongnan, T. Kangsadan, N. Laosiripojana, S. Jindasuwan, U.W. Hartley, Thermodynamic and mechanism study of syngas production via integration of nitrous oxide decomposition and methane partial oxidation in the presence of 10%NiO-$La_{0.3}Sr_{0.7}Co_{0.7}Fe_{0.3}O_{3-\delta}$, React. Kinet. Mech. Catal. 127 (2019) 839-855. https://doi.org/10.1007/s11144-019-01600-1.

[10] N. Ngoenthong, M. Hartley, T. Sornchamni, N. Siri-nguan, N. Laosiripojana, U.W. Hartley, Comparison of packed-bed and micro-channel reactors for hydrogen production via thermochemical cycles of water splitting in the presence of ceria-based catalysts, Processes. 7 (2019) 1-12. https://doi.org/10.3390/pr7100767.

[11] N. Ngoenthong, V. Tongnan, T. Sornchamni, N. Siri-nguan, N. Laosiripojana, U.W. Hartley, Application of a micro-channel reactor for process intensification in high purity syngas production via H_2O/CO_2 co-splitting, Int. J. Hydrogen Energy. 46 (2021) 24581-24590. https://doi.org/10.1016/j.ijhydene.2019.11.240.

[12] T. Khamhangdatepon, V. Tongnan, M. Hartley, T. Sornchamni, N. Siri-Nguan, N. Laosiripojana, K. Li, U.W. Hartley, Mechanisms of synthesis gas production via thermochemical cycles over $La_{0.3}Sr_{0.7}Co_{0.7}Fe_{0.3}O_3$, Int. J. Hydrogen Energy. (2020). https://doi.org/10.1016/j.ijhydene.2019.12.148.

[13] J.R. Scheffe, D. Weibel, A. Steinfeld, Lanthanum-strontium-manganese perovskites as redox materials for solar thermochemical splitting of H_2O and CO_2, in: Energy and Fuels, 2013: pp. 4250-4257. https://doi.org/10.1021/ef301923h.

[14] X. Yuan, X. Wu, J. Wang, Y. Wu, T. van Ree, Solar-driven fuel production by metal-oxide thermochemical cycles, in: Met. Oxides Energy Technol., 2018: pp. 321-340. https://doi.org/10.1016/b978-0-12-811167-3.00012-2.

[15] I. Alxneit, Assessing the feasibility of separating a stoichiometric mixture of zinc vapor and oxygen by a fast quench - Model calculations, Sol. Energy. 82 (2008) 959-964. https://doi.org/10.1016/j.solener.2008.05.009.

[16] J.E. Miller, A.H. McDaniel, M.D. Allendorf, Considerations in the design of materials for solar-driven fuel production using metal-oxide thermochemical cycles, Adv. Energy Mater. 4 (2014). https://doi.org/10.1002/aenm.201300469.

[17] J.R. Scheffe, A.H. McDaniel, M.D. Allendorf, A.W. Weimer, Kinetics and mechanism of solar-thermochemical H_2 production by oxidation of a cobalt ferrite-zirconia composite, Energy Environ. Sci. 6 (2013) 963-973. https://doi.org/10.1039/c3ee23568h.

[18] E. Koepf, W. Villasmil, A. Meier, Pilot-scale solar reactor operation and characterization for fuel production via the Zn/ZnO thermochemical cycle, Appl. Energy. 165 (2016) 1004-1023. https://doi.org/10.1016/j.apenergy.2015.12.106.

[19] A. Berman, M. Epstein, Kinetics of hydrogen production in the oxidation of liquid zinc with water vapor, Int. J. Hydrogen Energy. 25 (2000) 957-967. https://doi.org/10.1016/S0360-3199(00)00015-X.

[20] H. Kaneko, T. Yokoyama, A. Fuse, H. Ishihara, N. Hasegawa, Y. Tamaura, Synthesis of new ferrite, Al-Cu ferrite, and its oxygen deficiency for solar H_2 generation from H_2O, Int. J. Hydrogen Energy. 31 (2006) 2256-2265. https://doi.org/10.1016/j.ijhydene.2006.03.008.

[21] S. Abanades, G. Flamant, Thermochemical hydrogen production from a two-step solar-driven water-splitting cycle based on cerium oxides, Sol. Energy. 80 (2006) 1611-1623. https://doi.org/10.1016/j.solener.2005.12.005.

[22] W.C. Chueh, S.M. Haile, Ceria as a thermochemical reaction medium for selectively generating syngas or methane from H_2O and CO_2, ChemSusChem. 2 (2009) 735-739. https://doi.org/10.1002/cssc.200900138.

[23] J.R. Scheffe, A. Steinfeld, Oxygen exchange materials for solar thermochemical splitting of H_2O and CO_2: a review, Mater. Today. 17 (2014) 341-348. https://doi.org/10.1016/j.mattod.2014.04.025.

[24] D. Schneider, M. Gödickemeier, L.J. Gauckler, Nonstoichiometry and defect chemistry of ceria solid solutions, J. Electroceramics. 1 (1997) 165-172. https://doi.org/10.1023/a:1009928817542.

[25] T. Kobayashi, S. Wang, M. Dokiya, H. Tagawa, T. Hashimoto, Oxygen nonstoichiometry of $Ce_{1-y}Sm_yO_{2-0.5y-x}$ (y = 0.1, 0.2), Solid State Ionics. 126 (1999) 349-357. https://doi.org/10.1016/S0167-2738(99)00259-3.

[26] S. Wang, T. Kobayashi, M. Dokiya, T. Hashimoto, Electrical and ionic conductivity of Gd-doped ceria, J. Electrochem. Soc. 147 (2000) 3606. https://doi.org/10.1149/1.1393946.

[27] W.C. Chueh, S.M. Haile, A thermochemical study of ceria: exploiting an old material for new modes of energy conversion and CO_2 mitigation, Philos. Trans. R. Soc. A Math. Phys. Eng. Sci. 368 (2010) 3269-3294. https://doi.org/10.1098/rsta.2010.0114.

[28] Q.L. Meng, C. Il Lee, T. Ishihara, H. Kaneko, Y. Tamaura, Reactivity of CeO_2-based ceramics for solar hydrogen production via a two-step water-splitting cycle with concentrated solar energy, Int. J. Hydrogen Energy. 36 (2011) 13435-13441. https://doi.org/10.1016/j.ijhydene.2011.07.089.

[29] J.R. Scheffe, A. Steinfeld, Thermodynamic analysis of cerium-based oxides for solar thermochemical fuel production, Energy and Fuels. 26 (2012) 1928-1936. https://doi.org/10.1021/ef201875v.

[30] A. Le Gal, S. Abanades, Dopant incorporation in ceria for enhanced water-splitting activity during solar thermochemical hydrogen generation, J. Phys. Chem. C. 116 (2012) 13516-13523. https://doi.org/10.1021/jp302146c.

[31] P.R. Shah, T. Kim, G. Zhou, P. Fornasiero, R.J. Gorte, Evidence for entropy effects in the reduction of ceria - zirconia solutions, Chem. Mater. 18 (2006) 5363-5369.

[32] A.H. McDaniel, E.C. Miller, D. Arifin, A. Ambrosini, E.N. Coker, R.O'Hayre, W.C. Chueh, J. Tong, Sr- and Mn-doped $LaAlO_{3-\delta}$ for solar thermochemical H_2 and CO production, Energy Environ. Sci. 6 (2013) 2424-2428. https://doi.org/10.1039/c3ee41372a.

[33] M. Roeb, C. Sattler, Isothermal water splitting, Science. 341 (2013) 470-471. https://doi.org/10.1126/science.1241311.

[34] C.L. Muhich, B.W. Evanko, K.C. Weston, P. Lichty, X. Liang, J. Martinek, C.B. Musgrave, A.W. Weimer, Efficient generation of H_2 by splitting water with an isothermal redox cycle, Science. 341 (2013) 540-542. https://doi.org/10.1126/science.1239454.

[35] I. Ermanoski, J.E. Miller, M.D. Allendorf, Efficiency maximization in solar-Thermochemical fuel production: challenging the concept of isothermal water splitting, Phys. Chem. Chem. Phys. 16 (2014) 8418-8427. https://doi.org/10.1039/c4cp00978a.

[36] D. Yadav, R. Banerjee, A review of solar thermochemical processes, Renew. Sustain. Energy Rev. 54 (2016) 497-532. https://doi.org/10.1016/j.rser.2015.10.026.

[37] M.M. Nair, S. Abanades, Tailoring Hybrid nonstoichiometric ceria redox cycle for combined solar methane reforming and thermochemical conversion of H_2O/CO_2, Energy and Fuels. 30 (2016) 6050-6058. https://doi.org/10.1021/acs.energyfuels.6b01063.

[38] Y. Zhang, C. Xu, J. Chen, X. Zhang, Z. Wang, J. Zhou, K. Cen, A novel photo-thermochemical cycle for the dissociation of CO_2 using solar energy, Appl. Energy. 156 (2015) 223-229. https://doi.org/10.1016/j.apenergy.2015.07.028.

[39] X. Yuan, X. Wu, Y. Wu, T. van Ree, Metal oxides for emission control, in: Met. Oxides Energy Technol., 2018: pp. 391-414. https://doi.org/10.1016/b978-0-12-811167-3.00015-8.

[40] G.C. Dhal, D. Mohan, R. Prasad, Preparation and application of effective different catalysts for simultaneous control of diesel soot and NO_X emissions: An overview, Catal. Sci. Technol. 7 (2017) 1803-1825. https://doi.org/10.1039/c6cy02612e.

[41] X. Auvray, Fundamental studies of catalytic systems for diesel emission control aging and sulfur treatment of a DOC, spatial investigation and kinetic modeling of NOx reduction by ammonia, Göteborg: Chalmers Univ. of Technology, 2013.

[42] B. Choi, K.S. Lee, LNT/CDPF catalysts for simultaneous removal of NO_x and PM from diesel vehicle exhaust, Chem. Eng. J. 240 (2014) 476-486. https://doi.org/10.1016/j.cej.2013.10.100.

[43] Y. Cheng, J. Liu, Z. Zhao, W. Song, Y. Wei, Highly efficient and simultaneously catalytic removal of PM and NO_x from diesel engines with 3DOM $Ce_{0.8}M_{0.1}Zr_{0.1}O_2$ (M = Mn, Co, Ni) catalysts, Chem. Eng. Sci. 167 (2017) 219-228. https://doi.org/10.1016/j.ces.2017.04.023.

[44] N.D. Wasalathanthri, T.M. SantaMaria, D.A. Kriz, S.L. Dissanayake, C.H. Kuo, S. Biswas, S.L. Suib, Mesoporous manganese oxides for NO_2 assisted catalytic soot oxidation, Appl. Catal. B Environ. 201 (2017) 543-551. https://doi.org/10.1016/j.apcatb.2016.08.052.

[45] L.M. Thang, Preparation of the catalyst for the total oxidation hydrocarbon applying for treatment of exhaust automobile gas, Hanoi: Hanoi University of Science and Technology, 1999.

[46] G. Cocito, V. Patierno, Chemical — Physical characterization of aluminas in the car exhaust gas treatment, Mater. Chem. 3 (1978) 233-253. https://doi.org/10.1016/0390-6035(78)90036-6.

[47] T.M.P. Pham, Study on the impregnation procedures to prepare catalytic complexes for the treatment of motorbike's exhaust gases, Ghent: Ghent University, 2013.

[48] B. Levasseur, S. Kaliaguine, Effects of iron and cerium in $La_{1-y}Ce_yCo_{1-x}Fe_xO_3$ perovskites as catalysts for VOC oxidation, Appl. Catal. B Environ. 88 (2009) 305-314. https://doi.org/10.1016/j.apcatb.2008.11.007.

[49] R. Di Monte, J. Kašpar, Heterogeneous environmental catalysis - a gentle art: CeO_2-ZrO_2 mixed oxides as a case history, in: Catal. Today, 2005: pp. 27-35. https://doi.org/10.1016/j.cattod.2004.11.005.

[50] T. Li, T. Kamhangdatepon, B. Wang, U.W. Hartley, K. Li, New bio-inspired design for high-performance and highly robust $La_{0.6}Sr_{0.4}Co_{0.2}Fe_{0.8}O_{3-\delta}$ membranes for oxygen permeation, J. Memb. Sci. 578 (2019) 203-208. https://doi.org/10.1016/j.memsci.2019.02.042.

[51] C. Wongsartsai, V. Tongnan, T. Sornchamni, N. Siri-nguan, N. Laosiripojana, M. Hartley, U.W. Hartley, CO_2 utilization via methanation using 40%Ni/$Ce_xCr_{1-x}O_2$ as a novel catalyst: a comparative study of packed-bed and micro-channel reactors, React. Kinet. Mech. Catal. (2020). https://doi.org/10.1007/s11144-020-01853-1.

[52] Q. Shen, G. Lu, C. Du, Y. Guo, Y. Wang, Y. Guo, X. Gong, Role and reduction of NO_x in the catalytic combustion of soot over iron-ceria mixed oxide catalyst, Chem. Eng. J. 218 (2013) 164-172. https://doi.org/10.1016/j.cej.2012.12.010.

[53] K. Yoshida, S. Makino, S. Sumiya, G. Muramatsu, R. Helferich, Simultaneous reduction of NO_x and particulate emissions from diesel engine exhaust, in: SAE Tech. Pap., 1989. https://doi.org/10.4271/892046.

[54] P.G. Smirniotis, D.A. Peña, B.S. Uphade, Low-temperature selective catalytic reduction (SCR) of NO with NH_3 by using Mn, Cr, and Cu oxides supported on hombikat TiO_2, Angew. Chemie - Int. Ed. 40 (2001) 2479-2482. https://doi.org/10.1002/1521-3773(20010702)40:13<2479::AID-ANIE2479>3.0.CO;2-7.

[55] R.Q. Long, R.T. Yang, R. Chang, Low temperature selective catalytic reduction (SCR) of NO with NH_3 over Fe-Mn based catalysts, Chem. Commun. 2 (2002) 452-453. https://doi.org/10.1039/b111382h.

[56] W.S. Kijlstra, D.S. Brands, H.I. Smit, E.K. Poels, A. Bliek, Mechanism of the selective catalytic reduction of NO with NH_3 over MnO_x/Al_2O_3 II. Reactivity of adsorbed NH_3 and NO complexes, J. Catal. 171 (1997) 219-230. https://doi.org/10.1006/jcat.1997.1789.

[57] G.Q. and R.T. Yang, Characterization and FTIR Studies of MnO_x-CeO_2 catalyst for low-temperature., J. Phys. Chem. B. 108 (2004) 15738-15747.

[58] G. Marbán, T. Valdés-Solís, A.B. Fuertes, Mechanism of low-temperature selective catalytic reduction of NO with NH_3 over carbon-supported Mn_3O_4 role of surface NH_3 species: SCR mechanism, J. Catal. 226 (2004) 138-155. https://doi.org/10.1016/j.jcat.2004.05.022.

[59] E. Tronconi, I. Nova, C. Ciardelli, D. Chatterjee, M. Weibel, Redox features in the catalytic mechanism of the "standard" and "fast" NH_3-SCR of NO_x over a V-based catalyst investigated by dynamic methods, J. Catal. 245 (2007) 1-10. https://doi.org/10.1016/j.jcat.2006.09.012.

[60] T.S. Park, S.K. Jeong, S.H. Hong, S.C. Hong, Selective catalytic reduction of nitrogen oxides with NH_3 over natural manganese ore at low temperature, Ind. Eng. Chem. Res. 40 (2001) 4491-4495. https://doi.org/10.1021/ie010218+.

[61] B. Huang, R. Huang, D. Jin, D. Ye, Low temperature SCR of NO with NH_3 over carbon nanotubes supported vanadium oxides, Catal. Today. 126 (2007) 279-283. https://doi.org/10.1016/j.cattod.2007.06.002.

[62] H. Chang, X. Chen, J. Li, L. Ma, C. Wang, C. Liu, J.W. Schwank, J. Hao, Improvement of activity and SO_2 tolerance of Sn-modified MnO_x-CeO_2 catalysts for NH_3-SCR at low temperatures, Environ. Sci. Technol. 47 (2013) 5294-5301. https://doi.org/10.1021/es304732h.

[63] F. Kapteijn, L. Singoredjo, A. Andreini, J.A. Moulijn, Activity and selectivity of pure manganese oxides in the selective catalytic reduction of nitric oxide with ammonia, Appl. Catal. B, Environ. 3 (1994) 173-189.

[64] X. Tang, J. Li, L. Sun, J. Hao, Origination of N_2O from NO reduction by NH_3 over β-MnO_2 and α-Mn_2O_3, Appl. Catal. B Environ. 99 (2010) 156-162. https://doi.org/10.1016/j.apcatb.2010.06.012.

[65] M. V. Twigg, "Urea-SCR technology for deNO_x after treatment of diesel exhausts," Johnson Matthey Technol. Rev. 59 (2015) 221-232. https://doi.org/10.1595/205651315x688280.

[66] G. Qi, R.T. Yang, R. Chang, MnO_x-CeO_2 mixed oxides prepared by co-precipitation for selective catalytic reduction of NO with NH_3 at low temperatures, Appl. Catal. B Environ. 51 (2004) 93-106. https://doi.org/10.1016/j.apcatb.2004.01.023.

[67] F. Liu, H. He, Selective catalytic reduction of NO with NH_3 over manganese substituted iron titanate catalyst: reaction mechanism and H_2O/ SO_2 inhibition mechanism study, in: Catal. Today, 2010: pp. 70-76. https://doi.org/10.1016/j.cattod.2010.02.043.

[68] H. Chang, J. Li, X. Chen, L. Ma, S. Yang, J.W. Schwank, J. Hao, Effect of Sn on MnO_x-CeO_2 catalyst for SCR of NO_x by ammonia: Enhancement of activity and remarkable resistance to SO_2, Catal. Commun. 27 (2012) 54-57. https://doi.org/10.1016/j.catcom.2012.06.022.

[69] D.A. Peña, B.S. Uphade, P.G. Smirniotis, TiO_2-supported metal oxide catalysts for low-temperature selective catalytic reduction of NO with NH_3: I. Evaluation and characterization of first row transition metals, J. Catal. 221 (2004) 421-431.

[70] Z. Wu, B. Jiang, Y. Liu, Effect of transition metals addition on the catalyst of manganese/titania for low-temperature selective catalytic reduction of nitric oxide with ammonia, Appl. Catal. B Environ. 79 (2008) 347-355. https://doi.org/10.1016/j.apcatb.2007.09.039.

[71] X. Song, J.H. Johnson, J.D. Naber, A review of the literature of selective catalytic reduction catalysts integrated into diesel particulate filters, Int. J. Engine Res. 16 (2015) 738-749. https://doi.org/10.1177/1468087414545094.

[72] J. Suzuki, S. Matsumoto, Development of catalysts for diesel particulate NO_x reduction, Top. Catal. 28 (2004) 171-176.

[73] A. Bueno-López, D. Lozano-Castelló, A.J. McCue, J.A. Anderson, NO_x storage and reduction over copper-based catalysts. part 3: simultaneous NO_x and soot removal, Appl. Catal. B Environ. 198 (2016) 266-275. https://doi.org/10.1016/j.apcatb.2016.05.068.

[74] J. Liu, Z. Zhao, C. ming Xu, A. jun Duan, Simultaneous removal of NO_x and diesel soot over nanometer Ln-Na-Cu-O perovskite-like complex oxide catalysts, Appl. Catal. B Environ. 78 (2008) 61-72. https://doi.org/10.1016/j.apcatb.2007.09.001.

[75] D. Fino, N. Russo, G. Saracco, V. Specchia, Catalytic removal of NO_x and diesel soot over nanostructured spinel-type oxides, J. Catal. 242 (2006) 38-47. https://doi.org/10.1016/j.jcat.2006.05.023.

[76] D. Fino, N. Russo, G. Saracco, V. Specchia, Removal of NO_x and diesel soot over catalytic traps based on spinel-type oxides, Powder Technol. 180 (2008) 74-78. https://doi.org/10.1016/j.powtec.2007.03.003.

[77] Q. Li, M. Meng, H. Xian, N. Tsubaki, X. Li, Y. Xie, T. Hu, J. Zhang, Hydrotalcite-derived $Mn_xMg_{3-x}AlO$ catalysts used for soot combustion, NO_x storage and simultaneous soot-NO_x removal, Environ. Sci. Technol. 44 (2010) 4747-4752. https://doi.org/10.1021/es9033638.

[78] Q. Li, M. Meng, F. Dai, Y. Zha, Y. Xie, T. Hu, J. Zhang, Multifunctional hydrotalcite-derived K/MnMgAlO catalysts used for soot combustion, NO_x storage and simultaneous soot-NO_x removal, Chem. Eng. J. 184 (2012) 106-112. https://doi.org/10.1016/j.cej.2012.01.009.

[79] X. Yu, J. Li, Y. Wei, Z. Zhao, J. Liu, B. Jin, A. Duan, G. Jiang, Three-dimensionally ordered macroporous $Mn_xCe_{1-x}O_\delta$ and $Pt/Mn_{0.5}Ce_{0.5}O_\delta$ catalysts: synthesis and catalytic performance for soot oxidation, Ind. Eng. Chem. Res. 53 (2014) 9653-9664. https://doi.org/10.1021/ie500666m.

[80] M. Piumetti, S. Bensaid, N. Russo, D. Fino, Nanostructured ceria-based catalysts for soot combustion: investigations on the surface sensitivity, Appl. Catal. B Environ. 165 (2015) 742-751. https://doi.org/10.1016/j.apcatb.2014.10.062.

[81] S. Wagloehner, M. Nitzer-Noski, S. Kureti, Oxidation of soot on manganese oxide catalysts, Chem. Eng. J. 259 (2015) 492-504. https://doi.org/10.1016/j.cej.2014.08.021.

[82] P. Sudarsanam, B. Hillary, B. Mallesham, B.G. Rao, M.H. Amin, A. Nafady, A.M. Alsalme, B.M. Reddy, S.K. Bhargava, Designing CuO_x nanoparticle-decorated CeO_2 nanocubes for catalytic soot oxidation: role of the nanointerface in the catalytic performance of heterostructured nanomaterials, Langmuir. 32 (2016) 2208-2215. https://doi.org/10.1021/acs.langmuir.5b04590.

[83] G. Mul, F. Kapteijn, C. Doornkamp, J.A. Moulijn, Transition metal oxide catalyzed carbon black oxidation: a study with $18O_2$, J. Catal. 179 (1998) 258-266. https://doi.org/10.1006/jcat.1998.2201.

[84] R. Yang, Y. Gao, J. Wang, Q. Wang, Layered double hydroxide (LDH) derived catalysts for simultaneous catalytic removal of soot and NO_x, Dalt. Trans. 43 (2014) 10317-10327. https://doi.org/10.1039/c3dt52896k.

[85] D. Fino, P. Fino, G. Saracco, V. Specchia, Studies on kinetics and reactions mechanism of $La_{2-x}K_xCu_{1-y}V_yO_4$ layered perovskites for the combined removal of diesel particulate and NO_x, Appl. Catal. B Environ. 43 (2003) 243-259. https://doi.org/10.1016/S0926-3373(02)00311-9.

[86] Y. Cheng, W. Song, J. Liu, H. Zheng, Z. Zhao, C. Xu, Y. Wei, E.J.M. Hensen, Simultaneous NO_x and particulate matter removal from diesel exhaust by hierarchical Fe-doped Ce-Zr oxide, ACS Catal. 7 (2017) 3883-3892. https://doi.org/10.1021/acscatal.6b03387.

[87] A. Mishra, R. Prasad, Preparation and application of perovskite catalysts for diesel soot emissions control: an overview, Catal. Rev. - Sci. Eng. 56 (2014) 57-81. https://doi.org/10.1080/01614940.2014.866438.

[88] C. Lee, J. Il Park, Y.G. Shul, H. Einaga, Y. Teraoka, Ag supported on electrospun macro-structure CeO_2 fibrous mats for diesel soot oxidation, Appl. Catal. B Environ. 174-175 (2015) 185-192. https://doi.org/10.1016/j.apcatb.2015.03.008.

[89] A. Bueno-López, Diesel soot combustion ceria catalysts, Appl. Catal. B Environ. 146 (2014) 1-11. https://doi.org/10.1016/j.apcatb.2013.02.033.

[90] A.L. Carrascull, M.I. Ponzi, E.N. Ponzi, Catalytic combustion of soot on KNO_3/ZrO_2 catalysts. effect of potassium nitrate loading on activity, Ind. Eng. Chem. Res. 42 (2003) 692-697. https://doi.org/10.1021/ie020482i.

[91] L. Castoldi, R. Matarrese, L. Lietti, P. Forzatti, Intrinsic reactivity of alkaline and alkaline-earth metal oxide catalysts for oxidation of soot, Appl. Catal. B Environ. 90 (2009) 278-285. https://doi.org/10.1016/j.apcatb.2009.03.022.

[92] Q. Wang, Z. Guo, J.S. Chung, Formation and structural characterization of potassium titanates and the potassium ion exchange property, Mater. Res. Bull. 44 (2009) 1973-1977. https://doi.org/10.1016/j.materresbull.2009.06.009.

[93] Q. Wang, J.S. Chung, Z. Guo, Promoted soot oxidation by doped $K_2Ti_2O_5$ catalysts and no oxidation catalysts, Ind. Eng. Chem. Res. 50 (2011) 8384-8388. https://doi.org/10.1021/ie200698j.
[94] Z.P. Wang, M.X. Chen, W.F. Shangguan, Simultaneous catalytic removal of NO_x and diesel soot over Cu-containing hydrotalcite derived catalysts, Wuli Huaxue Xuebao/ Acta Phys. - Chim. Sin. 25 (2009) 79-85. https://doi.org/10.3866/pku.whxb20090114.
[95] M. Machida, Y. Murata, K. Kishikawa, D. Zhang, K. Ikeue, On the reasons for high activity of CeO_2 catalyst for soot oxidation, Chem. Mater. 20 (2008) 4489-4494. https://doi.org/10.1021/cm800832w.
[96] W.B. Li, X.F. Yang, L.F. Chen, J.A. Wang, Adsorption/desorption of NO_x on MnO_2/ZrO_2 oxides prepared in reverse microemulsions, Catal. Today. 148 (2010) 75-80. https://doi.org/10.1016/j.cattod.2009.03.028.
[97] Q. Li, M. Meng, Z.Q. Zou, X.G. Li, Y.Q. Zha, Simultaneous soot combustion and nitrogen oxides storage on potassium-promoted hydrotalcite-based CoMgAlO catalysts, J. Hazard. Mater. 161 (2009) 366-372. https://doi.org/10.1016/j.jhazmat.2008.03.103.
[98] Z. Wang, Q. Li, L. Wang, W. Shangguan, Simultaneous catalytic removal of NO_x and soot particulates over CuMgAl hydrotalcites derived mixed metal oxides, Appl. Clay Sci. 55 (2012) 125-130. https://doi.org/10.1016/j.clay.2011.11.003.
[99] F. Dai, M. Meng, Y. Zha, Z. Li, T. Hu, Y. Xie, J. Zhang, Performance of Ce substituted hydrotalcite-derived mixed oxide catalysts $Co_{2.5}Mg_{0.5}$Al1-X%Cex%O used for soot combustion and simultaneous NO_x-soot removal, Fuel Process. Technol. 104 (2012) 43-49. https://doi.org/10.1016/j.fuproc.2012.07.002.
[100] P. Stelmachowski, G. Maniak, A. Kotarba, Z. Sojka, Strong electronic promotion of Co_3O_4 towards N_2O decomposition by surface alkali dopants, Catal. Commun. 10 (2009) 1062-1065. https://doi.org/10.1016/j.catcom.2008.12.057.
[101] S. Kumar Megarajan, S. Rayalu, Y. Teraoka, N. Labhsetwar, High NO oxidation catalytic activity on non-noble metal based cobalt-ceria catalyst for diesel soot oxidation, J. Mol. Catal. A Chem. 385 (2014) 112-118. https://doi.org/10.1016/j.molcata.2014.01.026.
[102] X. Niu, L. Zhou, X. Hu, W. Han, Mesoporous $Ce_xCo_{1-x}Cr_2O_4$ spinels: synthesis, characterization and catalytic application in simultaneous removal of soot particulate and NO, RSC Adv. 5 (2015) 52595-52601. https://doi.org/10.1039/c5ra04759e.
[103] H. Zhu, P. Zhang, S. Dai, Recent advances of Lanthanum-based perovskite oxides for catalysis, ACS Catal. 5 (2015) 6370-6385. https://doi.org/10.1021/acscatal.5b01667.
[104] X. Liu, X.Y. Shao, G.B. Fang, H.F. He, Z.G. Wan, Preparation and properties of chemically reduced graphene oxide/copolymer-polyamide nanocomposites, E-Polymers. 17 (2017) 3-14. https://doi.org/10.1515/epoly-2016-0094.

[105] C.H. Kim, G. Qi, K. Dahlberg, W. Li, Strontium-doped perovskites rival platinum catalysts for treating NO_x in simulated diesel exhaust, Science. 327 (2010) 1624-1627. https://doi.org/10.1126/science.1184087.

[106] J.P.A. Neeft, O.P. Van Pruissen, M. Makkee, J.A. Moulijn, Catalysts for the oxidation of soot from diesel exhaust gases. II. Contact between soot and catalyst under practical conditions, Appl. Catal. B Environ. 12 (1997) 21-31.

[107] N. Guillén-Hurtado, A. García-García, A. Bueno-López, Active oxygen by Ce-Pr mixed oxide nanoparticles outperform diesel soot combustion Pt catalysts, Appl. Catal. B Environ. 174-175 (2015) 60-66. https://doi.org/10.1016/j.apcatb.2015.02.036.

[108] G. Zhang, Z. Zhao, J. Liu, G. Jiang, A. Duan, J. Zheng, S. Chen, R. Zhou, Three dimensionally ordered macroporous $Ce_{1-x}Zr_xO_2$ solid solutions for diesel soot combustion, Chem. Commun. 46 (2010) 457-459.

[109] Y. Wei, J. Liu, Z. Zhao, A. Duan, G. Jiang, The catalysts of three-dimensionally ordered macroporous $Ce_{1-x}Zr_xO_2$-supported gold nanoparticles for soot combustion: The metal-support interaction, J. Catal. 287 (2012) 13-29. https://doi.org/10.1016/j.jcat.2011.11.006.

[110] J. Wang, G. Yang, L. Cheng, E.W. Shin, Y. Men, Three-dimensionally ordered macroporous spinel-type MCr_2O_4 (M = Co, Ni, Zn, Mn) catalysts with highly enhanced catalytic performance for soot combustion, Catal. Sci. Technol. 5 (2015) 4594-4601. https://doi.org/10.1039/c5cy00761e.

[111] Y. Wei, Z. Zhao, X. Yu, B. Jin, J. Liu, C. Xu, A. Duan, G. Jiang, S. Ma, One-pot synthesis of core-shell Au@$CeO_{2-\delta}$nanoparticles supported on three-dimensionally ordered macroporous ZrO_2 with enhanced catalytic activity and stability for soot combustion, Catal. Sci. Technol. 3 (2013) 2958-2970. https://doi.org/10.1039/c3cy00248a.

[112] N. Russo, D. Fino, G. Saracco, V. Specchia, Promotion effect of Au on perovskite catalysts for the regeneration of diesel particulate filters, Catal. Today. 137 (2008) 306-311. https://doi.org/10.1016/j.cattod.2007.09.010.

[113] S. Kaliaguine, V. Szabo, A. Van Neste, J.E. Gallot, M. Bassir, R. Muzychuk, Perovskite-type oxides synthesized by reactive grinding, J. Metastable Nanocrystalline Mater. 11 (2001) 39-56. https://doi.org/10.4028/www.scientific.net/jmnm.11.39.

[114] N. Russo, D. Fino, G. Saracco, V. Specchia, Studies on the redox properties of chromite perovskite catalysts for soot combustion, J. Catal. 229 (2005) 459-469. https://doi.org/10.1016/j.jcat.2004.11.025.

[115] X. Peng, H. Lin, W. Shangguan, Z. Huang, A highly efficient and porous catalyst for simultaneous removal of NO_x and diesel soot, Catal. Commun. 8 (2007) 157-161. https://doi.org/10.1016/j.catcom.2006.04.015.

[116] K. Wang, L. Qian, L. Zhang, H. Liu, Z. Yan, Simultaneous removal of NO_x and soot particulates over $La_{0.7}Ag_{0.3}MnO_3$ perovskite oxide catalysts, in: Catal. Today, 2010: pp. 423-426. https://doi.org/10.1016/j.cattod.2010.06.001.

[117] K. Hamamoto, Y. Fujishiro, M. Awano, Simultaneous removal of nitrogen oxides and diesel soot particulate in nano-structured electrochemical reactor, Solid State Ionics. 177 (2006) 2297-2300. https://doi.org/10.1016/j.ssi.2006.07.006.

[118] D.B. Kittelson, Engines and nanoparticles: a review, J. Aerosol Sci. 29 (1998) 575-588. https://doi.org/10.1016/S0021-8502(97)10037-4.

[119] D. Tichit, B. Coq, Catalysis by hydrotalcites and related materials, CATTECH. 7 (2003) 206-217. https://doi.org/10.1023/B:CATT.0000007166.65577.34.

[120] D. Ding, X. Li, S.Y. Lai, K. Gerdes, M. Liu, Enhancing SOFC cathode performance by surface modification through infiltration, Energy Environ. Sci. 7 (2014) 552-575. https://doi.org/10.1039/c3ee42926a.

[121] M. Han, Y. Zhang, Ceramic Materials for solid oxide fuel cell, Kuei Suan Jen Hsueh Pao/Journal Chinese Ceram. Soc. 45 (2017) 1548-1554. https://doi.org/10.14062/j.issn.0454-5648.2017.11.02.

[122] M. Winter, R.J. Brodd, What are batteries, fuel cells, and supercapacitors?, Chem. Rev. 104 (2004) 4245-4269. https://doi.org/10.1021/cr020730k.

[123] D. Simwonis, F. Tietz, D. Stöver, Nickel coarsening in annealed Ni/8YSZ anode substrates for solid oxide fuel cells, Solid State Ionics. 132 (2000) 241-251. https://doi.org/10.1016/s0167-2738(00)00650-0.

[124] W.Z. Zhu, S.C. Deevi, A review on the status of anode materials for solid oxide fuel cells, Mater. Sci. Eng. A. 362 (2003) 228-239. https://doi.org/10.1016/S0921-5093(03)00620-8.

[125] S.P. Jiang, S.H. Chan, A review of anode materials development in solid oxide fuel cells, J. Mater. Sci. 39 (2004) 4405-4439. https://doi.org/10.1023/b:jmsc.0000034135.52164.6b.

[126] B. Iwanschitz, L. Holzer, A. Mai, M. Schütze, Nickel agglomeration in solid oxide fuel cells: the influence of temperature, Solid State Ionics. 211 (2012) 69-73. https://doi.org/10.1016/j.ssi.2012.01.015.

[127] J. Van herle, D. Perednis, K. Nakamura, S. Diethelm, M. Zahid, A. Aslanides, T. Somekawa, Y. Baba, K. Horiuchi, Y. Matsuzaki, M. Yoshimoto, O. Bucheli, Ageing of anode-supported solid oxide fuel cell stacks including thermal cycling, and expansion behaviour of MgO-NiO anodes, J. Power Sources. 182 (2008) 389-399. https://doi.org/10.1016/j.jpowsour.2008.03.006.

[128] A. Utz, A. Leonide, A. Weber, E. Ivers-Tiffée, Studying the CO-CO_2 characteristics of SOFC anodes by means of patterned Ni anodes, in: J. Power Sources, 2011: pp. 7217-7224. https://doi.org/10.1016/j.jpowsour.2010.10.056.

[129] F. Tietz, F.J. Dias, D. Simwonis, D. Stöver, Evaluation of commercial nickel oxide powders for components in solid oxide fuel cells, J. Eur. Ceram. Soc. 20 (2000) 1023-1034. https://doi.org/10.1016/S0955-2219(99)00271-X.

[130] R.S. Amado, L.F.B. Malta, F.M.S. Garrido, M.E. Medeiros, Pilhas a combustível de óxido sólido: Materiais, componentes e configurações, Quim. Nova. 30 (2007) 189-197. https://doi.org/10.1590/S0100-40422007000100031.

[131] M.D. Gross, J.M. Vohs, R.J. Gorte, An examination of SOFC anode functional layers based on ceria in YSZ, J. Electrochem. Soc. 154 (2007) B694. https://doi.org/10.1149/1.2736647.

[132] V. V. Kharton, A.A. Yaremchenko, A.A. Valente, E. V. Frolova, M.I. Ivanovskaya, J.R. Frade, F.M.B. Marques, J. Rocha, Methane oxidation over SOFC anodes with nanocrystalline ceria-based phases, Solid State Ionics. 177 (2006) 2179-2183. https://doi.org/10.1016/j.ssi.2006.04.037.

[133] E. Ramírez-Cabrera, A. Atkinson, D. Chadwick, Influence of point defects on the resistance of ceria to carbon deposition in hydrocarbon catalysis, Solid State Ionics. 136-137 (2000) 825-831. https://doi.org/10.1016/S0167-2738(00)00507-5.

[134] S. Ball, J. Sharman, I. Harkness, Proton exchange membrane fuel cells: materials properties and performance, Platin. Met. Rev. 55 (2011) 225-228. https://doi.org/10.1595/147106711X595102.

[135] T. Horita, K. Yamaji, N. Sakai, M. Ishikawa, H. Yokokawa, M. Dokiya, Electrode reaction at platinum/ceria surface modified YSZ interface, in: Ionics (Kiel)., 1997: pp. 67-74. https://doi.org/10.1007/BF02375526.

[136] J. Qiao, K. Sun, N. Zhang, B. Sun, J. Kong, D. Zhou, Ni/YSZ and Ni-CeO_2/YSZ anodes prepared by impregnation for solid oxide fuel cells, J. Power Sources. 169 (2007) 253-258. https://doi.org/10.1016/j.jpowsour.2007.03.006.

[137] M.J. Escudero, A. Fuerte, Electrochemical analysis of a system based on W and Ni combined with CeO_2 as potential sulfur-tolerant SOFC anode, Fuel Cells. 16 (2016) 340-348. https://doi.org/10.1002/fuce.201500076.

[138] A. Fuerte, R.X. Valenzuela, M.J. Escudero, L. Daza, Effect of cobalt incorporation in copper-ceria based anodes for hydrocarbon utilisation in Intermediate temperature solid oxide fuel cells, in: J. Power Sources, 2011: pp. 4324-4331. https://doi.org/10.1016/j.jpowsour.2010.12.053.

[139] A. Fuerte, R.X. Valenzuela, M.J. Escudero, L. Daza, Study of a SOFC with a bimetallic Cu-Co-ceria anode directly fuelled with simulated biogas mixtures, in: Int. J. Hydrogen Energy, 2014: pp. 4060-4066. https://doi.org/10.1016/j.ijhydene.2013.06.142.

[140] A. Kulkarni, S. Giddey, S.P.S. Badwal, Yttria-doped ceria anode for carbon-fueled solid oxide fuel cell, J. Solid State Electrochem. 19 (2015) 325-335. https://doi.org/10.1007/s10008-014-2604-y.

[141] S. Sengodan, S. Choi, A. Jun, T.H. Shin, Y.W. Ju, H.Y. Jeong, J. Shin, J.T.S. Irvine, G. Kim, Layered oxygen-deficient double perovskite as an efficient and stable anode for direct hydrocarbon solid oxide fuel cells, Nat. Mater. 14 (2015) 205-209. https://doi.org/10.1038/nmat4166.

[142] Z. Han, Y. Wang, Y. Yang, L. Li, Z. Yang, M. Han, High-performance SOFCs with impregnated $Sr_2Fe_{1.5}Mo_{0.5}O_{6-\delta}$ anodes toward sulfur resistance, J. Alloys Compd. 703 (2017) 258-263. https://doi.org/10.1016/j.jallcom.2017.01.341.

[143] S. Tao, J.T.S. Irvine, S.M. Plint, Methane oxidation at redox stable fuel cell electrode $La_{0.75}Sr_{0.25}Cr_{0.5}Mn_{0.5}O_{3\pm\delta}$, J. Phys. Chem. B. 110 (2006) 21771-21776. https://doi.org/10.1021/jp062376q.

[144] S. Tao, J.T.S. Irvine, Catalytic properties of the perovskite oxide $La_{0.75}Sr_{0.25}Cr_{0.5}Fe_{0.5}O_{3-\delta}$ in relation to its potential as a solid oxide fuel cell anode material, Chem. Mater. 16 (2004) 4116-4121. https://doi.org/10.1021/cm049341s.

[145] O.A. Marina, N.L. Canfield, J.W. Stevenson, Thermal, electrical, and electrocatalytical properties of lanthanum-doped strontium titanate, Solid State Ionics. 149 (2002) 21-28. https://doi.org/10.1016/S0167-2738(02)00140-6.

[146] T. Li, M.F. Rabuni, L. Kleiminger, B. Wang, G.H. Kelsall, U.W. Hartley, K. Li, A highly-robust solid oxide fuel cell (SOFC): simultaneous greenhouse gas treatment and clean energy generation, Energy Environ. Sci. 9 (2016) 3682-3686. https://doi.org/10.1039/c6ee02562e.

[147] V. Kharton, F. Marques, A. Atkinson, Transport properties of solid oxide electrolyte ceramics: a brief review, Solid State Ionics. 174 (2004) 135-149. https://doi.org/10.1016/j.ssi.2004.06.015.

[148] M.A. Taylor, M. Kilo, G. Borchardt, S. Weber, H. Scherrer, 96Zr diffusion in polycrystalline scandia stabilized zirconia, J. Eur. Ceram. Soc. 25 (2005) 1591-1595. https://doi.org/10.1016/j.jeurceramsoc.2004.05.020.

[149] T.H. Etsell, S.N. Flengas, The electrical properties of solid oxide electrolytes, Chem. Rev. 70 (1970) 339-376. https://doi.org/10.1021/cr60265a003.

[150] Y. Li, Z. Wang, J. Li, X. Zhu, Y. Zhang, X. Huang, Y. Zhou, L. Zhu, Z. Lü, Sulfur poisoning and attempt of oxidative regeneration of $La_{0.75}Sr_{0.25}Cr_{0.5}Mn_{0.5}O_{3-\delta}$ anode for solid oxide fuel cell, J. Alloys Compd. 698 (2017) 794-799. https://doi.org/10.1016/j.jallcom.2016.12.313.

[151] A. Hornés, M.J. Escudero, L. Daza, A. Martínez-Arias, Electrochemical performance of a solid oxide fuel cell with an anode based on Cu-Ni/CeO_2 for methane direct oxidation, J. Power Sources. 249 (2014) 520-526. https://doi.org/10.1016/j.jpowsour.2013.05.159.

[152] H.J. Ko, J.H. Myung, S.H. Hyun, J.S. Chung, Synthesis of LSM-YSZ-GDC dual composite SOFC cathodes for high-performance power-generation systems, J. Appl. Electrochem. 42 (2012) 209-215. https://doi.org/10.1007/s10800-012-0390-8.

[153] J.S. Lee, Effects of strontium gallate additions on sintering behavior of gadolinia-doped ceria, in: J. Electroceramics, 2006: pp. 709-711. https://doi.org/10.1007/s10832-006-7775-1.

[154] G.S. Lewis, A. Atkinson, B.C.H. Steele, Cobalt additive for lowering the sintering temperature of yttria-stabilized zirconia, J. Mater. Sci. Lett. 20 (2001) 1155-1157. https://doi.org/10.1023/A:1010912912157.

[155] M.C. Tucker, G.Y. Lau, C.P. Jacobson, S.J. Visco, L.C. De Jonghe, Cu-YSZ cermet solid oxide fuel cell anode prepared by high-temperature sintering, J. Power Sources. 195 (2010) 3119-3123. https://doi.org/10.1016/j.jpowsour.2009.12.003.

[156] M. Feng, J.B. Goodenough, Improving stabilized zirconia with strontium gallate, J. Am. Ceram. Soc. 77 (1994) 1954-1956. https://doi.org/10.1111/j.1151-2916.1994.tb07077.x.

[157] T.S. Zhang, S.H. Chan, W. Wang, K. Hbaieb, L.B. Kong, J. Ma, Effect of Mn addition on the densification, grain growth and ionic conductivity of pure and SiO_2-containing 8YSZ electrolytes, Solid State Ionics. 180 (2009) 82-89. https://doi.org/10.1016/j.ssi.2008.10.010.

[158] S.P.S. Badwal, F.T. Ciacchi, D. Milosevic, Scandia-zirconia electrolytes for intermediate temperature solid oxide fuel cell operation, Solid State Ionics. 136-137 (2000) 91-99. https://doi.org/10.1016/S0167-2738(00)00356-8.

[159] C. Sánchez-Bautista, A.J. Dos Santos-García, J. Peña-Martínez, J. Canales-Vázquez, The grain boundary effect on dysprosium doped ceria, Solid State Ionics. 181 (2010) 1665-1673. https://doi.org/10.1016/j.ssi.2010.09.025.

[160] R.O. Fuentes, R.T. Baker, Synthesis and properties of gadolinium-doped ceria solid solutions for IT-SOFC electrolytes, Int. J. Hydrogen Energy. 33 (2008) 3480-3484. https://doi.org/10.1016/j.ijhydene.2007.10.026.

[161] J. Ding, J. Liu, G. Yin, Fabrication and characterization of low-temperature SOFC stack based on GDC electrolyte membrane, J. Memb. Sci. 371 (2011) 219-225. https://doi.org/10.1016/j.memsci.2011.01.051.

[162] M. Morales, S. Piñol, M. Segarra, Intermediate temperature single-chamber methane fed SOFC based on Gd doped ceria electrolyte and $La_{0.5}Sr_{0.5}CoO_{3-\delta}$ as cathode, J. Power Sources. 194 (2009) 961-966. https://doi.org/10.1016/j.jpowsour.2009.05.027.

[163] J. Patakangas, Y. Ma, Y. Jing, P. Lund, Review and analysis of characterization methods and ionic conductivities for low-temperature solid oxide fuel cells (LT-SOFC), J. Power Sources. 263 (2014) 315-331. https://doi.org/10.1016/j.jpowsour.2014.04.008.

[164] T. Tsuchiya, K. Terabe, M. Aono, All-solid-state electric-double-layer transistor based on oxide ion migration in Gd-doped CeO_2 on $SrTiO_3$ single crystal, Appl. Phys. Lett. 103 (2013). https://doi.org/10.1063/1.4818736.

[165] Q. Li, V. Thangadurai, Synthesis, structure and electrical properties of Mo-doped CeO_2-Materials for SOFCs, Fuel Cells. 9 (2009) 684-698. https://doi.org/10.1002/fuce.200900044.

[166] E.M. Levin, R.S. Roth, Polymorphism of bismuth sesquioxide. II. effect of oxide additions on the polymorphism of Bi_2O_3, J. Res. Natl. Bur. Stand. Sect. A Phys. Chem. 68A (1964) 197. https://doi.org/10.6028/jres.068a.020.

[167] R.D. Bayliss, S.N. Cook, S. Kotsantonis, R.J. Chater, J.A. Kilner, Ionic conductivity: oxygen ion diffusion and surface exchange properties of the α-and δ-phases of Bi_2O_3 (Adv. Energy Mater. 10/2014), Adv. Energy Mater. 4 (2014). https://doi.org/10.1002/aenm.201470049.

[168] K. Yamaji, H. Negishi, T. Horita, N. Sakai, H. Yokokawa, Vaporization process of Ga from doped $LaGaO_3$ electrolytes in reducing atmospheres, Solid State Ionics. 135 (2000) 389-396. https://doi.org/10.1016/S0167-2738(00)00474-4.

[169] K.C. Wincewicz, J.S. Cooper, Taxonomies of SOFC material and manufacturing alternatives, J. Power Sources. 140 (2005) 280-296. https://doi.org/10.1016/j.jpowsour.2004.08.032.

[170] E.J. Abram, D.C. Sinclair, A.R. West, A novel enhancement of ionic conductivity in the cation-deficient apatite $La_{9.33}(SiO_4)_6O_2$, J. Mater. Chem. 11 (2001) 1978-1979. https://doi.org/10.1039/b104006p.

[171] W.X. Kao, M.C. Lee, Y.C. Chang, T.N. Lin, C.H. Wang, J.C. Chang, Fabrication and evaluation of the electrochemical performance of the anode-supported solid oxide fuel cell with the composite cathode of $La_{0.8}Sr_{0.2}MnO_{3-\delta}$-Gadolinia-doped ceria oxide/$La_{0.8}Sr_{0.2}MnO_{3-\delta}$, J. Power Sources. 195 (2010) 6468-6472. https://doi.org/10.1016/j.jpowsour.2010.04.057.

[172] R.M. Belardi, J. Deseure, M.C. Brant, T. Matencio, R.Z. Domingues, Electrical study of cathodic activation and relaxation of $La_{0.80}Sr_{0.20}MnO_3$, Ionics (Kiel). 15 (2009) 227-232. https://doi.org/10.1007/s11581-008-0264-6.

[173] M. Gödickemeier, K. Sasaki, L.J. Gauckler, I. Riess, Perovskite cathodes for solid oxide fuel cells based on ceria electrolytes, Solid State Ionics. 86-88 (1996) 691-701. https://doi.org/10.1016/0167-2738(96)00149-X.

[174] Z. Yang, G.G. Xia, X.H. Li, J.W. Stevenson, $(Mn,Co)_3O_4$ spinel coatings on ferritic stainless steels for SOFC interconnect applications, Int. J. Hydrogen Energy. 32 (2007) 3648-3654. https://doi.org/10.1016/j.ijhydene.2006.08.048.

[175] Z. Yang, G. Xia, J.W. Stevenson, $Mn_{1.5}Co_{1.5}O_4$ spinel protection layers on ferritic stainless steels for SOFC interconnect applications, Electrochem. Solid-State Lett. 8 (2005) A168. https://doi.org/10.1149/1.1854122.

[176] Z. Yang, G. Xia, S.P. Simner, J.W. Stevenson, Thermal growth and performance of manganese cobaltite spinel protection layers on ferritic stainless steel SOFC interconnects, J. Electrochem. Soc. 152 (2005) A1896. https://doi.org/10.1149/1.1990462.

[177] Z.H. Bi, J.H. Zhu, J.L. Batey, $CoFe_2O_4$ spinel protection coating thermally converted from the electroplated Co-Fe alloy for solid oxide fuel cell interconnect application, J. Power Sources. 195 (2010) 3605-3611. https://doi.org/10.1016/j.jpowsour.2009.12.011.

[178] Y.K. Sun, Y.S. Lee, M. Yoshio, K. Amine, Synthesis and electrochemical properties of ZnO-coated $LiNi_{0.5}Mn_{1.5}O_4$ spinel as 5V cathode material for lithium secondary batteries, Electrochem. Solid-State Lett. 5 (2002). https://doi.org/10.1149/1.1465375.

[179] E. Chalkova, M.B. Pague, M.V. Fedkin, D.J. Wesolowski, S.N. Lvov, Nafion/TiO_2 Proton conductive composite membranes for PEM fuel cells operating at elevated temperature and reduced relative humidity, J. Electrochem. Soc. 152 (2005) A1035.

[180] J.A. Díaz-Real, E. Ortiz-Ortega, M.P. Gurrola, J. Ledesma-Garcia, L.G. Arriaga, Light-harvesting Ni/TiO_2 nanotubes as photo-electrocatalyst for alcohol oxidation in alkaline media, Electrochim. Acta. 206 (2016) 388-399. https://doi.org/10.1016/j.electacta.2016.04.163.

[181] K.T. Adjemian, S.J. Lee, S. Srinivasan, J. Benziger, A.B. Bocarsly, Silicon oxide nafion composite membranes for proton-exchange membrane fuel cell operation at 80-140 °C, J. Electrochem. Soc. 149 (2002) A256. https://doi.org/10.1149/1.1445431.

[182] C.H. Lee, K.A. Min, H.B. Park, Y.T. Hong, B.O. Jung, Y.M. Lee, Sulfonated poly(arylene ether sulfone)-silica nanocomposite membrane for direct methanol fuel cell (DMFC), J. Memb. Sci. 303 (2007) 258-266. https://doi.org/10.1016/j.memsci.2007.07.026.

[183] E. Antolini, E.R. Gonzalez, Tungsten-based materials for fuel cell applications, Appl. Catal. B Environ. 96 (2010) 245-266. https://doi.org/10.1016/j.apcatb.2010.02.039.

[184] J.B. Christian, S.P.E. Smith, M.S. Whittingham, H.D. Abruña, Tungsten based electrocatalyst for fuel cell applications, Electrochem. Commun. 9 (2007) 2128-2132. https://doi.org/10.1016/j.elecom.2007.06.001.

[185] B. Wickman, M. Wesselmark, C. Lagergren, G. Lindbergh, Tungsten oxide in polymer electrolyte fuel cell electrodes - a thin-film model electrode study, Electrochim. Acta. 56 (2011) 9496-9503. https://doi.org/10.1016/j.electacta.2011.08.046.

[186] Y. Zhou, X. Hu, Y. Xiao, Q. Shu, Platinum nanoparticles supported on hollow mesoporous tungsten trioxide microsphere as electrocatalyst for methanol oxidation, Electrochim. Acta. 111 (2013) 588-592. https://doi.org/10.1016/j.electacta.2013.08.057.

[187] F. Zhang, P. Zhao, M. Niu, J. Maddy, The survey of key technologies in hydrogen energy storage, Int. J. Hydrogen Energy. 41 (2016) 14535-14552. https://doi.org/10.1016/j.ijhydene.2016.05.293.

[188] N.T. Stetson, Hydrogen storage program area, 2014 Annual Merit Review and Peer Evaluation, 2014.

[189] B. Sakintuna, F. Lamari-Darkrim, M. Hirscher, Metal hydride materials for solid hydrogen storage: A review, Int. J. Hydrogen Energy. 32 (2007) 1121-1140. https://doi.org/10.1016/j.ijhydene.2006.11.022.

[190] A. Martínez-Mesa, G. Seifert, Adsorption of molecular hydrogen on nanostructured surfaces, Rev. Cuba. Fis. 31 (2014) 32-34.

[191] X.B. Yu, Z.X. Yang, H.K. Liu, D.M. Grant, G.S. Walker, The effect of a Ti-V-based BCC alloy as a catalyst on the hydrogen storage properties of MgH_2, Int. J. Hydrogen Energy. 35 (2010) 6338-6344. https://doi.org/10.1016/j.ijhydene.2010.03.089.

[192] W. Oelerich, T. Klassen, R. Bormann, Metal oxides as catalysts for improved hydrogen sorption in nanocrystalline Mg-based materials, J. Alloys Compd. 315 (2001) 237-242. https://doi.org/10.1016/S0925-8388(00)01284-6.

[193] G. Liang, J. Huot, S. Boily, A. Van Neste, R. Schulz, Catalytic effect of transition metals on hydrogen sorption in nanocrystalline ball milled MgH_2-Tm (Tm = Ti, V, Mn, Fe and Ni) systems, J. Alloys Compd. 292 (1999) 247-252.

[194] I.P. Jain, C. Lal, A. Jain, Hydrogen storage in Mg: a most promising material, Int. J. Hydrogen Energy. 35 (2010) 5133-5144. https://doi.org/10.1016/j.ijhydene.2009.08.088.

[195] M. Ismail, Influence of different amounts of $FeCl_3$ on decomposition and hydrogen sorption kinetics of MgH_2, Int. J. Hydrogen Energy. 39 (2014) 2567-2574. https://doi.org/10.1016/j.ijhydene.2013.11.084.

[196] K.S. Jung, E.Y. Lee, K.S. Lee, Catalytic effects of metal oxide on hydrogen absorption of magnesium metal hydride, J. Alloys Compd. 421 (2006) 179-184. https://doi.org/10.1016/j.jallcom.2005.09.085.

[197] N.S. Mustafa, M. Ismail, Influence of K_2TiF_6 additive on the hydrogen sorption properties of MgH_2, Int. J. Hydrogen Energy. 39 (2014) 15563-15569. https://doi.org/10.1016/j.ijhydene.2014.07.114.

[198] M. Ismail, Effect of $LaCl_3$ addition on the hydrogen storage properties of MgH_2, Energy. 79 (2015) 177-182. https://doi.org/10.1016/j.energy.2014.11.001.

[199] A. Ranjbar, M. Ismail, Z.P. Guo, X.B. Yu, H.K. Liu, Effects of CNTs on the hydrogen storage properties of MgH_2 and MgH_2-BCC composite, Int. J. Hydrogen Energy. 35 (2010) 7821-7826. https://doi.org/10.1016/j.ijhydene.2010.05.080.

[200] C.Z. Wu, P. Wang, X. Yao, C. Liu, D.M. Chen, G.Q. Lu, H.M. Cheng, Hydrogen storage properties of MgH_2/SWNT composite prepared by ball milling, J. Alloys Compd. 420 (2006) 278-282. https://doi.org/10.1016/j.jallcom.2005.10.028.

[201] A.R. Yavari, J.F.R. De Castro, G. Vaughan, G. Heunen, Structural evolution and metastable phase detection in MgH_2-5%NbH nanocomposite during in-situ H-desorption in a synchrotron beam, J. Alloys Compd. 353 (2003) 246-251.

[202] H. Gasan, O.N. Celik, N. Aydinbeyli, Y.M. Yaman, Effect of V, Nb, Ti and graphite additions on the hydrogen desorption temperature of magnesium hydride, in: Int. J. Hydrogen Energy, 2012: pp. 1912-1918. https://doi.org/10.1016/j.ijhydene.2011.05.086.

[203] M. Ismail, Y. Zhao, X.B. Yu, J.F. Mao, S.X. Dou, The hydrogen storage properties and reaction mechanism of the MgH_2-$NaAlH_4$ composite system, Int. J. Hydrogen Energy. 36 (2011) 9045-9050. https://doi.org/10.1016/j.ijhydene.2011.04.132.

[204] M. Ismail, Y. Zhao, S.X. Dou, An investigation on the hydrogen storage properties and reaction mechanism of the destabilized MgH_2-Na_3AlH_6 (4:1) system, Int. J. Hydrogen Energy. 38 (2013) 1478-1483. https://doi.org/10.1016/j.ijhydene.2012.11.035.

[205] A. Ranjbar, Z.P. Guo, X.B. Yu, D. Attard, A. Calka, H.K. Liu, Effects of SiC nanoparticles with and without Ni on the hydrogen storage properties of MgH_2, Int. J. Hydrogen Energy. 34 (2009) 7263-7268. https://doi.org/10.1016/j.ijhydene.2009.07.005.

[206] M. Baricco, M.W. Rahman, S. Livraghi, A. Castellero, S. Enzo, E. Giamello, Effects of $BaRuO_3$ addition on hydrogen desorption in MgH_2, in: J. Alloys Compd., 2012. https://doi.org/10.1016/j.jallcom.2011.12.008.

[207] D.L. Croston, D.M. Grant, G.S. Walker, The catalytic effect of titanium oxide based additives on the dehydrogenation and hydrogenation of milled MgH_2, J. Alloys Compd. 492 (2010) 251-258. https://doi.org/10.1016/j.jallcom.2009.10.199.

[208] H. Simchi, A. Kaflou, A. Simchi, Synergetic effect of Ni and Nb_2O_5 on dehydrogenation properties of nanostructured MgH_2 synthesized by high-energy mechanical alloying, Int. J. Hydrogen Energy. 34 (2009) 7724-7730. https://doi.org/10.1016/j.ijhydene.2009.07.038.

[209] M.W. Rahman, A. Castellero, S. Enzo, S. Livraghi, E. Giamello, M. Baricco, Effect of Mg-Nb oxides addition on hydrogen sorption in MgH_2, in: J. Alloys Compd., 2011. https://doi.org/10.1016/j.jallcom.2011.02.064.

[210] L. Yu, L. Zhang, H. Bin Wu, G. Zhang, X.W. Lou, Controlled synthesis of hierarchical $Co_xMn_{3-x}O_4$ array micro-/nanostructures with tunable morphology and composition as integrated electrodes for lithium-ion batteries, Energy Environ. Sci. 6 (2013) 2664-2671. https://doi.org/10.1039/c3ee41181h.

[211] E. David, An overview of advanced materials for hydrogen storage, in: J. Mater. Process. Technol., 2005: pp. 169-177. https://doi.org/10.1016/j.jmatprotec.2005.02.027.

[212] W. Grochala, P.P. Edwards, Thermal decomposition of the non-interstitial hydrides for the storage and production of hydrogen, Chem. Rev. 104 (2004) 1283-1315. https://doi.org/10.1021/cr030691s.

[213] E.M. Eyring, Topics in Applied Physics, Nucl. Technol. 39 (1978) 327-328.

[214] Y. Fukai, The metal-hydrogen system basic bulk properties, in: Springer Ser. Mater. Sci., 2005: pp. 1-28. https://doi.org/10.1007/978-3-662-02801-8_1.

[215] A. Zaluska, L. Zaluski, J.O. Ström-Olsen, Nanocrystalline magnesium for hydrogen storage, J. Alloys Compd. 288 (1999) 217-225. https://doi.org/10.1016/S0925-8388(99)00073-0.

[216] G. Barkhordarian, T. Klassen, R.U. Bormann, Effect of Nb_2O_5 content on hydrogen reaction kinetics of Mg, J. Alloys Compd. 364 (2004) 242-246. https://doi.org/10.1016/S0925-8388(03)00530-9.

[217] B. Bogdanović, K. Bohmhammel, B. Christ, A. Reiser, K. Schlichte, R. Vehlen, U. Wolf, Thermodynamic investigation of the magnesium-hydrogen system, J. Alloys Compd. 282 (1999) 84-92. https://doi.org/10.1016/S0925-8388(98)00829-9.

[218] B.H. Chen, Y.S. Chuang, C.K. Chen, Improving the hydrogenation properties of MgH_2 at room temperature by doping with nano-size ZrO_2 catalyst, J. Alloys Compd. 655 (2016) 21-27. https://doi.org/10.1016/j.jallcom.2015.09.163.

[219] M. Zhu, W.H. Zhu, C.Y. Chung, Z.X. Che, Z.X. Li, Microstructure and hydrogen absorption properties of nano-phase composite prepared by mechanical alloying of $MmNi_{5-x}(CoAlMn)_x$ and Mg, J. Alloys Compd. 293 (1999) 531-535. https://doi.org/10.1016/S0925-8388(99)00406-5.

[220] L. Guoxian, W. Erde, F. Shoushi, Hydrogen absorption and desorption characteristics of mechanically milled Mg35wt.%$FeTi_{1.2}$ powders, J. Alloys Compd. 223 (1995) 111-114. https://doi.org/10.1016/0925-8388(94)01465-5.

[221] S. Bouaricha, J.P. Dodelet, D. Guay, J. Huot, S. Boily, R. Schulz, Hydriding behavior of Mg-Al and leached Mg-Al compounds prepared by high-energy ball-milling, J. Alloys Compd. 297 (2000) 282-293. https://doi.org/10.1016/S0925-8388(99)00612-X.

[222] M. Bououdina, Z.X. Guo, Comparative study of mechanical alloying of (Mg+Al) and (Mg+Al+Ni) mixtures for hydrogen storage, J. Alloys Compd. 336 (2002) 222-231. https://doi.org/10.1016/S0925-8388(01)01856-4.

[223] P. Wang, A. Wang, H. Zhang, B. Ding, Z. Hu, Hydriding properties of a mechanically milled Mg-50wt%$ZrFe_{1.4}Cr_{0.6}$ composite, J. Alloys Compd. 297 (2000) 240-245. https://doi.org/10.1016/S0925-8388(99)00590-3.

[224] M.Y. Song, J.L. Bobet, B. Darriet, Improvement in hydrogen sorption properties of Mg by reactive mechanical grinding with Cr_2O_3, Al_2O_3 and CeO_2, J. Alloys Compd. 340 (2002) 256-262. https://doi.org/10.1016/S0925-8388(02)00019-1.

[225] N.E. Tran, S.G. Lambrakos, M.A. Imam, Analyses of hydrogen sorption kinetics and thermodynamics of magnesium-misch metal alloys, J. Alloys Compd. 407 (2006) 240-248. https://doi.org/10.1016/j.jallcom.2005.07.007.

[226] P. Wang, H.F. Zhang, B.Z. Ding, Z.Q. Hu, Direct hydrogenation of Mg and decomposition behavior of the hydride formed, J. Alloys Compd. 313 (2000) 209-213. https://doi.org/10.1016/S0925-8388(00)01186-5.

[227] K.J. Gross, P. Spatz, A. Züttel, L. Schlapbach, Mechanically milled Mg composites for hydrogen storage: The transition to a steady state composition, J. Alloys Compd. 240 (1996) 206-213. https://doi.org/10.1016/0925-8388(96)02261-X.

[228] K.J. Gross, D. Chartouni, E. Leroy, A. Züttel, L. Schlapbach, Mechanically milled Mg composites for hydrogen storage: the relationship between morphology and kinetics, J. Alloys Compd. 269 (1998) 259-270. https://doi.org/10.1016/S0925-8388(97)00627-0.

[229] Q. Li, K.C. Chou, K. Di Xu, L.J. Jiang, Q. Lin, G.W. Lin, X.G. Lu, J.Y. Zhang, Hydrogen absorption and desorption characteristics in the $La_{0.5}Ni_{1.5}Mg_{17}$ prepared by hydriding combustion synthesis, Int. J. Hydrogen Energy. 31 (2006) 497-503. https://doi.org/10.1016/j.ijhydene.2005.04.027.

[230] G. Liang, S. Boily, J. Huot, A. Van Neste, R. Schulz, Hydrogen absorption properties of a mechanically milled Mg-50wt.%$LaNi_5$ composite, J. Alloys Compd. 268 (1998) 302-307. https://doi.org/10.1016/S0925-8388(97)00607-5.

[231] Y. Chen, C.Z. Wu, P. Wang, H.M. Cheng, Structure and hydrogen storage property of ball-milled $LiNH_2/MgH_2$ mixture, Int. J. Hydrogen Energy. 31 (2006) 1236-1240. https://doi.org/10.1016/j.ijhydene.2005.09.001.

[232] Z. Xiong, G. Wu, J. Hu, P. Chen, Ternary imides for hydrogen storage, Adv. Mater. 16 (2004) 1522-1525. https://doi.org/10.1002/adma.200400571.

[233] A. Reiser, B. Bogdanović, K. Schlichte, Application of Mg-based metal-hydrides as heat energy storage systems, Int. J. Hydrogen Energy. 25 (2000) 425-430. https://doi.org/10.1016/S0360-3199(99)00057-9.

[234] W. Luo, ($LiNH_2$-MgH_2): A viable hydrogen storage system, J. Alloys Compd. 381 (2004) 284-287. https://doi.org/10.1016/j.jallcom.2004.03.119.

[235] P. Chen, Z. Xiong, J. Luo, J. Lin, K. Lee Tan, Interaction of hydrogen with metal nitrides and imides, Nature. 420 (2002) 302-304. https://doi.org/10.1038/nature 01210.

[236] P. Wang, A.M. Wang, H.F. Zhang, B.Z. Ding, Z.Q. Hu, Hydrogenation characteristics of Mg-TiO_2 (rutile) composite, J. Alloys Compd. 313 (2000) 218-223. https://doi.org/ 10.1016/S0925-8388(00)01188-9.

[237] D.J. Davidson, S.S. Sai Raman, O.N. Srivastava, Investigation on the synthesis, characterization and hydrogenation behaviour of new Mg-based composite materials Mg-x wt.%$MmNi_{4.6}Fe_{0.4}$ prepared through mechanical alloying, J. Alloys Compd. 292 (1999) 194-201. https://doi.org/10.1016/S0925-8388(99)00190-5.

[238] Z. Dehouche, R. Djaozandry, J. Huot, S. Boily, J. Goyette, T.K. Bose, R. Schulz, Influence of cycling on the thermodynamic and structure properties of nanocrystalline magnesium based hydride, J. Alloys Compd. 305 (2000) 264-271. https://doi.org/10.1016/S0925-8388(00)00718-0.

[239] B. Bogdanovi, A. Reiser, K. Schlichte, B. Spliethoff, B. Tesche, Thermodynamics and dynamics of the Mg-Fe-H system and its potential for thermochemical thermal energy storage, J. Alloys Compd. 345 (2002) 77-89. https://doi.org/10.1016/ S0925-8388(02)00308-0.

[240] F. Li, L. Jiang, J. Du, S. Wang, X. Liu, F. Zhan, Synthesis and hydrogenation properties of Mg-La-Ni-H system by reactive mechanical alloying, Int. J. Hydrogen Energy. 31 (2006) 581-585. https://doi.org/10.1016/j.ijhydene.2005.06.007.

[241] M. Song, I. Kwon, S. Kwon, C. Park, H. Park, J.S. Bae, Preparation of hydrogen-storage alloy Mg-10wt%Fe_2O_3 under various milling conditions, Int. J. Hydrogen Energy. 31 (2006) 43-47. https://doi.org/10.1016/j.ijhydene.2005.03.008.

[242] S.S.S. Raman, O.N. Srivastava, Hydrogenation behaviour of the new composite storage materials Mg-x wt.%$CFMmNi_5$, J. Alloys Compd. 241 (1996) 167-174. https://doi.org/10.1016/0925-8388(96)02332-8.

[243] G. Liang, J. Huot, S. Boily, A. Van Neste, R. Schulz, Hydrogen storage properties of the mechanically milled MgH_2-V nanocomposite, J. Alloys Compd. 291 (1999) 295-299. https://doi.org/10.1016/S0925-8388(99)00268-6.

[244] Z. Dehouche, T. Klassen, W. Oelerich, J. Goyette, T.K. Bose, R. Schulz, Cycling and thermal stability of nanostructured MgH_2-Cr_2O_3 composite for hydrogen storage, J. Alloys Compd. 347 (2002) 319-323. https://doi.org/10.1016/S0925-8388(02)00784-3.

[245] N. Hanada, T. Ichikawa, H. Fujii, Catalytic effect of nanoparticle 3d-transition metals on hydrogen storage properties in magnesium hydride MgH_2 prepared by mechanical milling, J. Phys. Chem. B. 109 (2005) 7188-7194. https://doi.org/10.1021/jp044576c.

[246] J. Huot, G. Liang, S. Boily, A. Van Neste, R. Schulz, Structural study and hydrogen sorption kinetics of ball-milled magnesium hydride, J. Alloys Compd. 293 (1999) 495-500. https://doi.org/10.1016/S0925-8388(99)00474-0.

[247] H.Y. Leng, T. Ichikawa, S. Isobe, S. Hino, N. Hanada, H. Fujii, Desorption behaviours from metal-N-H systems synthesized by ball milling, J. Alloys Compd. 404-406 (2005) 443-447. https://doi.org/10.1016/j.jallcom.2004.09.082.

[248] H. Imamura, K. Masanari, M. Kusuhara, H. Katsumoto, T. Sumi, Y. Sakata, High hydrogen storage capacity of nanosized magnesium synthesized by high energy ball-milling, J. Alloys Compd. 386 (2005) 211-216. https://doi.org/10.1016/j.jallcom.2004.04.145.

[249] F.C. Gennari, F.J. Castro, G. Urretavizcaya, G. Meyer, Catalytic effect of Ge on hydrogen desorption from MgH_2, J. Alloys Compd. 334 (2002) 277-284. https://doi.org/10.1016/S0925-8388(01)01786-8.

[250] H. Reule, M. Hirscher, A. Weißhardt, H. Kronmüller, Hydrogen desorption properties of mechanically alloyed MgH_2 composite materials, J. Alloys Compd. 305 (2000) 246-252. https://doi.org/10.1016/S0925-8388(00)00710-6.

[251] R.L. Holtz, Basic user's guide for NRL 6323 hydrogen storage system, 1996.

[252] G. Friedlmeier, M. Groll, Experimental analysis and modelling of the hydriding kinetics of Ni-doped and pure Mg, J. Alloys Compd. 253-254 (1997) 550-555. https://doi.org/10.1016/S0925-8388(96)03003-4.

[253] A. Zaluska, L. Zaluski, J.O. Ström-Olsen, Synergy of hydrogen sorption in ball-milled hydrides of Mg and Mg_2Ni, J. Alloys Compd. 289 (1999) 197-206. https://doi.org/10.1016/S0166-0462(99)00013-7.

[254] R.W.P. Wagemans, J.H. Van Lenthe, P.E. De Jongh, A.J. Van Dillen, K.P. De Jong, Hydrogen storage in magnesium clusters: Quantum chemical study, J. Am. Chem. Soc. 127 (2005) 16675-16680. https://doi.org/10.1021/ja054569h.

[255] T.W. Hong, S.K. Kim, Y.J. Kim, Dehydrogenation properties of nano-/amorphous Mg_2NiH_x by hydrogen induced mechanical alloying, J. Alloys Compd. 312 (2000) 60-67. https://doi.org/10.1016/S0925-8388(00)01131-2.

[256] P. Tessier, H. Enoki, M. Bououdina, E. Akiba, Ball-milling of Mg_2Ni under hydrogen, J. Alloys Compd. 268 (1998) 285-289. https://doi.org/10.1016/S0925-8388(97)00585-9.

[257] J. Huot, E. Akiba, T. Takada, Mechanical alloying of MgNi compounds under hydrogen and inert atmosphere, J. Alloys Compd. 231 (1995) 815-819. https://doi.org/10.1016/0925-8388(95)01764-X.

[258] Y. Chen, J.S. Williams, Formation of metal hydrides by mechanical alloying, J. Alloys Compd. 217 (1995) 181-184. https://doi.org/10.1016/0925-8388(94)01338-1.

[259] S.I. Orimo, H. Fujii, Effects of nanometer-scale structure on hydriding properties of Mg-Ni alloys: a review, Intermetallics. 6 (1998) 185-192. https://doi.org/10.1016/S0966-9795(97)00064-2.

[260] M. Abdellaoui, D. Cracco, A. Percheron-Guegan, Structural characterization and reversible hydrogen absorption properties of Mg_2Ni rich nanocomposite materials synthesized by mechanical alloying, J. Alloys Compd. 268 (1998) 233-240. https://doi.org/10.1016/S0925-8388(97)00560-4.

[261] G. Barkhordarian, T. Klassen, R. Bormann, Kinetic investigation of the effect of milling time on the hydrogen sorption reaction of magnesium catalyzed with different Nb_2O_5 contents, J. Alloys Compd. 407 (2006) 249-255. https://doi.org/10.1016/j.jallcom.2005.05.037.

[262] R.L. Holtz, M.A. Imam, Hydrogen storage characteristics of ball-milled magnesium-nickel and magnesium-iron alloys, J. Mater. Sci. 34 (1999) 2655-2663. https://doi.org/10.1023/A:1004617203266.

[263] K. Higuchi, H. Kajioka, K. Toiyama, H. Fujii, S. Orimo, Y. Kikuchi, In situ study of hydriding-dehydriding properties in some Pd/Mg thin films with different degree of Mg crystallization, J. Alloys Compd. 293 (1999) 484-489. https://doi.org/10.1016/S0925-8388(99)00470-3.

[264] H. Akyildiz, M. Özenbaş, T. Öztürk, Hydrogen absorption in magnesium based crystalline thin films, Int. J. Hydrogen Energy. 31 (2006) 1379-1383. https://doi.org/10.1016/j.ijhydene.2005.11.003.

[265] H. Imamura, N. Sakasai, Y. Kajii, Hydrogen absorption of Mg-based composites prepared by mechanical milling: factors affecting its characteristics, J. Alloys Compd. 232 (1996) 218-223. https://doi.org/10.1016/0925-8388(95)01882-4.

[266] C.X. Shang, Z.X. Guo, Effect of carbon on hydrogen desorption and absorption of mechanically milled MgH_2, in: J. Power Sources, 2004: pp. 73-80. https://doi.org/10.1016/j.jpowsour.2003.11.013.

[267] R. Vijay, R. Sundaresan, M.P. Maiya, S.S. Murthy, Comparative evaluation of Mg-Ni hydrogen absorbing materials prepared by mechanical alloying, Int. J. Hydrogen Energy. 30 (2005) 501-508. https://doi.org/10.1016/j.ijhydene.2004.04.019.

[268] S.S. Han, N.H. Goo, K.S. Lee, Effects of sintering on composite metal hydride alloy of Mg_2Ni and TiNi synthesized by mechanical alloying, J. Alloys Compd. 360 (2003) 243-249. https://doi.org/10.1016/S0925-8388(03)00360-8.

[269] S. Orimo, H. Fujii, Materials science of Mg-Ni-based new hydrides, Appl. Phys. A Mater. Sci. Process. 72 (2001) 167-186. https://doi.org/10.1007/s003390100771.

[270] T. Sato, H. Blomqvist, D. Noréus, Attempts to improve Mg_2Ni hydrogen storage by aluminium addition, in: J. Alloys Compd., 2003: pp. 494-496. https://doi.org/10.1016/S0925-8388(02)01247-1.

[271] L. Zaluski, A. Zaluska, J.O. Ström-Olsen, Hydrogen absorption in nanocrystalline Mg_2Ni formed by mechanical alloying, J. Alloys Compd. 217 (1995) 245-249. https://doi.org/10.1016/0925-8388(94)01348-9.

[272] A.K. Singh, A.K. Singh, O.N. Srivastava, On the synthesis of the Mg_2Ni alloy by mechanical alloying, J. Alloys Compd. 227 (1995) 63-68. https://doi.org/10.1016/0925-8388(95)01625-2.

[273] M. Abdellaoui, S. Mokbli, F. Cuevas, M. Latroche, A. Percheron Guegan, H. Zarrouk, Structural, solid-gas and electrochemical characterization of Mg_2Ni-rich and Mg_xNi_{100-x} amorphous-rich nanomaterials obtained by mechanical alloying, in: Int. J. Hydrogen Energy, 2006: pp. 247-250. https://doi.org/10.1016/j.ijhydene.2005.04.044.

[274] G. Liang, S. Boily, J. Huot, A. Van Neste, R. Schulz, Mechanical alloying and hydrogen absorption properties of the Mg-Ni system, J. Alloys Compd. 267 (1998) 302-306. https://doi.org/10.1016/S0925-8388(97)00533-1.

[275] M. Terzieva, M. Khrussanova, P. Peshev, D. Radev, Hydriding and dehydriding characteristics of mixtures with a high magnesium content obtained by sintering and mechanical alloying, Int. J. Hydrogen Energy. 20 (1995) 53-58. https://doi.org/10.1016/0360-3199(93)E0009-A.

[276] M. Terzieva, M. Khrussanova, P. Peshev, Hydriding and dehydriding characteristics of Mg-$LaNi_5$ composite materials prepared by mechanical alloying, J. Alloys Compd. 267 (1998) 235-239. https://doi.org/10.1016/S0925-8388(97)00556-2.

[277] U. Haussermann, H. Blomqvist, D. Noréus, Bonding and stability of the hydrogen storage material Mg_2NiH_4, Inorg. Chem. 41 (2002) 3684-3692. https://doi.org/10.1021/ic0201046.

[278] L. Zaluski, A. Zaluska, P. Tessier, J.O. Ström-Olsen, R. Schulz, Catalytic effect of Pd on hydrogen absorption in mechanically alloyed Mg_2Ni, $LaNi_5$ and FeTi, J. Alloys Compd. 217 (1995) 295-300. https://doi.org/10.1016/0925-8388(94)01358-6.

[279] N.E. Tran, M.A. Imam, C.R. Feng, Evaluation of hydrogen storage characteristics of magnesium-misch metal alloys, J. Alloys Compd. 359 (2003) 225-229. https://doi.org/10.1016/S0925-8388(03)00176-2.

[280] G. Friedlmeier, A. Manthey, M. Wanner, M. Groll, Cyclic stability of various application-relevant metal hydrides, J. Alloys Compd. 231 (1995) 880-887. https://doi.org/10.1016/0925-8388(95)01776-3.

[281] Z. Dehouche, R. Djaozandry, J. Goyette, T.K. Bose, Thermal cyclic charge and discharge stability of nanocrystalline Mg_2Ni alloy, J. Alloys Compd. 288 (1999) 312-318. https://doi.org/10.1016/S0925-8388(99)00118-8.

[282] A.S. Pedersen, B. Larsen, The storage of industrially pure hydrogen in magnesium, Int. J. Hydrogen Energy. 18 (1993) 297-300.

[283] S. Bouaricha, J. Huot, D. Guay, R. Schulz, Reactivity during cycling of nanocrystalline Mg-based hydrogen storage compounds, Int. J. Hydrogen Energy. 27 (2002) 909-913. https://doi.org/10.1016/S0360-3199(01)00183-5.

[284] Z. Dehouche, J. Goyette, T.K. Bose, R. Schulz, Moisture effect on hydrogen storage properties of nanostructured MgH_2-V-Ti composite, Int. J. Hydrogen Energy. 28 (2003) 983-988. https://doi.org/10.1016/S0360-3199(02)00196-9.

[285] A. Zaluska, L. Zaluski, New catalytic complexes for metal hydride systems, J. Alloys Compd. 404-406 (2005) 706-711. https://doi.org/10.1016/j.jallcom.2005.03.104.

[286] A. Züttel, P. Wenger, S. Rentsch, P. Sudan, P. Mauron, C. Emmenegger, $LiBH_4$ a new hydrogen storage material, in: J. Power Sources, 2003: pp. 1-7. https://doi.org/10.1016/S0378-7753(03)00054-5.

[287] B. Bogdanović, M. Schwickardi, Ti-doped $NaAlH_4$ as a hydrogen-storage material - Preparation by Ti-catalyzed hydrogenation of aluminum powder in conjunction with sodium hydride, Appl. Phys. A Mater. Sci. Process. 72 (2001) 221-223. https://doi.org/10.1007/s003390100774.

[288] B. Bogdanović, M. Schwickardi, Ti-doped alkali metal aluminium hydrides as potential novel reversible hydrogen storage materials, J. Alloys Compd. 253-254 (1997) 1-9. https://doi.org/10.1016/S0925-8388(96)03049-6.

[289] C.M. Jensen, K.J. Gross, Development of catalytically enhanced sodium aluminum hydride as a hydrogen-storage material, Appl. Phys. A Mater. Sci. Process. 72 (2001) 213-219. https://doi.org/10.1007/s003390100784.

[290] L. Zaluski, A. Zaluska, J.. O. Ström-Olsen, Hydrogenation properties of complex alkali metal hydrides fabricated by mechano-chemical synthesis, J. Alloys Compd. 290 (1999) 71-78. https://doi.org/10.1016/S0925-8388(99)00211-X.

[291] R. Genma, N. Okada, T. Sobue, H. Uchida, Mechanically milled alanates as hydrogen storage materials, Int. J. Hydrogen Energy. 31 (2006) 309-311. https://doi.org/10.1016/j.ijhydene.2005.04.040.

[292] G. Sandrock, K. Gross, G. Thomas, C. Jensen, D. Meeker, S. Takara, Engineering considerations in the use of catalyzed sodium alanates for hydrogen storage, J. Alloys Compd. 330-332 (2002) 696-701. https://doi.org/10.1016/S0925-8388(01)01505-5.

[293] P. Wang, C.M. Jensen, Method for preparing Ti-doped $NaAlH_4$ using Ti powder: Observation of an unusual reversible dehydrogenation behavior, J. Alloys Compd. 379 (2004) 99-102. https://doi.org/10.1016/j.jallcom.2004.02.006.

[294] D. Sun, S.S. Srinivasan, T. Kiyobayashi, N. Kuriyama, C.M. Jensen, Rehydrogenation of dehydrogenated $NaAlH_4$ at low temperature and pressure, J. Phys. Chem. B. 107 (2003) 10176-10179. https://doi.org/10.1021/jp030637f.

[295] R.A. Zidan, S. Takara, A.G. Hee, C.M. Jensen, Hydrogen cycling behavior of zirconium and titanium-zirconium-doped sodium aluminum hydride, J. Alloys Compd. 285 (1999) 119-122. https://doi.org/10.1016/S0925-8388(99)00006-7.

[296] A. Zaluska, L. Zaluski, J.O. Ström-Olsen, Sodium alanates for reversible hydrogen storage, J. Alloys Compd. 298 (2000) 125-134. https://doi.org/10.1016/S0925-8388(99)00666-0.

[297] C.M. Jensen, R. Zidan, N. Mariels, A. Hee, C. Hagen, Advanced titanium doping of sodium aluminum hydride: segue to a practical hydrogen storage material?, Int. J. Hydrogen Energy. 24 (1999) 461-465.

[298] B. Bogdanović, M. Felderhoff, S. Kaskel, A. Pommerin, K. Schlichte, F. Schüth, Improved hydrogen storage properties of Ti-doped sodium alanate using titanium nanoparticles as doping agents, Adv. Mater. 15 (2003) 1012-1015. https://doi.org/10.1002/adma.200304711.

[299] G. Sandrock, K. Gross, G. Thomas, Effect of Ti-catalyst content on the reversible hydrogen storage properties of the sodium alanates, J. Alloys Compd. 339 (2002) 299-308. https://doi.org/10.1016/S0925-8388(01)02014-X.

[300] M. Fichtner, O. Fuhr, O. Kircher, J. Rothe, Small Ti clusters for catalysis of hydrogen exchange in $NaAlH_4$, Nanotechnology. 14 (2003). https://doi.org/10.1088/0957-4484/14/7/314.

[301] O. Kircher, M. Fichtner, Kinetic studies of the decomposition of $NaAlH_4$ doped with a Ti-based catalyst, J. Alloys Compd. 404-406 (2005) 339-342. https://doi.org/10.1016/j.jallcom.2004.11.121.

[302] Y.E. Filinchuk, K. Yvon, Boron-induced hydrogen localization in the novel metal hydride $LaNi_3BH_x$ ($x = 2.5$-3.0), Inorg. Chem. 44 (2005) 4398-4406. https://doi.org/10.1021/ic050416j.

[303] Y.H. Hu, E. Ruckenstein, Hydrogen storage of Li_2NH prepared by reacting Li with NH_3, Ind. Eng. Chem. Res. 45 (2006) 182-186. https://doi.org/10.1021/ie050690l.

[304] T. Ichikawa, S. Isobe, N. Hanada, H. Fujii, Lithium nitride for reversible hydrogen storage, J. Alloys Compd. 365 (2004) 271-276. https://doi.org/10.1016/S0925-8388(03)00637-6.

[305] Y.H. Hu, E. Ruckenstein, Highly Effective Li_2O/Li_3N with ultrafast kinetics for H_2 storage, Ind. Eng. Chem. Res. 43 (2004) 2464-2467. https://doi.org/10.1021/ie049947q.

[306] Y.H. Hu, E. Ruckenstein, H_2 storage in Li_3N. temperature-programmed hydrogenation and dehydrogenation, Ind. Eng. Chem. Res. 42 (2003) 5135-5139.

[307] F.E. Pinkerton, G.P. Meisner, M.S. Meyer, M.P. Balogh, M.D. Kundrat, Hydrogen desorption exceeding ten weight percent from the new quaternary hydride $Li_3BN_2H_8$, J. Phys. Chem. B. 109 (2005) 6-8. https://doi.org/10.1021/jp0455475.

[308] J.J. Vajo, S.L. Skeith, F. Mertens, Reversible storage of hydrogen in destabilized $LiBH_4$., ChemInform. 36 (2005) 3219-3722. https://doi.org/10.1002/chin.200521016.

[309] H. Morioka, K. Kakizaki, S.C. Chung, A. Yamada, Reversible hydrogen decomposition of $KAlH_4$, J. Alloys Compd. 353 (2003) 310-314. https://doi.org/10.1016/S0925-8388(02)01307-5.

[310] F.W. Dafert, R. Miklauz, Über einige neue verbindungen von stickstoff und wasserstoff mit lithium, Monatshefte Für Chemie. 31 (1910) 981-996. https://doi.org/10.1007/BF01518423.

[311] O. Ruff, H. Goerges, Über das Lithium-imid und einige bemerkungen zu der arbeit von dafert und miklauz: “über einige neue verbindungen von stickstoff und wasserstoff mit lithium,” Berichte Der Dtsch. Chem. Gesellschaft. 44 (1911) 502-506. https://doi.org/10.1002/cber.19110440178.

[312] Y.H. Hu, E. Ruckenstein, Ultrafast reaction between LiH and NH_3 during H_2 storage in Li_3, J. Phys. Chem. A. 107 (2003) 9737-9739. https://doi.org/10.1021/jp036257b.

[313] S. Orimo, Y. Nakamori, G. Kitahara, K. Miwa, N. Ohba, T. Noritake, S. Towata, Destabilization and enhanced dehydriding reaction of $LiNH_2$: An electronic structure viewpoint, Appl. Phys. A Mater. Sci. Process. 79 (2004) 1765-1767. https://doi.org/10.1007/s00339-004-2927-0.

[314] H.I. Schlesinger, H.C. Brown, Metallo borohydrides. III. lithium borohydride, J. Am. Chem. Soc. 62 (1940) 3429-3435. https://doi.org/10.1021/ja01869a039.

[315] D.S. Stasinevich, G.A. Egorenko, Thermographic investigation of alkali metal and magnesium tetrahydroborates at pressure up to 10 atm, Russ. J. Inorg. Chem. 13 (1968) 341-343.

[316] A. Züttel, S. Rentsch, P. Fischer, P. Wenger, P. Sudan, P. Mauron, C. Emmenegger, Hydrogen storage properties of $LiBH_4$, J. Alloys Compd. 356-357 (2003) 515-520. https://doi.org/10.1016/S0925-8388(02)01253-7.

[317] A. Zaluska, L. Zaluski, J.O. Ström-Olsen, Lithium-beryllium hydrides: the lightest reversible metal hydrides, J. Alloys Compd. 307 (2000) 157-166. https://doi.org/10.1016/S0925-8388(00)00883-5.

[318] R.H. Wiswall, J.J. Reilly, Hydrogen storage in metal hydrides, Science. 186 (1974) 1158. https://doi.org/10.1126/science.186.4170.1158-a.

[319] N.H. Goo, M. Hirscher, Synthesis of the nanocrystalline MgS and its interaction with hydrogen, J. Alloys Compd. 404-406 (2005) 503-506. https://doi.org/10.1016/j.jallcom.2004.12.192.

[320] V. Iosub, M. Latroche, J.M. Joubert, A. Percheron-Guégan, Optimisation of $MmNi_{5-x}Sn_x$ (Mm = La, Ce, Nd and Pr, $0.27<x<0.5$) compositions as hydrogen storage materials, Int. J. Hydrogen Energy. 31 (2006) 101-108. https://doi.org/10.1016/j.ijhydene.2005.02.004.

[321] M. Bououdina, J.L. Soubeyroux, P. De Rango, D. Fruchart, Phase stability and neutron diffraction studies of the laves phase compounds $Zr(Cr_{1-x}Mo_x)_2$ with $0.0 \le x \le 0.5$ and their hydrides, Int. J. Hydrogen Energy. 25 (2000) 1059-1068. https://doi.org/10.1016/S0360-3199(99)00087-7.

[322] Y. Chen, C.A.C. Sequeira, C. Chen, X. Wang, Q. Wang, Metal hydride beds and hydrogen supply tanks as minitype PEMFC hydrogen sources, Int. J. Hydrogen Energy. 28 (2003) 329-333. https://doi.org/10.1016/S0360-3199(02)00064-2.

[323] Z. Dehouche, N. Grimard, F. Laurencelle, J. Goyette, T.K. Bose, Hydride alloys properties investigations for hydrogen sorption compressor, J. Alloys Compd. 399 (2005) 224-236. https://doi.org/10.1016/j.jallcom.2005.01.029.

[324] S. Challet, M. Latroche, A. Percheron-Guégan, F. Heurtaux, Crystallographic and thermodynamic study of $La_{0.55}Y_{0.45}Ni_5$-H_2, a candidate system for hydrogen buffer tanks, J. Alloys Compd. 404-406 (2005) 85-88. https://doi.org/10.1016/j.jallcom.2005.01.127.

[325] P. Muthukumar, M.P. Maiya, S.S. Murthy, Experiments on a metal hydride-based hydrogen storage device, Int. J. Hydrogen Energy. 30 (2005) 1569-1581. https://doi.org/10.1016/j.ijhydene.2004.12.007.

[326] X. Wang, R. Chen, Y. Zhang, C. Chen, Q. Wang, Hydrogen storage alloys for high-pressure suprapure hydrogen compressor, J. Alloys Compd. 420 (2006) 322-325. https://doi.org/10.1016/j.jallcom.2005.11.001.

[327] D.S. Dos Santos, M. Bououdina, D. Fruchart, Structural and hydrogenation properties of an 80wt%$TiCr_{1.1}V_{0.9}$-20wt%$LaNi_5$ composite material, Int. J. Hydrogen Energy. 28 (2003) 1237-1241. https://doi.org/10.1016/S0360-3199(03)00006-5.

[328] Y. Liu, H. Pan, M. Gao, R. Li, X. Sun, Y. Lei, Investigation on the characteristics of $La_{0.7}Mg_{0.3}Ni_{2.65}Mn_{0.1}Co_{0.75+x}$ (x = 0.00-0.85) metal hydride electrode alloys for Ni/MH batteries Part II: electrochemical performances, J. Alloys Compd. 388 (2005) 109-117. https://doi.org/10.1016/j.jallcom.2004.07.014.

[329] M. Bououdina, H. Enoki, E. Akiba, The investigation of the $Zr_{1-y}Ti_y(Cr_{1-x}Ni_x)_2$-$H_2$ system 0.0≤y≤1.0 and 0.0≤x≤1.0 Phase composition analysis and thermodynamic properties, J. Alloys Compd. 281 (1998) 290-300. https://doi.org/10.1016/S0925-8388(98)00792-0.

[330] Y. Kojima, Y. Kawai, S. ichi Towata, T. Matsunaga, T. Shinozawa, M. Kimbara, Development of metal hydride with high dissociation pressure, J. Alloys Compd. 419 (2006) 256-261. https://doi.org/10.1016/j.jallcom.2005.08.078.

[331] L. Zaluski, A. Zaluska, P. Tessier, J.O. Ström-Olsen, R. Schulz, Effects of relaxation on hydrogen absorption in FeTi produced by ball-milling, J. Alloys Compd. 227 (1995) 53-57. https://doi.org/10.1016/0925-8388(95)01623-6.

[332] T. Kuriiwa, T. Tamura, T. Amemiya, T. Fuda, A. Kamegawa, H. Takamura, M. Okada, New V-based alloys with high protium absorption and desorption capacity, J. Alloys Compd. 293 (1999) 433-436. https://doi.org/10.1016/S0925-8388(99)00325-4.

[333] C.Y. Seo, J.H. Kim, P.S. Lee, J.Y. Lee, Hydrogen storage properties of vanadium-based b.c.c. solid solution metal hydrides, J. Alloys Compd. 348 (2003) 252-257. https://doi.org/10.1016/S0925-8388(02)00831-9.

[334] A. Takasaki, K.F. Kelton, Hydrogen storage in Ti-based quasicrystal powders produced by mechanical alloying, Int. J. Hydrogen Energy. 31 (2006) 183-190. https://doi.org/10.1016/j.ijhydene.2005.04.025.

[335] M. Okada, T. Kuriiwa, T. Tamura, H. Takamura, A. Kamegawa, Ti–V–Cr b.c.c. alloys with high protium content, J. Alloys Compd. 330-332 (2002) 511-516. https://doi.org/10.1016/S0925-8388(01)01647-4.

[336] X.B. Yu, Z.X. Yang, S.L. Feng, Z. Wu, N.X. Xu, Influence of Fe addition on hydrogen storage characteristics of Ti-V-based alloy, Int. J. Hydrogen Energy. 31 (2006) 1176-1181. https://doi.org/10.1016/j.ijhydene.2005.09.008.

[337] K. Nomura, E. Akiba, H_2 Absorbing-desorbing characterization of the TiVFe alloy system, J. Alloys Compd. 231 (1995) 513-517. https://doi.org/10.1016/0925-8388(95)01862-X.

[338] X.B. Yu, Z. Wu, B.J. Xia, N.X. Xu, Enhancement of hydrogen storage capacity of Ti-V-Cr-Mn BCC phase alloys, J. Alloys Compd. 372 (2004) 272-277. https://doi.org/10.1016/j.jallcom.2003.09.153.

[339] L. Gao, C. Chen, L. Chen, X. Wang, J. Zhang, X. Xiao, Q. Wang, Hydriding/dehydriding behaviors of $La_{1.8}Ca_{0.2}Mg_{14}Ni_3$ alloy modified by mechanical ball-milling under argon, J. Alloys Compd. 399 (2005) 178-182. https://doi.org/10.1016/j.jallcom.2005.03.028.

[340] H. Aoyagi, K. Aoki, T. Masumoto, Effect of ball milling on hydrogen absorption properties of FeTi, Mg_2Ni and $LaNi_5$, J. Alloys Compd. 231 (1995) 804-809. https://doi.org/10.1016/0925-8388(95)01721-6.

[341] D. Lu, W.S. Li, S. Hu, F. Xiao, R. Tang, Uniform nanocrystalline AB_5-type hydrogen storage alloy: Preparation and properties as negative materials of Ni/MH battery, Int. J. Hydrogen Energy. 31 (2006) 678-682. https://doi.org/10.1016/j.ijhydene.2005.07.006.

[342] S. Corré, M. Bououdina, D. Fruchart, G.Y. Adachi, Stabilisation of high dissociation pressure hydrides of formula $La_{1-x}Ce_xNi_5$ (x=0-0.3) with carbon monoxide, J. Alloys Compd. 275-277 (1998) 99-104. https://doi.org/10.1016/S0925-8388(98)00283-7.

[343] P. Dantzer, Properties of intermetallic compounds suitable for hydrogen storage applications, Mater. Sci. Eng. A. 329-331 (2002) 313-320. https://doi.org/10.1016/S0921-5093(01)01590-8.

[344] D.V. Bavykin, A.A. Lapkin, P.K. Plucinski, J.M. Friedrich, F.C. Walsh, Reversible storage of molecular hydrogen by sorption into multilayered TiO_2 nanotubes, J. Phys. Chem. B. 109 (2005) 19422-19427. https://doi.org/10.1021/jp0536394.

[345] J. Wu, J. Cao, W.Q. Han, A. Janotti, H.C. Kim, Functional Metal Oxide Nanostructures, Springer Ser. Mater. Sci. 149 (2012) 337-363. https://doi.org/10.1007/978-1-4419-9931-3.

[346] M.S. Whittingham, R.R. Chianelli, Layered compounds and intercalation chemistry: An example of chemistry and diffusion in solids, J. Chem. Educ. 57 (1980) 569-574. https://doi.org/10.1021/ed057p569.

[347] M.M. Thackeray, P.J. Johnson, L.A. de Picciotto, P.G. Bruce, J.B. Goodenough, Electrochemical extraction of lithium from $LiMn_2O_4$, Mater. Res. Bull. 19 (1984) 179-187. https://doi.org/10.1016/0025-5408(84)90088-6.

[348] K.M. Colbow, J.R. Dahn, R.R. Haering, Structure and electrochemistry of the spinel oxides $LiTi_2O_4$ and $Li_{4/3}Ti_{5/3}O_4$, J. Power Sources. 26 (1989) 397-402. https://doi.org/10.1016/0378-7753(89)80152-1.

[349] E. Ferg, R.J. Gummow, A. de Kock, M.M. Thackeray, Spinel anodes for lithium-ion batteries, J. Electrochem. Soc. 141 (1994) L147-L150.

[350] T. Ohzuku, A. Ueda, N. Yamamoto, Zero-Strain Insertion Material of $Li[Li_{1/3}Ti_{5/3}]O_4$ for Rechargeable Lithium Cells, J. Electrochem. Soc. 142 (1995) 1431-1435. https://doi.org/10.1149/1.2048592.

[351] J. Kim, J. Cho, Spinel $Li_4Ti_5O_{12}$ nanowires for high-rate Li-ion intercalation electrode, Electrochem. Solid-State Lett. 10 (2007) 81-84. https://doi.org/10.1149/1.2431242.

[352] Z. Yang, D. Choi, S. Kerisit, K.M. Rosso, D. Wang, J. Zhang, G. Graff, J. Liu, Nanostructures and lithium electrochemical reactivity of lithium titanites and titanium oxides: A review, J. Power Sources. 192 (2009) 588-598. https://doi.org/10.1016/j.jpowsour.2009.02.038.

[353] F. Tielens, M. Calatayud, A. Beltrán, C. Minot, J. Andrés, Lithium insertion and mobility in the TiO_2-anatase/titanate structure: A periodic DFT study, J. Electroanal. Chem. 581 (2005) 216-223.

[354] F. Gligor, S.W. de Leeuw, Lithium diffusion in rutile structured titania, Solid State Ionics. 177 (2006) 2741-2746. https://doi.org/10.1016/j.ssi.2006.03.017.

[355] S. Lunell, A. Stashans, L. Ojamäe, H. Lindström, A. Hagfeldt, Li and Na diffusion in TiO_2 from quantum chemical theory versus electrochemical experiment, J. Am. Chem. Soc. 119 (1997) 7374-7380. https://doi.org/10.1021/ja9708629.

[356] G. Armstrong, A.R. Armstrong, P.G. Bruce, P. Reale, B. Scrosati, TiO_2(B) nanowires as an improved anode material for lithium-ion batteries containing $LiFePO_4$ or $LiNi_{0.5}Mn_{1.5}O_4$ cathodes and a polymer electrolyte, Adv. Mater. 18 (2006) 2597-2600. https://doi.org/10.1002/adma.200601232.

[357] M.S. Whittingham, The role of ternary phases in cathode reactions, J. Electrochem. Soc. 123 (1976) 315-320. https://doi.org/10.1149/1.2132817.

[358] W. Li, J.R. Dahn, D.S. Wainwright, Rechargeable lithium batteries with aqueous electrolytes, Science. 264 (1994) 1115-1118. https://doi.org/10.1126/science.264.5162.1115.

[359] S. Zhang, Y. Li, C. Wu, F. Zheng, Y. Xie, Novel flowerlike metastable vanadium dioxide (B) micronanostructures: Facile synthesis and application in aqueous lithium ion batteries, J. Phys. Chem. C. 113 (2009) 15058-15067. https://doi.org/10.1021/jp903312h.

[360] N.S. Choi, J.S. Kim, R.Z. Yin, S.S. Kim, Electrochemical properties of lithium vanadium oxide as an anode material for lithium-ion battery, Mater. Chem. Phys. 116 (2009) 603-606. https://doi.org/10.1016/j.matchemphys.2009.05.013.

[361] J. Köhler, H. Makihara, H. Uegaito, H. Inoue, M. Toki, LiV_3O_8: Characterization as anode material for an aqueous rechargeable Li-ion battery system, Electrochim. Acta. 46 (2000) 59-65. https://doi.org/10.1016/S0013-4686(00)00515-6.

[362] S.S. Kim, H. Ikuta, M. Wakihara, Synthesis and characterization of MnV_2O_6 as a high capacity anode material for a lithium secondary battery, Solid State Ionics. 139 (2001) 57-65. https://doi.org/10.1016/S0167-2738(00)00816-X.

[363] S. Denis, E. Baudrin, M. Touboul, J. Tarascon, Synthesis and Electrochemical Properties of Amorphous Vanadates of General Formula RVO_4 (R = In, Cr, Fe, Al, Y) vs. Li, J. Electrochem. Soc. 144 (1997) 4099-4109. https://doi.org/10.1149/1.1838150.

[364] D. Guyomard, C. Sigala, A. Le Gal La Salle, Y. Piffard, New amorphous oxides as high capacity negative electrodes for lithium batteries: The $LixMVO_4$ (M = Ni, Co, Cd, Zn; $1 < x \leq 8$) series, J. Power Sources. 68 (1997) 692-697.

[365] S.H. Lee, Y.H. Kim, R. Deshpande, P.A. Parilla, E. Whitney, D.T. Gillaspie, K.M. Jones, A.H. Mahan, S. Zhang, A.C. Dillon, Reversible lithium-ion insertion in molybdenum oxide nanoparticles, Adv. Mater. 20 (2008) 3627-3632. https://doi.org/10.1002/adma.200800999.

[366] P. Balaya, H. Li, L. Kienle, J. Maier, Fully reversible homogeneous and heterogeneous Li storage in RuO_2 with high capacity, Adv. Funct. Mater. 13 (2003) 621-625. https://doi.org/10.1002/adfm.200304406.

[367] J. Hu, H. Li, X. Huang, Cr_2O_3-based anode materials for Li-ion batteries, Electrochem. Solid-State Lett. 8 (2005) A66. https://doi.org/10.1149/1.1836123.

[368] J. Chen, L. Xu, W. Li, X. Gou, α-Fe_2O_3 nanotubes in gas sensor and lithium-ion battery applications, Adv. Mater. 17 (2005) 582-586.

[369] Y. He, L. Huang, J.S. Cai, X.M. Zheng, S.G. Sun, Structure and electrochemical performance of nanostructured Fe_3O_4/carbon nanotube composites as anodes for lithium ion batteries, Electrochim. Acta. 55 (2010) 1140-1144. https://doi.org/10.1016/j.electacta.2009.10.014.

[370] A.L.M. Reddy, M.M. Shaijumon, S.R. Gowda, P.M. Ajayan, Coaxial MnO_2/Carbon Nanotube Array Electrodes for High-Performance Lithium Batteries, Nano Lett. 9 (2009) 1002-1006. https://doi.org/10.1021/nl803081j.

[371] N. Du, H. Zhang, B. Chen, J. Wu, X. Ma, Z. Liu, Y. Zhang, D. Yang, X. Huang, J. Tu, Porous Co_3O_4 nanotubes derived from $Co_4(CO)_{12}$ clusters on carbon nanotube templates: A highly efficient material for Li-battery applications, Adv. Mater. 19 (2007) 4505-4509. https://doi.org/10.1002/adma.200602513.

[372] Y. Li, B. Tan, Y. Wu, Freestanding mesoporous quasi-single-crystalline Co_3O_4 nanowire arrays, J. Am. Chem. Soc. 128 (2006) 14258-14259. https://doi.org/10.1021/ja065308q.

[373] Y. Li, B. Tan, Y. Wu, Mesoporous Co_3O_4 Nanowire Arrays for Lithium Ion Batteries with High Capacity and Rate Capability, Nano Lett. 8 (2008) 265-270. https://doi.org/10.1021/nl0725906.

[374] J. Ryu, S.W. Kim, K. Kang, C.B. Park, Synthesis of diphenylalanine/cobalt oxide hybrid nanowires and their application to energy storage, ACS Nano. 4 (2010) 159-164. https://doi.org/10.1021/nn901156w.

[375] J. Jiang, J. Liu, R. Ding, X. Ji, Y. Hu, X. Li, A. Hu, F. Wu, Z. Zhu, X. Huang, Direct synthesis of CoO porous nanowire arrays on Ti substrate and their application as lithium-ion battery electrodes, J. Phys. Chem. C. 114 (2010) 929-932.

[376] P.L. Taberna, S. Mitra, P. Poizot, P. Simon, J.M. Tarascon, High rate capabilities Fe_3O_4-based Cu nano-architectured electrodes for lithium-ion battery applications, Nat. Mater. 5 (2006) 567-573. https://doi.org/10.1038/nmat1672.

[377] L. Wang, Y. Yu, P.C. Chen, D.W. Zhang, C.H. Chen, Electrospinning synthesis of C/Fe_3O_4 composite nanofibers and their application for high performance lithium-ion batteries, J. Power Sources. 183 (2008) 717-723. https://doi.org/10.1016/j.jpowsour.2008.05.079.

[378] J. Liu, Y. Li, H. Fan, Z. Zhu, J. Jiang, R. Ding, Y. Hu, X. Huang, Iron oxide-based nanotube arrays derived from sacrificial template-accelerated hydrolysis: Large-area design and reversible lithium storage, Chem. Mater. 22 (2010) 212-217. https://doi.org/10.1021/cm903099w.

[379] M. V. Reddy, T. Yu, C.H. Sow, Z.X. Shen, C.T. Lim, G.V.S. Rao, B.V.R. Chowdari, α-Fe_2O_3 nanoflakes as an anode material for li-ion batteries, Adv. Funct. Mater. 17 (2007) 2792-2799. https://doi.org/10.1002/adfm.200601186.

[380] W.M. Zhang, X.L. Wu, J.S. Hu, Y.G. Guo, L.J. Wan, Carbon coated Fe_3O_4 nanospindles as a superior anode material for lithium-ion batteries, Adv. Funct. Mater. 18 (2008) 3941-3946. https://doi.org/10.1002/adfm.200801386.

[381] J.Y. Xiang, J.P. Tu, Y.F. Yuan, X.L. Wang, X.H. Huang, Z.Y. Zeng, Electrochemical investigation on nanoflower-like CuO/Ni composite film as anode for lithium ion batteries, Electrochim. Acta. 54 (2009) 1160-1165. https://doi.org/10.1016/j.electacta.2008.08.066.

[382] J.Y. Xiang, J.P. Tu, L. Zhang, Y. Zhou, X.L. Wang, S.J. Shi, Self-assembled synthesis of hierarchical nanostructured CuO with various morphologies and their application as anodes for lithium ion batteries, J. Power Sources. 195 (2010) 313-319. https://doi.org/10.1016/j.jpowsour.2009.07.022.

[383] B. Li, G. Rong, Y. Xie, L. Huang, C. Feng, Low-temperature synthesis of α-MnO_2 hollow urchins and their application in rechargeable Li+ batteries, Inorg. Chem. 45 (2006) 6404-6410. https://doi.org/10.1021/ic0606274.

[384] K.M. Shaju, F. Jiao, A. Débart, P.G. Bruce, Mesoporous and nanowire Co_3O_4 as negative electrodes for rechargeable lithium batteries, Phys. Chem. Chem. Phys. 9 (2007) 1837-1842. https://doi.org/10.1039/b617519h.

[385] U.W. Hartley, unpublished work, (n.d.).

[386] J. Liu, Y. Li, R. Ding, J. Jiang, Y. Hu, X. Ji, Q. Chi, Z. Zhu, X. Huang, Carbon/ZnO nanorod array electrode with significantly improved lithium storage capability, J. Phys. Chem. C. 113 (2009) 5336-5339. https://doi.org/10.1021/jp900427c.

[387] S.A. Needham, G.X. Wang, K. Konstantinov, Y. Tournayre, Z. Lao, H.K. Liu, Electrochemical performance of Co_3O_4-C composite anode materials, Electrochem. Solid-State Lett. 9 (2006) 315-319.

[388] Y. Yu, C.H. Chen, Y. Shi, A tin-based amorphous oxide composite with a porous, spherical, multideck-cage morphology as a highly reversible anode material for lithium-ion batteries, Adv. Mater. 19 (2007) 993-997. https://doi.org/10.1002/adma.200601667.

[389] H.K. Liu, G.X. Wang, Z. Guo, J. Wang, K. Konstantinov, Nanomaterials for lithium-ion rechargeable batteries, J. Nanosci. Nanotechnol. 6 (2006) 1-15. https://doi.org/10.1166/jnn.2006.103.

[390] S.H. Ye, J.Y. Lv, X.P. Gao, F. Wu, D.Y. Song, Synthesis and electrochemical properties of $LiMn_2O_4$ spinel phase with nanostructure, Electrochim. Acta. 49 (2004) 1623-1628. https://doi.org/10.1016/j.electacta.2003.12.001.

[391] S. Nordlinder, K. Edström, T. Gustafsson, The performance of vanadium oxide nanorolls as cathode material in a rechargeable lithium battery, Electrochem. Solid-State Lett. 4 (2001) 129-131. https://doi.org/10.1149/1.1382888.

[392] C.J. Patrissi, C.R. Martin, Sol-gel-based template synthesis and li-insertion rate performance of nanostructured vanadium pentoxide, J. Electrochem. Soc. 146 (1999) 3176-3180. https://doi.org/10.1149/1.1392451.

[393] F. Jiao, K.M. Shaju, P.G. Bruce, Synthesis of nanowire and mesoporous low-temperature $LiCoO_2$ by a post-templating reaction, Angew. Chemie - Int. Ed. 44 (2005) 6550-6553. https://doi.org/10.1002/anie.200501663.

[394] Y. Zhu, C. Wang, Galvanostatic intermittent titration technique for phase-transformation electrodes, J. Phys. Chem. C. 114 (2010) 2830-2841. https://doi.org/10.1021/jp9113333.

[395] Z. Chen, J.R. Dahn, Reducing Carbon in $LiFePO_4$/C Composite Electrodes to Maximize Specific Energy, Volumetric Energy, and Tap Density, J. Electrochem. Soc. 149 (2002) A1184. https://doi.org/10.1149/1.1498255.

[396] A.D. Robertson, A.R. Armstrong, P.G. Bruce, Layered $Li_xMn_{1-y}Co_yO_2$ intercalation electrodes - Influence of ion exchange on capacity and structure upon cycling, Chem. Mater. 13 (2001) 2380-2386. https://doi.org/10.1021/cm000965h.

[397] J.B. Goodenough, Y. Kim, Challenges for rechargeable Li batteries, Chem. Mater. 22 (2010) 587-603. https://doi.org/10.1021/cm901452z.

[398] P. Lightfoot, M.A. Mehta, P.G. Bruce, Crystal structure of the polymer electrolyte poly(ethylene oxide)$_3$:$LiCF_3SO_3$, Science. 262 (1993) 883-885. https://doi.org/10.1126/science.262.5135.883.

ABBRIVIATIONS AND ACRONYM

BCG	*bio-circular-green economy*
WS	*water splitting*
CDS	*CO_2 splitting*

TPR	*temperature-programmed reduction*
OSC	*oxygen storage capacity*
LSM	$La_{1+x}Sr_xMnO_{3-\delta}$
LSCF	$La_{0.3}Sr_{0.7}Co_{0.7}Fe_{0.3}O_3$
TPSR	*temperature-programmed surface reaction*
BF	$BaFeO_{3-\delta}$
E_a	*activation energy*
k_0	*pre-exponential factor*
BLF	$Ba_{0.95}La_{0.05}FeO_{3-\delta}$
PTC	*photo-thermochemical cycles*
SO_2	*sulfur dioxide*
VOCs	*volatile organic compounds*
NO_x	*nitrogen oxides*
PM	*particulate matter*
soot	*solid carbon*
HC	*hydrocarbon*
TWCs	*three-way catalysts*
DOCs	*diesel oxidation catalysts*
DPFs	*diesel particulate filters*
SCR	*selective catalytic reduction*
LNT	*lean* NO_x *trapping*
DPNR	*diesel particulate* NO_x *reduction*
TOF	*turnover frequency*

ER	*Eley-Rideal mechanism partway*
LH	*Langmuir-Hinshelwood mechanism pathway*
CRT	*continuous regenerating trap*
NSR	NO_x *storage reduction*
MMO	*mixed metal oxide*
LDHs	*layered double hydroxides*
3DOM	*three-dimensional ordered macroporous*
SCS	*solution combustion synthesis*
LDOs	*layered double oxides*
SOFCs	*solid oxide fuel cells*
AFCs	*alkaline fuel cells*
DMFCs	*direct methanol fuel cells*
PEMFCs	*proton exchange membrane fuel cells*
PAFCs	*phosphoric acid fuel cells*
MCFCs	*molten carbonate fuel cells*
YSZ	*yttria-stabilized zirconia*
MIEC	*mixed ionic and electronic conductivity*
PBCO	$PrBaCo_2O_5$
PBMO	$PrBaMn_2O_{5+\delta}$
SFM-GDC	$Sr_2Fe_{1.5}Mo_{0.5}O_{6-\delta}/Gd_{0.1}Ce_{0.9}O_{2-\delta}$
LSCM	$La_{0.75}Sr_{0.25}Cr_{0.5}Mn_{0.5}O_3$
LSCrF	$La_{0.75}Sr_{0.25}Cr_{0.5}Fe_{0.5}O_{3-\delta}$
LSM	$La_xSr_{1-x}MnO_3$

OCPDs	*open-circuit potential differences*
LSCF	$La_{0.6}Sr_{0.4}Co_{0.2}Fe_{0.8}O_{3-\delta}$
OPM	*ceramic-based oxygen permeation membrane*
8YSZ	8% by mole of Y_2O_3-ZrO_2
ScSZ	Sc_2O_3 *doped* ZrO_2
LSM	*lanthanum strontium manganite*
MOFs	*metal-organic frameworks*
TMOs	*transition metal oxides*
HNs	*hierarchical nanostructures*
HMFs	*hollow microflowers*
P-C	*pressure-composition*
Mm	*Misch metals*
BM	*ball-milling*
BCC	*body centered cubic*
Li-ion	*lithium-ion*
SEI	*solid electrolyte interface*
PEO	*poly (ethylene oxide)*

INDEX